High-Efficiency III-V Semiconductor Device and System Optimization for Photovoltaic Applications

by

Gavin Forcade

A thesis presented to the University of Ottawa
in fulfillment of the thesis requirement for the degree of:
Doctor of Philosophy in Physics

Ottawa, Ontario, Canada, 2025

© Gavin Forcade, Ottawa, Canada 2025

Examining Committee Membership

The following people served on the Examining Committee for this thesis.

Supervisor:	Karin Hinzer University Research Chair in Photonic Devices for Energy Vice-Dean, Research, Faculty of Engineering School of Electrical Engineering and Computer Science University of Ottawa
Internal Examiner:	Dan Dalacu Adjunct Professor Department of Physics University of Ottawa
Internal Examiner:	Ksenia Dolgaleva Associate Professor School of Electrical Engineering and Computer Science University of Ottawa
External Examiner:	Yue Zhang Associate Professor Department of Physics Carleton University
External Examiner:	Stephen Goodnick David and Darleen Ferry Professor of Electrical Engineering School of Electrical, Computer, and Energy Engineering Arizona State University

Abstract

This thesis addresses barriers to adopting high-efficiency photovoltaic devices through innovative structured surfaces, device designs, and epitaxial growth. I demonstrate improvements using these techniques, through a combination of experiments and simulations. First, structured surfaces are investigated to enhance the performance of photovoltaic systems under concentrated sunlight. Second, novel photovoltaic designs are explored to improve the conversion of infrared or monochromatic light into electrical power. Third, the properties of III-V epitaxy on nonplanar surfaces are studied for substrate reuse applications.

Integrating structured surfaces into photovoltaic systems enhances their performance. High-efficiency photovoltaic devices, based on the epitaxial growth of III-V semiconductor materials, are expensive due to the scarcity of these elements. They are integrated into concentrator photovoltaic systems, which focus sunlight onto the photovoltaic cell, making terrestrial III-V solar cells cost-competitive with silicon-based solar cells. These cells are coated with an encapsulant to shield them from environmental damage. This thesis explores a microstructured encapsulant, comparing it with a standard encapsulant for these systems, and finds up to a 3.4% improvement in optical performance. Additionally, this thesis shows that the new encapsulant could extend the concentrator system's temperature range operating at high efficiencies.

Optimizing devices at the component level enhances photovoltaic performance for infrared to electrical power conversion. Waste heat is an abundant and largely untapped energy source that can be harnessed using high-efficiency photovoltaic devices. Existing photovoltaic devices achieve efficiencies of less than 1.5% for waste heat applications. This thesis presents a III-V photovoltaic device design optimized for waste heat recovery, predicted to achieve up to 15% efficiency in converting waste heat at 900 K into electrical power. A modified version of this optimized device is then fabricated and characterized.

Device-level optimization augments photovoltaic performance for monochromatic to electrical power conversion. Power by light offers an attractive alternative to transmitting power over metallic wires, especially when wires are unfavorable or impractical. These systems generally consist of lasers (at the light source) and photonic power converters. Most commercially available photonic power converters are based on GaAs and require optical wavelengths with

short-range transmission through optical fibers. This thesis presents the design and characterization of photonic power converters for optical wavelengths within the transmission window of optical fibers, enabling much longer power transmission capabilities. These optimized devices breach the 50% efficiency barrier, achieving efficiencies of up to 53.6%.

Epitaxial growth provides an effective method to planarize faceted surfaces, facilitating the substrate reuse process. Substrate reuse promises significant cost reductions for III-V photovoltaics. A promising method is to fracture the epitaxial layers from the bulk substrate crystal, known as spalling. Spalling GaAs(100) substrates, commonly used for III-V photovoltaics, generates a rough surface of faceted ridges that need to be planarized for reuse. This thesis explores planarizing this surface using metal-organic vapor phase epitaxy. The optimized process planarizes the surface within 8 minutes of growth, using up to 95% of the nominally deposited material, which is much faster than the hours required to grow high-efficiency devices. Overall, this thesis aims to increase efficiencies and reduce the costs of III-V photovoltaics.

Acknowledgements

First, I'd like to thank my supervisor, Prof. Karin Hinzer, for her guidance throughout my graduate studies. I always looked forward to my meetings with Karin due to her unabated positive attitude. Her resourcefulness helped me tremendously by allowing me to work on several different projects during my Ph.D. research, which gave me experience working collaboratively with the top two photovoltaic research centers in the world, Fraunhofer ISE and National Renewable Energy Laboratory (NREL).

Second, I would like to thank the "co-supervisors" who had a significant impact on my research journey. I am very grateful to Christopher Valdivia, a research scientist at SUNLAB, who essentially co-supervised me during my first 5 years as a graduate student. His patience towards my initial crappy writing is much appreciated. The improvement in my writing skills, evident in the chronological progression of my published manuscripts, is largely due to his guidance. I am also grateful to Prof. Jacob Krich for his exceptional input on my research direction and his super helpful feedback on my scientific writing and presentation. Although his initial critiques of my oral presentations were daunting, they proved crucial in preparing me for the numerous conferences I attended. A special thanks goes to Bill McMahon, who dedicated hours to teaching me III-V epitaxial growth, warmly welcomed me during my visit at NREL, and even provided me with a rice cooker. Lastly, sincere thanks to Raphael St-Gelais for his crucial guidance during my research on near-field thermophotovoltaics.

Thanks to Erin Tonita for her invaluable assistance with writing my grant proposals, which was essential for my well-being and my internship at NREL. She also taught me the beast that is Sentaurus. I am very grateful for the support and love she provided me. I also thank Mathieu de LaFontaine for teaching me the ways of semiconductor device fabrication and showing me how to enjoy the process.

I would also like to express my gratitude to Alexandre Walker for his recent involvement in my life/work. His feedback on my writing has shifted my perspective on editing for the better. Thank you to Paige Wilson, Meghan Beattie, and Louis-Philippe St-Arnaud for their company and input during experiments. A special thanks to Robert Hunter for his amazing memes and humor; we formed a formidable graduate student team for the Aiirpower project.

I would like to thank the following people that I interacted with during my internship at NREL: Ryan France, Myles Steiner, Anica Neumann, Theresa Saenz, Nicholas Yoo, Sarah Collins, Corinne E. Packard, and Emily Warren. They provided me with an amazingly warm welcome, it was awesome to be surrounded by these hyper-smart people. Special thanks to Ryan for answering the cold email I sent which created the collaboration.

I would also like to thank the following folks from Fraunhofer ISE: Henning Helmers, Oliver Hohn, David Lackner, and Carmine Pellegrino. They all provided invaluable input for my research on photonic power converters and their growth and fabrication of my designs.

I would also like to thank my collaborators from Université de Sherbrooke: Arnaud Ritou, Maxime Darnon, and Philippe St-Pierre. They performed most of the experimental work on the microstructured surfaces project. Special thanks to Arnaud for hosting me and some fellow SUNLABourers during a trip to Sherbrooke.

I extend my thanks to the rest of the SUNLAB graduate and undergraduate students who came and left during my studies. They made graduate life fun and were a large reason for my choice to fast-track toward my PhD. I also wanted to thank the Canadian taxpayers and my parents for supporting me since I was born, I am eager to contribute back to society through my tax dollars.

I used Microsoft's Copilot and Grammarly for editing the writing in this thesis.

Statement of originality

I am the sole author of this thesis. Chapters 1 and 2 provide background information from literature for my thesis research. Chapters 3 to 6 are original contributions. A detailed breakdown of the specific contributions of each author precedes each publication within the chapters. Unless otherwise stated, I performed the experiments, simulations, and data analysis, and was the main author of the text and figures.

Contributions

The research presented in this thesis has led to several publications and conference presentations, listed below.

Journal articles

1. **G.P. Forcade**, D.P. Wilson, M.N. Beattie, C. Pellegrino, H. Helmers, R.F.H. Hunter, O. Hohn, D. Lackner, L-P. St-Arnaud, T.N.D. Tibbits, C.E. Valdivia, Y. Grinberg, A.W. Walker, J.J. Krich, and K. Hinzer, "53.6% efficient multi-junction laser power converter for extended telecom range operation", under revisions 2024.

2. **G.P. Forcade**, M. de Lafontaine, M. Giroux, A. Tam, Z. Wasilewski, J.J. Krich, R. St-Gelais, and K. Hinzer, "Epi-grown broadband reflector for InA-based thermophotovoltaics", under review 2024.

3. **G.P. Forcade**, W.E. McMahon, N. Yoo, A.N. Neumann, M. Young, J. Goldsmith, S. Collins, K. Hinzer, C.E. Packard, and M.A. Steiner, "Planarizing spalled GaAs(100) surfaces by MOVPE Growth", *Crystal Growth & Design*, 23, 24, 2024. DOI: 10.1021/acs.cgd.4c01152

4. M.N Beattie, H. Helmers, **G.P. Forcade**, C.E. Valdivia, O. Hohn, and K. Hinzer, "InP- and GaAs-Based Photonic Power Converters Under O-Band Laser Illumination: Performance Analysis and Comparison", *IEEE Journal of Photovoltaics*, 13, 1, 2023.

5. **G.P. Forcade**, C.E. Valdivia, S. Molesky, S. Lu, A.W. Rodriguez, J.J. Krich, R. St-Gelais, and K. Hinzer, "Efficiency-Optimized Near-Field Thermophotovoltaics Using InAs and InAsSbP", *Applied Physics Letters*, 121, 19, 2022. [**Featured Article**]
6. **G.P. Forcade**, A. Ritou, P. St-Pierre, O. Dellea, M. Volatier, A. Jaouad, C.E. Valdivia, K. Hinzer, and M. Darnon, "Microstructured Antireflective Encapsulant on Concentrator Solar Cells", *Progress in Photovoltaics: Research and Applications*, 30, 2, 2021.

Conference proceedings

1. A. Ritou, P. St-Pierre, P. Provost, **G.P. Forcade**, C. Duboc, O. Dellea, G. Hamon, M. Volatier, A. Jaouad, C.E. Valdivia, K. Hinzer, V. Aimez, and M. Darnon, "CPV Module to Rate Antireflective and Encapsulant Coating in Outdoor Conditions", *AIP Conference Proceedings*, 2550, 030004, 2022.
2. **G.P. Forcade**, C.E. Valdivia, P. St-Pierre, A. Ritou, M. Volatier, A. Jaouad, M. Darnon, and K. Hinzer, "Nanostructured Surface for Extended Temperature Operating Range in Concentrator Photovoltaic Modules", *CPV-16 Conference proceedings*, 6145, 2020.

Conference presentations

Presenter

1. **G.P. Forcade**, W.E. McMahon, N. Yoo, A.N. Neumann, M. Young, J. Goldsmith, K. Hinzer, C.E. Packard, M.A. Steiner, "Planarizing Spalled GaAs(100) Surfaces by MOVPE Growth", *52nd IEEE Photovoltaic Specialists Conference (PVSC)*, Seattle, USA, 2024. [Oral, **Best student finalist**]
2. **G.P. Forcade**, M.N. Beattie, C.E. Valdivia, H. Helmers, O. Hohn, P. Wilson, L-P. St-Arnaud, R.F. Hunter, D. Lackner, J.J. Krich, A.W. Walker, and K. Hinzer, "High-Performance Multi-Junction C-Band Photonic Power Converters: Calibrated Optoelectronic Model for Next Generation Designs", *50th IEEE Photovoltaic Specialists Conference (PVSC)*, San Juan, Puerto Rico, 2023. [Oral, **Best student finalist**]

3. **G.P. Forcade**, C. E. Valdivia, S. Molesky, S. Lu, A.W. Rodriguez, J.J. Krich, R. St-Gelais, and K. Hinzer, "Optimized Near-Field Thermophotovoltaic Cell using InAs and InAsSbP", *49th IEEE Photovoltaic Specialists Conference (PVSC)*, Philadelphia, USA, 2022. [Poster, **Best poster finalist**]

4. **G.P. Forcade**, C. E. Valdivia, S. Lu, S. Molesky, A.W. Rodriguez, J.J. Krich, R. St-Gelais, and K. Hinzer, "Impact of Absorption Layer Thickness on InAs-based NFTPV Device Performance", *TPV 13*, Virtual, Miyazaki, Japan, 2022. [Oral]

5. **G.P. Forcade**, C. E. Valdivia, S. Lu, S. Molesky, A.W. Rodriguez, J.J. Krich, R. St-Gelais, and K. Hinzer, "Modeling Efficiency of InAs-Based Near-Field Thermophotovoltaic Devices", *Numerical Simulation of Optoelectronic Devices (NUSOD)*, Virtual, Torino, Italy, 2021. [Oral]

6. **G.P. Forcade**, C. E. Valdivia, M. Darnon, and K. Hinzer, "Nanostructured Surfaces in Concentrator Photovoltaic Systems to Improve Temperature-Dependent Energy Output", *Canadian Semiconductor Science and Technology Conference (CSSTC)*, Saskatoon, Canada, 2019. [Oral]

7. **G.P. Forcade**, C. E. Valdivia, P. St-Pierre, M. Darnon, and K. Hinzer, "Improving Temperature-Dependent Energy Output of Concentrator Photovoltaic Systems using Nanotextured Surfaces" *Numerical Simulation of Optoelectronic Devices (NUSOD)*, Ottawa, Canada, 2019. [Oral]

8. **G.P. Forcade**, C. E. Valdivia, P. St-Pierre, M. Darnon, and K. Hinzer, "Modeling the Incorporation of Microbeads into Concentrator Photovoltaic Systems", *Photonics North*, Quebec City, Canada, 2019. [Poster]

Co-author

1. A.N. Neumann, **G.P. Forcade**, W.E. McMahon, P.G. Coll, M.I. Bertoni, M.A. Steiner, E.L. Warren, "In-Situ MOVPE Smoothing of Acoustically Spalled GaAs for Substrate Reuse", *52nd IEEE Photovoltaic Specialists Conference (PVSC)*, Seattle, USA, 2024. [Oral, **Best student finalist**]

2. M. de Lafontaine, R.F.H. Hunter, **G.P. Forcade**, J.P.D. Cook, D. Drouin, J.J. Krich, K. Hinzer, “p-i-n Betavoltaic Cells under 63Ni Irradiation: Quantifying Carrier Collection and Power Output”, *52nd IEEE Photovoltaic Specialists Conference (PVSC)*, Seattle, USA, 2024. [Oral]

3. K. Hinzer, R.F. Hunter, D.P. Wilson, **G.P. Forcade**, M.N. Beattie, C.E. Valdivia, O.Hohn, L-P.St-Arnaud, C. Pellegrino, D. Lackner, Y. Grinberg, J.J. Krich, A.W. Walker, H. Helmers, “Multi-junction photonic power converters: AI enhanced design optimization”, *52nd IEEE Photovoltaic Specialists Conference (PVSC)*, Seattle, USA, 2024. [Poster]

4. N.J. Yoo, S. Collins, **G.P. Forcade**, W.E. McMahon, M. Young, J. Goldsmith, C.E. Packard, M.A. Steiner, “Full Wafer Spalling and Cell Processing of Devices Grown on GaAs(100) Substrates”, *52nd IEEE Photovoltaic Specialists Conference (PVSC)*, Seattle, USA, 2024. [Poster]

5. Y. Grinberg, D.-X. Xu, M.Al-Digeil, D. Melati, R.F. Hunter, A.W. Walker, **G.P. Forcade**, J.J. Krich, K.Hinzer, M.M. Masnad, O. Liboiron-Ladoceur, P. Cheben, J. H. Schid, and S. Janz, “Dimensionality Reduction in Photonics Design – New Methods and Applications”, *Photonics North*, Vancouver, Canada, 2024. [Invited talk]

6. K. Hinzer, R.F. Hunter, D.P. Wilson, **G.P. Forcade**, M.N. Beattie, C.E. Valdivia, O.Hohn, L-P.St-Arnaud, D. Lackner, Y. Grinberg, M. de Lafontaine, C. Pellegrino, J.J. Krich, A.W. Walker, H. Helmers, “C-band Multi-Junction Photonic Power Converters: AI Techniques for Optimized Designs and Role of Luminescent Coupling”, *6th Optical Wireless and Fiber Power Transmission Conference (OWPT)*, Japan, 2024. [Invited talk]

7. R.F. Hunter, **G.P. Forcade**, Y. Grinberg, M.N. Beattie, D.P. Wilson, C.E. Valdivia, M. de Lafontaine, L-P. St-Arnaud, H. Helmers, O. Hohn, D. Lackner, C. Pellegrino, J.J. Krich, A.W. Walker, K. Hinzer, “Using machine learning to optimize multi-junction photonic power converters”, *Photonics West*, San Fransisco, USA, 2024. [Oral]

8. P. Wilson, **G.P. Forcade**, R.F. Hunter, M.N. Beattie, A.W. Walker, Y. Grinberg, H. Helmers, O. Hohn, D. Lackner, J.J. Krich, K. Hinzer, “Quantifying the luminescent coupling process in C-band multi-junction photonic power converters”, *Photonics West*, San Fransisco, USA, 2024. [Oral]

9. K. Hinzer, M.N. Beattie, N. Nouri, H. Helmers, **G.P. Forcade**, C.E. Valdivia, O. Hohn, J.J. Krich, "Strategies for High-Performance O-Band Photonic Power Converters," *Physics, Simulations, and Photonic Engineering of Photovoltaic Devices XII*, San Fransisco, USA, 2023. [Invited talk]

10. M. Giroux, C. Zhang, **G.P. Forcade**, M. Stephan, M. Brazeau, S. Molesky, A.W. Rodriguez, J.J. Krich, K. Hinzer, and R. St-Gelais, "Nanomechanical Resonators and High Flatness Silicon MEMS Radiators for Near-Field Radiative Heat Transfer Measurements", *TPV-14*, Virtual, 2023. [Oral]

11. M. De LaFontaine, **G.P. Forcade**, P. Wilson, J. Patel, B. Ellis, H. Fritzsche, S. Suppiah, J.P.D. Cook, C.E. Valdivia, and K. Hinzer, "GaAs Betavoltaic Cell Modeling for Light to Medium Element Radiation Conversion into Electrical Power," *50th IEEE Photovoltaics Specialists Conference (PVSC)*, San Juan, Puerto Rico, 2023. [Poster]

12. M.N. Beattie, H. Helmers, **G.P. Forcade**, C.E. Valdivia, D. Lackner, O. Hohn, and K. Hinzer, "High-Performance O-Band Photonic Power Converters Under Non-Uniform Laser Illumination," *49th IEEE Photovoltaics Specialists Conference (PVSC)*, Philadelphia, USA, 2022. [Oral]

Table of contents

Examining Committee **ii**

Abstract **iii**

Acknowledgements **v**

Statement of originality **vii**

List of figures **xv**

List of abbreviations **xviii**

List of Symbols **xx**

1 Introduction **1**

1.1 Concentrator photovoltaics 2

1.2 Waste heat recovery 4

1.3 Power-by-light 6

1.4 Cost reduction 8

1.5 Thesis outline 10

2 **Physics of semiconductors, light, & photovoltaics** **12**

2.1 Inorganic semiconductor materials . . . 12

2.1.1 Crystal structure . . . 13

2.1.2 Crystal growth . . . 13

2.1.3 Binary, ternary, and quaternary alloys . . . 15

2.1.4 Energy band structure . . . 17

2.1.5 Density of states, carrier density, and doping . . . 18

2.1.6 Carrier mobility . . . 21

2.1.7 Transport equations . . . 21

2.1.8 Drift and diffusion . . . 23

2.1.9 Generation-recombination . . . 23

2.2 Light-semiconductor properties . . . 26

2.2.1 Semiconductor optical properties . . . 27

2.2.2 Bulk-semiconductor optics . . . 29

2.2.3 Thin-film semiconductor optics . . . 30

2.2.4 Structured surface optics . . . 32

2.2.5 Thermal radiation . . . 34

2.3 Photovoltaic power conversion . . . 38

2.3.1 p-n junctions . . . 38

2.3.2 Current-voltage characteristics . . . 40

2.3.3 Quantum efficiency . . . 42

2.3.4 Multi-junction photovoltaics . . . 44

2.4 Simulating optoelectronic devices . . . 47

2.4.1 Optical models . . . 47

2.4.2 Distributed circuit model . . . 48

2.4.3 Drift diffusion model . . . 50

3 Microstructured surfaces for concentrator photovoltaics 52

3.1 Nanostructured surface for extended temperature operating range in CPV modules 53

3.2 Microstructured antireflective encapsulant on concentrator solar cells 62

4 Near-field thermophotovoltaics (NFTPVs) 73

4.1 Efficiency-optimized near-field thermophotovoltaics using InAs and InAsSbP . . 73

4.2 Fabricated NFTPV devices 90

4.2.1 Device design and epi-growth 90

4.2.2 Fabrication process 91

4.2.3 Ohmic contact deposition 94

4.2.4 Mesa etching 95

4.2.5 Manuscript 96

5 Photonic power converters (PPCs) for 1-1.6 μm laser wavelengths 110

5.1 InP- and GaAs-based photonic power converters under O-band laser illumination: performance analysis and comparison 110

5.2 53.6% Efficient multi-junction laser power converters for extended telecom range operation 122

6 Substrate reuse 153

6.1 Planarizing spalled GaAs(100) surfaces by MOVPE growth 153

7 Summary & outlook 171

References 174

List of Figures

1.1 Concentrator photovoltaics introduction 3

1.2 Waste heat introduction 5

1.3 Photonic power converter introduction 7

1.4 III-V cost reduction pathways 8

1.5 Substrate reuse introduction 10

2.1 GaAs crystal 14

2.2 Surface reconstruction of GaAs 16

2.3 Schematic diagrams of the charge carrier energy (E) as a function of its wavevector (k) for **a** direct bandgaps and **b** indirect bandgaps. The photon absorption processes are also highlighted for both types of bandgaps. The conduction band is at the top and the valence band is at the bottom. 18

2.4 Density of states and charge carrier populations 20

2.5 Doping dependent mobilities 22

2.6 Schematic representations of **a** photogeneration and thermalization, **b** radiative recombination (left) and photon recycling (right), **c** Shockley-Read-Hall recombination, and **d** Auger recombination. 24

2.7 Band filling effect. 29

2.8 Schematic diagrams of light management for: **a** light impinging an air/semiconductor interface, **b** all light transmitting into the semiconductor due to an antireflection coating and all light reflecting off a perfect back reflector for a two-pass chance at absorption, **c** sub-wavelength structured surface which creates an effective gradual change in refractive index to eliminate reflection, and **d** a light-trapping scheme for a multi-junction device. 31

2.9 Schematic showing the propagation of electric fields through a layer stack as defined by TMM. 33

2.10 Solar and blackbody spectra 36

2.11 Band profiles as a function of the spatial coordinate going across a p-n homojunction. In the dark and **a** at equilibrium, or **b** in forward bias. Under illumination **c** at short-circuit, or **d** in forward bias. E_{c} and E_{v} is the conduction and valence band energies, $E_{\mathrm{F}n}$ and $E_{\mathrm{F}p}$ are the electron and hole quasi-Fermi levels, E_{F} is the Fermi level, V is the applied bias, q is the elementary charge, and V_{bi} is the built-in bias. 40

2.12 Current-voltage characteristics of a photovoltaic device, **a** in the dark with a logarithmic scaled vertical axis and **b** under illumination. **a** The dark current includes the diffusion current I_{diff} and the space charge region current I_{scr}. **b** The short-circuit current I_{sc}, open-circuit voltage V_{oc}, maximum power point P_{MPP}, current at maximum power I_{MPP}, and voltage at maximum power V_{MPP} are highlighted. **c** An example external quantum efficiency curve for a PV device with bandgap E_{g} 43

2.13 **a** Schematic diagram of a multi-junction photovoltaic device where part of the light is absorbed in each subcell. **b** Band diagram of a multi-junction device in the dark and under forward bias, with 2 subcells and a tunnel diode (TD). . . 45

2.14 Ray tracing used for a concentrator photovoltaic submodule. Light rays emitted from the source are directed towards a Fresnel lens, which refracts and focuses the rays onto the solar cell. 48

2.15 Representation of photovoltaic devices with a distributed circuit. 49

2.16 TCAD Sentaurus tool flow. 51

4.1 Redesigned near-field thermophotovoltaic device to follow constraints for fabrication, designed for a highly doped Silicon radiator at 750 K and a 0.1 μm gap. **a** Schematic of the new design. **b** Simulated performance of the device. **c** Stack plot of the simulated spectral absorption within each layer. 91

4.2 Fabrication process for the near-field thermophotovoltaic device. 92

4.3 **a** Schematic diagram of circular transfer length method contact pads. **b** Sample transfer length method measurements for an ohmic contact to p-InAs compared to the fit to Eq. (4.1). 95

4.4 Measured etched depth as a function of etching time for InAs etched with a citric acid solution. "No stirring" and "Large sample" were both not stirred. The rest were etched with a stirred solution. 96

List of abbreviations

CPV concentrator photovoltaic 1–3, 10, 11, 47, 52, 53, 62, 171, 173

DCM distributed circuit model 50, 172

EQE external quantum efficiency 42, 44

GaAs gallium arsenide 13–16, 110, 111, 153, 154

Ge germanium 13

InP indium phosphide 13, 28, 29, 110, 111

IQE internal quantum efficiency 44

IV current-voltage 40–42, 48, 50, 94, 122, 123

MBE molecular beam epitaxy 13–15, 90

MOCVD metalorganic chemical vapor deposition 14

MOVPE metalorganic vapor phase epitaxy 13–15, 153, 172

NFTPV near-field thermophotovoltaic 4, 5, 11, 28, 73, 74, 90, 91, 96, 97, 171–173

NREL National Renewable Energy Laboratory v, vi

OMVPE organometallic vapor phase epitaxy 14

PDMS polydimethylsiloxane 3, 52, 53, 62, 171, 173

PPC photonic power converter 6, 7, 11, 26, 46, 110, 111, 122, 123, 171–173

PV photovoltaic 1, 2, 4, 6, 8–12, 26, 28, 32, 34, 38–42, 44, 46, 47, 50, 51, 74, 95, 153, 171–173

QE quantum efficiency 62

RCWA rigorous coupled wave analysis 33, 34, 47, 48, 122

RHEED reflection high-energy electron diffraction 14

Si silicon 2, 13, 26

SRH Shockley-Read-Hall 25, 26, 40, 41, 172

TMM transfer matrix method 30, 32–34, 37, 47

List of Symbols

E_{g} Semiconductor bandgap energy 17, 28, 42, 44

I_{sc} Short-circuit current 41, 42, 44, 46

V_{oc} Open-circuit voltage 41, 42, 46

Chapter 1

Introduction

Photovoltaic (PV) devices are designed to convert photonic irradiance into electrical power. Among various material classes, III-V PVs have achieved the highest efficiencies due to their superior crystalline quality and tuneable bandgaps [1]. However, using scarce elements makes them prohibitively expensive for all but space [2] and some terrestrial applications. For terrestrial applications, existing III-V devices have been tested in several areas, including concentrated solar PV [3], power-by-light transmission [4], waste-heat energy recovery [5–7], and energy storage [8].

To increase the utilization of III-V PVs, this thesis focuses on integrating structured surfaces into PV systems, improving PV device design, and using epitaxial growth to advance III-V substrate reuse. I start by integrating structured surfaces into III-V based concentrator photovoltaic (CPV) systems to improve their efficiency. However, it became evident that the high costs associated with III-V PVs render them ill-suited for most terrestrial solar applications. Consequently, my focus shifted towards optimizing device designs for two other terrestrial applications where high costs are less prohibitive; waste-heat recovery and power-by-light transmission. After optimizing for these applications, it was determined that significant cost reductions are necessary to increase the deployment of III-V PV technology, prompting research into epitaxial growth on non-planar surfaces for cost reduction strategies.

1.1 Concentrator photovoltaics

This section explores using a microstructured encapsulant to enhance system-level performance for the CPV technology. One method to improve the economics of III-V solar PVs is to use the CPV technology, which consists of using a cheaper optical system to concentrate sunlight onto small but highly efficient PV cells [3]. A CPV sub-module is depicted in Fig. 1.1a. These optical systems consist of mirrors or lenses concentrating direct sunlight onto the solar cells. A promising concentrating technology uses Fresnel lenses made of flat glass sheets with molded silicone lenses to focus sunlight on solar cells, as they use less material than spherical lenses which can lower absorption losses. In addition to reducing costs, concentrating sunlight increases the theoretical maximum efficiency of solar cells [9], helping CPV reach record module efficiencies up to 38.9% for converting solar irradiance to electrical power [10]. The CPV technology requires precise sun-tracking capabilities, with a decreasing tolerance for sun-tracking errors as sunlight concentration increases [9]. CPV systems don't collect diffuse light, which can account for a large portion of incoming solar energy on cloudy days [3].

In general, the efficiencies of utility-scale CPV systems are about 30% [11], which is higher than the approximately 22% efficiency of unconcentrated silicon (Si) based PV systems, but lower than the record device efficiency of 47.1% achieved by III-V PVs [12]. This large difference in efficiency from devices to systems is due to the optical system's absorption, reflection, misalignment, and diffuse light losses [11]. CPV systems that use silicone-on-glass technology can also suffer from reduced efficiency due to temperature variations, which cause the silicone's refractive index and shape to change, leading to optical misalignment [13]. We distinguish the losses at each level of a standard CPV system [11] in Fig. 1.1c.

CPV modules are enclosed to shield PV devices from most weathering processes, which minimizes long-term degradation losses. A solar cell encapsulant layer is required to provide additional protection from moisture and oxidation. A commercialized encapsulant technology involves depositing approximately 100 nm of SiO_x by atmospheric plasma, which can be easily integrated into assembly lines due to its atmospheric pressure deposition. This thin layer induces optical interference, thereby reducing reflection losses. However, the deposited SiO_x layer consists of a random mixture of silica, amorphous Si, and air [14–17]. The amorphous Si introduces optical absorption within the encapsulant layer for photons with energy above 2 eV,

inhibiting the performance of the CPV submodule. Another encapsulation approach involves coating the solar cell with an optically thick layer of transparent polydimethylsiloxane (PDMS). However, this optically thick layer introduces a reflective interface between the air/PDMS, resulting in a 3% reflection loss.

In this thesis, a novel microstructured encapsulant based on PDMS is explored for CPV systems. This new encapsulant consists of a 2 μm thick layer of PDMS with partially submerged silica micro-sized beads to create a microstructured surface. The microstructured surface eliminates reflection losses at the air/PDMS interface by providing a smooth refractive index transition for the impinging light. In Chapter 3, I demonstrate that the new encapsulant improves the overall performance by up to 3.6% over the standard commercialized SiO_x encapsulant by reducing absorption and reflection losses. Additionally, I show that the new encapsulant can help to stabilize the CPV system's performance over an extended operating temperature range.

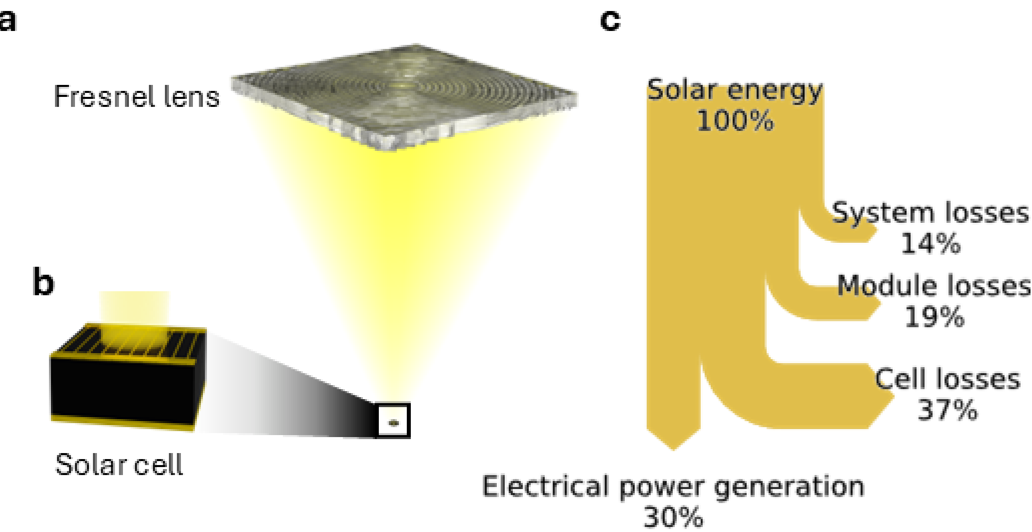

Figure 1.1: **a** Schematic diagram of a CPV sub-module and **b** a zoom in on the high-efficiency solar cell. **c** Sankey diagram of the energy flow within the CPV sub-module, using data from Ref. [11].

1.2 Waste heat recovery

This section considers optimizing the design of PV devices to harness waste heat. Waste heat is a vast, mostly untapped energy source produced on earth, with over 72% of energy use in the world presently lost as waste heat [18]. Fig. 1.2 shows a Sankey diagram visualization. Of that waste heat, 79% is below 600 K which can only be efficiently used for heating (such as heating buildings) near the waste heat source. The rest, 21%, is above 600 K with a limiting Carnot efficiency above 50%, making it an attractive energy source to generate electricity. Assuming the energy landscape from Forman et al. [18], and waste heat to electricity conversion efficiency of 15% for all waste heat above 600 K [19], there is a global electrical power generation potential for waste heat above 600 K of $\sim$28 000 TWh in 2023 which is 43 times more electrical power than what Canada generated in 2023 [20].

Solid-state electrical generators promise modularity and high efficiency for converting waste heat into electrical power without the high maintenance costs of technologies involving moving parts such as turbines. The most popular solid-state waste heat recovery technologies are themoelectric generators, thermophotovoltaics, and near-field thermophotovoltaics (NFTPVs). For 600-900 K heat sources, thermoelectric generators produce high power densities up to 20 W/cm^2 but suffer from low efficiencies up to 12% [21]. Thermophotovoltaics have theoretical efficiencies up to 40% but orders of magnitude lower power densities [21], making them uneconomical for this low-temperature waste heat application. Instead, NFTPVs use the high-efficiency thermophotovoltaic technology but operate with much higher currents thereby boosting power densities [21]. The higher currents of NFTPVs come from the orders of magnitude higher near-field radiative heat transfer compared to far-field radiation transfer. Far-field radiation includes classically escapable rays generated within the material, giving rise to Planck's blackbody spectrum. Near-field radiation transfer also includes totally internally reflected rays and surface polaritons which can greatly enhance radiative heat transfer. This near-field radiation transfer occurs when two objects are distanced much closer than the wavelength of light (it becomes substantial at a distance of 100 nm for near-infrared to visible light).

So far, NFTPV devices have not exceeded 1.5% efficiency for 600-900 K radiator temperatures [5–7, 22]. This low efficiency is due to the use of thermophotovoltaic cells that were not optimized for near-field operation [7, 22] or NFTPV cells with larger-than-optimal

bandgaps [5, 6]. However, if NFTPV devices with too low a bandgap are used (such as InSb at 0.17 eV), they require cryogenic cooling to reach high efficiencies [23] making them impractical for waste heat recovery applications.

In this thesis, InAs-based NFTPV devices with optimal bandgaps (0.356 eV) for 600-900 K heat sources are designed and fabricated. In Chapter 4, I first optimize NFTPV devices and predict realistic efficiencies reaching up to 15% for cells operating at room temperature. A large loss in NFTPV devices is the high absorption of sub-bandgap photons. Therefore, I fabricate NFTPV devices similar to the optimized design but with a novel epitaxially grown broadband sub-bandgap reflective layer consisting of highly doped n-InAs. I characterize the NFTPV devices' optical and electrical characteristics, showing that the new reflective layer does not impact electrical properties but improves the spectral efficiency of the device to 68% from 44%. I also predict that a realistic increase in doping concentration to the reflective layer could make it better than gold at reflecting sub-bandgap photons. These advancements could guide the fabrication and design of future NFTPV devices.

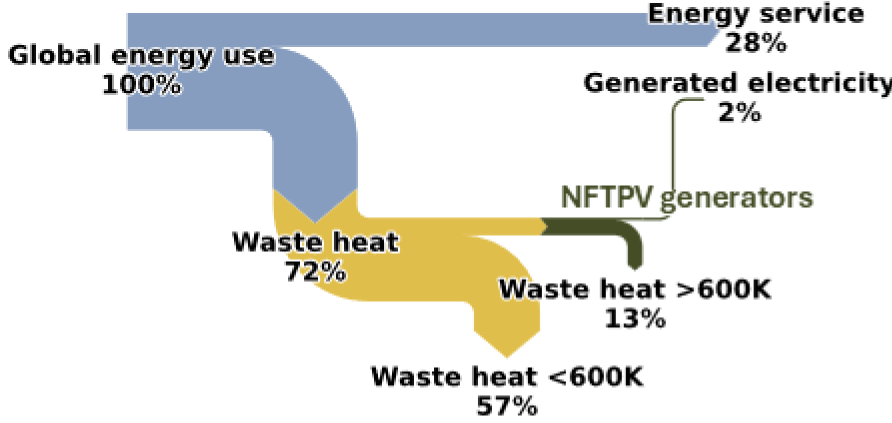

Figure 1.2: Sankey diagram of the global energy landscape [18] with waste heat to electricity recovery via NFTPV assuming an efficiency of 15% from Ref. [19]

1.3 Power-by-light

This section investigates optimizing the design of PV devices used in power-by-light systems. Power-by-light systems are safer and more secure than conventional power transmission (metallic wire). For instance, power-by-light systems can be helpful in high fire or explosion risk areas [24], high voltage situations to prevent electrical equipment malfunctions [25,26], remote powering of rechargeable batteries [27], space exploration [2], and powering 5G technologies [28]. In addition to transporting energy, power-by-light systems can be adapted to transmit data simultaneously [24, 26, 29]. For example, Helmers *et al.* [29] transmitted up to 6 W of power at 115 kb/s data rates via amplitude modulation.

Power-by-light systems use a laser or LED to create optical power from electrical power. The generated light is transported through free-space or an optical fiber to photonic power converters (PPCs). PPCs are specialized PV devices designed to convert monochromatic light to electrical power. To minimize system complexity, PPCs are designed to directly produce voltages above the operating voltages of the devices they are powering. To reach operating voltages (ex: 5 V) [30], PPCs require multiple PV junctions connected in series with horizontal or vertical interconnected architectures [31]. Single-junction devices typically output voltages around 0.5-1.4 V depending on the bandgap of the PV device. The vertical architecture, defined here as multijunction cells, consists of an epitaxially grown stack of PVs interconnected with tunnel diodes. The horizontal architecture employs series-connected single junction cells on a common substrate forming a mini-module. Although multijunction cells require difficult and expensive crystal growth such as high tunnel diode doping and a thick epitaxial growth, subsequent device fabrication steps are easier and cheaper than laterally segmented device architectures which require complicated metallic interconnections. Additionally, multijunction cells promise the highest efficiency as they avoid both trench illumination and laser misalignment losses [31]. However, multijunction PPCs experience greater wavelength sensitivity compared to single-junction devices [31], which must be accounted for in system designs.

When designing PPCs, the optical-to-electrical power conversion efficiency is another important consideration. Some PPCs designed for laser wavelengths of 0.8-0.85 μm and 0.98 μm have achieved efficiencies surpassing 65% [4]. However, 1.0-1.6 μm laser wavelengths are needed to minimize absorption losses when transporting power over distances longer than about 1 km

through optical fibers [31], as can be deduced from Fig. 1.3 which shows the attenuation in optical fiber versus wavelength.

Results in this thesis demonstrate PPCs designed for these laser wavelengths breaching the 50% efficiency barrier [30]. Chapter 5 presents these results, where I designed and measured a PPC device with a record efficiency of 53.6±1.3% in converting 1.446 μm laser light into electrical power. I developed a predictive model to optimize the PPC device, an optimization process that yields designs with higher efficiencies than the conventional absorption-matching method, and a method for extracting layer thicknesses of multi-junction PPCs. Advancements from my results create new pathways for integrating photonic power converters in long-distance fiber optic power transmission applications.

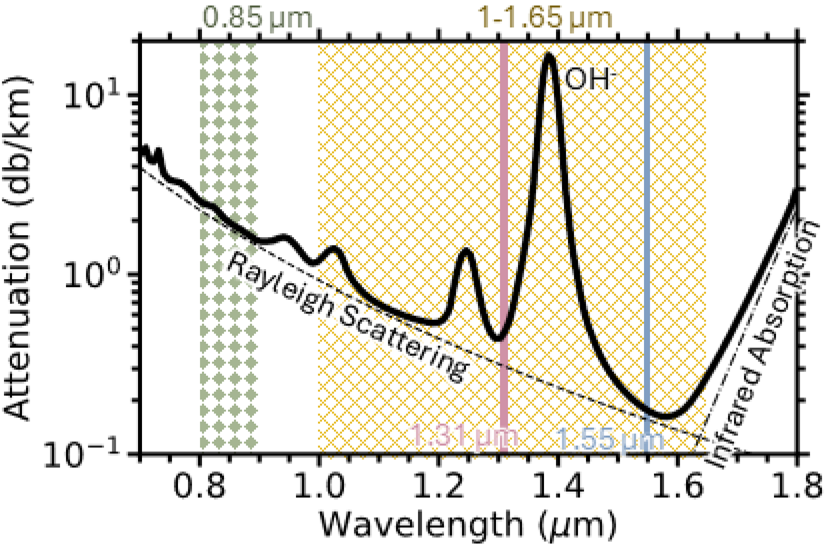

Figure 1.3: Attenuation within an optical fiber as a function of the photon wavelength, a reproduction from Ref. [32]. Photon propagation within the fiber is limited by Rayleigh scattering for shorter wavelengths and infrared absorption through multi-phonon interactions for longer wavelengths. The transparency windows at 1.31 μm and 1.55 μm and the original PPC wavelength operation around 0.85 μm are highlighted by vertical lines and shaded area. The attenuation peak at 1.4 μm is from OH vibrational absorption which can be minimized with pure SiO_2 fibers.

1.4 Cost reduction

This final section of my thesis investigates using epitaxial growth to facilitate substrate reuse, thereby reducing the costs of III-V PVs. Lowering III-V PV costs necessitates improving fabrication processes in three main categories, outlined by a techno-economic analysis for triple junction solar cells from Horowitz *et al.* [33]. Their conclusions and results are summarized in Fig. 1.4. From their cost analysis, they created four categories: Substrate, Epitaxial growth, Processing, and Other. The "Other" category includes costs such as administration, research & development, and corporate profits, which can be reduced with economies of scale. Therefore, addressing the rest of the categories is imperative to improve the economics of early-stage III-V PVs. If the solutions provided in the table in Fig. 1.4 are realized, III-V PVs have the potential to be part of the global energy transition away from fossil fuels.

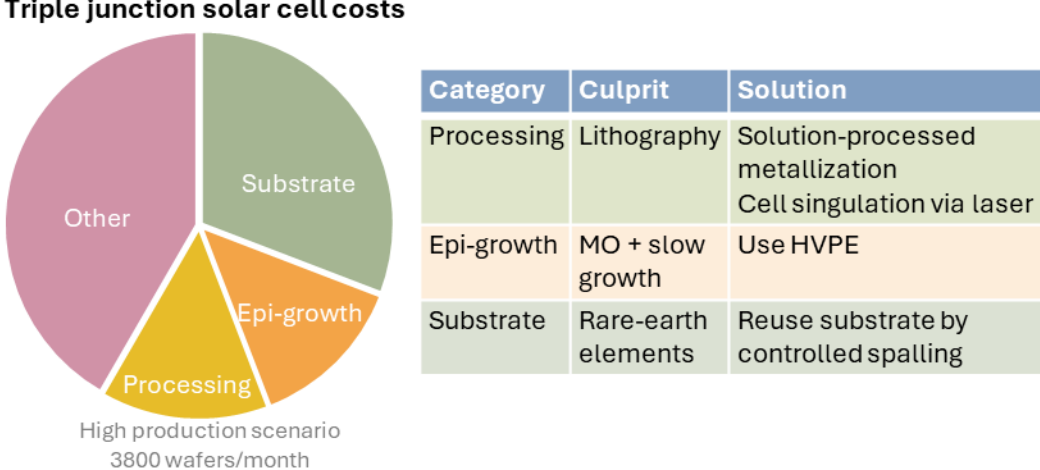

Category	Culprit	Solution
Processing	Lithography	Solution-processed metallization Cell singulation via laser
Epi-growth	MO + slow growth	Use HVPE
Substrate	Rare-earth elements	Reuse substrate by controlled spalling

Figure 1.4: Cost breakdown of a triple junction III-V based solar cell assuming a high production scenario of 3800 wafers/month processing. The table highlights three high-cost categories for the triple junction solar cell, with the categories' main cost culprits, and some proposed solutions to minimize the category costs. MO represents metal-organic molecules. These results are based on findings from Ref. [33].

The substrate accounts for 33% of the cost of high-efficiency GaAs solar cells as substrates

use significant quantities of scarce elements [33]. High-quality substrates are required for device growth [34] but need not be present for device operation thanks to the high absorption rate of substrate-grown III-V materials. Therefore, substrate reuse could dramatically reduce III-V PV costs.

Mechanically fracturing off the epitaxial layers from the substrate with the help of a stressor layer to control the fracture depth [35] (Fig. 1.5), defined as controlled spalling, has the highest potential for PV substrate reuse among the many methods proposed so far [35]. Competing methods include laser lift-off, epitaxial lift-off, porous substrates, remote epitaxy, and acoustic spalling. Laser lift-off rasters a beam across the whole wafer, making this technique low throughput. Epitaxial lift-off selectively etches a sacrificial layer to enable lift-off, requiring corrosive etchants and resulting in a rough contaminated surface. Porous substrates use a weakened porous layer near the substrate surface but generally require expensive low-throughput tooling. Remote epitaxy uses an embedded van der Waals bonding layer to enable lift-off (such as graphene) but is a less mature method. Acoustic spalling is a technique that uses sound waves to propagate the crystal crack during the spall but results in large defective regions on the substrate surface [36]. Controlled spalling has a high-speed throughput, lower capital expenses, reduced chemical hazards, and a relatively uniform surface across the substrate.

Spalled solar cells have the same performance as cells processed in the standard method [35], but further research is needed to assess the impact of reusing the substrate to grow multiple rounds of PV devices. Ideally, the spalled surfaces would be smooth to facilitate the growth of the next devices [34]. Instead, spalled GaAs(100) substrates, which are common III-V PV wafers, have a periodic array of faceted ridges lying on or near natural cleavage directions since the spall crack follows the path of maximum energy release rate [35]. These surfaces need to be planarized to grow high-quality solar cells, as III-V material growth is not conformal with the surface causing parasitic shunts [34].

This thesis presents a method to planarize a spalled GaAs(100) surface via epitaxial growth. Chapter 6 details the results, showcasing a process I designed to planarize spalled GaAs(100) substrate surfaces with just 8 minutes of epitaxial growth, achieving up to 95% material utilization rates relative to nominal growth. This process is compatible with high-efficiency III-V PV epitaxy and requires significantly less growth time [12], thus resulting in a negligible impact on the III-V PV fabrication process.

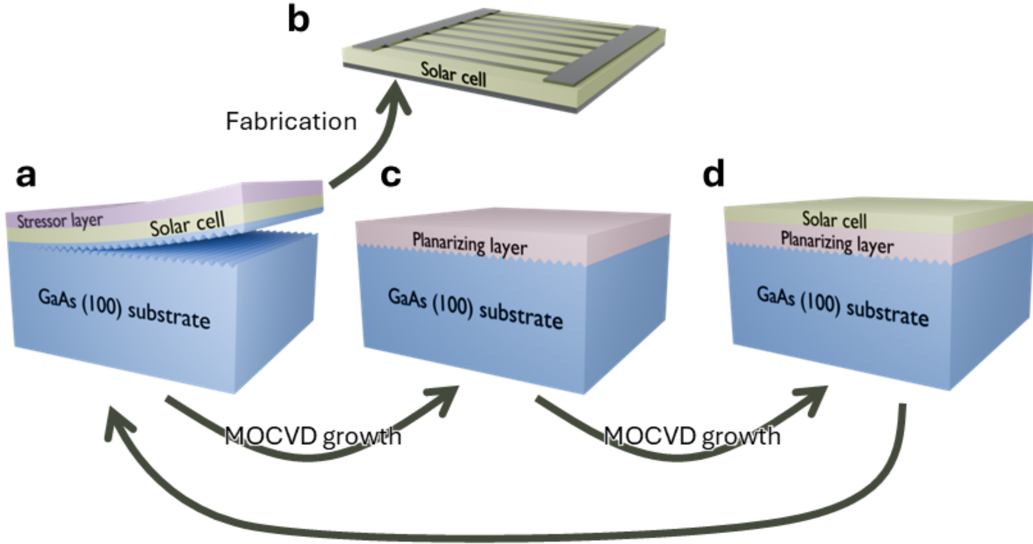

Figure 1.5: Schematic diagram of the GaAs(100) substrate reuse process via controlled spalling. **a** Deposition and controlled spalling using a stressor layor, **b** processing of the spalled material into solar cells, **c** planarizing the bottom GaAs(100) substrate, and **d** growing a new high-efficiency solar cell, which can then be re-spalled.

1.5 Thesis outline

This thesis is comprised of seven chapters. Chapter 3 focuses on using structured surfaces to improve the III-V based CPV systems, Chapters 4 and 5 each explore III-V PV device design optimization for waste heat harnessing and power transmission applications, while Chapter 6 demonstrates how epitaxial growth can address issues in the substrate reuse process. This thesis by paper includes five journal papers and one conference proceeding. My contributions are stated at the beginning of each publication.

Chapter 2 introduces the background material used in this thesis, detailing important concepts related to the physics of semiconductors, light-semiconductor interactions, and PV devices. This chapter also includes an overview of the simulation techniques used to model these devices.

Chapter 3 presents an investigation into the optical properties of a new solar cell encapsulant featuring a microstructured surface for CPV technology. The modeled impact of this new encapsulant on extending the operating range of CPV modules is outlined in a conference proceeding for the 16th International Conference on Concentrator Photovoltaics (Section 3.1). Model validation, using optical characterization results of both a standard encapsulant and the new encapsulant prepared at Université de Sherbrooke, as well as microstructure optimization, are outlined in a journal paper published in *Progress in Photovoltaics* (Section 3.2).

Chapter 4 details the development of NFTPVs targeting radiator temperatures of 600-900 K. Section 4.1 is a featured journal article published in *Applied Physics Letters* that presents simulation results for optimized InAs-based NFTPV devices, using a model validated with devices from literature. The following section (Section 4.2) continues with the fabrication and characterization of an InAs-based NFTPV device grown by molecular beam epitaxy at the University of Waterloo.

Chapter 5 explores improving the design of PPCs for 1.31 μm and 1.55 μm laser wavelengths. Experimental characterization along with electrical modeling of PPCs designed for 1.31 μm lasers, designed and fabricated at Fraunhofer ISE, is outlined in a journal paper published in *IEEE Journal of Photovoltaics* (Section 5.1). Section 5.2 consists of a submitted journal paper that presents experimental characterization and model-facilitated design optimization of multi-junction PPCs for laser wavelengths around 1.55 μm, all fabricated at Fraunhofer ISE.

Chapter 6 investigates reducing the costs of III-V PVs by reusing GaAs(100) substrates via controlled spalling. Section 6.1 is a submitted journal paper that details the experimental and modeling analysis of planarizing faceted GaAs(100) offcut wafers by epitaxial growth, performed during a visit to the US National Renewable Energy Laboratory.

This thesis concludes with Chapter 7, which provides a comprehensive overview of the work and explores the prospects for each technology discussed.

Chapter 2

Physics of semiconductors, light, & photovoltaics

This thesis encompasses interdisciplinary work that combines materials science (structured surfaces and epitaxial growth) and semiconductor device engineering (device design). Given the importance of understanding semiconductor physics, light-matter interactions, and photovoltaic principles for the research presented, this chapter briefly overviews these topics. Most of the content in this chapter is based on material from [9, 37].

2.1 Inorganic semiconductor materials

The following section provides background information essential for designing PV devices, which is useful for Chapters 4 and 5, and for understanding epitaxial growth as required for Chapter 6.

Semiconductors are a material class with electrical conductivity properties between insulators and conductors. The conductivity of semiconductors can be tuned by changing the number of free electrons in the material. One common method to increase the semiconductors' electron concentrations is to dope the material by introducing impurity atoms. This tunability makes semiconductors very attractive for electronic device applications.

Semiconductors can be elemental or compound and are classified by the number of valence electrons their elements have that make the material. Elemental semiconductors contain a single element and are usually made of group IV materials from the periodic table, examples include Si and germanium (Ge). Compound semiconductors include more than one element, common examples are the binaries gallium arsenide (GaAs) and indium phosphide (InP). Compound semiconductors can have more than two elements allowing enhanced device design flexibility.

In the following sections, I will describe the basic properties of semiconductors.

2.1.1 Crystal structure

Atoms within a semiconductor form covalent bonds in specific directions, creating a crystal lattice. High-quality semiconductors have atoms arranged periodically to form a monocrystalline structure. Lower quality crystals can form in sub-optimal conditions, creating polycrystalline material composed of small conglomerated monocrystals joined by grain boundaries. Finally, the lowest-quality crystals are amorphous, meaning they only have short-range periodic structures.

The periodic structure can be represented by the smallest unit cell which captures the periodicity. The width of the unit cell is known as the lattice constant. Group IV semiconductors, such as Si and Ge, arrange their atoms in a diamond cubic lattice structure where each atom bonds to its neighbors in a tetrahedral configuration. The diamond cubic lattice structure can be decomposed into two superimposed face-centered cubic structures. Most III-V semiconductors form a Zinc blend structure which is the same as the diamond structure but where the groups III and V atoms occupy either face-centered cubic structures as depicted in Fig. 2.1.

2.1.2 Crystal growth

Crystalline material can be obtained by epitaxial growth, where one atomic layer at a time is deposited on a crystal substrate. The highest quality crystal structures are grown on monocrystalline substrates with near identical lattice constants. There are two popular and commercialized forms of epitaxy: molecular beam epitaxy (MBE) and metalorganic vapor phase epitaxy (MOVPE).

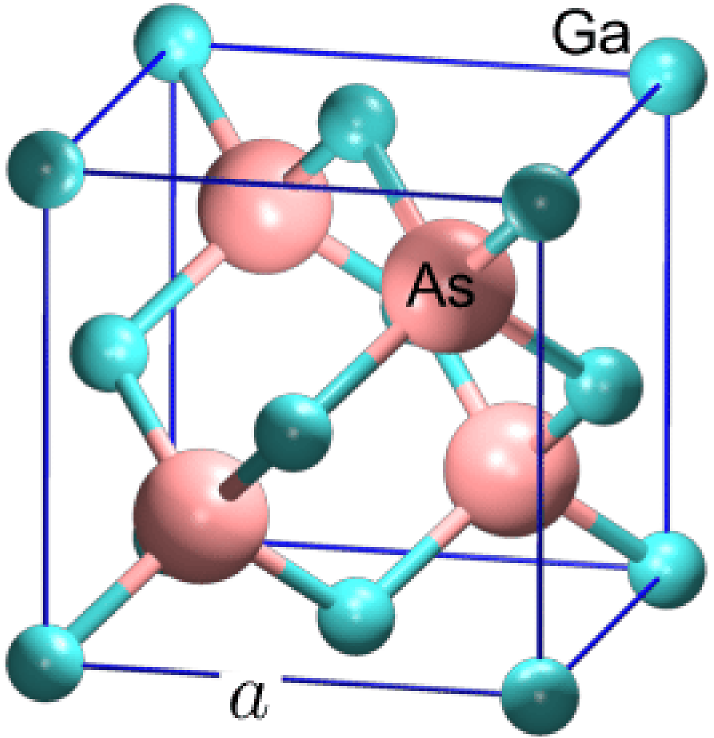

Figure 2.1: Schematic diagram of the GaAs crystal structure with lattice constant *a*, copied from Ref. [38].

MBE systems heat elemental sources in an effusion cell and beam the atoms toward the temperature-controlled substrate where they bond. The thickness of the epitaxial layers is monitored with reflection high-energy electron diffraction (RHEED). A glancing angle electron beam is shot at the surface and a detector is placed to capture the diffraction pattern of the electrons. MBE growth is under ultra-high vacuum (10^{-11} torr) to maximize the path length of atoms towards the substrate, and as required by RHEED. This vacuum also minimizes contamination of the epitaxial material. Due to its slow growth, MBE can produce sharp layer boundaries [39]. However, the ultra-high vacuum requirement (which can be time-consuming to repair if broken) and slow growth make them uneconomical for large-scale production, therefore they are mostly used for research purposes. Instead, MOVPE (also known as metalorganic chemical vapor deposition (MOCVD) and organometallic vapor phase epitaxy (OMVPE)) is the

growth method of choice for most commercial applications due to its order of magnitude faster growth rates over MBE and growth capability at higher pressures (15-750 torr) in hydrogen-rich environments [40]. MOVPE introduces metal-organic gaseous precursors that react with the temperature-controlled substrate surface to deposit atoms.

In both growth techniques, when atoms initially deposit on the substrate, they form adatoms. These adatoms diffuse across the substrate's surface and either adhere to atomic sites with typically high sticking coefficients such as atomic steps or evaporate into a gaseous phase. Adatom evaporation leads to parasitic material loss, which can increase the cost of growth. Since adatoms can migrate [41, 42] and favor sites with a high sticking coefficient, growth on a non-planar substrate surface can be non-conformal. We use this non-conformal growth property to planarize a surface by MOVPE growth in Chapter 6.

Atoms at the crystal's surface would have dangling bonds due to the absence of neighboring atoms to bond with. However, these surface atoms tend to reconstruct relative to the bulk crystal to minimize the surface energy by pairing their dangling bonds with neighboring surface atoms, known as atomic surface reconstructions [43, 44]. The organization of these reconstructions can depend on many factors, to name a few: surface temperature, crystal facet direction, adatom elements present on the surface, and gas composition near the surface [44, 45]. An example of a GaAs(100) surface reconstruction under an As-rich atmosphere is given in Fig. 2.2. Such surface reconstructions can significantly impact epitaxial growth by altering the surface and introducing sites with differing sticking coefficients. Further discussion will be presented in Chapter 6.

2.1.3 Binary, ternary, and quaternary alloys

Compound semiconductors offer flexibility in material properties. For example, alloying III-V binaries with a third element from the III or V elemental groups creates a ternary material, allowing to adjust a material parameter of choice. Typically, for ternary compounds, the composition is fixed to match the lattice constant of the substrate, thereby maximizing the material quality. Introducing a fourth element forms quaternaries, unlocking further adjustable material parameters, usually the bandgap due to its significant impact on both optical and electrical

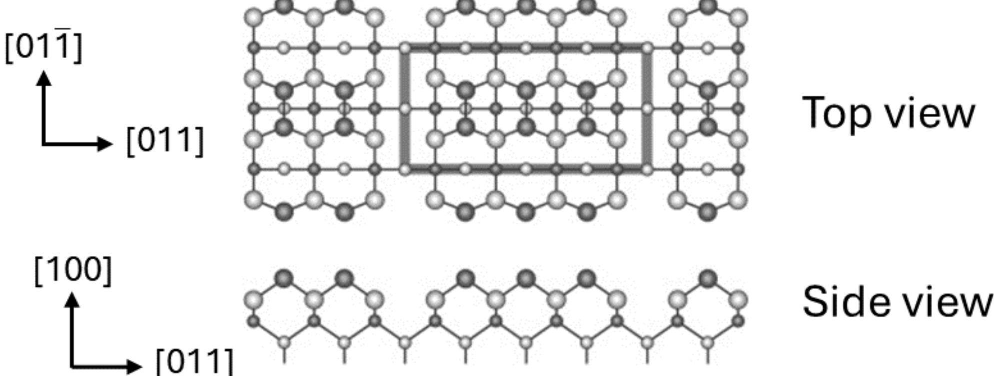

Figure 2.2: Atomic structure model for As-rich GaAs(100) surface with a $\beta(2{\times}4)$ reconstruction. Filled circles represent As atoms while open circles denote Ga atoms. Modified from Ref. [44].

properties. While further alloying with additional elements can enhance flexibility, the epitaxy quality diminishes considerably beyond quaternaries due to surging growth complexity.

Material parameters for ternaries of the form $A_xB_{1-x}C$ are usually accurately interpolated from their binary constituents as follows:

$$P_{ABC}(x) = P_{AC}x + P_{BC}(1-x) - Cx(1-x) \tag{2.1}$$

Where P_{AC} and P_{BC} are the material parameter values corresponding to the binaries AC and BC, and C is the bowing parameter specific to the material parameter P_{ABC}. Two lattice-matched binary or ternary endpoints, α and β, can be combined with arbitrary composition z to form a lattice-matched quaternary alloy $\alpha_{1-z}\beta_z$. The material parameters for such quaternaries are most accurately interpolated from from the endpoints as follows [46]:

$$P_{\alpha\beta}(z) = P_{\alpha}z + P_{\beta}(1-z) - C_{\alpha\beta}z(1-z) \tag{2.2}$$

where P_α and P_β are the values of the material parameter for the endpoints and $C_{\alpha\beta}$ is the bowing parameter associated with combining the two endpoint materials to form the quaternary.

2.1.4 Energy band structure

Isolated atoms have electrons at quantized energy levels, and they occupy the lowest energy levels at ground state. When two atoms create a covalent bond, their energy levels split, since Pauli's exclusion principle asserts that only two electrons with opposite spin can occupy the same energy state. As atoms are clustered to create a bulk crystal, the energy states split and create effectively continuous energy bands. When the band of highest occupied energy states intersects with the band of unoccupied energy states, we have a metal. Conversely, if the bands have a large energy gap it is an insulator. Between the two endpoints lies the semiconductor. We call the band with occupied levels the valence band and the band with unoccupied levels the conduction band. At room temperature, the semiconductors' valence band is mostly occupied and those electrons have limited mobility. At higher temperatures or under illumination, electrons can acquire enough energy to be promoted to the conduction band leaving behind holes (positive charges defined by lack of electrons at the valence band). Once promoted, electrons and holes can freely move through the mostly unoccupied states and we call these particles free charge carriers.

Due to the periodicity of the crystal, electron wavefunctions occupy the whole crystal. These wavefunctions have wavevectors (k) in the momentum space and relate to the crystal's reciprocal lattice. The reciprocal space is calculated by taking the Fourier transform of the lattice in real space. The central primitive unit cell of the reciprocal space is known as the first Brillouin zone. The Brillouin zone can encompass all wavefunction solutions for the periodic structure, providing the band structure of crystals.

Semiconductors can have direct or indirect bandgaps. Direct bandgap crystals have their minimum energy in the conduction band and their maximum energy in the valence bands at the same wavevector k in reciprocal space. These energies do not align in momentum-space for indirect bandgap crystals as depicted in Fig. 2.3. Since photons have relatively negligible momentum compared to the electrons in semiconductors, a two-particle photon-electron interaction can promote the electron with minimal change to the electron's momentum (k). Therefore, direct bandgap semiconductors can absorb photons with this two-particle interaction down to the bandgap energy (E_{g}). However, to conserve momentum (k), indirect bandgap semiconductors require a three-particle interaction (photon-electron-phonon) to promote elec-

trons from the valence band edge to the conduction band edge.

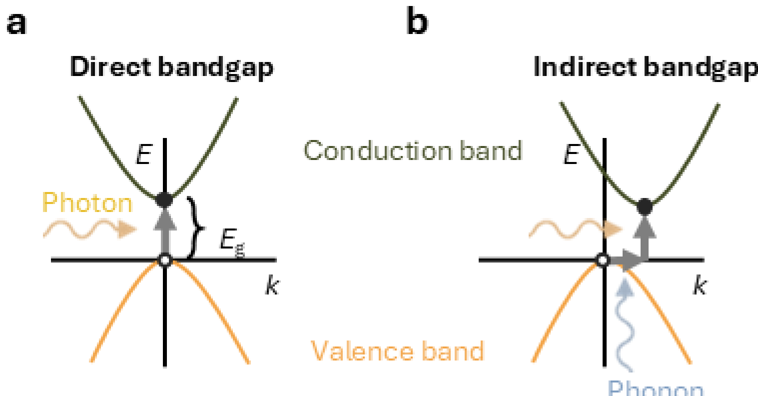

Figure 2.3: Schematic diagrams of the charge carrier energy (E) as a function of its wavevector (k) for **a** direct bandgaps and **b** indirect bandgaps. The photon absorption processes are also highlighted for both types of bandgaps. The conduction band is at the top and the valence band is at the bottom.

Electrons and holes that are energized (for example from photon absorption) can change their momentum (k) within the conduction and valence bands, respectively, when subjected to an electric field allowing for a net movement of charge carriers. This net movement of charge is macroscopically known as current.

2.1.5 Density of states, carrier density, and doping

Pauli's exclusion principle states that no two electrons can occupy the same quantum state, thus only two electrons can occupy the same energy level if they have opposite spins. With this principle and assuming isotropic parabolic energy bands with dispersion $E = (\hbar k)^2/(2m)$, which is a good approximation near the band edge, the conduction and valence band density of states are:

$$g_i(E) = \frac{1}{2\pi^2}\left(\frac{2m_i^*}{\hbar^2}\right)^{3/2}(E - E_i)^{1/2} \quad (2.3)$$

where *i* can be either c or v to represent the conduction and valence band parameters, *E* is the energy, m_i^* is the density-of-states effective mass of band type *i*, and E_i is the energy of the band nearest to the middle of band type *i*. A representation of Eq. (2.3) is provided in Fig. 2.4a.

The nonparabolic band approximation provides a better representation of the density of states within the bands but further from the band edge. Assuming an isotropic bandstructure, we can introduce the nonparabolicity parameter α into the dispersion $E(1+\alpha E) = (\hbar \mathbf{k})^2/2m$ and use this relation to more accurately equate the density of states in the conduction and valence band as follows:

$$g_i(E) = \frac{1}{2\pi^2}\left(\frac{2m_i^*}{\hbar^2}\right)^{3/2}(1+\alpha(E_i - E))\left(\frac{\sqrt{E_i - E}}{2} + \sqrt{\alpha}(E_i - E)\right) \tag{2.4}$$

where again *i* can be either c or v to represent the conduction or valence band, respectively.

Between the conduction band and valence band lies the Fermi energy (E_F). At a crystal temperature of absolute zero, the electrons fill all the energy levels below E_F. At a non-zero temperature (T), there is a finite number of electrons that occupy energy levels above E_F, and its energy distribution is described by the Fermi-Dirac equation:

$$f(E,T) = \frac{1}{1+\exp\left(\frac{E-E_\mathrm{F}}{k_\mathrm{B}T}\right)} \tag{2.5}$$

where k_B is Boltzmann's constant. A representation of this function is provided in Fig. 2.4b at zero kelvin and finite temperatures.

The temperature-dependent density of electrons in the conduction band can be calculated by combining Eq. (2.3) or Eq. (2.4) with Eq. (2.5) as follows:

$$n = \int_{E_\mathrm{c}}^{\infty} g_\mathrm{c}(E) f(E,T) dE \tag{2.6}$$

Similarly, the temperature-dependent density of holes in the valence band is calculated by combining Eq. (2.3) or Eq. (2.4) with Eq. (2.5) as follows:

$$p = \int_{E_\mathrm{v}}^{\infty} g_\mathrm{v}(E) f(E,T) dE \tag{2.7}$$

Figures 2.4c,d show schematics of the density of charge carriers in both the valence and conduction bands for semiconductors at zero kelvin and finite temperatures. In this figure, we assumed an intrinsic semiconductor, where the concentration of electrons and holes are perfectly balanced such that $n = p = n_\mathrm{i}$. The intrinsic carrier density (n_i) is defined by:

$$n_\mathrm{i}^2 = np \tag{2.8}$$

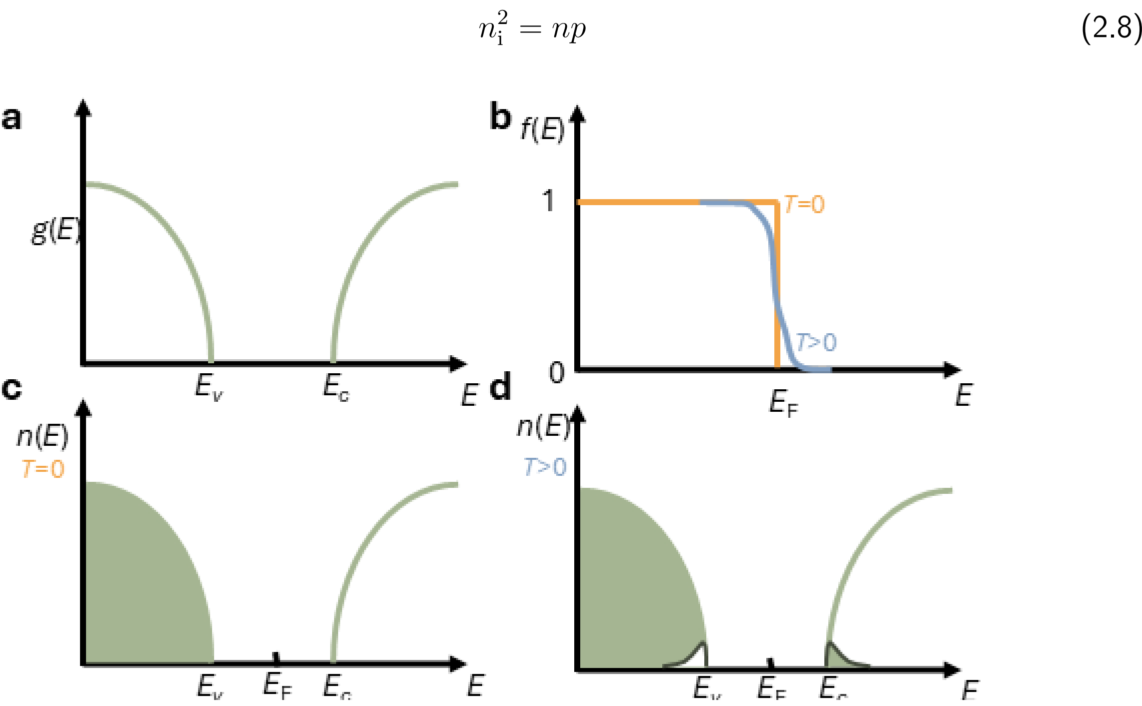

Figure 2.4: Schematic representations of **a** density of states function of a semiconductor with parabolic bands, **b** the Fermi-Dirac distribution function and energy distribution of electrons at **c** zero kelvin and **d** a finite temperature. The shaded area in **c,d** represents electron populations. This figure is a modification from [9].

Doping semiconductors with impurity atoms can change this electron-hole balance, but Eq. (2.8) always holds. Dopants are impurity atoms that replace atoms in the crystal lattice and require little energy to donate free charge carriers to the conduction or valence bands. Dopant

concentrations near or exceeding the intrinsic carrier density create a doped semiconductor. For high concentrations of dopants that donate electrons, N_d, $n \approx N_\mathrm{d}$ and $p = n_\mathrm{i}^2/N_\mathrm{d}$. Conversely, for high acceptor atom doping concentrations, N_a, $p \approx N_\mathrm{a}$ and $n = p_\mathrm{i}^2/N_\mathrm{a}$. In either case, the most populous charge carrier in the semiconductor is called the majority carrier and the other is called the minority carrier.

2.1.6 Carrier mobility

Free charge carriers have finite mobility in crystal structures which are limited by scattering processes including phonon scattering, carrier-carrier scattering, and defect scattering. Therefore, doping and temperature strongly influence carrier mobilities as they can affect free carrier concentrations, defect concentrations, and/or phonon count. The doping and temperature-dependent mobility ($\mu(N,T)$) of bulk III-V semiconductors are well described by the following empirical model, which was presented in Ref. [47]:

$$\mu(N,T) = \mu_\mathrm{min} + \frac{\mu_\mathrm{max}(300\mathrm{K})(300\mathrm{K}/T)^{\theta_1} - \mu_\mathrm{min}}{1 + (\frac{N}{N_\mathrm{ref}(300\mathrm{K})(T/300\mathrm{K})^{\theta_2}})^\lambda} \tag{2.9}$$

where N is the doping density and the rest are fitting parameters with positive values. A fit of Eq. (2.9) to measured InAs mobilities, is shown in Fig. 2.5. Notice that electron mobility is orders of magnitude higher than hole mobility, which is usually the case for III-V semiconductors. This mobility difference is primarily due to the higher scattering probabilities within the valence bands.

2.1.7 Transport equations

The core equations that can describe the electrical properties of semiconductor physics are based on 2 principles: the electrostatic potential from charge carriers obeying Poisson's equation and net neutrality (no creation or loss of total charge). For semiconductors containing electrons and holes, the conservation of electrons over time requires:

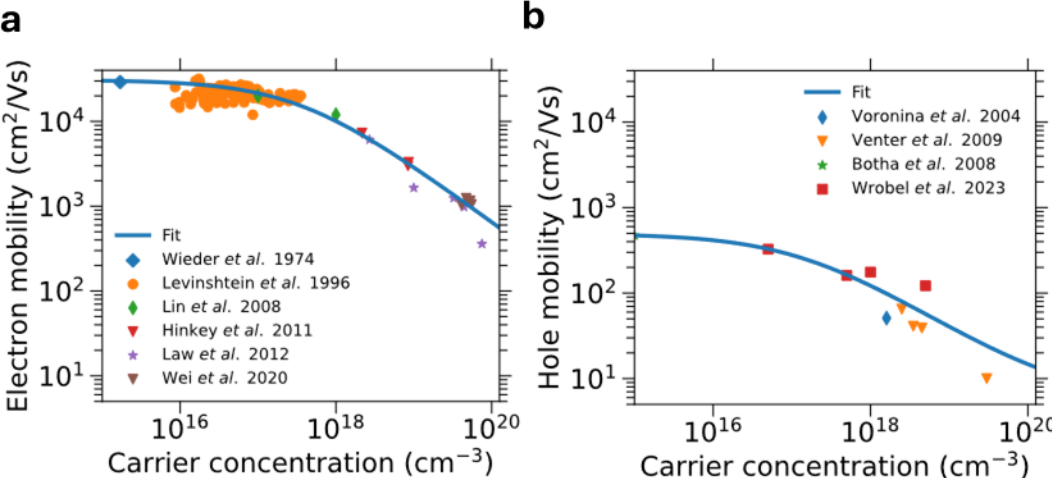

Figure 2.5: Doping dependent mobilities of **a** electrons and **b** holes, for InAs. Fit with the model from Eq. (2.9) to measured data from literature [48–57].

$$\frac{\partial n}{\partial t} = \frac{1}{q}\nabla J_{\mathrm{n}} + G_{\mathrm{n}} - U_{\mathrm{n}} \tag{2.10}$$

and for holes:

$$\frac{\partial p}{\partial t} = -\frac{1}{q}\nabla J_{\mathrm{p}} + G_{\mathrm{p}} - U_{\mathrm{p}} \tag{2.11}$$

where $J_{\mathrm{n,p}}$ is the electron (hole) current density, $G_{\mathrm{n,p}}$ is the volume generation rate, $U_{\mathrm{n,p}}$ is the volume recombination rate. Poisson's equation is:

$$\nabla^2\phi = \frac{q}{\epsilon_{\mathrm{s}}}(p - n + N_{\mathrm{d}} - N_{\mathrm{a}}) \tag{2.12}$$

where ∇^2 is the Laplace operator, ϕ is the electrostatic potential and ϵ_{s} is the static dielectric permittivity of the semiconductor. Equations (2.10) to (2.12) are general. We can simplify the continuity equations by assuming steady state, with constant carrier densities over time such that $\frac{\partial n}{\partial t} = \frac{\partial p}{\partial t} = 0$. We also need to relate J, G, U to n, p, ϕ, and then we can use the coupled

differential equations to solve for the three unknowns. In the next couple of subsections, we will derive these relations.

2.1.8 Drift and diffusion

The charge carrier current densities $J_{\mathrm{n,p}}$ can be related to the sum of carrier drift and diffusion current densities. The total electron current density becomes:

$$J_{\mathrm{n}} = q\mu_{\mathrm{n}}Fn + qD_{\mathrm{n}}\nabla n \tag{2.13}$$

and for holes:

$$J_{\mathrm{p}} = q\mu_{\mathrm{p}}Fp - qD_{\mathrm{p}}\nabla p \tag{2.14}$$

where $D_{\mathrm{n,p}}$ are the diffusion coefficients of electrons and holes, which are related to their corresponding mobilities by Einstein's relation, $D_{\mathrm{n,p}} = \mu_{\mathrm{n,p}}k_{\mathrm{B}}T/q$. The first terms in Eqs. (2.13) and (2.14) represent the drift currents induced by an electrostatic field F. The second terms are diffusion currents induced by gradients in the charge carrier concentrations.

2.1.9 Generation-recombination

Semiconductors at temperatures above zero kelvin will have electrons promoted to the conduction band due to thermal excitation. They can also be promoted optically by absorbing a photon with energy larger than the bandgap energy, called photogeneration, as is depicted in Fig. 2.6a. After absorbing a photon with energy larger than the bandgap, the photogenerated charge carriers lose their excess kinetic energy by colliding with the lattice, generating phonons (within picoseconds), until the charge carriers reach the band edges. This process is called thermalization and is depicted in Fig. 2.6a. After thermalization, the charge carriers reside at the band edges for durations on the order of nano to microseconds (for high-quality semiconductors) before recombining.

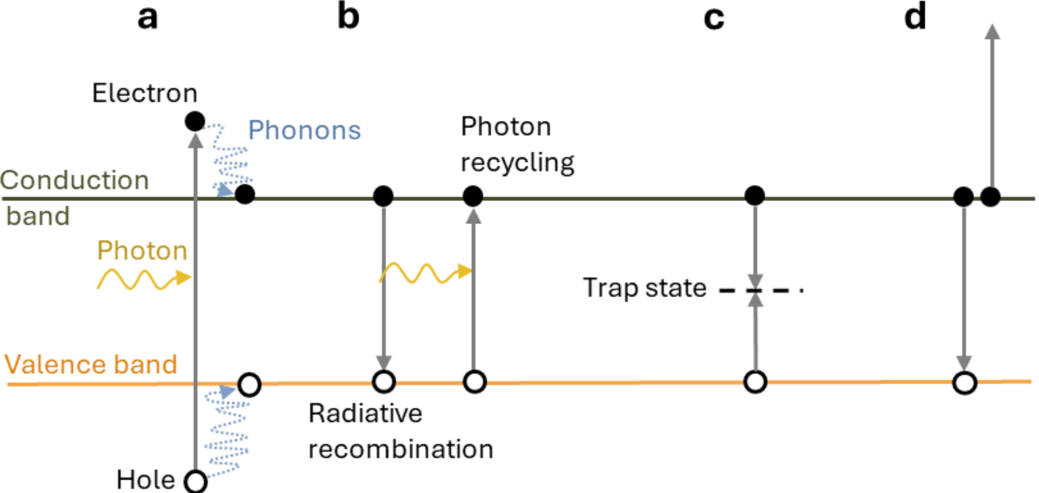

Figure 2.6: Schematic representations of **a** photogeneration and thermalization, **b** radiative recombination (left) and photon recycling (right), **c** Shockley-Read-Hall recombination, and **d** Auger recombination.

One such recombination mechanism is radiative recombination, where a photon is emitted from an electron and hole recombining, as shown on the left in Fig. 2.6b. The radiative recombination rate is related to the carrier concentrations as follows [58]:

$$R_{\mathrm{rad}}(n,p) = B_{\mathrm{rad}}(np - \gamma_{\mathrm{n}}\gamma_{\mathrm{p}}n_{\mathrm{i}}^2) \tag{2.15}$$

where γ_{n} and γ_{p} are correction factors that are needed for simulations using the more physically accurate Fermi-Dirac statistics, and are defined by:

$$\gamma_{\mathrm{n}} = \frac{n}{N_{\mathrm{c}}} \exp\left(\frac{E_{\mathrm{c}} - E_{\mathrm{F_n}}}{k_{\mathrm{B}}T}\right) \tag{2.16}$$

$$\gamma_{\mathrm{p}} = \frac{p}{N_{\mathrm{v}}} \exp\left(\frac{E_{\mathrm{v}} - E_{\mathrm{F_p}}}{k_{\mathrm{B}}T}\right) \tag{2.17}$$

B_{rad} in Eq. (2.15) is the radiative recombination coefficient that can be calculated from the optical properties of the semiconductor, assuming isotropic emission, as follows:

$$B_{\mathrm{rad}} = \frac{8\pi}{h^3 c^2 n_{\mathrm{i}}^2} \int_0^{\infty} \frac{\alpha(E) n^2(E) E^2}{\exp\left(E/k_{\mathrm{B}}T\right) - 1} dE \tag{2.18}$$

where h is Planck's constant, c is the speed of light in vacuum, α is the absorption coefficient and n is the refractive index of the material as a function of photon energy E (Section 2.2.1 will further define n and α).

Radiatively recombined light can be reabsorbed within the semiconductor and is called photon recycling with the process depicted in Fig. 2.6b. This process effectively increases the radiative recombination lifetime of finitely thick semiconductors.

Shockley-Read-Hall (SRH) recombination is due to carriers recombining with trap states within the bandgap as shown in Fig. 2.6c. These trap states originate from impurities in the crystal lattice; therefore, the SRH lifetime serves as a measure of semiconductor quality. The rate of SRH recombination can be calculated from the lifetimes and the carrier densities as [58]:

$$R_{\mathrm{SRH}}(n,p) = \frac{np - \gamma_{\mathrm{n}}\gamma_{\mathrm{p}} n_{\mathrm{i}}^2}{\tau_{\mathrm{SRH,n}}(p + \gamma_{\mathrm{p}} p_{\mathrm{t}}) + \tau_{\mathrm{SRH,p}}(n + \gamma_{\mathrm{n}} n_{\mathrm{t}})} \tag{2.19}$$

where p_{t} and n_{t} are the carrier densities of holes and electrons when $E_{\mathrm{F_p}}$ and $E_{\mathrm{F_n}}$ are equal to the energy of the trap state. Also, $\tau_{\mathrm{SRH,n}}$ and $\tau_{\mathrm{SRH,p}}$ are the electron and hole SRH lifetimes. Equation (2.19) is maximized when the electron and hole SRH lifetimes are similar and short ($\tau_{\mathrm{SRH,n}} \approx \tau_{\mathrm{SRH,p}} \ll 1$), the trap levels are near the middle of the gap ($n_{\mathrm{t}} \approx p_{\mathrm{t}}$), and the carrier populations are nearly equal ($n \approx p$).

Auger recombination is due to a three-particle interaction between charge carriers with an example shown in Fig. 2.6d. For this recombination mechanism, the energy from the electron-hole recombination is transferred to either an electron in the conduction band or a hole in the valence band thereby promoting them to a higher energy state. The excited charge carrier subsequently thermalizes back to the band edge thereby losing the energy. The Auger recombination rate varies with carrier concentration as follows [58]:

$$R_{\mathrm{Aug}}(n,p) = (A_{\mathrm{Aug,n}}n + A_{\mathrm{Aug,p}}p)(np - n_{\mathrm{i}}^2) \tag{2.20}$$

where $A_{\mathrm{Aug,n}}$ and $A_{\mathrm{Aug,p}}$ are the Auger recombination coefficients for interactions involving two electrons and two holes, respectively. These coefficients follow a general trend of increasing magnitude with decreasing bandgap [59].

Generally, radiative recombination dominates for high-quality direct-bandgap semiconductors, SRH recombination may become dominant in semiconductors with significant defects and impurities or at low injection rates (ex: low irradiance), and Auger recombination prevails in small bandgap semiconductors with high carrier concentrations or high-quality crystals with indirect bandgaps such as Si.

2.2 Light-semiconductor properties

Light management is crucial for maximizing the performance of PV systems. The following section discusses light-matter interaction for bulk, thin film, and structured surfaces. Thin films are commonly exploited in the PV community to create antireflection coatings that minimize reflection between the air/semiconductor interface. I implement this technology in Chapter 5 to minimize reflection losses in PPC devices. Another way to minimize reflection at an interface involves using a structured surface to smooth the refractive index transition, offering better transmission at large incident angles compared to conventional thin film antireflection coatings [60]. I apply structured surfaces in Chapter 3 to enhance transmission into the PV device.

Photons, the fundamental particles of light, exhibit pronounced wavelike characteristics. These wavelike characteristics can be mathematically modeled as electromagnetic waves. A key property of these waves is polarization, which refers to the orientation of their electromagnetic oscillations—always perpendicular to the direction in which the light travels. The light's polarization can be decomposed into a linear combination of s and p polarizations that are normal and parallel to the material interface plane, respectively. The direction of polarization significantly affects how light interacts with different media. It can influence whether light is transmitted, reflected, or absorbed when encountering a new medium. Moreover, within a medium, light and matter interact reciprocally such that light can be absorbed or emitted.

Due to their ability to carry substantial amounts of energy, photons are particularly useful in energy-related applications. They play a crucial role in technologies such as solar cells, where sunlight is converted into electricity, and in power-by-light systems, where power is transported by light.

In the following section, I will describe the optical properties of semiconductors and present methods to describe photon-semiconductor interactions.

2.2.1 Semiconductor optical properties

The optical properties of semiconductors are described by their complex refractive index:

$$\overline{n} = n + i\kappa \tag{2.21}$$

where n is the real part of the refractive index and represents the speed of light within the medium relative to free space ($v = c/n$). The complex part, κ, is known as the extinction coefficient, which describes the absorption within the medium. The extinction coefficient is related to the absorption coefficient and the photon's wavelength (λ) as follows: $\alpha = 4\pi\kappa/\lambda$. The complex refractive index is related to the material's complex dielectric permittivity as follows: $\epsilon = (n + i\kappa)^2$.

The complex refractive index of a semiconductor can be determined through ellipsometry. However, this method's accuracy diminishes near the band edge. A more precise measurement of the band edge extinction coefficient can be achieved by evaluating the internal quantum efficiency (Section 2.3.3) of a thin single-junction semiconductor device with a known thickness and applying the relationship given by Eq. (2.27) (Section 2.2.2). This technique is applied in Section 5.2 of this thesis. However, acquiring complex refractive indexes via measurements necessitates many semiconductor samples to account for each material parameter influencing optical properties, which can be costly and time-consuming. An alternative approach involves interpolating the complex refractive index across the range of semiconductor parameters using an advanced algorithm, as was done in Ref. [61]. This approach is undertaken in Section 5.2. Furthermore, for device design exploration, employing a physics-based model that reasonably

predicts the effects of semiconductor parameters on optical properties can provide sufficient accuracy.

An important semiconductor parameter that can impact band-to-band absorption is doping. Degenerately n-doped semiconductors with small conduction band density of states have their conduction band edge filled, which impacts the absorption of photons with energies near the bandgap, known as the Moss-Burstein shift, depicted in Fig. 2.7a. This effect is important for small bandgap materials such as InGaAs lattice-matched to InP, as measured by Hahn *et al.* [62] and reproduced in Fig. 2.7b. Anderson [63] developed a physics-based model that accurately predicts the doping-dependent optical absorption, as shown in the comparison between Hahn's [62] measurements to the model in Fig. 2.7b.

Free carrier and lattice absorption can be significant at photon energies less than the semiconductor bandgap ($E_{\mathrm{photon}} < E_{\mathrm{g}}$). These absorptions are related to intraband transitions (e.g., exciting an electron within the conduction band) and lattice vibration production (photon-phonon interaction). Generally, these mechanisms do not contribute to power output for PV devices and, instead, parasitically heat the semiconductor (there are special cases such as hot-carrier solar cells where energy from free-carrier absorption could be extracted, see [9] for details). The contributions of these mechanisms to the optical properties as a function of photon frequency (ω) in most III-V semiconductors can be simulated by the Drude-Lorentz model [49, 64]:

$$\epsilon(\omega) = \epsilon_\infty \left[1 + \frac{\omega_{\mathrm{LO}}^2 - \omega_{\mathrm{TO}}^2}{\omega_{\mathrm{TO}}^2 - \omega^2 - i\omega\gamma} - \frac{\omega_{\mathrm{p}}^2}{\omega(\omega + i\Gamma)}\right] \tag{2.22}$$

where ϵ_∞ is the high-frequency permittivity, ω_{LO} and ω_{TO} are the longitudinal and transverse optical phonon frequencies, respectively, γ is the damping coefficient due to phonons, ω_{p} is the plasma frequency given by $\omega_{\mathrm{p}} = \frac{N_i q^2}{\epsilon_0 \epsilon_\infty m_i^*}$, and Γ is the damping coefficient due to free carriers given by $\frac{q}{m_i^* \mu_i}$. There is q which is the elementary charge, ϵ_0 is the vacuum permittivity, N_i is the majority carrier concentration, m_i^* is the charge's effective mass, and μ_i is the charge mobility. The second term in Eq. (2.22) represents photon-phonon interactions, while the third describes photon-free carrier interactions. These properties are important to model for NFTPV and thermophotovoltaic applications to calculate the total system efficiency, as will be discussed in Chapter 4.

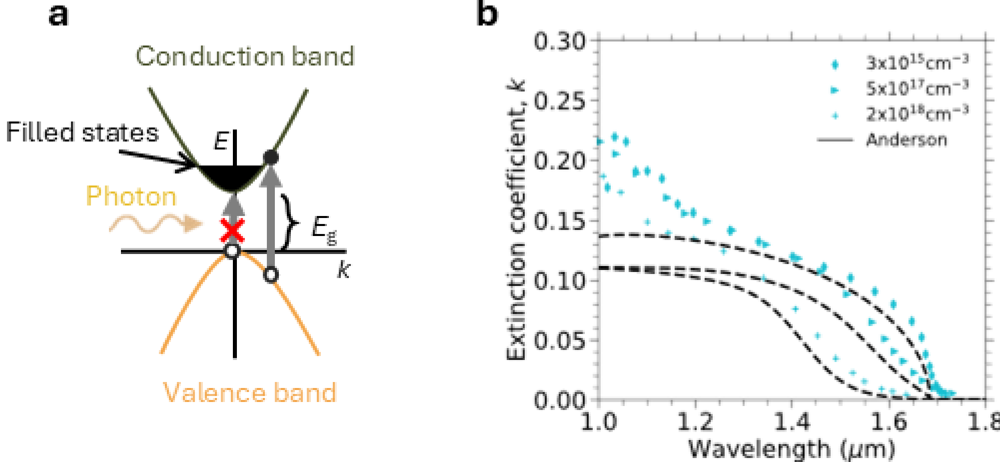

Figure 2.7: **a** Schematic representations of the Moss-Burstein effect which limits photon absorption near the band edge due to a filled conduction band. **b** Extinction coefficient (κ) as a function of wavelength for n-InGaAs lattice matched to InP. Measured data from [62] is compared to simulation using the model proposed by Anderson [63].

2.2.2 Bulk-semiconductor optics

Ray optics can describe light interaction with structures larger than the light's wavelength. The transmission and reflection of light between bulk semiconductors are calculated differently for either s and p polarizations. At a given interface, the reflection coefficient, defined as the ratio between the reflected and incident wave amplitudes between the first and second medium (see the schematic example in Fig. 2.8a), is given by:

$$r_{\mathrm{s}} = \frac{\overline{n_1}\cos\theta_1 - \overline{n_2}\cos\theta_2}{\overline{n_1}\cos\theta_1 + \overline{n_2}\cos\theta_2} \tag{2.23}$$

and

$$r_{\mathrm{p}} = \frac{\overline{n_1}\cos\theta_2 - \overline{n_2}\cos\theta_1}{\overline{n_1}\cos\theta_2 + \overline{n_2}\cos\theta_1} \tag{2.24}$$

where $\overline{n}_i$ is the refractive index and θ_i is the light's angle relative to the interface normal in medium i. The angles can be related using Snell's law. The transmission coefficient, defined

as the ratio between transmitted and incident wave amplitudes between the first and second medium, is given by:

$$t_{\mathrm{s}} = \frac{2\overline{n_1}\cos\theta_1}{\overline{n_1}\cos\theta_1 + \overline{n_2}\cos\theta_2} \tag{2.25}$$

and

$$t_{\mathrm{p}} = \frac{2\overline{n_1}\cos\theta_1}{\overline{n_2}\cos\theta_1 + \overline{n_1}\cos\theta_2} \tag{2.26}$$

The fraction of light reflected at the interface of two media with differing refractive indexes is known as reflectivity. The reflectivity of *j*-polarized light is $\mathcal{R}_j = |r_j|^2$. For unpolarized light, such as sunlight, the reflectivity at the air-semiconductor interface can be calculated by taking the average of the two polarized components of light $\mathcal{R} = (\mathcal{R}_s + \mathcal{R}_p)/2$.

Absorption as a function of depth, within bulk semiconductors, follows Beer-Lambert's law:

$$\mathcal{A}_{\mathrm{BL}} = 1 - e^{-\alpha x} \tag{2.27}$$

where α is the medium's absorption coefficient and x is the distance traveled within the absorptive medium. Finally, transmission ($\mathcal{T}$) can be calculated using the relation, $1 = \mathcal{A} + \mathcal{R} + \mathcal{T}$.

2.2.3 Thin-film semiconductor optics

In thin-film semiconductor structures that employ layer thicknesses around or thinner than the light's wavelength, interference due to Fabry-Perot resonances impacts the optical properties. These interference effects influence the reflection, absorption, and transmission of light within the structure and are captured by the transfer matrix method (TMM). TMM describes the amplitude of the forward (E^+_{m}) and backward (E^-_{m}) propagating waves at the end of the *mth* layer from a known initial field by a matrix operation as follows [65]:

$$\begin{pmatrix} E^+_{\mathrm{m}} \\ E^-_{\mathrm{m}} \end{pmatrix} = M_m \begin{pmatrix} E^+_{\mathrm{m+1}} \\ E^-_{\mathrm{m+1}} \end{pmatrix} \tag{2.28}$$

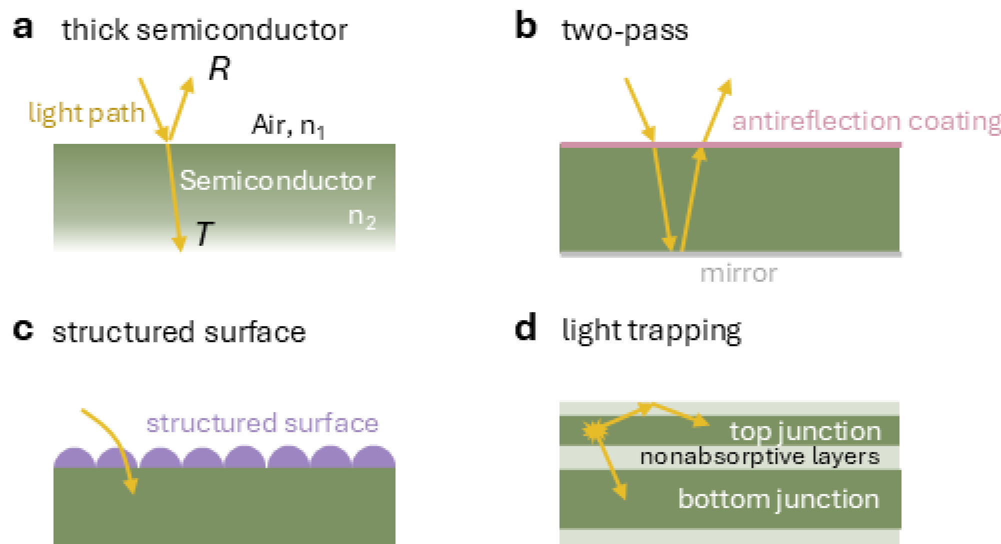

Figure 2.8: Schematic diagrams of light management for: **a** light impinging an air/semiconductor interface, **b** all light transmitting into the semiconductor due to an antireflection coating and all light reflecting off a perfect back reflector for a two-pass chance at absorption, **c** sub-wavelength structured surface which creates an effective gradual change in refractive index to eliminate reflection, and **d** a light-trapping scheme for a multi-junction device.

for $m = 1, 2, 3, ..., N-1$ and *N* is the total number of layers, where

$$M_m = \begin{pmatrix} \exp -ik_m d_m & 0 \\ 0 & \exp ik_m d_m \end{pmatrix} \begin{pmatrix} 1 & r_{n,n+1} \\ r_{n,n+1} & 1 \end{pmatrix} \frac{1}{t_{n,n+1}} \tag{2.29}$$

where d_m is the layer thickness, $k_m = 2\pi \overline{n}_m \cos\theta_m / (\lambda_0 \overline{n}_0)$ is the angular wavevector for the forward-traveling wave in the *mth* layer with θ_m calculated from Snell's law ($n_0 \sin\theta_0 = n_m \sin\theta_m$). The Fresnel reflection and transmission coefficients are $r_{n,n+1}$ and $t_{n,n+1}$ (Eq. 2.23 or 2.24 and Eq. 2.25 or 2.26 depending on the light's polarization) between layers n and $n+1$. TMM assumes the layers at either end are semi-infinite. The *m*th layer is absorptive when k_m is complex.

To know the absorption in each layer with TMM, we first need to calculate the amplitude of the transmitted wave through the whole layer stack (E_N^+). We do so by propagating the matrix through each layer and then solving for E_N^+ as follows [65]:

$$\begin{pmatrix} E_0^+ \\ E_0^- \end{pmatrix} = \frac{1}{t_{0,1}} \begin{pmatrix} 1 & r_{0,1} \\ r_{0,1} & 1 \end{pmatrix} M_1 M_2 ... M_{N-1} \begin{pmatrix} E_N^+ \\ 0 \end{pmatrix} \tag{2.30}$$

Using the results from Eq. (2.30), we can calculate the amplitudes of reflected and transmitted waves with Eq. (2.28) for each layer. From these, we can calculate the layer resolved absorption. The propagation of the electric field amplitude through a 2-layer stack is shown in Fig. 2.9. TMM is used in Chapter 3 and in Section 4.2.

In Chapter 4, we employ a basic form of light-trapping known as a flat back reflector, which is a reflective material placed directly below the PV device (see Fig. 2.8b for a schematic of the light path for a device with a back reflector). The back reflector reflects photons to provide a second opportunity for absorption and/or to eliminate parasitic sub-bandgap photon absorption in the substrate.

2.2.4 Structured surface optics

For structures in two or three spatial dimensions with similar sizes to the light's wavelength, diffraction becomes important. For features much smaller than the wavelength, light interacting

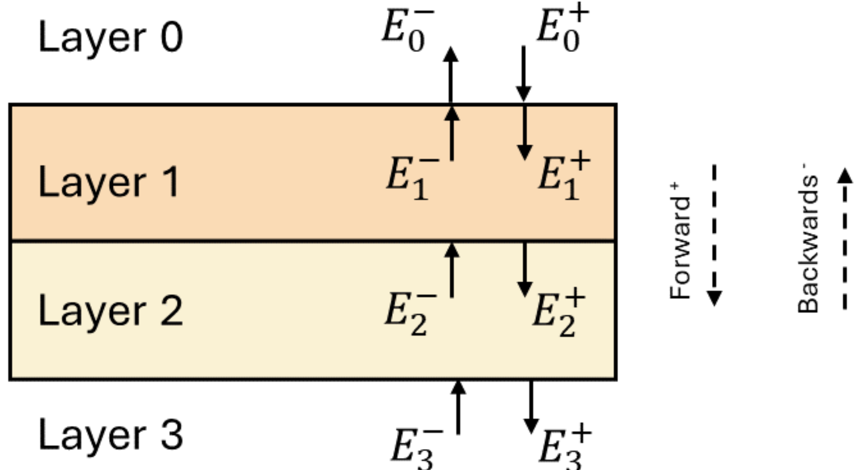

Figure 2.9: Schematic showing the propagation of electric fields through a layer stack as defined by TMM.

with these features can behave as if it is encountering an effective medium which smooths the refractive index transition between media (see Fig. 2.8c for a schematic of a light path through such a surface). In either case, TMM does not accurately predict the optical properties of these structures which influences the reflection, absorption, and transmission within the structures. If this structure is periodic, rigorous coupled wave analysis (RCWA) can be used to model its optical properties.

RCWA models a three-dimensional structure by slicing the periodic array into layers with two spatial dimensions and then expanding those layers in the third spatial dimension to form a staircase approximation. For each layer, RCWA solves Maxwell's equations of electrodynamics using Floquet functions (similar to Bloch Functions for solid-state physics) to separate the in-plane from out-of-plane spacial variations of the Fourier series expanded electric field amplitude. The spatially varying permittivity for each layer is also expanded with a Fourier series. The resulting infinite system of equations is truncated to achieve a specified accuracy and computational speed. The eigenmodes of the system of equations are calculated for each layer by matching the boundary conditions and are propagated through the structure via the scattering matrix method. For details on RCWA calculations, see [66].

For non-periodic two- and three-dimensional structures, finite-element and finite-difference time-domain methods are required. Both solve the electric and magnetic field strengths throughout the spatially meshed domain making them computationally intensive. The finite element method is a frequency-based approach and is most useful when the system is in a steady state (no time dependence), which is the case for most PV applications. The finite-difference time-domain method is a time-based modeling method that solves electric and magnetic field amplitudes at each point in the computational grid using previous and adjacent values for a given grid point. Electric and magnetic field amplitude values are calculated at each grid point for each timestep. The finite-difference time-domain method can simulate the optical properties over a wavelength spectrum in a single simulation. For a detailed comparison between these optical models see [67].

In general, RCWA is computationally faster than both the finite element and the finite difference time domain methods, but requires the structure to be periodic. RCWA is just as fast and accurate as TMM for computing the optical properties of thin films, which is used in the PV community to optimize antireflection coatings. These coatings consist of a stack of transparent thin layers with thicknesses optimized to minimize reflection at the air/semiconductor interface (see Fig. 2.8b for a schematic of light paths). RCWA is used in Chapter 3 to simulate the optical properties of a periodic structured surface, and in Chapter 5 to model thin films, optimize the antireflection coating, and enable future modeling capabilities of structured surfaces.

2.2.5 Thermal radiation

Objects at non-zero kelvin emit a spectrum of optical radiation. At distances from the object much greater than the radiation wavelength (far-field), the emitted spectral irradiance can be described by Planck's law:

$$B_\lambda(T,\lambda) = \frac{2hc^2}{\lambda^5}\frac{1}{e^{hc/\lambda k_\mathrm{B}T}-1} \tag{2.31}$$

where h is Planck's constant, c is the speed of light in vacuum, and λ is the wavelength of light. The solar spectrum is an example of a far-field quasi-blackbody spectrum. The sun's direct spectrum and that of a blackbody radiator at 5800K (Eq. (2.31)) are shown in

Fig. 2.10a. The majority of the discrepancy between the spectra can be explained by the sun's atomic composition, which absorbs and/or transmits specific wavelengths. The sun's power density reaching Earth's atmosphere is about 1360 W/m^2.

When the radiator is within a thermal wavelength from the receiver, given by $\frac{\hbar c}{k_\mathrm{B}T} \approx 7.6\mu\mathrm{m}(\frac{300\mathrm{K}}{T})$ which is a condition known as the near-field, the radiative power transfer can be significantly enhanced compared to far-field. Near-field radiative transfer is enhanced as it encompasses both propagative waves (far-field radiation) and evanescent waves, as illustrated in Fig. 2.10b. An example of an evanescent wave is when light traveling within a high refractive index medium encounters an interface with a lower refractive index medium at an angle larger than the critical angle, resulting in total internal reflection. While the light undergoes total internal reflection in the far-field, it can tunnel to a neighboring material in the near-field. This tunneling can boost the radiative power transfer by a couple orders of magnitude relative to the far-field. For example, Fig. 2.10c shows measured [68] radiative transfer increasing up to 82 times in the near-field compared to the far-field between parallel SiC nanobeams held at different temperatures.

Near-field radiative transfer can be modeled by assuming microscopic fluctuating currents in finite-temperature bodies producing electromagnetic fields that radiate energy. According to the fluctuation-dissipation theorem, the fluctuating currents obey the following relation [69]:

$$\langle J_i(\omega, \mathbf{x}) J_j^*(\omega, \mathbf{x}') \rangle = \frac{1}{\pi} \delta_{ij} \delta(\mathbf{x} - \mathbf{x}') \left[\frac{\hbar\omega}{2} \coth\left(\frac{\hbar\omega}{2k_\mathrm{B}T} \right) \right] \sigma(\omega, \mathbf{x}) \tag{2.32}$$

where $\langle\rangle$ is the ensemble average, $J_i(\omega, \mathbf{x})$ is the *i*th cartesian component of the microscopic current density at vector position $\mathbf{x}$ and frequency ω, $\sigma(\omega, \mathbf{x})$ is the position- and frequency-dependent conductivity which is related to the permittivity of the material as $\sigma(\omega, \mathbf{x}) = \omega \mathrm{Im}\epsilon(\omega, \mathbf{x})$, δ_{ij} is the Kronecker delta function, and $\delta(\mathbf{x} - \mathbf{x}')$ is the Dirac delta function. These point current sources have electric and magnetic fields given at arbitrary points in space ($\mathbf{x}$) by:

$$E_i(\omega, \mathbf{x}) = \int G_{ij}^E(\omega, \mathbf{x}, \mathbf{x}') J_j(\omega, \mathbf{x}') d\mathbf{x}' \tag{2.33}$$

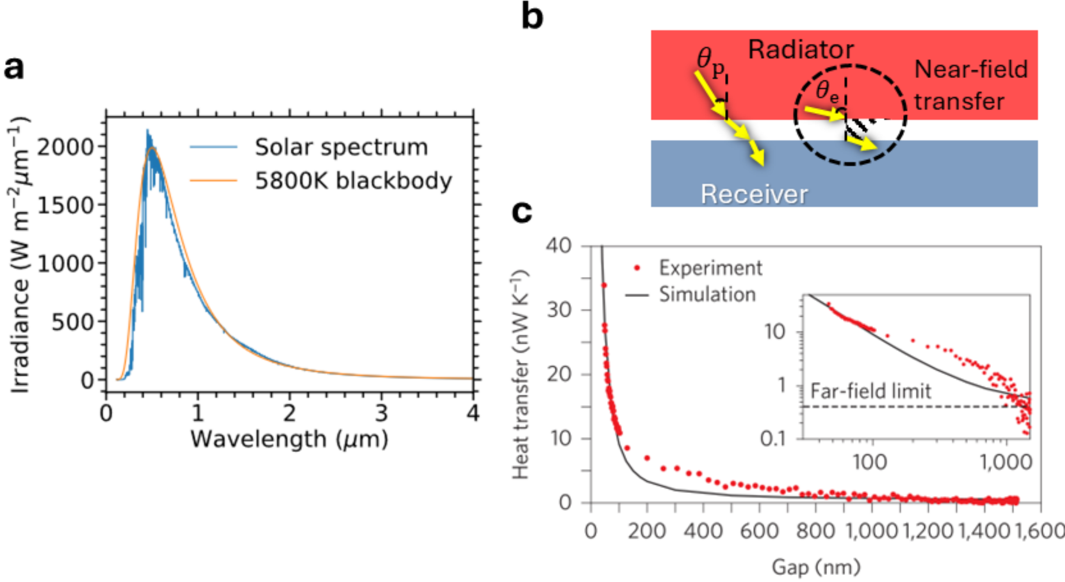

Figure 2.10: **a** Comparing the ASTM E490-00 reference solar spectrum to the blackbody spectrum from a 5800K heat source (Eq. (2.31)) that is reduced by a factor of about 15000 to account for the view factor of the sun from the earth. **b** Schematic diagram showing two pathways for optical radiation transfer from a radiator to a receiver: the left-hand pathway is propagative radiation transfer and the right-hand pathway is evanescent radiation transfer. **c** Measurement and simulation of heat transfer between parallel SiC nanobeams as a function of the separation between the beams. Inset: the same data but on a logarithmic scale. The figure **c** is a copy from [68].

$$H_i(\omega, \mathbf{x}) = \int G^M_{ij}(\omega, \mathbf{x}, \mathbf{x}') J_j(\omega, \mathbf{x}') d\mathbf{x}' \tag{2.34}$$

where G^E_{ij} and G^M_{ij} are the electric and magnetic dyadic green's functions with the *i*-component of the field at **x** due to a *j*-directed point current source at **x**'.

Assuming two homogenous bodies $B_{1,2}$ maintained at temperatures $T_{1,2}$, the net radiation transfer rate from body 1 to body 2 is given by the mean Poynting flux:

$$P(\omega) = \frac{1}{2} \int_{S_1} \langle \mathbf{E}(\omega, \mathbf{x}) \times \mathbf{H}^*(\omega, \mathbf{x}) \rangle d\mathbf{S} \tag{2.35}$$

where S_1 is the surface of body 1 and $d\mathbf{S}$ is the inward-pointing surface normal. Combining Eqs. (2.32), (2.34) and (2.35), the integral is now over the volumes of the bodies:

$$\begin{aligned} P(\omega) =& \frac{\epsilon_{ijk}}{2} \int_{S_1} \Big\{ \sigma_1(\omega) \Theta[\omega, T_1] \int_{B_1} G^E_{il}(\omega, \mathbf{x}, \mathbf{x}') G^{M*}_{jl}(\omega, \mathbf{x}, \mathbf{x}') d\mathbf{x}' \\ &+ \sigma_2(\omega) \Theta[\omega, T_2] \int_{B_2} G^E_{il}(\omega, \mathbf{x}, \mathbf{x}') G^{M*}_{jl}(\omega, \mathbf{x}, \mathbf{x}') d\mathbf{x}' \Big\} dS_k \end{aligned} \tag{2.36}$$

where ϵ_{ijk} is the Levi-Civita symbol with $(\mathbf{A} \times \mathbf{B})_k = \epsilon_{ijk} A_i B_j$. Eq. (2.36) integrates over each body, as radiation can be generated in both.

To compute the net radiative heat transfer between two bodies using Eq. (2.36), it is now required to derive an equation for the electric and magnetic dyadic Green's functions. For one-dimensional spatially varying applications, such as near-field thermophotovoltaics discussed in Chapter 4, the dyadic Green's function can be expressed as plane waves into s- and p-polarizations using a two-dimensional Fourier transform. Then the amplitudes within the structure are calculated using the scattering matrix method, refer to Ref. [70] for the formalism. Note, that the scattering matrix method is similarly derived as the TMM formalism in this case.

2.3 Photovoltaic power conversion

The following section provides background to understand the optoelectronic properties of PV devices, which is necessary for PV device design and is used in Chapters 4 and 5.

When photons with energy greater than the bandgap are absorbed by a semiconductor, they excite electrons from the valence band into the conduction band, leaving behind holes (as was discussed in Section 2.1.9). These photogenerated charge carriers can be extracted using an electric field applied across the illuminated semiconductor, creating a photocurrent. Extracting the photocurrent (I) by applying a voltage (V) to generate an electric field requires power ($P = IV$). However, if the semiconductor has a built-in anisotropy that creates an electric field, these photo-excited charge carriers can be extracted without supplying power. In structures with a built-in electric field, applying a forward voltage bias (V) reduces the built-in electric field and collected photocurrent (I), but allows for power extraction equivalent to $P = IV$. This section takes a deeper dive into the physical processes enabling the conversion of optical power to electrical power for PV devices.

2.3.1 p-n junctions

A common method to create a built-in electric field is to vary the dopant type in semiconductor materials to create two regions, forming a p-n junction at the interface. As this structure forms, majority charge carriers diffuse across the junction leaving behind charged impurities and creating a built-in bias. This bias causes a drift current. This current is equal to the current diffusing across the junction from charge population gradients when the system is at equilibrium. At equilibrium, there is a constant Fermi level throughout the semiconductor. The built-in bias is calculated by taking the difference between the p-side and n-side work functions, which are equal to $\Phi = (E_{\mathrm{vac}} - E_{\mathrm{F}})/q$. For a homojunction where the same semiconductor material is used on either side of the junction, the built-in bias is [9]:

$$V_{\mathrm{bi}} = \frac{k_{\mathrm{B}}T}{q} \ln\left(\frac{N_{\mathrm{d}}N_{\mathrm{a}}}{n_{\mathrm{i}}^2}\right) \tag{2.37}$$

The image in Fig. 2.11a shows an example of an unilluminated p-n homojunction at equilibrium. By applying a forward bias (V) to the p-side relative to the n-side, as illustrated in Fig. 2.11b, the energy barrier to minority carriers on either side of the junction (V_{bi}) is lowered by V due to a decrease in the number of ionized impurities. The region in the semiconductor with ionized dopants is known as the depletion region and/or space charge region. Under the depletion approximation, where a depleted space-charge region is assumed, its width can be estimated. Using Poisson's equation and that the field must vanish at the edges of the depleted layer, the depletion width on either side of the p-n junction can be expressed as follows:

$$w_{\mathrm{n}} = \frac{1}{N_{\mathrm{d}}}\sqrt{\frac{2\epsilon_{\mathrm{s}}V_{\mathrm{bi}}}{q\left(\frac{1}{N_{\mathrm{a}}}+\frac{1}{N_{\mathrm{d}}}\right)}} \tag{2.38}$$

$$w_{\mathrm{p}} = \frac{1}{N_{\mathrm{a}}}\sqrt{\frac{2\epsilon_{\mathrm{s}}V_{\mathrm{bi}}}{q\left(\frac{1}{N_{\mathrm{a}}}+\frac{1}{N_{\mathrm{d}}}\right)}} \tag{2.39}$$

The width of the depletion region w_{scr} is the sum of equations Eqs. (2.38) and (2.39). Within this region, photogenerated electron-hole pairs separate and drift to either edge. Meanwhile outside the depletion region, photogenerated minority carriers must diffuse to the depletion region before drifting to the opposite side to become majority carriers and contribute to power generation. Recombination limits the diffusion length of minority carriers, so increasing the width of the depletion region maximizes current collection. The w_{scr} can be widened by reducing the p- and n-type doping concentrations, although this will lower V_{bi}. Lowering V_{bi} limits the maximum forward bias (V) that can be applied to the p-side relative to the n-side for power extraction, as $V < V_{\mathrm{bi}}$ to extract power. Therefore, the interaction between current collection and built-in bias poses an important optimization challenge for maximizing the power output of PV devices.

Under illumination, the quasi-Fermi levels for electrons $E_{\mathrm{F_n}}$ and holes $E_{\mathrm{F_p}}$ split giving rise to minority carrier densities that exceed the equilibrium concentrations. The band profile of an illuminated p-n junction at V=0, known as the short-circuit condition, is depicted in Fig. 2.11c. The $E_{\mathrm{F_n}}$ on the n-side equals to $E_{\mathrm{F_p}}$ on the p-side of the homojunction. Applying a forward bias separates these quasi-Fermi levels, which is necessary to extract power from the illuminated

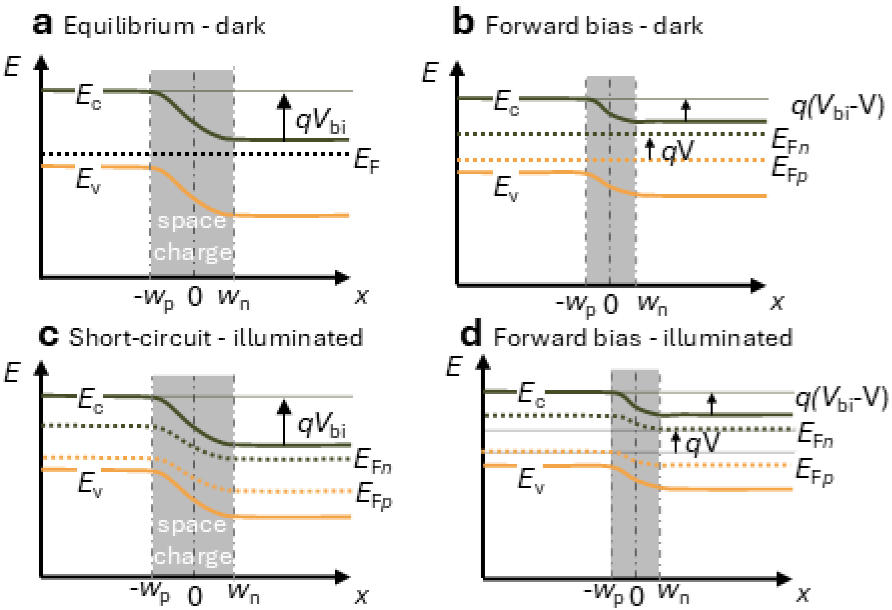

Figure 2.11: Band profiles as a function of the spatial coordinate going across a p-n homojunction. In the dark and **a** at equilibrium, or **b** in forward bias. Under illumination **c** at short-circuit, or **d** in forward bias. E_{c} and E_{v} is the conduction and valence band energies, $E_{\mathrm{F}n}$ and $E_{\mathrm{F}p}$ are the electron and hole quasi-Fermi levels, E_{F} is the Fermi level, V is the applied bias, q is the elementary charge, and V_{bi} is the built-in bias.

junction. The band profile of a forward-biased p-n junction under illumination is illustrated in 2.11d. Power can be extracted up to the forward bias value which causes the quasi-Fermi levels to become flat across the space-charge region, corresponding to open-circuit voltage. Applying a forward bias larger than the open-circuit voltage supplies current to the p-n junction, thereby requiring input power. Therefore, the region between short-circuit and open-circuit voltage is the most important part of the current-voltage characteristics for PV devices.

2.3.2 Current-voltage characteristics

The current-voltage (IV) characteristics of a typical high-quality PV device in the dark are shown in Fig. 2.12a. At low forward biases, the current primarily arises from SRH recombination in

the space-charge region, where the electron and hole populations are similar. As the forward bias increases, the diffusion current can become dominant, originating from recombination outside the space-charge region. In high-quality direct bandgap materials, such as most III-V materials used in PVs, radiative recombination constitutes the majority of the diffusion current. At high forward biases, series resistance typically limits the current. However, if not for this limitation, the dominant current source would transition to Auger recombination (see Fig. 2.6 for recombination process), which has a slope 50% steeper than that of the diffusion current as shown in Fig. 2.12a. At low reverse bias, the current drawn from the PV device is mainly due to SRH generation in the space-charge region. At high reverse biases, the energy bands bend enough to enable electron and/or hole tunneling between the conduction and valence bands within the space charge region.

The forward bias part of the dark IV curve shown in Fig. 2.12a can be represented by the two-diode model given by the following equation:

$$I(V) = I_{01}\left[\exp\left(\frac{q(V-IR_{\mathrm{s}})}{k_{\mathrm{B}}T}\right)-1\right] + I_{02}\left[\exp\left(\frac{q(V-IR_{\mathrm{s}})}{2k_{\mathrm{B}}T}\right)-1\right] + \frac{V-IR_{\mathrm{s}}}{R_{\mathrm{shunt}}} \quad (2.40)$$

where I_{01} and I_{02} are dark saturation currents, R_{s} is the series resistance, and R_{shunt} is the shunt resistance. The R_{shunt} encompasses all current paths parallel to the diodes that act as resistors, having their strongest impact near 0 V. One example contributor to R_{shunt} is conductive pinholes through the p-n junction. The first and second terms in Eq. (2.40) represents I_{diff} and I_{scr}, respectively, and increases exponentially with temperature. The I_{scr} is dominated by SRH recombination. Under illumination, a current source is added to Eq. (2.40), and the diode model then becomes:

$$I(V) = I_{\mathrm{sc}} - I_{01}\left[\exp\left(\frac{q(V+IR_{\mathrm{s}})}{k_{\mathrm{B}}T}\right)-1\right] - I_{02}\left[\exp\left(\frac{q(V+IR_{\mathrm{s}})}{2k_{\mathrm{B}}T}\right)-1\right] - \frac{V+IR_{\mathrm{s}}}{R_{\mathrm{shunt}}} \quad (2.41)$$

where I_{sc} is the short-circuit current source which scales linearly with illumination. Eq. (2.41) is the photocurrent minus Eq. (2.40), following the convention in the PV scientific community. When the dark current equals I_{sc}, the device is at the open-circuit voltage (V_{oc}). The V_{oc}

generally increases logarithmically with intensity but not above the bandgap of the absorbing semiconductor ($V_{\mathrm{oc}} < E_{\mathrm{g}}/q$).

The maximum power point ($P_{\mathrm{MPP}} = I_{\mathrm{MPP}} V_{\mathrm{MPP}}$) is the point on the IV curve at which maximum power is achieved and is given by the multiplication of the current and voltage at maximum power. The P_{MPP} is maximized when the IV curve is square, assuming I_{sc} and V_{oc} are unaffected. The squareness of the curve is quantified as the fill factor (FF) and is given by:

$$FF = \frac{P_{\mathrm{MPP}}}{I_{\mathrm{sc}} V_{\mathrm{oc}}} = \frac{I_{\mathrm{MPP}} V_{\mathrm{MPP}}}{I_{\mathrm{sc}} V_{\mathrm{oc}}} \tag{2.42}$$

A non-negligible R_{shunt} will create a downward slope for the IV curve near I_{sc}, while R_{s} reduces the slope near V_{oc}. Both factors decrease *FF*. For direct bandgap PV devices limited by radiative recombination, the ideal conditions are $R_{\mathrm{shunt}} \to \infty$, $R_{\mathrm{s}} \to 0$, and $I_{02} \to 0$. Figure 2.12b shows a sample light-IV curve of such a device.

A sought-after figure of merit for PV devices is the optical-to-electrical conversion efficiency (η), defined as:

$$\eta = \frac{P_{\mathrm{MPP}}}{P_{\mathrm{in}}} \tag{2.43}$$

where P_{in} is the power of the incident light.

2.3.3 Quantum efficiency

The I_{sc} is limited to the photogenerated current, which is the current when all photogenerated electron-hole pairs are collected. The I_{sc} can be calculated by integrating over the photon energy (E) as:

$$I_{\mathrm{sc}} = qA \int_0^{\infty} \Phi_{\mathrm{in}}(E) EQE(E) dE \tag{2.44}$$

where A is the illuminated semiconductor area of the PV device, Φ_{in} is the incident photon flux, and external quantum efficiency (EQE) is defined as the ratio between the number of

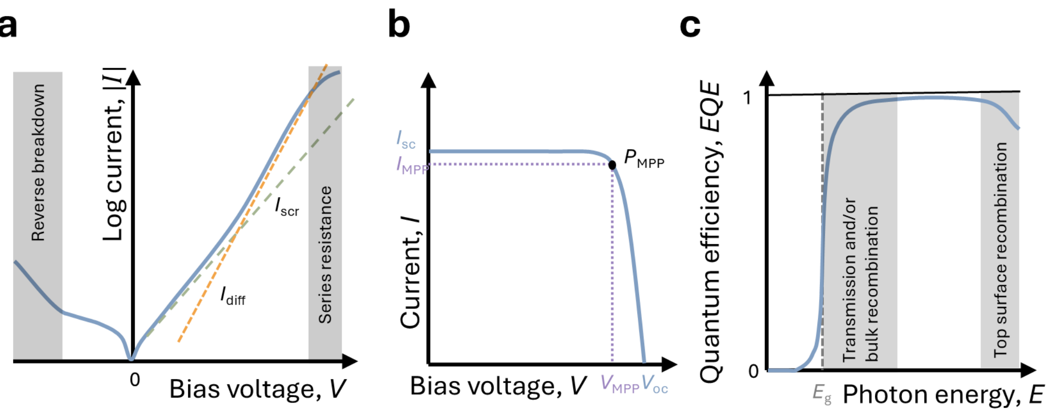

Figure 2.12: Current-voltage characteristics of a photovoltaic device, **a** in the dark with a logarithmic scaled vertical axis and **b** under illumination. **a** The dark current includes the diffusion current I_{diff} and the space charge region current I_{scr}. **b** The short-circuit current I_{sc}, open-circuit voltage V_{oc}, maximum power point P_{MPP}, current at maximum power I_{MPP}, and voltage at maximum power V_{MPP} are highlighted. **c** An example external quantum efficiency curve for a PV device with bandgap E_{g}

carriers collected by the external circuit at I_{sc} to the number of incident photons. Ideally EQE $=$ 1 for $E > E_{\text{g}}$ but in reality, factors limit the EQE such as reflection from surfaces and interfaces, transmission through the absorbing layer, recombination of photogenerated carriers before they are collected, and parasitic absorption in regions other than the active layers. In theory, the EQE $= 0$ for $E < E_{\text{g}}$ but in practice, it is slightly higher due to sub-bandgap absorption enabled by exciton formation, phonon-electron interactions, and impurity states [71]. An example EQE curve of a PV device is shown in Fig. 2.12c.

Since EQE depends on lots of factors, some of which can be decoupled by measuring instead internal quantum efficiency (IQE) given by:

$$IQE(E) = \frac{EQE(E)}{1 - \mathcal{R}(E) - \mathcal{T}(E)} \tag{2.45}$$

where $\mathcal{R}(E)$ and $\mathcal{T}(E)$ are the spectral reflectance and transmittance of the device, respectively. The IQE accounts for the impact of optical reflection and transmission on the collection of charge carriers making it easier to isolate the effects of the remaining phenomena.

2.3.4 Multi-junction photovoltaics

Most photons with energy below the bandgap do not contribute to the I_{sc} as they typically don't generate electron-hole pairs. Photons with energy greater than the bandgap can contribute to I_{sc}, but the photogenerated carriers lose energy equal to (E - E_{g}) due to thermalization, as was discussed in Section 2.1.9. Therefore, optimizing the bandgap of the absorbing material in a single-junction PV device is crucial to maximizing optical-to-electrical conversion efficiency, which can reach up to about 33% for the solar spectrum on earth with a PV device with a bandgap of about 1.4 eV [9]. The multi-junction architecture (see Fig. 2.13a) can address thermalization/transparency losses, achieving a theoretical limiting efficiency of about 69% under one sun illumination.

Multi-junction devices consist of multiple p-n junctions, called subcells, stacked on top of one another and are usually interconnected in series with tunnel diodes that act as low-resistance ohmic interfaces. When incoming light spans a spectrum, the optimized multi-junction architecture follows the optical path, starting with a large bandgap subcell, followed by

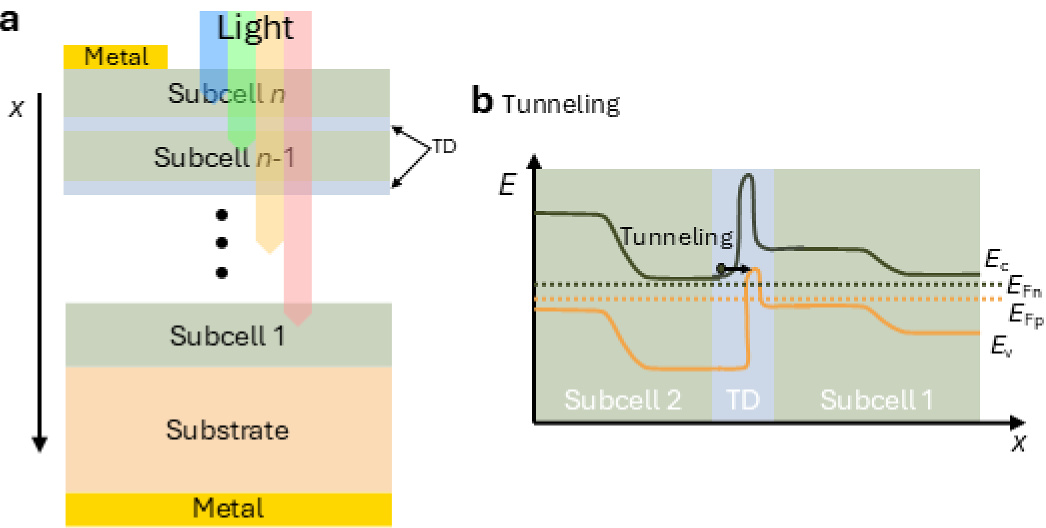

Figure 2.13: **a** Schematic diagram of a multi-junction photovoltaic device where part of the light is absorbed in each subcell. **b** Band diagram of a multi-junction device in the dark and under forward bias, with 2 subcells and a tunnel diode (TD).

subcells with progressively smaller bandgaps as the light moves further into the device. Ideally, the top subcell (*n*) absorbs all photons with energy $E > E_{g,n}$, the second from top subcell (*n-1*) absorbs all photons with energy $E_{g,n} > E > E_{g,n-1}$ and so on. This arrangement eliminates thermalization and transparency losses.

Multi-junction architectures can also include multiple series-connected subcells of the same absorbing material. Such designs can simultaneously lower the current and boost the voltage. Lowering the current helps minimize series resistance losses, while the voltage boost can eliminate the need for post-voltage-boosting power electronics. This voltage boost is beneficial in PPC applications (as will be discussed in Chapter 5), as single-junction devices output voltages too low for the electronic devices they power.

To maximize the voltage boost, low-resistance tunnel diodes are crucial. Tunnel diodes provide low-resistance interconnections between the absorbing subcells such that the total device voltage is approximately equal to the sum of the voltages of each subcell. Tunnel diodes consist of highly doped p-n junctions with opposite doping orientations compared to the subcells. The high doping creates a narrow depletion region with a large electric field, which significantly bends the bands. This band bending allows charge carriers to non-locally tunnel across the junction between the valence and conduction bands, as depicted in Fig. 2.13b.

The multi-junction's series-connected nature restricts the device's current to that of the current-limiting junction. Losses resulting from this current-matching requirement can be mitigated by optimizing the absorber layer thicknesses and bandgaps of all the junctions. Additionally, the current matching requirement can be relaxed by luminescent coupling, where a photon generated from radiative recombination is reabsorbed in a neighboring subcell. Similar to photon recycling (Section 2.1.9), luminescent coupling is strongest for PV devices using high material quality. At P_{MPP}, the current-limiting subcell operates near I_{sc}, while the other subcells operate closer to V_{oc}. Consequently, the current-limiting subcell experiences minimal recombination, whereas the other subcells undergo significant recombination, potentially increasing the current of the limiting subcell if it absorbs emitted photons from radiative recombination.

A new design approach to improving light management in multi-junction devices is introduced in Chapter 5. It involves a light-trapping scheme; a multi-junction PPC design that reabsorbs most of its emitted photons from radiative recombination by making the thick bottom

junction limiting (see Fig. 2.8d for a schematic example).

2.4 Simulating optoelectronic devices

I conducted several measurements in this thesis, including dark current-voltage, laser and solar simulator illuminated current-voltage, quantum efficiency, reflectivity by Fourier transform infrared spectroscopy, scanning electron microscopy, and profilometry. The methodology used for my measurements followed the approach outlined in Beattie's thesis [37] and is described in the manuscripts within Chapters 3 to 6.

The following section presents models that use the previously introduced physics to simulate various aspects of PV devices, which are useful for Chapters 3 to 5.

2.4.1 Optical models

Four distinct optical models are used throughout this thesis: ray tracing in Ansys Zemax Opticstudio, TMM implemented in Python, RCWA in open-source software using Matlab and Python, and a near-field heat transfer model in open-source software written in Julia. For multi-dimensional problems with non-trivial material shapes much larger than the wavelength of light, one can use ray tracing models such as the commercially available Ansys Zemax OpticStudio [72] to simulate the optical properties of the system. I employ this software in Chapter 3. An illustration of applying ray tracing to a CPV submodule is shown in Fig. 2.14. The model sends rays from a light source and simulates their optical path with geometrical considerations coupled with Eqs. (2.23), (2.24) and (2.27) and the relation $1 = \mathcal{A}_{\mathrm{BL}} + \mathcal{T} + \mathcal{R}$ to calculate the reflection ($\mathcal{R}$), Beer-Lambert absorption ($\mathcal{A}_{\mathrm{BL}}$), and transmission ($\mathcal{T}$) throughout the system.

To model the optical properties of thin films, I used the open-source software written in Python by Byrnes *et al.* [65], which is based on TMM (see Section 2.2.3 for method details). I utilized this software in Chapter 3 and in Section 4.2.

I also modeled thin films and structured surfaces with RCWA. For model details, see Section 2.2.4. In Chapter 3, I used the open-source RCWA software "RETICOLO", written in

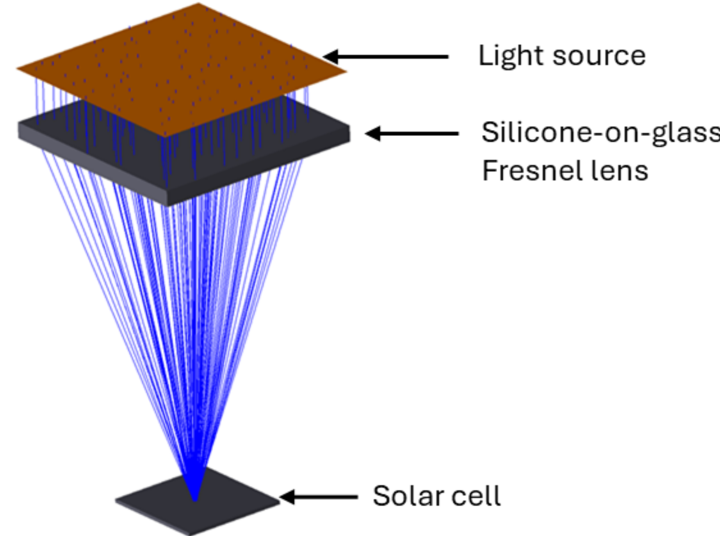

Figure 2.14: Ray tracing used for a concentrator photovoltaic submodule. Light rays emitted from the source are directed towards a Fresnel lens, which refracts and focuses the rays onto the solar cell.

Matlab by Hugonin *et al.* [73]. However, to avoid Matlab's licensing requirements, I used the open-source RCWA software "S4", written in Python by Liu *et al.* [74], in Chapter 5.

To model near-field heat transfer in Chapter 4, I used the open-source heatSlabs software written in Julia by Sean Molesky, available on his GitHub [75]. The modelling approach is described in Section 2.2.5 on near-field thermal radiation heat transfer.

2.4.2 Distributed circuit model

In Section 2.3.2, it was shown that the IV characteristics of an illuminated solar cell can be represented by a combination of diodes, resistors, and a current source (Eq. (2.41)). This equation models a circuit comprising two diodes (J_{01} and J_{02}), a current source (J_{sc}), and a shunt resistor (R_{SH}), all connected in parallel, and a series resistor (R_{series}) connected in series, as shown in Fig. 2.15a.

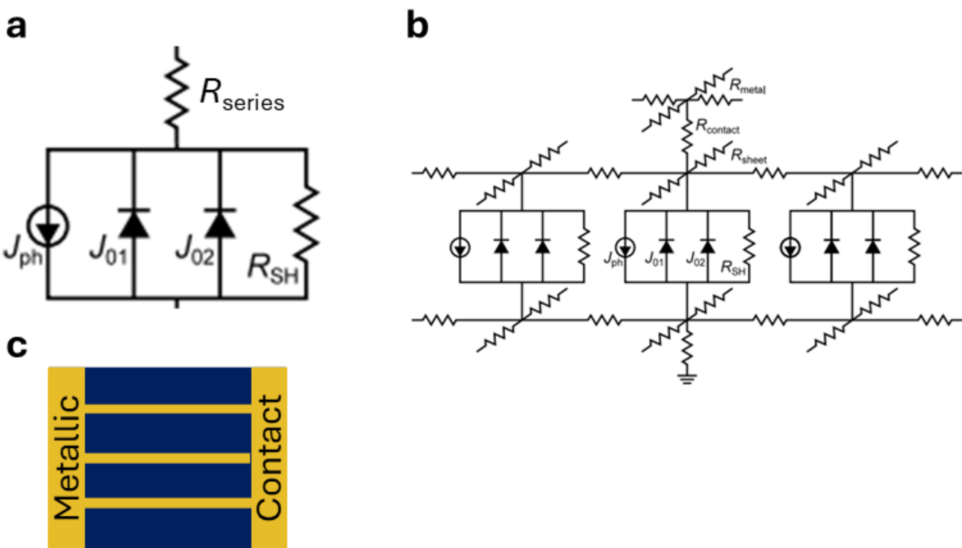

Figure 2.15: **a** Schematic diagram of a circuit representing the two-diode model (Eq. (2.41)) which can simulate the IV characteristics of a PV device. **b** Distributed circuit to represent the optoelectronic properties in multiple spatial dimensions for a PV device. Modified from [76]. **c** Diagram of the metallization pattern on the surface of the PV device assumed by DECIMOS.

This circuit can be distributed spatially throughout the device's geometry, forming a distributed circuit model (DCM) as shown in Fig. 2.15b. I employ a DCM in Chapter 5. In PV device DCMs, additional components such as sheet resistors (R_{sheet}), contact resistors (R_{contact}), and metal resistors (R_{metal}) are included. The R_{sheet} accounts for current moving laterally within the semiconductor from the illuminated region to contacts. The R_{contact} represents the series resistance from imperfect electrical contact at the metal-semiconductor interface, while the R_{metal} represents the series resistance affecting current flow within the metallic contacts. This DCM can simulate the impact of nonuniform illumination and resistive losses in the device. These models are typically used in PV research to optimize the top metallic contact geometry and window layer thicknesses based on an input illumination profile, aiming to minimize resistive losses.

In Chapter 5, I use DECIMOS, a custom-built DCM written in Matlab by SUNLAB researchers. DECIMOS takes input values for the circuit components shown in Fig. 2.15b and creates a distributed circuit to represent rectangular PV devices, as shown in Fig. 2.15c, with top contacts made of periodic thin metallic fingers and the option of including wide metallic busbars. For further model details, see Sanmeet Chahal's co-op report which can be accessed upon request from SUNLAB.

2.4.3 Drift diffusion model

DCMs simulate the IV characteristics of the PV device using the non-predictive two-diode model but are limited in optimizing the design of the semiconductor epitaxial stack. Instead, a calibrated drift-diffusion model can be used, such as the commercially available technology computer aided design (TCAD) Sentaurus software from Synopsys Inc. [77]. I employed Sentaurus to design high-efficiency PV devices in Chapters 4 and 5. Sentaurus uses a series of programs called "tools" that generally run sequentially to simulate the optoelectronic properties of PV devices under various conditions, as shown in Fig. 2.16.

Each tool has its inputs, outputs, and command file. A simulation starts with the *Epi tool* which generates the layer structure of a one-dimensional epitaxial device, taking as input the material's parameter file name, thickness, doping, material composition, and meshing parameters for each layer. The *Structure editor* creates contacts for current collection and generates

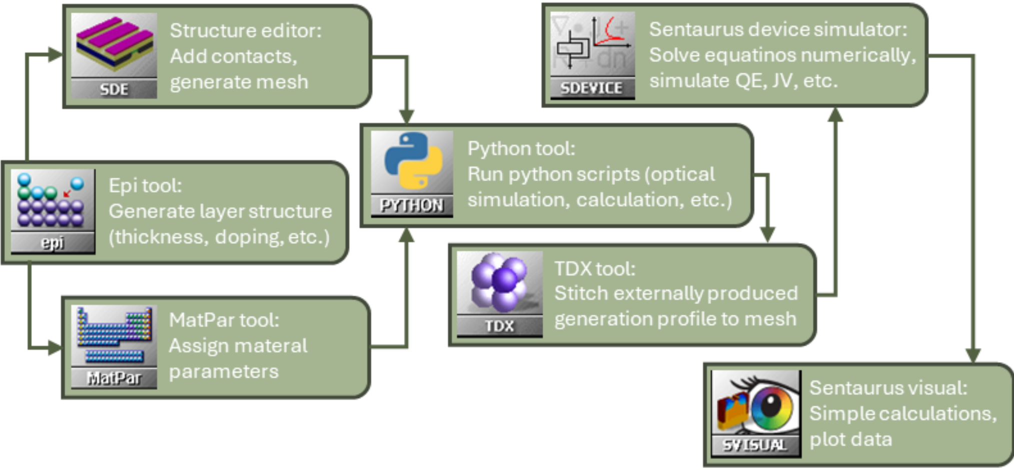

Figure 2.16: TCAD Sentaurus tool flow.

the final mesh, requiring denser meshing near the layer edges where the most extreme potential gradients are found. The *MatPar tool* takes the structure parameters from the *Epi tool* and creates parameter files for each layer with appropriate material parameters required for the opto-electronic model. The *Python tool* runs Python scripts; in my case, I used it to bridge Sentaurus to external optical software and to perform more complex calculations like root-mean-square errors between measured and simulated properties for optimization purposes. The *TDX tool* was used to stitch the externally generated electron-hole pair generation rate from the *Python tool* to the Sentaurus mesh. The *Sentaurus device simulator* takes the structure, mesh, material information, and optical generation profile and computes the electrical properties of the device by solving the Poisson and electron and hole continuity equations (Eqs. (2.10) to (2.12)) using the box discretization method [78, 79]. Finally, the *Sentaurus visual* tool is used to visualize the outputs of the *Sentaurus device simulator* and can perform simple calculations. A complete description of the simulation process of III-V multi-junction PVs in Sentaurus is provided by Walker [80] and by Wilkins and Hinzer [58].

Chapter 3

Microstructured surfaces for concentrator photovoltaics

This chapter details my work on integrating a microstructured surface designed for 500x CPV submodules, initially introduced in Section 1.1. This microstructured surface is embedded with a solar cell encapsulant comprising partially submerged silica microbeads in PDMS. I simulate the optical properties of the layer with ray tracing, rigorous-coupled wave analysis, and transfer matrix method models described in Sections 2.2.2, 2.2.3, and 2.2.4 respectively. The chapter is divided into two sections separating two published works: simulating the performance of the new encapsulant in a CPV system as a function of system temperature, and experimental characterization with model validation of the new encapsulant. Ideally, the efficiency of converting sunlight to electrical power is optimized. However, to minimize the impact of device-to-device variability, we optimized for the short-circuit current of the devices using the reference AM1.5D solar spectrum.

This research aims to advance CPV systems by enhancing their efficiency and resilience, potentially making them more cost-competitive with traditional silicon photovoltaic systems.

3.1 Nanostructured surface for extended temperature operating range in CPV modules

The conference proceeding presents my research on simulating the performance of CPV systems operating over realistic temperatures. This study evaluates the advantages of the newly developed encapsulant.

Impact

The following conference proceeding has the following novelties:

1. Developed model to simulate the impact of the new bead/PDMS encapsulant on the CPV submodule's temperature-dependent performance.
2. Discovered 400 nm diameter beads submerged halfway in the PDMS material results in the most stable performance for the CPV submodule, particularly when operating within the temperature range -25 °C to 50 °C. Potential current gains up to 2.6% are achievable using the beads.

These results suggest that this approach could lead to more efficient and cost-effective CPV systems, enhancing the viability of CPV solar energy in regions with significant temperature variations.

Author contribution

Gavin P. Forcade: As the lead University of Ottawa-based graduate student associated with the project, I performed the optical simulations and wrote the text. I was the lead author of the conference proceeding.

Dr. Christopher E. Valdivia: As a senior research scientist within the University of Ottawa's SUNLAB research group, Chris helped to guide my research, provided detailed feedback during the analysis of my simulation results, and assisted in editing the manuscript.

Philippe St-Pierre: As the lead Université de Sherbrooke-based graduate student associated with the project, Philippe helped guide simulations to represent his experimental findings and assisted in editing the manuscript.

Dr. Arnaud Ritou: As a postdoctoral researcher at Université de Sherbrooke, Arnaud helped guide simulations to represent his experimental findings and assisted in editing the manuscript.

Dr. Maïté Volatier: As a research professional at Université de Sherbrooke, Maïté oversaw the project.

Prof. Abdelatif Jaouad: As an adjunct professor at Université de Sherbrooke, Abdelatif oversaw the project.

Prof. Maxime Darnon: As the professor at Université de Sherbrooke, Maxime oversaw the research, provided detailed feedback during the analysis of results, and assisted in editing the manuscript.

Prof. Karin Hinzer: As the director of the University of Ottawa's SUNLAB research group, Karin oversaw my research, provided detailed feedback during the analysis of my simulation results, and assisted in editing the manuscript.

Reproduced from:

> G.P. Forcade, C.E. Valdivia, P. St-Pierre, A. Ritou, M. Volatier, A. Jaouad, M. Darnon, and K. Hinzer, "Nanostructured surface for extended temperature operating range in concentrator photovoltaic modules", *AIP conference proceedings*, 050002, 2020. DOI: 10.1063/5.0032134

with the permission of AIP Publishing. The conference was CPV-16.

AIP Conference Proceedings

RESEARCH ARTICLE | NOVEMBER 09 2020

Nanostructured surface for extended temperature operating range in concentrator photovoltaic modules

Gavin Forcade; Christopher E. Valdivia; Philippe St-Pierre; Arnaud Ritou; Maïté Volatier; Abdelatif Jaouad; Maxime Darnon; Karin Hinzer

AIP Conf. Proc. 2298, 050002 (2020)
https://doi.org/10.1063/5.0032134

06 August 2024 17:17:00

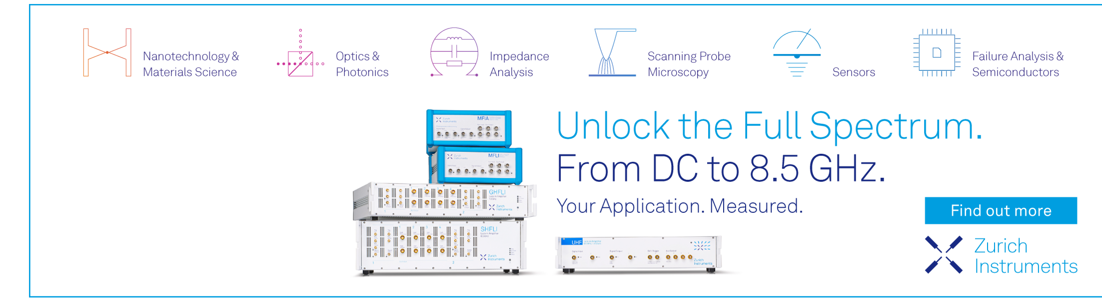

Nanostructured Surface for Extended Temperature Operating Range in Concentrator Photovoltaic Modules

Gavin Forcade[1, a)], Christopher E. Valdivia[1], Philippe St-Pierre[2], Arnaud Ritou[2], Maïté Volatier[2], Abdelatif Jaouad[2], Maxime Darnon[2], and Karin Hinzer[1]

[1]*SUNLAB, Centre for Research in Photonics, University of Ottawa, Ottawa, On, Canada.*
[2]*Laboratoire Nanotechnologies et Nanosystèmes, LN2, CNRS, Université de Sherbrooke, Institut Interdisciplinaire d'Innovation Technologique (3IT), QC, Canada.*

[a)] Corresponding author: gforc034@uottawa.ca

Abstract. Concentrator photovoltaic (CPV) systems that use silicone-on-glass Fresnel lenses as their primary optical element have reduced power output at high and low lens temperatures. We show that incorporating a nanostructured surface on the solar cell stabilizes best module performance over an extended operating temperature range. We model the optical properties of a self-organized monolayer of glass beads deposited on a polydimethylsiloxane (PDMS) encapsulated solar cell in a CPV sub-module. Our model combines transfer matrix method (TMM), rigorous coupled wave analysis (RCWA), and ray tracing to quickly and accurately simulate the system. We find the short-circuit current gain increases as the lens deviates from its designed working temperature for all bead sizes, and that 400 nm diameter beads submerged halfway into PMDS have the highest gain (up to 2.6%).

06 August 2024 17:17:00

INTRODUCTION

III-V photovoltaic cells have the highest conversion efficiency of sunlight to electrical energy, up to 47.1% under concentrated light [1]. However, high costs limit their applications to space where high power-to-weight ratio dominates over device cost [2]. Advances in cost, efficiency, and energy collection are required for wider adoption of these devices within terrestrial concentrator photovoltaic (CPV) systems. CPV modules use relatively inexpensive optics to concentrate sunlight by hundreds of times onto solar cells, demonstrating the highest module efficiency of 36.7% [3] and, with a highly transmissive lens, a sub-module efficiency of 43.4% [4]. CPV has the potential to provide energy at both high yields and low costs for locations with a high solar resource [5] but must compete with the low cost of conventional non-concentrating Si photovoltaic (PV) panels [6]. Silicone-on-glass (SoG) Fresnel lenses provide an inexpensive yet high-performance platform for solar concentration but suffer from temperature-related focusing errors, illustrated in Fig. 1. These focussing errors result from two orders of magnitude difference between the coefficients of thermal expansion of silicone and glass, and from the temperature-dependent refractive indices [7]. These effects reduce the annual energy yield of CPV systems, reaching a calculated 8% absolute reduction for regions with large temperature variations [8]. Curing the silicone at the lens operating temperature minimizes the focusing errors [9] but customizing modules for regional deployment greatly increases manufacturing costs. Instead, Hornung et al. [10] numerically optimized the SoG Fresnel lens structure to lower the thermally-varying optical efficiency from 11.6% to 3.1% (absolute) for lens temperatures from 10 to 60ºC. Performance can be further improved by placing a secondary optical element (SOE) on the solar cell [11] but adds cost and complexity to CPV modules.

The approach present herein employs a relatively inexpensive nanostructured surface on the solar cell to improve the temperature-dependent performance of the CPV system. Nanostructured surfaces can increase the transmission of light into the solar cell relative to flat surfaces by providing a smoothly-varying effective refractive index transition [12]. Researchers at CEA-LITEN (France) developed a colloidal dynamic fluid-flow process to create a micro- or nano-structured surface by depositing a self-organized monolayer of glass or silica beads on a polydimethylsiloxane

16th International Conference on Concentrator Photovoltaic Systems (CPV-16)
AIP Conf. Proc. 2298, 050002-1–050002-6; https://doi.org/10.1063/5.0032134
Published by AIP Publishing. 978-0-7354-4032-6/$30.00

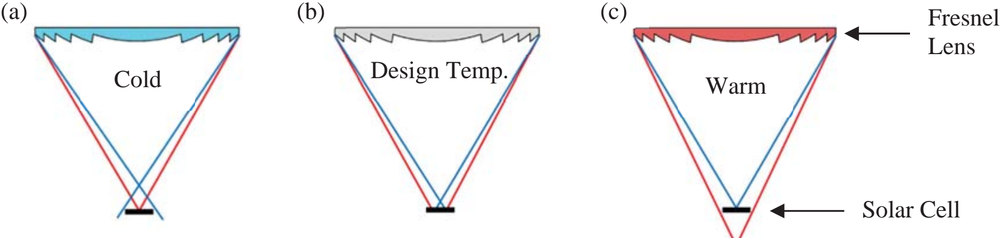

FIGURE 1. The modeled CPV sub-module (incorporating the SoG Fresnel lens and solar cell), illustrating the temperature-dependent focusing accuracy of a: (a) cold lens; (b) lens at its design temperature; and (c) warm lens. The blue and red lines represent short and long wavelengths, respectively.

(PDMS) layer [13]. We employ an optical model to explore the benefits of beads deposited on a PDMS-encapsulated triple-junction solar cell (3JSC) in a CPV sub-module. We optimize the bead size, its submergence depth into PDMS, and the PDMS layer thickness to maximize the system's short-circuit current. We find the highest current gain for 400 nm diameter beads submerged halfway into a 5 µm PDMS layer. We also show the beads reduce the impact of SoG Fresnel lenses varying from their design temperature.

MATERIALS AND METHODS

Optical Model Description

Our model simulates the optical behavior of a CPV sub-module, combining transfer matrix method (TMM), rigorous coupled wave analysis (RCWA), and ray tracing, as shown in Fig. 2(a,b). We apply an open-source TMM code [14] to simulate the optical behavior of the 3JSC, providing the external and internal reflections, transmissions and absorptions throughout the multi-layer stack. Since we did not know the exact design of the 3JSC, the parameters used in TMM were extracted from fits to measured reflection data of the 3JSC. To accurately simulate the optical effects of the sub-wavelength structure formed by the bead monolayer, we apply an open-source RCWA code, RETICOLO [15], which provides wavelength- and angle-resolved transmission, reflection, and scattering for the air-bead-PDMS interface. The results of both simulations are inserted as boundary conditions into the commercial ray tracing software, Zemax, allowing it to correctly simulate the optical properties of the entire sub-module [16], including the 3JSC stack and the sub-wavelength structures of the bead monolayer. The resulting angle dependent irradiance profile on the 3JSC for the CPV sub-module is shown in Fig. 2(c).

To model the temperature-dependent performance of the SoG Fresnel lens, we relate its temperature to a focal length using a linear coefficient (0.107 mm/°C) extracted from data measured over a temperature range of 25-50ºC [7]. To model a wider operational range, we applied the same coefficient for lens temperatures down to -25ºC.

06 August 2024 17:17:00

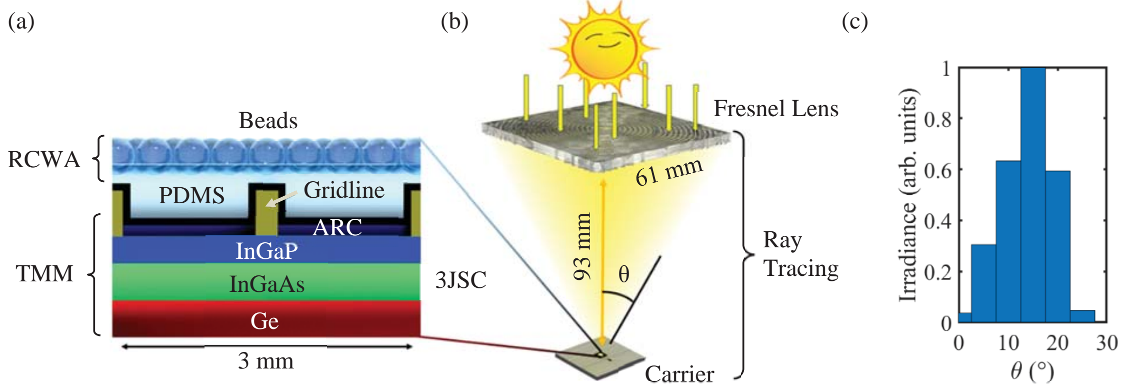

FIGURE 2. Illustration of the sections modeled by each optical software: (a) cross-sectional view of the PDMS-encapsulated 3JSC (TMM) with a micro-bead top surface (RCWA); and (b) CPV sub-module (ray tracing). (c) Irradiance profile on the 3JSC.

Optimization Procedure

To quantify the improved transmission of light through the air-bead-PDMS interface, we calculate the spectrum-weighted transmission for the ith subcell as follows:

$$T_{\mathrm{W},i} = \int T_{\mathrm{PDMS}}(\lambda) \frac{Irr_{\mathrm{AM1.5D}}(\lambda)}{E_{\mathrm{ph}}(\lambda)} \, IQE_i(\lambda) \, d\lambda \quad (1)$$

where λ is the wavelength of light, T_{PDMS} is the transmission from air through the beads and into the PDMS (see Fig. 4(a)), $Irr_{\mathrm{AM1.5D}}$ is the ASTM G173-03 direct-beam spectral irradiance, E_{ph} is the photon energy, and IQE_i is the internal quantum efficiency of the ith subcell, shown in Fig. 3. Experimental measurements validated that the IQE_i is constant for all incident angles of light encountered by the solar cell. Also, we assume the IQE_i is constant with cell temperature.

We find the optimal bead size by maximizing the short-circuit current of the solar cell. Since the 3JSC is made of 3 series-connected subcells, we calculate its short circuit current by taking the minimum of the subcell currents:

$$I_{\mathrm{sc}} = \min\left(q \int \frac{Irr_{\mathrm{AM1.5D}}(\lambda)}{E_{\mathrm{ph}}(\lambda)} \, T_{\mathrm{Total}}(\lambda) \, IQE_i(\lambda) \, d\lambda\right) \quad (2)$$

where q is the electronic charge, and T_{Total} is the total transmission from the SoG Fresnel lens through the PDMS and into the 3JSC. To quantify the impact of incorporating beads in our system, we investigate the gain of both the weighted transmission through the PDMS layer and the 3JSC short-circuit current as follows:

$$T_{\mathrm{W},i}^{\mathrm{gain}} = \left(\frac{T_{\mathrm{W},i}^{\mathrm{Beads}}}{T_{\mathrm{W},i}^{\mathrm{noBeads}}} - 1\right) \quad (3)$$

$$I_{\mathrm{sc}}^{\mathrm{gain}} = \left(\frac{I_{\mathrm{sc}}^{\mathrm{Beads}}}{I_{\mathrm{sc}}^{\mathrm{noBeads}}} - 1\right) \quad (4)$$

where $T_{\mathrm{W},i}^{\mathrm{Beads}}, I_{\mathrm{sc}}^{\mathrm{Beads}}$ and $T_{\mathrm{W},i}^{\mathrm{noBeads}}, \; I_{\mathrm{sc}}^{\mathrm{noBeads}}$ are calculated with and without beads, respectively.

06 August 2024 17:17:00

RESULTS AND DISCUSSION

Optical Performance at the Air-Bead-PDMS Interface

Figure 3 shows the transmission of perpendicularly incident light (relative to the solar cell) through the air-bead-PDMS interface as a function of wavelength for beads submerged halfway into PDMS. The 280 nm beads have a

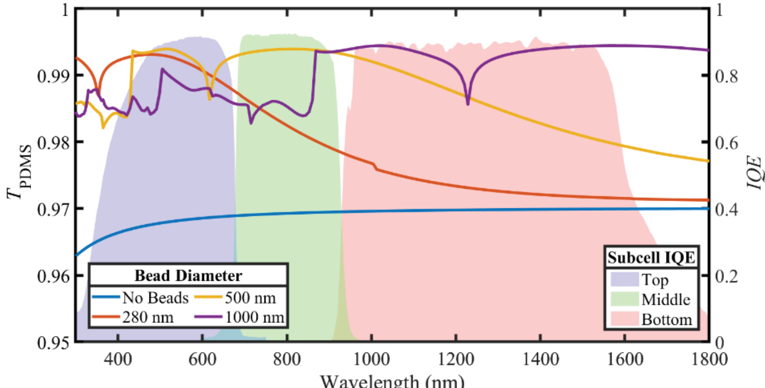

FIGURE 3. (Left-axis) Transmission of perpendicularly incident light through the air-bead-PDMS interface for beads submerged halfway into PDMS. (Right-axis) The measured internal quantum efficiency of the 3JSC used in our model.

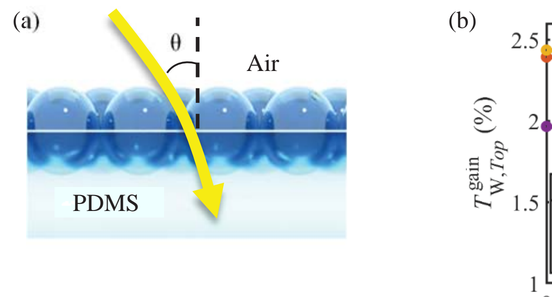

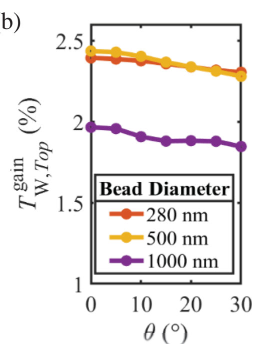

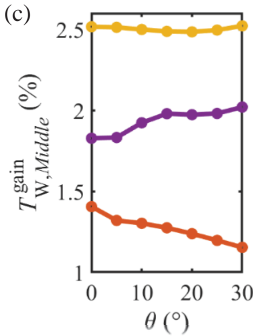

FIGURE 4. (a) Illustration of angled light transmitting through the air-bead-PDMS interface. The graphs show the spectrum-weighted transmission gai for beads submerged halfway into PDMS as a function of the incident angle of light relative to the PDMS surface normal for the (b) top subcell and (c) middle subcell.

relatively low transmission for long wavelengths because of the short transition distance for the effective refractive index relative to the wavelength size. The 1000 nm beads transmit less and has a rough profile at smaller wavelengths because the interaction regime changes from smoothly-varying effective refractive index to diffraction. Therefore, the highest overall transmission of wavelengths absorbed in the top 2 subcells is close to 500 nm.

Both Figures 4 and 5 present the spectrum-weighted transmission through the air-bead-PDMS interface for wavelengths absorbed within the top 2 subcells, ignoring the bottom subcell since we found it never limits the current for all the simulated conditions. Figure 4 depicts the transmission of light as a function of its angle of incidence relative to the cell surface normal. First, notice that transmission improves for all incident angles and bead sizes explored. Second, the transmission gain stays relatively stable for the angles of incidence shown. Finally, 500 nm beads have the highest overall transmission of wavelengths absorbed by the top 2 subcells, in agreement with results from Fig. 3.

Figure 5 depicts the transmission gain for beads submerged at various depths into PDMS. As can be seen, beads should be submerged at least 20% into PDMS and show optimal performance near ~50%. This behavior can be explained by the effective refractive index profile as the bead submergence is varied. Beads submerged less than halfway into PDMS yield an effective refractive index profile that transitions back towards air below the bead center. Conversely, beads submerged further than 50% into PDMS increase the abruptness of the effective refractive index transition at the PDMS surface.

06 August 2024 17:17:00

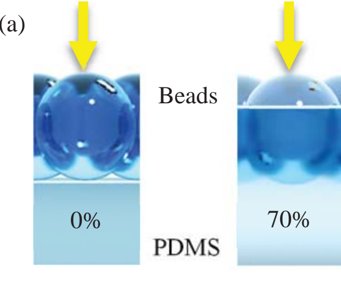

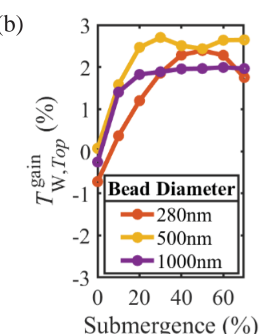

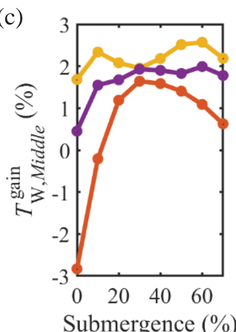

FIGURE 5. (a) Illustration of beads 0% and 70% submerged into PDMS. The graphs show the spectrum-weighted transmission gain for light perpendicularly incident to the PDMS surface with beads submerged at various depths into the PDMS for the (b) top subcell and (c) middle subcell.

Performance of CPV Sub-Modules with Beads

We now present simulation results of the complete CPV sub-module, with beads submerged halfway into the PDMS. Figure 6(a) shows the short-circuit current of the 3JSC for a range of lens temperatures. We calculate a higher and flatter current response for all bead sizes relative to no beads. Current curve flattening is largest at ~10ºC for

280 nm beads. The currents produced for a lens temperature of 10ºC versus the temperature producing the maximum current (30ºC) is 1.3% lower for 280 nm beads compared to 2.4% lower for no beads.

Figure 6(b) shows the short-circuit current gain of the 3JSC for a range of lens temperatures. Firstly, these calculations show an improved current generation for all conditions in comparison to the performance without beads. Secondly, the current gain improves for both a warmer and colder lens relative to the 30ºC designed temperature. As the lens temperature increases from 25ºC, longer wavelengths increasingly miss the 3JSC (see Fig. 1), transitioning to a current limited by the middle subcell. Under high temperatures, small beads better transmit this red-deficient spectrum (see 280 nm beads in Fig. 3) and reduced range of incident angles (see Fig. 4(c)), thus yielding an improved current gain. Conversely, as the lens temperature dips below 25ºC, short wavelengths increasingly miss the 3JSC (see Fig. 1), operating with a current-limiting top subcell. Under low temperatures, large beads better transmit the blue-deficient spectrum (see 1000 nm beads in Fig. 3) which improves the current gain. The two scenarios provide support to incorporate beads into our modeled CPV sub-module to improve its temperature-dependent short-circuit current output. Finally, Fig. 6(b) shows the largest current gain (2.6%) is reached at a -25ºC lens for 400 nm beads because they provide the highest transmission for wavelengths absorbed by the top limiting subcell. However, the best average performance is reached by ~500 nm beads, since they have the highest overall transmission within the absorption range of both limiting subcells.

Figure 6(c) presents the effects of PDMS layer thickness on the short-circuit current of the CPV sub-module. The blue curves show the current gain for a PDMS layer that is thicker than 5 µm, without the incorporation of beads. As shown, a thicker PDMS layer improves the short-circuit current gain of cold lenses but suffers a small loss for warm lenses. The relatively large improvement of ~0.8% at -25ºC is due to a combination of a low starting point efficiency and that all rays that hit the PDMS top surface reach the solar cell. The red curves show the current gain from incorporating 400 nm beads, submerged halfway in PDMS. Hot lenses have improved short-circuit current gains for thicker PDMS layers, because longer wavelengths increasingly miss the PDMS top surface (see Fig. 1(c)) and 400 nm beads better transmit this red-deficient spectrum.

Our model does not consider the absorption in PDMS, and since the improvement from having a thicker PDMS layer is relatively small it is likely that the best thickness is closer to ~5 µm. Finally, both Fig. 6(b,c) have a large jump at a lens temperature of ~15ºC because the current limiting subcell switches. The jump is less prominent for large beads since they improve the current relatively equally for both subcells.

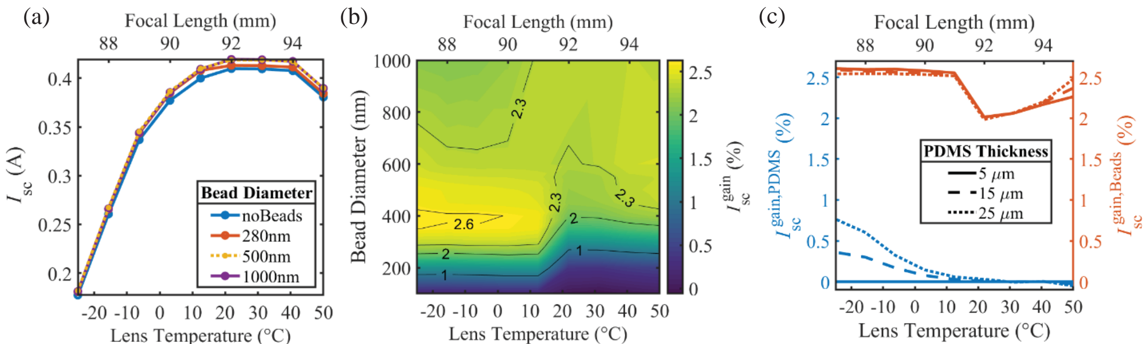

FIGURE 6. Short-circuit current, (a) absolute and (b,c) gain, of our modeled CPV sub-module as a function of lens temperature. (a,b) Compares effects of bead sizes on current. (c) Blue lines compare thicker layers to a 5 µm PDMS layer, all without beads; red lines compare gains when adding 400 nm beads on PDMS layers of differing thickness.

CONCLUSION

We modeled the optical behavior of a CPV sub-module with a nanostructured surface on a PDMS-encapsulated III-V 3JSC. The nanostructured surface consists of a deposited self-organized monolayer of silica beads that sink into PDMS. Sunlight perceives an effective refractive index that smoothly changes from air to PDMS which improves its transmission. We find the PDMS layer thickness does not have a significant impact on the short-circuit current of the system, thus its thickness should be designed with respect to other aspects not considered here, such as absorption. We find the nanostructured surface improves the sub-module’s current output by reducing its temperature dependence.

06 August 2024 17:17:00

Also, 400 nm beads submerged halfway into PDMS has the highest short-circuit current gain up to ~2.6%, but ~500 nm beads have a better overall performance over the full temperature range explored.

ACKNOWLEDGMENTS

We acknowledge the support from STACE, the Quebec Ministry of Economy and Innovation, MITACS, CMC microsystems, NSERC, and the Ontario Research Fund. The support from CEA-LITEN is also acknowledged. LN2 is a joint International Research Laboratory (Unité Mixte Internationale UMI 3463) funded and co-operated in Canada by Université de Sherbrooke (UdeS) and in France by CNRS as well as Université de Lyon (UdL , especially including ECL, INSA Lyon, CPE) and Université Grenoble Alpes (UGA). It is also associated to the French national nanofabrication network RENATECH and is supported by the Fonds de Recherche du Québec Nature et Technologie (FRQNT).

REFERENCES

1. J. F. Geisz, R. M. France, K. L. Schulte, M. A. Steiner, A. G. Norman, H. L. Guthrey, M. R. Young, T. Song, and T. Moriarty, "Six-junction III–V solar cells with 47.1% conversion efficiency under 143 Suns concentration," *Nature Energy* **5**, 326–335 (2020).
2. X. Q. Liu, C. Fetzer, P. Chiu, M. Haddad, X. Zhang, R. Cravens, D. Law, J. Ermer, J. Krogen, S. Sharma, and J. Hanley, "Large Area Multijunction III-V Space Solar Cells Over 31% Efficiency," *44th Photovoltaic Specialist Conference (PVSC)*, 2094-2098 (2017).
3. M. Steiner, A. Bosch, A. Dilger, F. Dimroth, T. Dorsam, M. Muller, T. Hornung, G. Siefer, M. Wiesenfarth, and A. Bett, "FLATCON CPV module with 36.7% efficiency equipped with four-junction solar cells," *Progress in Photovoltaics: Research and Applications* **23**, 1323-1329 (2015).
4. M. Steiner, G. Siefer, T. Schmidt, M. Wiesenfarth, F. Dimroth, and A. W. Bett, "43% Sunlight to electricity conversion efficiency using CPV," *Journal of Photovoltaics* **6**, 1020-1024 (2016).
5. E. F. Fernandez, D. L. Talavera, F. M. Almonacid, and G. P. Smestad, "Investigating the impact of weather variables on the energy yield and cost of energy of grid-connected solar concentrator systems," *Energy* **106**, 790-801 (2016).
6. K. A. W. Horowitz, M. Woodhouse, H. Lee, and G. P. Smestad, "A bottom-up cost analysis of a high concentration PV module," *11th International Conference on Cncentrator Photovoltaic Systems* **1679**, 100001 (2015).
7. V. D. Rumyantsev, N. Y. Davidyuk, E. A. Ionova, and V. M. Andreev, "Thermal regimes of Fresnel lenses and cells in all glass HCPV modules," *6th International Conference on Concentrator Photovoltaic Systems* **1277**, (2010).
8. T. Hornung, M. Steiner and P. Nitz, "Estimation of the influence of Fresnel lens temperature on energy generation of a concentrator photovoltaic system," *Solar Energy Materials & Solar Cells* ***99***, 333 - 338 (2012).
9. S. Askins, M. Victoria, R. Herrero, C. Dominguez, I. Anton, and G. Sala, "Effects of temperature on hybrid lens performance," 7*th International Conference on Concentrator Photovoltaic Systems* **1407**, 57 (2011).
10. T. Hornung, M. Neubauer, A. Gombert, and P. Nitz, "Fresnel lens concentrator with improved thermal behavior," 7*th International Conference on Concentrator Photovoltaic Systems* **1407**, 66 (2011).
11. S. Askins, M. Perez, R. Gerrero, C. Dominguez, I. Anton, A. Coutinho, and J. Amador, "Optimizing CPV systems for thermal and spectral tolerance," *27th European Photovoltaic Solar Energy Conference and Exhibition*, 194 – 198 (2012).
12. W. Wang and A. Freundlich, "Simulation and development of sub-wavelength grated dielectric ARCs for CPV applications," *39th Photovoltaic Specialists Conference*, 3049-3052 (2013).
13. P. Garcia-Linares, C. Dominguez, O. Dellea, T. Kampfe, Y. Hourlin, P. Besson, C. Weick, and M. Baudrit, "Improving optical performance of concentrator cells by means of a deposited nanopattern layer," *11th International Conference on Concentrator Photovoltaic Systems* **1679**, 40004 (2015).
14. S. J. Byrnes, "Multilayer optical calculations," arXiv: 1603.02720 (2016).
15. J. P. Hugonin and P. Lalanne, "RETICOLO software for grating analysis," Institut d'Optique. Orsay, France (2005).
16. P. Sharma, M. M. Wilkins, H. P. Schriemer, and K. Hinzer, "Concentrating optical system optimization for 3- and 4-junction solar cells: impact of illumination profiles," *J. Photon. Energy* **7**(**1**), 014501 (2017).

06 August 2024 17:17:00

3.2 Microstructured antireflective encapsulant on concentrator solar cells

The article presents research on characterizing and simulating the optical performance of a new encapsulant. It aims to demonstrate the potential advantages of this new encapsulant compared to a standard encapsulant for CPV systems.

Impact

The following journal article has the following novelties:

1. Developed a reproducible and low-cost method to tailor the bead submergence into the PDMS layer for a bead/PDMS encapsulant.
2. Measured 2.6% current gain and reduced sample-to-sample performance variability with the new bead/PDMS encapsulant compared to the baseline encapsulant used commercially in CPV manufacturing.
3. Developed and validated model, which predicted a potential current gain up to 3.4% with optimized bead diameter and submergence into the PDMS.

Our results rigorously demonstrate the potential of the bead/PDMS encapsulation layer for present CPV systems. Additionally, this coating could be applied to other optical elements within the CPV submodule for further performance improvements.

Author contribution

Gavin P. Forcade: As the lead University of Ottawa-based graduate student associated with the project, I developed the model, performed the simulations, and took quantum efficiency (QE) measurements for model validation. I contributed 60% to the lead authorship of the article.

Dr. Arnaud Ritou: As a postdoctoral researcher at Université de Sherbrooke, Arnaud took experimental measurements and contributed 40% to the lead authorship of the article.

Philippe St-Pierre: As the lead Université de Sherbrooke-based graduate student associated with the project, Philippe led the experiments and contributed to the initial draft of the article.

Dr. Olivier Dellea: As a research engineer at CEA, Olivier was the expert on microbead deposition, thus providing feedback when needed.

Dr. Maïté Volatier: As a research professional at Université de Sherbrooke, Maïté oversaw the project.

Prof. Abdelatif Jaouad: As an adjunct professor at Université de Sherbrooke, Abdelatif oversaw the project.

Dr. Christopher E. Valdivia: As a senior research scientist within the University of Ottawa's SUNLAB research group, Chris helped to guide my research, provided detailed feedback during the analysis of my simulation results, and assisted in editing the manuscript.

Prof. Karin Hinzer: As the director of the University of Ottawa's SUNLAB research group, Karin oversaw my research, provided detailed feedback during the analysis of my simulation results, and assisted in editing the manuscript.

Prof. Maxime Darnon: As the principal investigator of the project and professor at Université de Sherbrooke, Maxime oversaw the research, provided detailed feedback during the analysis of results, and assisted in editing the manuscript.

The Version of Record is available online at:

G.P. Forcade, A. Ritou, P. St-Pierre, O. Dellea, M. Volatier, A. Jaouad, C.E. Valdivia, K. Hinzer, and M. Darnon, "Microstructured Antireflective Encapsulant on Concentrator Solar Cells", *Progress in Photovoltaics: Research and Applications*, 30, 2, 2021. DOI: 10.1002/pip.3468

Check for updates

Received: 10 May 2021 | Revised: 22 July 2021 | Accepted: 20 August 2021

DOI: 10.1002/pip.3468

RESEARCH ARTICLE

Microstructured antireflective encapsulant on concentrator solar cells

Gavin P. Forcade[1] | Arnaud Ritou[2,3] | Philippe St-Pierre[2,3] | Olivier Dellea[4] | Maïté Volatier[2,3] | Abdelatif Jaouad[2,3] | Christopher E. Valdivia[1] | Karin Hinzer[1] | Maxime Darnon[2,3]

[1]SUNLAB Centre for Research in Photonics, University of Ottawa, Ottawa, Ontario, Canada

[2]Laboratoire Nanotechnologies Nanosystèmes (LN2), CNRS, Université de Sherbrooke, Sherbrooke, Québec, Canada

[3]Institut Interdisciplinaire d'Innovation Technologique (3IT), Université de Sherbrooke, Sherbrooke, Québec, Canada

[4]CEA, Liten, DTNM, Université Grenoble Alpes, Grenoble, France

Correspondence
Maxime Darnon, Institut Interdisciplinaire d'Innovation Technologique (3IT), 3000 Boulevard de l'Université, Sherbrooke, Qc, J1K015, Canada.
Email: maxime.darnon@usherbrooke.ca

Funding information
Fonds de Recherche du Québec Nature et Technologie; Quebec Ministère de l'Économie, de la Science et de l'Innovation; MITACS; STACE

Abstract

Microstructured antireflective coatings (ARCs) can reduce reflection losses over a wide range of incidence angles when applied to the surface of a high-efficiency III-V photovoltaic cell in a concentrator photovoltaic (CPV) system. In this article, we present a microstructured ARC consisting of a monolayer of close-packed silica microbeads partially submerged within a polydimethylsiloxane (PDMS) cell encapsulant for use within a reference 500× CPV submodule. Comparing a commercialized SiO_x encapsulant to this microstructured coating with 25% submerged 1,000 nm-diameter beads, angle-dependent external quantum efficiency measurements yield a 2.6% current gain for the microstructured coating. Simulations demonstrate good agreement with measurements, predicting a 2.4% current gain for the same configuration. Extrapolating with our validated model, we estimate a maximum and achievable (within a large manufacturing tolerance) current gain of 3.4% and 2.9 ± 0.4% using 60% submerged and 10%–32% submerged 760 nm-diameter beads, respectively.

KEYWORDS
antireflection, concentrator photovoltaic, encapsulant, external quantum efficiency, microstructuring, ray tracing, RCWA, TMM

1 | INTRODUCTION

Concentrator photovoltaic (CPV) systems can be less costly than Si PV in high DNI regions[1,2] with lower lifecycle impacts and a smaller energy payback time.[3,4] Sustained technological advances have significantly reduced CPV costs by increasing system efficiency.[5] Among the largest losses, optical reflections are generally minimized by depositing an antireflective coating (ARC) on the surface of the photovoltaic cell. Most CPV systems use high-efficiency triple-junction solar cells (3JSCs) with a multilayer ARC made from two or more thin transparent layers of increasing refractive index. Patterned surfaces, or moth-eye structures, offer the potential for improved performance in comparison with standard ARC designs, reducing reflections over a wide range of incidence angles. Either nanometric or micrometric structures create an effective refractive index gradient that smooths the optical transition between two media.[6] Such ARC structures can be effective over a wide spectral range and insensitive to the polarization of incident light.[7]

Several methods have been studied to achieve surface microstructuring, either depositing or removing material to create

This is an open access article under the terms of the Creative Commons Attribution-NonCommercial-NoDerivs License, which permits use and distribution in any medium, provided the original work is properly cited, the use is non-commercial and no modifications or adaptations are made.
© 2021 The Authors. Progress in Photovoltaics: Research and Applications published by John Wiley & Sons Ltd.

the structures. Deposition approaches include sol–gel processing,[8,9] glancing angle deposition,[10–15] and colloidal infiltration with etching.[16] Conversely, material removal approaches include colloidal nanosphere lithography[17–20] or laser interference lithography[21] combined with an etching step. Of these, only some sol–gel methods are performed under atmospheric pressure and do not require microfabrication techniques. García-Linares et al. demonstrated the concept of an ARC consisting of a layer of silica microbeads[22] deposited by a colloidal sol–gel method.[23] That study showed a 1.8% increase in short-circuit current density (J_{sc}) for normally incident irradiance on a 3JSC with 530 nm beads deposited on a silicone encapsulant, as compared with the same cell without beads. Their study included a simulation suggesting that beads submerged halfway into the silicone could potentially provide greater gains. Simulations carried out by Forcade et al.[24] showed that controlling the submergence of the beads in a layer of silicone can also improve the temperature dependency of a concentrator system and led to a J_{sc} enhancement up to 2.6%, compared with devices without beads.

The objective of this work is to study and understand the performance enhancements of a microstructure produced from an ordered monolayer of silica beads deposited on a polydimethylsiloxane (PDMS) encapsulant layer for a 3JSC. The novelty of our work lies in the improved deposition process allowing greater control over the microbead submergence into PDMS. We measure and compare the 3JSC J_{sc} gain for various ARCs and use the results to calibrate our model. We then employ our calibrated model to optimize the bead size and submergence into PDMS to maximize the electrical performance of the 3JSC.

In this work, we study a 500× CPV system composed of a 50 × 50 mm^2 silicone-on-glass (SoG) Fresnel lens concentrating direct sunlight onto a hexagonally shaped high-efficiency 3JSC at its focal length (93 mm), as depicted in Figure 1A. Each hexagonal cell is 3 mm in width and has a grid line pattern optimized for a 500× concentration ratio (Figure 1B). Finally, the cells are coated with a dual-layer thin film ARC of AlO_x/TiO_x optimized for an encapsulating layer with refractive index near 1.5 (Figure 1C). Presently, STACE 500× modules have a 100 ± 30 nm SiO_x encapsulating layer on the 3JSC for an intended use without a secondary optical element (SOE), as shown in Figure 1D. Although the enclosed modules shield the PV devices from most weathering processes, the encapsulation layer is required to protect the 3JSC against moisture and oxidation and is deposited with an atmospheric plasma.

Our encapsulation involves coating cells with 6.0 ± 0.2 μm of Sylgard 184 PDMS (Figure 1E),[25] with a refractive index of $n_{PDMS}(650\,\text{nm}) = 1.410$.[26] PDMS is a common protective layer for CPV solar cells[27] but induces parasitic reflections at the air/PDMS interface.[28] We minimize this reflection by incorporating a microstructured ARC consisting of a monolayer of silica beads, with refractive index $n_{bead}(650\,\text{nm}) = 1.457$,[29] partially submerged into the PDMS layer, as shown in Figure 1F. We calculated the optical properties of the microstructured ARC for 0 to 1,200 nm-diameter beads using our numerical model, which was validated from measurements of 1,000 nm-diameter bead samples.

We compare the current generated by four PV device configurations, shown in Figure 1C–F, while under illumination from the AM1.5D spectrum. Each configuration employs the same commercial 3JSC using an AlO_x/TiO_x ARC with fixed thicknesses, which we take as the reference design for electrical performance. The SiO_x-encapsulated 3JSC is the commercial device design used by STACE. We explore a design consisting of the 3JSC with a PDMS encapsulant and monolayer of silica beads with partial submergence into the PDMS. We do not include results for beads directly on the 3JSC or SiO_x/3JSC (i.e., without PDMS) because the beads do not properly adhere to the AlO_x and SiO_x surfaces. Moreover, our numerical model predicted a decrease in current for the 3JSC with beads but without PDMS, in agreement with previous results.[22] Further discussion is provided in the morphology study section. Finally, we compare all configurations to the 3JSC without SiO_x or PDMS (Figure 1C), which we refer to as our *reference* configuration.

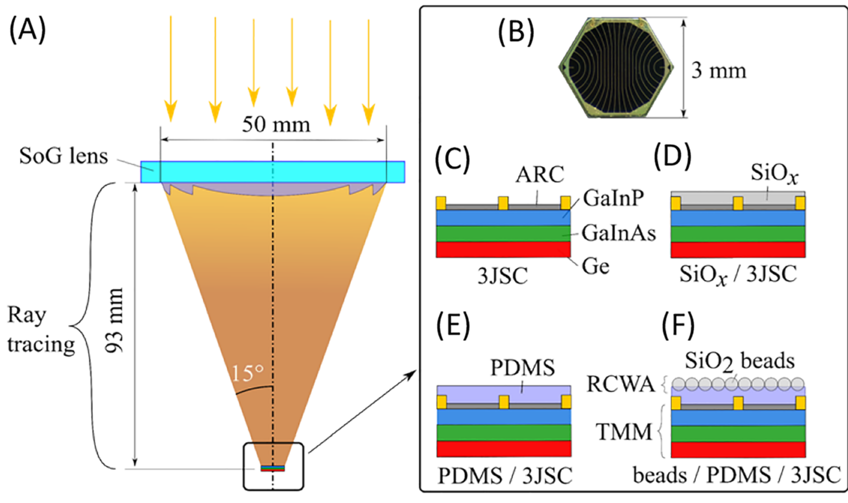

FIGURE 1 (A) Schematic cross section of the concentrator photovoltaic (CPV) submodule. (B) Top view of cell, and cross sections (not to scale) of (C) bare triple-junction solar cell (3JSC), (D) STACE SiO_x encapsulated 3JSC, (E) polydimethylsiloxane (PDMS)-coated 3JSC, and (F) patterned microbead layer partially submerged into a PDMS layer encapsulating the 3JSC [Colour figure can be viewed at wileyonlinelibrary.com]

2 | EXPERIMENTAL STUDY

2.1 | Fabrication

To deposit the PDMS layer, we spin coat liquid PDMS on a 3JSC at a spin rate of 6,000 rpm for 120 s to obtain a thickness of 6.0 ± 0.2 μm. Simulations confirm that the PDMS layer is optically incoherent and that the thickness uncertainty has negligible effects on the optical performance of the device. Subsequently, we deposit a monolayer of hexagonally close-packed silica beads on the PDMS, using a patented method based on a dynamic fluid flow process, called Boostream, described in Delléa and Lebaigue.[30] This method involves first depositing the beads on an easy-to-handle substrate,[31] then transferring them onto the PDMS surface.

As illustrated in Figure 2, the beads can be controllably submerged into the PDMS layer via a curing step. We define the *submergence* of the beads into the PDMS as the depth the beads penetrate below the PDMS surface, normalized to the bead diameter. Prior to the deposition of the beads, the PDMS is partially heat-cured for a time t_1, referred to as the pre-cure. Once the beads are deposited, they are left to rest and sink in the PDMS for a time t_{rest} at room temperature. A final bake referred to as the post-cure, lasting $t_2 = 20\text{ min} - t_1$, is performed to complete the crosslinking of the PDMS, complying with $t_1 + t_2$ fixed at 20 min at 125°C as instructed in the Sylgard 184 guidebook.[25] The pre-cure fraction, $t_1/(t_1 + t_2)$, represents the percentage of PDMS cure-time completed before bead deposition and is proportional to the chemical crosslinking that converts liquid PDMS to a solid.[32] The submergence of the beads is assessed by analyzing 4–10 beads per sample with cross-sectional scanning electron microscopy (SEM) images as in the example in Figure 2C. The analyzed beads are either at various locations on a sample or on one SEM image.

Figure 3 shows the submergence of 500 and 1,000 nm beads in PDMS as a function of its pre-cure fraction. The four curves correspond to various resting times (t_{rest}) and bead diameters. The colored regions delimit the minimum and maximum measured submergences for several beads on the same sample. For a pre-cure fraction <15%, 500 nm beads were completely submerged into PDMS. The 15% threshold is representative of the gel point, that is, the transition point between liquid and solid PDMS. For a pre-cure fraction >15%, the average bead submergence comprises between 10% and 32%, with a lower submergence for larger pre-cure fractions. For pre-cure fractions between 30% and 50%, 1,000 nm-diameter beads tend to have a larger submergence than 500 nm-diameter beads. For t_{rest} between 1 and 21 h, a similar submergence is observed indicating that within these process conditions, the rest time has little impact on the bead's submergence.

Results from our numerical model, described in Section 3, show a significant improvement for the beads/PDMS/3JSC over the 3JSC configuration with little sensitivity to the submergence. For instance, in Figure 8B, we calculate a current gain of 3%–4% for 1,000 nm-diameter beads submerged 10%–70%. The experimental results of Figure 3 indicate that the process window to obtain a submergence in this range is very broad and corresponds to a pre-cure fraction larger than 15% and rest time between 1 and 21 h. To

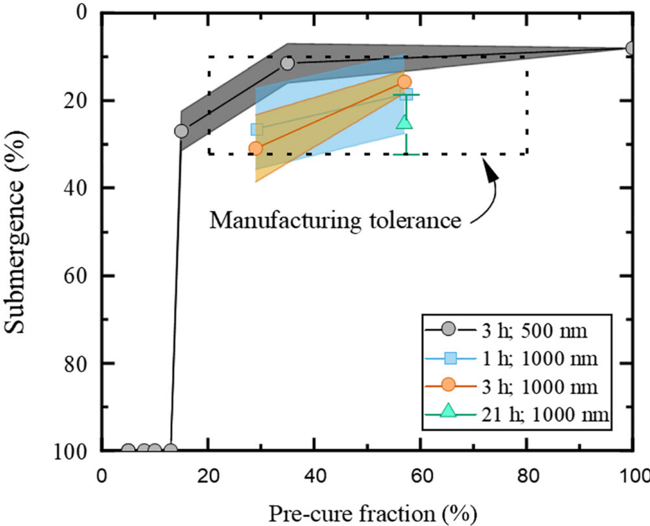

FIGURE 3 Submergence of 500- and 1,000-nm beads in polydimethylsiloxane (PDMS) as a function of the pre-cure fraction of PDMS corresponding to three resting times [Colour figure can be viewed at wileyonlinelibrary.com]

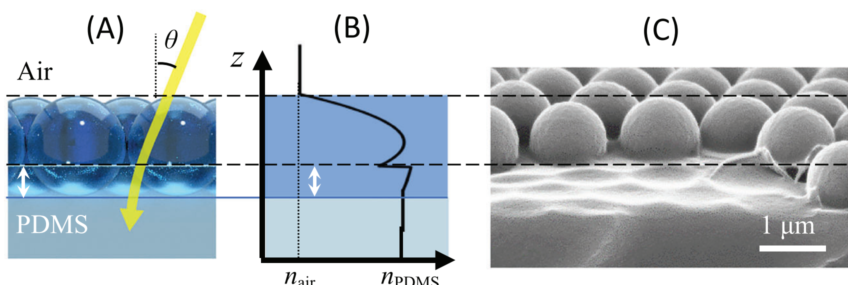

FIGURE 2 (A) Cross-sectional depiction of a microstructured layer made from ordered close-packed silica beads partially submerged into polydimethylsiloxane (PDMS). (B) Representation of the effective refractive index as function of depth across the structured interface, from air (n_{air}) to PDMS (n_{PDMS}). (C) Angled scanning electron microscope view of 1,000 nm-diameter beads submerged ~25% into the PDMS layer [Colour figure can be viewed at wileyonlinelibrary.com]

highlight the high manufacturing tolerance of the beads/PDMS encapsulant, we define a wide processing range of 20%–80% pre-cure fraction that corresponds to 10%–32% submergence and is represented by the dotted rectangle in Figure 3. These boundaries will be used to calculate the achievable performance of the beads/PDMS/3JSC configuration.

2.2 | Morphology study

Microbead layers were inspected for uniformity, defect density, and submergence into PDMS. Figure 4A shows an optical microscopy image of beads deposited on SiO_x/3JSC, whereas Figure 4B–D show SEM images of beads deposited on PDMS/3JSC, typically forming a uniform partially submerged 2D hexagonal close-packed monolayer structure throughout the surface. Beads exhibit better adherence to PDMS than to SiO_x due to their submergence into the soft PDMS layer (Figure 4D) and due to the strong hydrogen bonds between silica beads and terminating silanol groups of PDMS. The 6 μm-thick PDMS layer smooths out the topography of the cell surface by covering the ~2 μm-thick metal fingers, visible as the dark band in Figure 4C. Figure 4B is representative of the flat monolayer formed by the beads with only a few topology defects. Only 10 vacancies are counted in the $130 \times 90\ \mu m^2$ area ($<10^4/cm^2$), but more cracks with various widths and lengths are visible. From the 9,900 beads counted in this image, 8,750 have six nearest neighbors; meaning, 88% of the structure is hexagonally close packed. However, studying similar structures to ours (i.e. domes patterned pseudo-periodically across a flat surface), Battaglia et al.[33] and Ferry et al.[34] demonstrated an equivalent J_{sc} using either random or periodic structures.

From our SEM investigations, we did not observe any defects in the PDMS layers such as cracks, bubbling, or swelling.

2.3 | Characterization method

The microstructure formed by the bead monolayer increases the light intensity entering the cell, influencing the electric current. To quantify this performance enhancement, we calculate the cell's J_{sc} by integrating the external quantum efficiency (EQE) with the 1-sun AM1.5D spectrum (900 W/m^2), taking the smallest J_{sc} of the three series-connected junctions. The J_{sc} gain is then defined as the relative difference between sample configurations shown in Figure 1D–F and the reference device (Figure 1C):

$$\Delta J_{sc} = \frac{\left[J_{sc}^{i} - J_{sc}^{Ref}\right]}{J_{sc}^{Ref}}, \tag{1}$$

where i denotes the device configuration to be compared with the reference device, *Ref*. The EQE (Figure 5) is measured on a PV measurement QEX7 system at 3IT, with filtered white light, and voltage biasing to ensure the subcell of interest is in short circuit. The EQE measurement procedure follows the methodology proposed by Meusel et al.[35] We maintained the samples at 25°C during measurements. We also measured the angular dependent EQE, by placing our samples on tapered holders for incident angles up to 30°.

Our numerical model required the internal quantum efficiency (IQE) of the 3JSC as a main input. Therefore, we measured the IQE (Figure 5) using an Oriel IQE-200 test station following the same procedure as the EQE measurements above, while simultaneously measuring specular reflection. However, points at 825, 885, and 965–1,020 nm were manually smoothed by interpolating between adjacent points, due to high variability at the xenon lamp spectrum peaks. The smoothing performed at 965–1020 nm mainly affects the bottom subcell, which overproduces current for all our configurations, and therefore does not affect the outcome of our results. The bottom

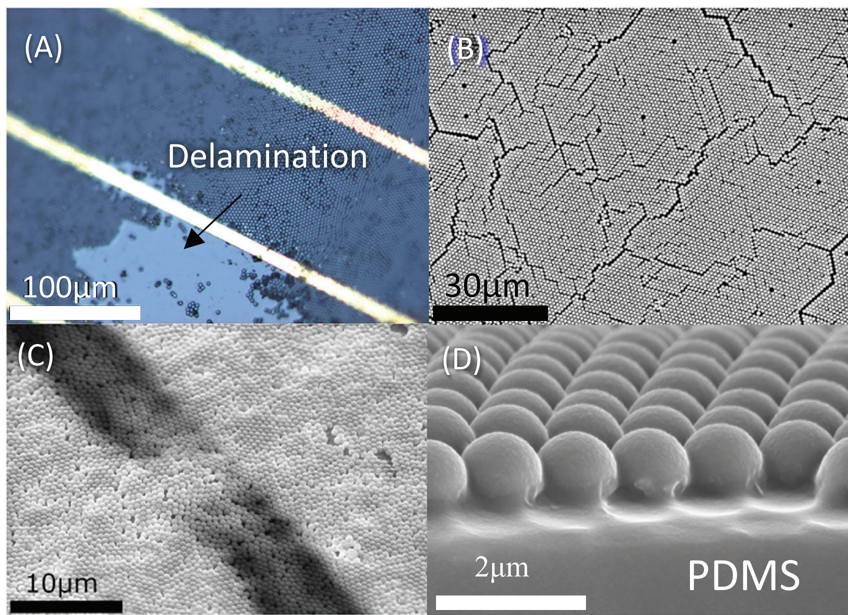

FIGURE 4 Micrographs of beads deposited on: (A) SiO_x and (B–D) polydimethylsiloxane (PDMS). (A) Delamination of the beads (optical microscope); (B) top view image (scanning electron microscopy [SEM]); (C) 45° view of a metal finger (dark band) underneath the beads/PDMS coating (SEM); and (D) glancing angle cross-sectional close-up (SEM) [Colour figure can be viewed at wileyonlinelibrary.com]

subcell QE artifact is corrected using the method described in Ferry et al.[36] Comparing the EQE to the IQE and reflection in Figure 5 confirms that the QE measured by both QEX7 and Oriel IQE-200 systems is in good agreement.

2.4 | Measured current gain

Solar cells were fabricated in the four configurations shown in Figure 1C–F, to compare their electrical properties. We investigate the commercial design consisting of a 3JSC with an atmospheric plasma deposited SiO_x layer acting as both a third layer to the ARC and an encapsulant. We explore the benefits of the PDMS encapsulant as well as the microstructured surface composed of 1,000 nm-diameter beads submerged ~25% into PDMS.

Figure 6 shows the J_{sc} gain (calculated using Equation 1) for normally incident light on the four types of configurations. The gain is averaged over the number of devices measured, which is represented by the number in parenthesis, with an error bar width equal to the difference between the maximum and minimum J_{sc} gain of all samples. The SiO_x encapsulating layer improves the J_{sc} by 1.1 ± 1.6% over the reference 3JSC. This increase is expected because the dual-layer ARC is optimized for the refractive index of silica. The J_{sc} gain of SiO_x/3JSC has a large uncertainty because the encapsulating layer is deposited by an atmospheric plasma, which fabricates thin films with relatively large variations in thickness and refractive index but at fast speeds and low costs.[37] With a similar refractive index, PDMS improves the J_{sc} by 1.8 ± 0.6% from the reference. The uncertainty is smaller because light travels incoherently within the optically thick PDMS layer, which makes thickness and refractive index variations unimportant. Finally, adding a monolayer of 1,000 nm-diameter beads on PDMS improves the J_{sc} up to 3.7 ± 1% from the reference, which is the largest gain demonstrated here. The slightly higher uncertainty for beads/PDMS/3JSC is attributed to sample-to-sample variation of bead submergence.

Figure 7 investigates the measured angle-dependent current produced by the reference 3JSC, the commercial SiO_x/3JSC, and beads/PDMS/3JSC with 1,000 nm-diameter beads submerged 25% into the PDMS encapsulant. The histogram in Figure 7A displays the calculated angular distribution of irradiance on the cell in the simulated submodule represented in Figure 1A and previously shown in Forcade et al.[24] Notice that most of the irradiance comes within an incident angle of 10–15°, as is expected for these square lenses. Figure 7B shows an increasing J_{sc} with angle for both encapsulated cells but the opposite for the reference device. This amplifies the J_{sc} gain calculated in Figure 7C, reaching 5% at 30°. The error bar range is calculated by taking the difference between the maximum and

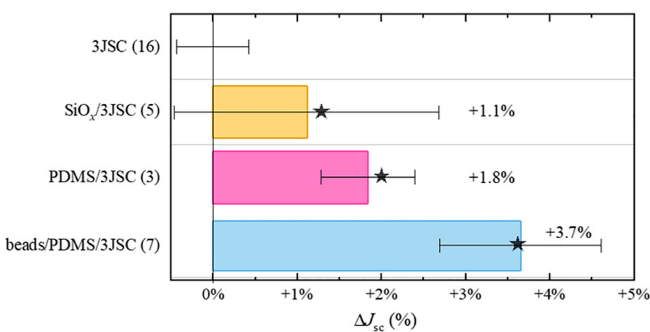

FIGURE 6 Current density gain between each device configuration and the reference, averaged over the number of tested photovoltaic (PV) devices shown in parenthesis, operating at 25°C. Black stars are the values calculated by our numerical model [Colour figure can be viewed at wileyonlinelibrary.com]

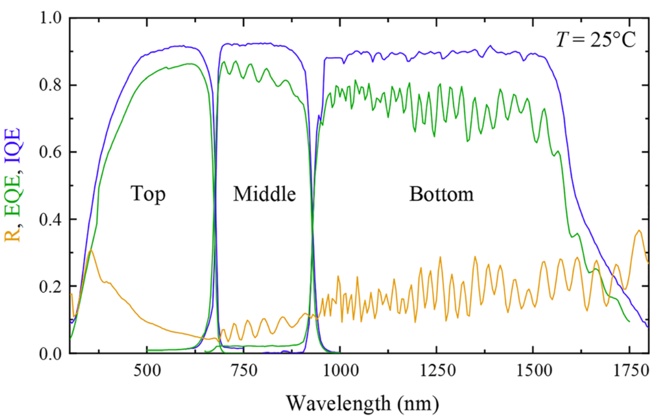

FIGURE 5 The measured internal and external quantum efficiency (IQE and EQE) of the top, middle, and bottom junction of the reference triple-junction solar cell (3JSC), together with the specular reflectance (R) [Colour figure can be viewed at wileyonlinelibrary.com]

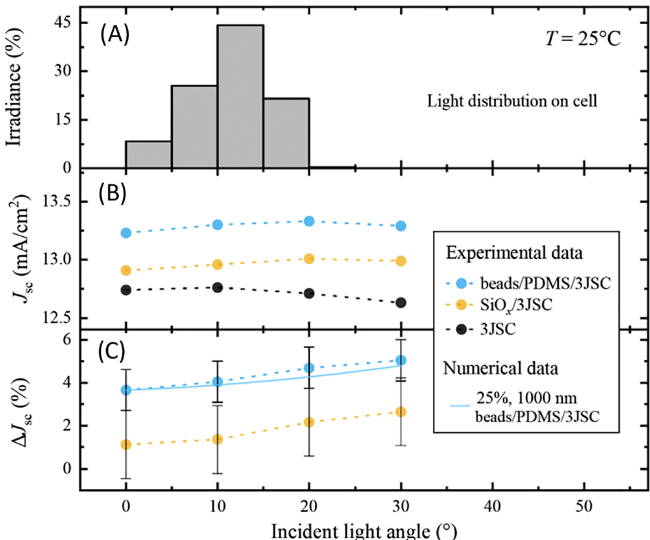

FIGURE 7 (A) Calculated angular distribution of irradiance on the cell in the 500× concentrator photovoltaic (CPV) submodule. (B) Measured J_{sc} as a function of the angle of incidence. (C) J_{sc} gain between the encapsulated and reference devices [Colour figure can be viewed at wileyonlinelibrary.com]

minimum J_{sc} gain for normally incident light, and we assume the uncertainty is constant for all angles measured. The solid blue line presents the simulated gain for the beads/PDMS/3JSC configuration for 25% bead submergence, showing good agreement with measurement.

3 | SIMULATION STUDY

3.1 | Numerical model

We have developed a computational model to simulate the optical properties of the CPV submodule, combining ray tracing, rigorous coupled wave analysis (RCWA), and the transfer matrix method (TMM) within different regions of the submodule, as shown in Figure 1. These calculations provide the fraction of rays transmitted into the 3JSC at a wavelength interval of 300–1,800 nm, which we weight by the AM1.5D solar spectrum and the measured IQE (Figure 5) to calculate the J_{sc} of the cell. Calculations of these wavelength-dependent transmissions across the beads/PMDS interface are presented in Forcade et al.[24] for several bead sizes.

The commercial ray tracing software, Zemax OpticStudio, sends incoherent rays through the Fresnel lens to the solar cell. Because ray tracing is unable to resolve scattering for the sub- and/or near-wavelength structure formed at the beads/PDMS interface, we employed an open-source RCWA code, RETICOLO,[38] to compute a bidirectional scattering distribution function (BSDF). The BSDF was then applied as an interface within OpticStudio to account for light transmitting from air into the PDMS layer and for light trapping within the PDMS layer. Rays transmitted into the PDMS layer travel incoherently, reaching the PDMS/3JSC interface, where they transmit and reflect via a boundary condition set by TMM[39] calculations of the 3JSC layer structure detailed in Figure 1C.

To approximate the proprietary design of the commercial 3JSC, we took SEM side-view images of a sliced 3JSC to obtain top layer thicknesses and subsequently fit TMM calculations to reflection measurements of 3JSC and PDMS/3JSC configurations. We achieved the best fit using the complex refractive indexes from Gupta et al., Kim et al., Ochoa-Martínez et al., Cui et al., Djurišić et al., Palik, and Aspnes and Studna.[40–46]

Although we measured a lower J_{sc} for SiO_x/3JSC versus PDMS/3JSC (see Figure 7), we also measured a lower spectral and IQE-weighted reflection for all junctions, which makes our model over-estimate the J_{sc} for the SiO_x/3JSC configuration by almost 5%. To account for the discrepancy, we adopted a SiO_x layer with non-negligible parasitic light absorption, which could be attributed to imperfections arising during deposition. To simulate the SiO_x layer, we applied a similar approach to Bedjaoui et al.[47] and assumed an effective medium with fractions of silica, a–Si, and air. Good match resulted between simulated and measured J_{sc}, while assuring a good fit between reflections, for a layer composed of 19.2% air, 80% silica, 0.8% a–Si, and an added extinction coefficient of $k \sim 0.01$ for all wavelengths in accordance with ellipsometry measurements. The constant extinction coefficient also agrees with absorption measurements of a similar SiO_x layer fabricated by Carneiro et al.[48] We also find that 19.2% porous SiO_x is reasonable because it is a little less than a previously reported porosity for a similar SiO_x layer.[49]

3.2 | Simulated current gain

Figure 8 displays simulated J_{sc} gain (Equation 1) of (A) normally incident and (B) submodule distributed AM1.5D spectrum on the beads/PDMS/3JSC configuration for varying bead diameters and submergence, relative to the reference device. Along the bead diameter axis, simulations used a graded step size starting with large 100 nm steps at the extremities and narrowing to 20 nm steps near the J_{sc}-gain peak, and for the bead submergence axis, we use a constant 10% spacing. The two horizontal-dashed lines represent the range of submergences obtained with 20%–80% precure time, as discussed in Figure 3. Within this window, Figure 8A,B has its highest average J_{sc} gain of 4.8 ± 0.4% and 4.4 ± 0.4% for 760 nm beads, respectively. The maximum J_{sc} gain over all our simulation space for Figure 8A,B is 5.2% and 4.8% for 760 nm beads with 60% submergence, respectively. We also note that our simulations of the beads/PDMS/3JSC configuration were always middle GaInAs subcell limited.

Our RCWA simulations showed that beads of ∼760 nm diameter provide an optimal balance between two opposing loss mechanisms.

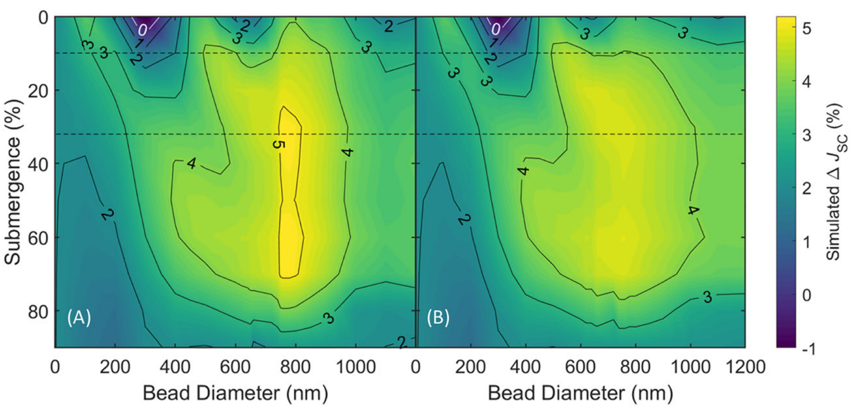

FIGURE 8 Simulated short-circuit current gain for the beads/polydimethylsiloxane (PDMS)/triple-junction solar cell (3JSC) configuration (Figure 1F) relative to the reference device (Figure 1C) as a function of bead size and submergence into PDMS for (A) normally incident light and (B) submodule distributed light. The dashed lines represent the boundaries of the manufacturing tolerance introduced in Figure 3 [Colour figure can be viewed at wileyonlinelibrary.com]

TABLE 1 J_{sc} gain of encapsulated cells (Figure 1D–F) relative to the reference (Figure 1C) for normal and submodule irradiance, comparing measured and simulated results

Configuration	Submergence	Normal irradiance ΔJ_{sc} (%)		Submodule ΔJ_{sc} (%)	
		Meas.	Sim.	Meas.	Sim.
SiO_x/3JSC	–	1.1 ± 1.6	1.3	1.6 ± 1.6	1.5
1,000-nm beads/PDMS/3JSC	25%	3.7 ± 1.0	3.7	4.2 ± 1.0	3.9
(Maximum)760-nm beads/PDMS/3JSC	60%	—	5.2	—	4.8
(Achievable) 760-nm beads/PDMS/3JSC	10–32%	—	4.8 ± 0.4	—	4.4 ± 0.4

Abbreviations: 3JSC, triple-junction solar cell; PDMS, polydimethylsiloxane.

For smaller beads, the shorter graded refractive index effective medium across the beads/PDMS interface diminishes transmission. For larger beads, stronger optical diffraction increased light scattering and front-surface reflectivity. Beads with a diameter of 760 nm produced diffraction for wavelengths <930 nm, which is near the absorption edge of the current limiting middle subcell (Figure 5). Therefore, both larger and smaller beads diminish the transmission of wavelengths absorbed within the current-limited middle subcell of theses PV devices, making ~760 nm beads the optimal size. Ultimately, the optimal bead size and submergence will depend on the device structure and subcell bandgaps.

Figure 8A,B displays J_{sc} gain oscillating as a function of bead diameter when submerged <50%. The oscillations are due to a reversion of the effective refractive index for the medium between the bead equator and PDMS surface that is dependent on bead diameter and submergence, as depicted in Figure 2B.

4 | DISCUSSION

Table 1 displays J_{sc} gain (Equation 1) for configurations with encapsulation relative to the reference device, comparing measurements to simulations. We show results for both normally incident irradiance and for submodule angular distributed irradiance (Figure 7A), integrated with the angle dependent EQE of devices. As before, the measured uncertainties represent the range between largest and smallest currents measured under normal incidence. The simulated uncertainties encompass all the currents obtained in the process window defined in Figure 3.

We find good agreement between our measurements and simulations for both 1,000 nm beads/PDMS/3JSC and SiO_x/3JSC configurations (see Table 1). Extrapolating with this model, we simulate a maximum gain of 4.8% for 760 nm beads submerged 60% and an achievable gain within the manufacturing tolerance window of 4.4 ± 0.4% for 760 nm beads, relative to the reference device.

Comparing the J_{sc} of simulation-optimized beads/PDMS/3JSC to the commercial SiO_x/3JSC design under normal irradiance (from Table 1), we calculate a maximum increase within our simulation space of 4.0% and an achievable gain within the process window of 3.5 ± 0.4%. Under submodule irradiance, we calculate maximum and achievable current gains of 3.4% and 2.9 ± 0.4%, respectively.

A large J_{sc} uncertainty between PV devices is detrimental to series connected CPV modules, because its current is limited by the worst performing submodule. These losses can be mitigated with bypass diodes but increases manufacturing costs. For the submodule under study (Figure 1A), we measured a large J_{sc} gain variability of 1.6% for the commercial SiO_x/3JSC configuration while only a 1% variability for the 1,000 nm beads/PDMS/3JSC. The J_{sc} gain uncertainty for 760 nm beads/PDMS/3JSC could reach ~1% assuming 0.6% and 0.4% variability from the 3JSC and process window, respectively. Assuming a series-connected CPV module, without bypass diodes and with J_{sc} variability solely from PV devices, we calculate a 3.4% J_{sc} gain for 760 nm beads/PDMS/3JSC relative to the commercial SiO_x/3JSC configuration.

Prior to implementation in commercial CPV systems, the beads/PDMS encapsulant will require further investigation and reliability studies. However, PDMS encapsulants have been extensively studied for CPV systems, showing excellent durability.[27] Partially submerged bead monolayers on PDMS have also demonstrated the ability to withstand harsh processing, such as ultrasonic cleaning.[50] Using an optical microscope, we observed only superficial damages to samples with 1,000 nm beads submerged 25% into PDMS after pick and place manipulation. The beads/PDMS deposition process is compatible with full-wafer manufacturing processes but has yet to be tested. Further study is needed to verify compatibility with all packaging steps, such as for cell singulation, soldering and wire-bonding.

5 | CONCLUSION

We presented a reliable method to produce a microstructured encapsulant coating using PDMS and silica microbeads on CPV solar cells. This method is based on a ~6 μm-thick encapsulating PDMS layer deposited on the 3JSC with a monolayer of hexagonal close-packed silica microbeads partially submerged into it and acts as an integral part of the ARC coating. The results presented here involve the control of the bead submergence into the PDMS layer via curing conditions, which was sufficient to reach a current gain close to the

maximum calculated within the simulation space. This fast-manufacturing process creates reproducible results without the use of expensive microfabrication methods or equipment.

We compared the angle dependent performance of a commercial SiO_x encapsulant to our beads/PDMS encapsulant, for STACE CPV modules using a single 3JSC design. By integrating measured angle-dependent EQE over the angular distribution of light on the cell in the 500× CPV submodule, we measure 1.6 ± 1.6% and 4.2 ± 1% J_{sc} gains for SiO_x/3JSC and beads/PDMS/3JSC with 1,000 nm-diameter beads submerged 25% into PDMS relative to the reference 3JSC, respectively. This was in good agreement with simulations which gave an increase of 1.5% and 3.9%, respectively. Our numerical model, validated by experimental data, predicts a maximum gain of 4.8% for beads/PDM/3JSC with 760 nm-diameter beads submerged 60% into PDMS, over 3JSC devices. In addition, we defined a large manufacturing tolerance window that provides a submergence control of 10%–32% and calculated an achievable gain of 4.4 ± 0.4% for 760 nm beads over 3JSC, where the uncertainty encompasses all values within the process window. For a series-connected CPV module without bypass diodes, we predict an average module current increase of 3.4% for the optimized beads/PDMS/3JSC configuration manufactured within the process window, relative to SiO_x/3JSC devices.

The microbeads have demonstrated their ability to lower the Fresnel reflection losses by providing a smooth optical transition from air to PDMS over a wide angular range. Therefore, they could be used to reduce reflection losses on various surfaces with refractive indices similar to PDMS, including SOEs used in CPV systems that inherently suffer from reflection losses on their air/glass interface. The application of a microbead coating would improve optical transmission and possibly improve the performance of the SOE or other optical elements.

ACKNOWLEDGEMENTS

We acknowledge the support from STACE, MITACS and Quebec Ministère de l'Économie, de la Science et de l'Innovation. LN2 is a joint International Research Laboratory (IRL 3463) funded and co-operated in Canada by Université de Sherbrooke (UdeS) and in France by CNRS as well as Université de Lyon (UdL, especially including ECL and INSA Lyon) and Université Grenoble Alpes (UGA). It is also supported by the Fonds de Recherche du Québec Nature et Technologie (FRQNT).

DATA AVAILABILITY STATEMENT

The data that support the findings of this study are available from the corresponding author upon reasonable request.

ORCID

Gavin P. Forcade https://orcid.org/0000-0001-9527-5661
Abdelatif Jaouad https://orcid.org/0000-0002-1466-7346
Christopher E. Valdivia https://orcid.org/0000-0002-6072-2959
Karin Hinzer https://orcid.org/0000-0002-2414-6288
Maxime Darnon https://orcid.org/0000-0002-6188-7157

REFERENCES

1. Aqachmar Z, Bouhal T, Lahrech K. Energetic, economic, and environmental (3 E) performances of high concentrated photovoltaic large scale installations: Focus on spatial analysis of Morocco. *Int J Hydrogen Energy*. 2020;45(18):10840-10861. https://doi.org/10.1016/j.ijhydene.2020.01.210
2. Oon LV, Tan MH, Wong CW, Chong KK. Optimization study of solar farm layout for concentrator photovoltaic system on azimuth-elevation sun-tracker. *Sol Energy*. 2020;204:726-737. https://doi.org/10.1016/j.solener.2020.05.032
3. Nishimura A, Hayashi Y, Tanaka K, et al. Life cycle assessment and evaluation of energy payback time on high-concentration photovoltaic power generation system. *Appl Energy*. 2010;87(9):2797-2807. https://doi.org/10.1016/j.apenergy.2009.08.011
4. Fthenakis VM, Kim HC. Life cycle assessment of high-concentration photovoltaic systems. *Prog Photovoltaics Res Appl*. 2013;21(3):379-388. https://doi.org/10.1002/pip.1186
5. Fraunhofer ISE: Photovoltaics Report, updated: 27 July 2021. https://www.ise.fraunhofer.de/content/dam/ise/de/documents/publications/studies/Photovoltaics-Report.pdf
6. Kost C, Shammugan S, Julch V, Nguyen H-T, Schlegl T. Levelized cost of electricity–renewable energy technologies. 2018.
7. Raut HK, Ganesh VA, Nair AS, Ramakrishna S. Anti-reflective coatings: a critical, in-depth review. *Energ Environ Sci*. 2011;4(10):3779-3804. https://doi.org/10.1039/c1ee01297e
8. Huang YF, Chattopadhyay S, Jen YJ, et al. Improved broadband and quasi-omnidirectional anti-reflection properties with biomimetic silicon nanostructures. *Nat Nanotechnol*. 2007;2(12):770-774. https://doi.org/10.1038/nnano.2007.389
9. Cannavale A, Fiorito F, Manca M, Tortorici G, Cingolani R, Gigli G. Multifunctional bioinspired sol-gel coatings for architectural glasses. *Build Environ*. 2010;45(5):1233-1243. https://doi.org/10.1016/j.buildenv.2009.11.010
10. Rambo CR, Cao J, Rusina O, Sieber H. Manufacturing of biomorphic (Si, Ti, Zr)-carbide ceramics by sol-gel processing. *Carbon N Y*. 2005;43(6):1174-1183. https://doi.org/10.1016/j.carbon.2004.12.009
11. Kennedy SR, Brett MJ. Porous broadband antireflection coating by glancing angle deposition. *Appl Optics*. 2003;42(22):4573-4579. https://doi.org/10.1364/ao.42.004573
12. Steele JJ, Brett MJ. Nanostructure engineering in porous columnar thin films: Recent advances. *J Mater Sci Mater Electron*. 2007;18(4):367-379. https://doi.org/10.1007/s10854-006-9049-8
13. Nam SH, Choi JW, Cho SJ, Kim KS, Boo JH. Growth of TiO 2 antireflection layer on textured Si (100) wafer substrate by metal-organic chemical vapor deposition method. *J Nanosci Nanotechnol*. 2011;11(8):7315-7318. https://doi.org/10.1166/jnn.2011.4813
14. Xi JQ, Schubert MF, Kim JK, et al. Optical thin-film materials with low refractive index for broadband elimination of Fresnel reflection. *Nat Photonics*. 2007;1(3):176-179. https://doi.org/10.1038/nphoton.2007.26
15. Xi J-Q, Kim JK, Schubert EF, et al. Very low-refractive-index optical thin films consisting of an array of SiO_2 nanorods. *Opt Lett*. 2006;31(5):601-603. https://doi.org/10.1364/ol.31.000601
16. Britten JA, Thomas IM. Sol-gel metal oxide and metal oxide/polymer multilayers applied by meniscus coating. In: Bennett HE, Chase LL, Guenther AH, Newnam BE, Soileau MJ, eds. *Laser-Induced Damage Optical Materials*. Vol.2114; 1993:244-250. https://doi.org/10.1117/12.180885
17. Nositschka WA, Beneking C, Voigt O, Kurz H. Texturisation of multicrystalline silicon wafers for solar cells by reactive ion etching through colloidal masks. *Sol Energy Mater sol Cells*. 2003;76(2):155-166. https://doi.org/10.1016/S0927-0248(02)00214-3
18. Yu P, Chiu M-Y, Chang C-H, et al. Towards high-efficiency multi-junction solar cells with biologically inspired nanosurfaces. *Prog*

Photovoltaics Res Appl. 2014;22(3):300-307. https://doi.org/10.1002/pip.2259
19. Chiu M-Y, Chang C-H, Tsai M-A, Chang F-Y, Yu P. Improved optical transmission and current matching of a triple-junction solar cell utilizing sub-wavelength structures. *Opt Express*. 2010;18(S3):A308-A313. https://doi.org/10.1364/oe.18.00a308
20. Asoh H, Oide A, Ono S. Formation of microstructured silicon surfaces by electrochemical etching using colloidal crystal as mask. *Electrochem Commun*. 2006;8(12):1817-1820. https://doi.org/10.1016/j.elecom.2006.08.021
21. Buencuerpo J, Torné L, Álvaro R, Llorens JM, Dotor ML, Ripalda JM. Nano-cones for broadband light coupling to high index substrates. *Sci Rep*. 2016;6(1):1-7. https://doi.org/10.1038/srep38682
22. Garciá-Linares P, Dominguez C, Dellea O, et al. Improving optical performance of concentrator cells by means of a deposited nanopattern layer. *AIP Conf. Proc.* 2015;1679(1):040004-1-040004-9. https://doi.org/10.1063/1.4931515
23. Delléa O, Shavdina O, Fugier P, Coronel P, Ollier E, Désage SF. Control methods in microspheres precision assembly for colloidal lithography. *IFIP Adv Inf Commun Technol*. 2014;435:107-117. https://doi.org/10.1007/978-3-662-45586-9_14
24. Forcade G, Valdivia CE, St-Pierre P, et al. Nanostructured surface for extended temperature operating range in concentrator photovoltaic modules. *AIP Conf. Proc.* 2020;2298:050002-1-050002-6. https://doi.org/10.1063/5.0032134
25. SYLGARD. 184 Silicone Elastomer 2017. https://www.dow.com/en-us/document-viewer.html?ramdomVar=1321611859083267856&docPath=/content/dam/dcc/documents/en-us/productdatasheet/11/11-31/11-3184-sylgard-184-elastomer.pdf
26. Schneider F, Draheim J, Kamberger R, Wallrabe U. Process and material properties of polydimethylsiloxane (PDMS) for optical MEMS. *Sensors Actuators, a Phys*. 2009;151(2):95-99. https://doi.org/10.1016/j.sna.2009.01.026
27. Miller DC, Kempe MD, Muller MT, Gray MH, Araki K, Kurtz SR. Durability of polymeric encapsulation materials in a PMMA/glass concentrator photovoltaic system. *Prog Photovoltaics Res Appl*. 2016;24(11):1385-1409. https://doi.org/10.1002/PIP.2796
28. Hasan O, Arif AFM. Performance and life prediction model for photovoltaic modules: Effect of encapsulant constitutive behavior. *Sol Energy Mater Sol Cells*. 2014;122:75-87. https://doi.org/10.1016/j.solmat.2013.11.016
29. Malitson IH. Interspecimen comparison of the refractive index of fused silica. *J Opt Soc Am*. 1965;55(10):1205-1209.
30. Delléa O, Lebaigue O. Boostream: a dynamic fluid flow process to assemble nanoparticles at liquid interface. *Mech Ind*. 2017;18(6):1-7. https://doi.org/10.1051/meca/2017026
31. Dellea O, Lebaigue O, Poncelet O. Method for forming a film of particles on the surface of a substrate. WO2020212286A1, 2020.
32. Wong EJ. *Modeling and control of rapid cure in polydimethylsiloxane (PDMS) for microfluidic device applications*. Massachusetts Institute of Technology; 2010.
33. Battaglia C, Hsu CM, Söderström K, et al. Light trapping in solar cells: can periodic beat random? *ACS Nano*. 2012;6(3):2790-2797. https://doi.org/10.1021/nn300287j
34. Siefer G, Baur C, Bett AW. External quantum efficiency measurements of Germanium bottom subcells: Measurement artifacts and correction procedures. *Conf. Rec. IEEE Photovolt. Spec. Conf.* 2010;704-707. https://doi.org/10.1109/PVSC.2010.5616919
35. Meusel M, Baur C, Létay G, Bett AW, Warta W, Fernandez E. Spectral response measurements of monolithic GaInP/Ga (In)As/Ge triple-junction solar cells: Measurement artifacts and their explanation. *Prog Photovoltaics Res Appl*. 2003;11(8):499-514. https://doi.org/10.1002/pip.514
36. Ferry VE, Verschuuren MA, van Lare MC, Schropp REI, Atwater HA, Polman A. Optimized spatial correlations for broadband light trapping nanopatterns in high efficiency ultrathin film a-Si:H solar cells. *Nano Lett*. 2011;11(10):4239-4245. https://doi.org/10.1021/nl202226r
37. Schäfer J, Foest R, Quade A, Ohl A, Weltmann KD. Local deposition of SiOx plasma polymer films by a miniaturized atmospheric pressure plasma jet (APPJ). *J Phys D Appl Phys*. 2008;41(19):194010. https://doi.org/10.1088/0022-3727/41/19/194010
38. Hugonin JP, Lalanne P. *Reticolo software for grating analysis*. arXiv preprint arXiv:2101.00901; 2021.
39. Byrnes SJ. *Multilayer optical calculations*. arXiv preprint arXiv:1603.02720; 2016.
40. Gupta V, Probst PT, Goßler FR, et al. Mechanotunable surface lattice resonances in the visible optical range by soft lithography templates and directed self-assembly. *ACS Appl Mater Interfaces*. 2019;11(31):28189-28196. https://doi.org/10.1021/acsami.9b08871
41. Kim Y, Lee SM, Park CS, Lee SI, Lee MY. Substrate dependence on the optical properties of Al2O3 films grown by atomic layer deposition. *Appl Phys Lett*. 1997;71(25):3604-3606. https://doi.org/10.1063/1.120454
42. Ochoa-Martínez E, Barrutia L, Ochoa M, et al. Refractive indexes and extinction coefficients of n- and p-type doped GaInP, AlInP and AlGaInP for multijunction solar cells. *Sol Energy Mater Sol Cells*. 2018;174:388-396. https://doi.org/10.1016/j.solmat.2017.09.028
43. Cui J, Allen T, Wan Y, et al. Titanium oxide: a re-emerging optical and passivating material for silicon solar cells. *Sol Energy Mater sol Cells*. 2016;158:115-121. https://doi.org/10.1016/j.solmat.2016.05.006
44. Djurišić AB, Rakić AD, Kwok PCK, Li EH, Majewski ML, Elazar JM. Modeling the optical constants of AlxGa1-xAs alloys. *J Appl Phys*. 1999;86(1):445-451. https://doi.org/10.1063/1.370750
45. Palik E. *Handbook of Optical Constants of Solids*. 3rd ed. Academic Press; 1998.
46. Aspnes DE, Studna AA. Dielectric functions and optical parameters of Si, Ge, GaP, GaAs, GaSb, InP, InAs, and InSb from 1.5 to 6.0 eV. *Phys Rev B*. 1983;27(2):985-1009. https://doi.org/10.1103/PhysRevB.27.985
47. Bedjaoui M, Despax B, Caumont M, Bonafos C. Si nanocrystal-containing SiO_x ($x < 2$) produced by thermal annealing of PECVD realized thin films. *Mater. Sci. Eng. B Solid-State Mater. Adv. Technol.* 2005;124–125:508-512. https://doi.org/10.1016/j.mseb.2005.08.066
48. Carneiro JO, Machado F, Rebouta L, et al. Compositional, optical and electrical characteristics of SiO_x thin films deposited by reactive pulsed DC magnetron sputtering. *Coatings*. 2019;9(8):1-18. https://doi.org/10.3390/coatings9080468
49. Zhang G, Cao Y, Zhang Y, Song X, Lu J, Li S. Preparation and characteristic analysis of ultra-low dielectric constant nano-porous silicon oxide films. *Lect. Notes Electr. Eng.* 2020;600:730-736. https://doi.org/10.1007/978-981-15-1864-5_99
50. Zhang Q, Xu JJ, Chen HY. Patterning microbeads inside poly (dimethylsiloxane) microfluidic channels and its application for immobilized microfluidic enzyme reactors. *Electrophoresis*. 2006;27(24):4943-4951. https://doi.org/10.1002/ELPS.200600024

How to cite this article: Forcade GP, Ritou A, St-Pierre P, et al. Microstructured antireflective encapsulant on concentrator solar cells. *Prog Photovolt Res Appl*. 2021;1-9. doi:10.1002/pip.3468

Chapter 4

Near-field thermophotovoltaics (NFTPVs)

This chapter presents my work optimizing NFTPV device designs, initially introduced in Section 1.2, by leveraging the physics described in Sections 2.1, 2.2.5, 2.3 and 2.4. The chapter is divided into two sections: published work on optimizing an InAs-based NFTPV device and unpublished work on the fabrication and characterization of such a device. In this chapter, efficiency is defined as the ratio of the power output at the maximum power point to the total irradiance absorbed by the device which differs slightly from Eq. (2.43). Consequently, any photons reflected back to the radiative source are considered recycled.

4.1 Efficiency-optimized near-field thermophotovoltaics using InAs and InAsSbP

The article details my work designing an InAs-based NFTPV device for waste-heat to electrical power conversion. I combine the near-field heat transfer model and the electrical model described in Sections 2.2.5 and 2.1 to design the device. This research aims to understand the new design requirements and realistic performance of thermophotovoltaics under near-field illumination, to guide their fabrication.

Impact

The manuscript has the following novelties:

1. Developed a validated optoelectronic model using measurements from literature.
2. Designed three NFTPV devices, discovering that an n-i-p structure offers the best performance.
3. Calculated 9- and 11-times higher efficiency and power output compared to the present record-measured NFTPV device for a 900 K radiator with a 70 nm radiator-PV gap.
4. Found that incorporating InAsSbP as minority carrier blocking layers improves device performance by 1.9 times versus using InAs.
5. Determined that integrating a gold back-reflector directly behind the active layers enhances optical efficiency by 2.9 times over a design with a substrate.

Our results rigorously demonstrate realistic design requirements for high-efficiency NFTPV cells. Our best-proposed design has the potential to outperform the best-measured NFTPV device by an order of magnitude in converting waste heat within the 600-900 K range into electrical power.

Author contribution

Gavin P. Forcade: As the lead University of Ottawa-based graduate student associated with the project, I developed the optoelectronic model, validated it, and used it to perform the simulations. I was the lead author of the article.

Dr. Christopher E. Valdivia: As a senior research scientist within the University of Ottawa's SUNLAB research group, Chris helped to guide my research, provided detailed feedback during the analysis of my simulation results, and assisted in editing the manuscript.

Prof. Sean Molesky: As a postdoctoral researcher at Princeton University, Sean wrote the optical software, helped validate the optical model, provided detailed feedback during the analysis of my simulation results, and assisted in editing the manuscript.

Shengyuan Lu: As an Undergraduate student at Princeton University, Shengyuan helped validate the optical model.

Prof. Alejandro Rodriguez: As a professor at Princeton University, Alejandro helped conceptualize the project.

Prof. Jacob J. Krich: As a professor at the University of Ottawa, Jacob helped to guide my research, provided detailed feedback during the analysis of my simulation results, and assisted in editing the manuscript.

Prof. Raphael St-Gelais: As the principal investigator of the project and professor at the University of Ottawa, Raphael led the conceptualization of the project, helped to guide my research, provided detailed feedback during the analysis of my simulation results, and assisted in editing the manuscript.

Prof. Karin Hinzer: As the director of the University of Ottawa's SUNLAB research group, Karin oversaw my research, provided detailed feedback during the analysis of my simulation results, and assisted in editing the manuscript.

Reproduced from:

> G.P. Forcade, C.E. Valdivia, S. Molesky, S. Lu, A.W. Rodriguez, J.J. Krich, R. St-Gelais, and K. Hinzer, "Efficiency-Optimized Near-Field Thermophotovoltaics Using InAs and InAsSbP", *Applied Physics Letters*, 121, 19, 2022. DOI: 10.1063/5.0116806

with the permission of AIP Publishing.

Applied Physics Letters ARTICLE scitation.org/journal/apl

Efficiency-optimized near-field thermophotovoltaics using InAs and InAsSbP

Cite as: Appl. Phys. Lett. **121**, 193903 (2022); doi: 10.1063/5.0116806
Submitted: 29 July 2022 · Accepted: 23 October 2022 ·
Published Online: 10 November 2022

Gavin P. Forcade,[1,a)] Christopher E. Valdivia,[2] Sean Molesky,[3,4] Shengyuan Lu,[5] Alejandro W. Rodriguez,[3] Jacob J. Krich,[1] Raphael St-Gelais,[6] and Karin Hinzer[2]

AFFILIATIONS

[1]Department of Physics, University of Ottawa, Ottawa, Ontario K1N 1K5, Canada
[2]SUNLAB, School of Electrical Engineering and Computer Science, University of Ottawa, Ottawa, Ontario K1N 1K5, Canada
[3]Department of Electrical and Computer Engineering, Princeton University, Princeton, New Jersey 08544, USA
[4]Department of Engineering Physics, Polytechnique Montreal, Montreal, Quebec H3T 1J4, Canada
[5]Department of Physics, Princeton University, Princeton, New Jersey 08544, USA
[6]Department of Mechanical Engineering, University of Ottawa, Ottawa, Ontario K1N 1K5, Canada

Note: This paper is part of the APL Special Collection on Thermal Radiation at the Nanoscale and Applications.
[a)]**Author to whom correspondence should be addressed:** gforc034@uottawa.ca

ABSTRACT

Waste heat is a free and abundant energy source, with 15% of global total energy use existing as waste heat above 600 K. For 600–900 K temperature range, near-field thermophotovoltaics (NFTPVs) are theorized to be the most effective technology to recycle waste heat into electrical power. However, to date, experimental efficiencies have not exceeded 1.5%. In this work, we optimize the efficiency of three modeled InAs/InAsSbP-based room-temperature NFTPV devices positioned 0.1 μm from a 750 K p-doped Si radiator. We couple a one-dimensional fluctuational electrodynamics model for the near field optics to a two-dimensional drift-diffusion model, which we validated by reproducing measured dark current–voltage curves of two previously published InAs and InAsSbP devices. The optimized devices show four to six times higher above-bandgap energy transfer compared to the blackbody radiative limit, yielding enhanced power density, while simultaneously lowering parasitic sub-bandgap energy transfer by factors of 0.68–0.85. Substituting InAs front- and back-surface field layers with InAsSbP show 1.5- and 1.4-times higher efficiency and power output, respectively, from lowered parasitic diffusion currents. Of our three optimized designs, the best performing device has a double heterostructure with an n–i–p doping order from front to back. For radiator-thermophotovoltaic gaps of 0.01–10 μm and radiators within 600–900 K, this device has a maximum efficiency of 14.2% and a maximum power output of 1.55 W/cm^2, both at 900 K. Within 600–900 K, the efficiency is always higher with near- vs far-field illumination; we calculate up to 3.7- and 107-times higher efficiency and power output, respectively, using near-field heat transfer.

© *2022 Author(s). All article content, except where otherwise noted, is licensed under a Creative Commons Attribution (CC BY) license (http://creativecommons.org/licenses/by/4.0/).* https://doi.org/10.1063/5.0116806

Waste heat above 600 K represents 15% of global total energy use,[1] and recycling this waste heat to electrical power with solid-state modules could be a general solution to improve energy-use efficiency. For 600–900 K heat sources, existing commercial waste-heat-to-electricity solid-state converters, thermoelectric generators (TEGs), have high power densities of 2 W/cm^2 but suffer from low efficiencies less than 12%.[2] Conversely, thermophotovoltaic (TPV) systems have high theoretical efficiencies up to 45% but low power densities of 0.2 W/cm^2.[3] Near-field thermophotovoltaic (NFTPV) systems, which position a heat source (radiator) and a TPV cell in extreme proximity, present both high theoretical efficiency and power density, up to 40% and 10 W/cm^2 for practical devices.[3,4] Although NFTPV systems with cells operating at room temperature have experimentally achieved 40-fold increases in power density over TPV systems,[5] they have not exceeded 1.5% efficiency for 600–900 K radiator temperatures. This low efficiency is due to the use of TPV cells that were not optimized for near-field operation[5,6] or InGaAs-based cells with larger-than-optimal bandgaps (0.73 eV at 300 K).[7,8] Conversely, Lucchesi *et al.* designed a low bandgap (0.23 eV at 77 K) InSb-based NFTPV cell that was cooled to 77 K and measured a 14% efficiency with a power density of 0.75 W/cm^2 with a 732 K radiator.[9] Although they reached a high efficiency, these cells only function properly

© Author(s) 2022

when cooled to cryogenic temperatures, making them impractical for most situations.

Although the spectral characteristics required for high performance in NFTPV systems are well known,[4,10–26] concurrent optimization of the interrelated optical and electronic properties of NFTPV systems remains largely unexplored. Prior studies have not solved the full two-dimensional (2D) drift-diffusion equations in the cell, although such simulation allows realistic representation of both lateral and vertical current flow and carrier collection and is industry-standard in many other contexts.[27–30] Many studies calculated NFTPV electrical performance using detailed balance analysis, assuming radiative recombination loss only[10,19–22] or also including nonradiative recombination mechanisms.[4,23–26] Other analyses have employed the diode equation with a saturation current calculated using experimentally measured lifetimes of the studied materials.[21–28] An improved electrical model, solving the drift-diffusion equations in the low injection limit, was also employed to analyze NFTPV performance.[31–35] Recently, studies have solved the full 1D drift-diffusion equations,[36–39] which leads to more realistic results,[36] though still without lateral transport effects.

In the present work, we investigate the performance of NFTPV cells based on InAs, which has an ideal bandgap (0.353 eV at 300 K) for 600–900 K radiator temperatures and proven room temperature operating performance.[40–46] We optimize the coupled electrical and optical properties of three NFTPV designs, all with back reflectors and two with InAs/InAsSbP double-heterostructures, by maximizing their efficiency under the illumination of a 750 K p-doped Si radiator separated by 0.1 μm. We compare their performances to a baseline design on a 500 μm substrate, shown in Fig. 1(a). We further investigate the performance for the highest-efficiency design for radiator temperatures from 600 to 900 K and with radiator-TPV gaps from 0.01 to 10 μm.

We propose three designs, presented in Figs. 1(b)–1(d). The pin and pin-Q cell designs have a p–i–n doping order from top to bottom. Conversely, the nip-Q design reverses this order to reduce lateral sheet resistance in the front-surface field (FSF) layer since electron mobilities are higher than hole mobilities (see Sec. 1 of the supplementary material). The pin-Q and nip-Q designs include the quaternary (Q) $InAs_xSb_{0.31(1-x)}P_{0.69(1-x)}$ lattice matched to InAs with bandgap up to 0.495 eV at 300 K[47] in the FSF and base layers to reduce undesirable diffusion currents, but at the cost of higher growth complexity. All cells have a uniform temperature of 300 K (see Sec. 2 of the supplementary material) and are illuminated by high-temperature 5×10^{18} cm^{-3} p-type silicon radiators, separated by vacuum. The distance between gridlines is $d_{G\text{-}G}$ while the distance between the bottom of the radiator and the top of the FSF layer is $d_{R\text{-}FSF}$. For comparison, we consider the baseline design [Fig. 1(a)], which is based on the fabricated TPV cell from Lu *et al.*[40] In contrast to the baseline design, we added cap and back-surface field (BSF) layers to each new design to minimize contact resistance[48–50] and reduce undesirable minority diffusion currents. In addition, our three proposed designs have their substrates removed, increasing fabrication complexity but minimizing parasitic sub-bandgap (SBG) photon absorption. Substrate-less devices with a back reflector (BR) layer reflect SBG photons for re-absorption within the radiator, increasing efficiency, and decreasing cooling requirements for the TPV cell.

Our coupled optoelectronic model simulates the radiative thermal transport and the electrical response of the NFTPV device by combining the results of two software packages. We model radiation transport using a custom fluctuational electrodynamics solver[51,52] that treats the devices as laterally infinite layered structures. We compute depth- and frequency-resolved radiation transfer, separated by the physical absorption mechanism, allowing us to calculate the depth-resolved electron-hole generation rate from interband absorption and

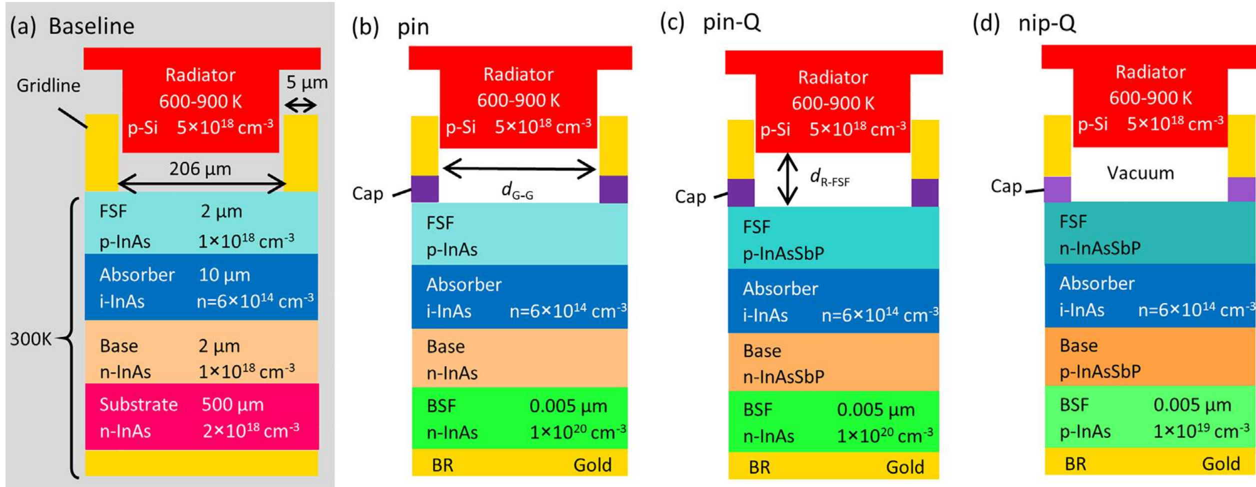

FIG. 1. Schematic diagrams of NFTPV devices: (a) TPV cell from Ref. 40 and (b)–(d) our new NFTPV designs, starting from the simplest growth of InAs only (b), then increasing performance by adding the quaternary InAsSbP [(c) and (d)]. The baseline design (a) from Ref. 40 is intended for far-field TPV and is used here for baseline comparison and simulation validation. All designs have vacuum separating the radiator and TPV cell, equal gridline widths (5 μm), and 300 K cells. Cap layer thickness is 0.02 μm and composed of (b) and (c) n-InAs doped at 1×10^{20} cm^{-3} and (d) p-InAs doped at 1×10^{19} cm^{-3}. Structural parameters not given in figure for designs [(b)–(d)] are optimized with the results in Table I.

© Author(s) 2022

total heat transfer from lattice, free-carrier, and interband processes (see Sec. 3 of the supplementary material for model details). We verify the optical model by reproducing the spectral absorption calculated in Ref. 8; the results are shown in Sec. 4 of the supplementary material.

We model the electrical transport for the NFTPV device using Synopsys TCAD Sentaurus. This software solves Poisson's equation coupled with electron and hole drift and diffusion equations to determine the TPV cell current–voltage curves as well as depth-resolved recombination rate profiles including radiative, Auger, Shockley–Read–Hall (SRH), and surface recombinations.[27] We apply the 1D electron–hole pair generation rate profiles, extracted from the optical model, uniformly across the illuminated portion of the 2D TPV cell, with no generation directly below the top contacts. We assume no contact and sheet resistance for both top and bottom electrodes, as they can be designed to be negligible.[48–50] We calculate radiative and Auger recombination coefficients following the method in Ref. 53, providing Auger coefficients for InAs ($C_n = 0.48 \times 10^{-26}$ and $C_p = 1.01 \times 10^{-26}$ cm^6/s) within the experimental uncertainties of Ref. 54. We employ a constant SRH lifetime (3.7×10^{-7} s) for both n- and p-type InAs, which provided the best fit to the measured dark-I–V curve of the TPV cell from Ref. 40. Subtracting Auger and radiative contributions from the total lifetime of Ref. 55 using Matthiessen's rule, we estimate the SRH lifetime of $InAs_xSb_{0.31(1-x)}P_{0.69(1-x)}$ for $x \neq 1$ to be 3.2×10^{-8} s. We include a doping-dependent surface recombination velocity at the vacuum/FSF interface, discussed further in Sec. 5 of the supplementary material. Due to the low conduction band density of states of InAs and InAsSbP lattice matched to InAs, we use a non-parabolic band model to calculate the electron quasi-Fermi level.[56] We employ the model and parameters from Ref. 57 to calculate the bandgap and electron affinity for all stoichiometric compositions of InAsSbP. The energy band diagrams of baseline and optimized nip-Q cells at maximum power point voltage (V_{mpp}) are presented in Fig. 2, including conduction band (E_C) and valence band (E_V) edges and the Fermi levels of electrons (E_{Fe}) and holes (E_{Fh}). Figure 2(b) shows abrupt band offsets at the heterojunctions with the FSF and BSF layers, which effectively block parasitic hole and electron transport, respectively. We validate the electrical model, comparing measured and simulated dark current–voltage curves of p–i–n InAs[40] and p-InAsSbP/n-InAs/n$^+$-InAs[41] devices, with the results given in Sec. 6 of the supplementary material.

With a goal to efficiently recover 600–900 K waste heat while considering achievable radiator-TPV gaps ($d_{R\text{-}FSF}$) of present NFTPV devices,[5–9,58] we optimize the three NFTPV designs of Figs. 1(b)–1(d) for a radiator temperature of 750 K and $d_{R\text{-}FSF} = 0.1$ μm. We calculate the total optical power density absorbed by the TPV cell (P_{in}) and its maximum power point density (P_{mpp}), with power densities defined as power divided by the illuminated area. We then optimize the device structure to maximize device efficiency, $\eta = P_{mpp}/P_{in}$, using an iterative optimizer with parameter domain sampling defined by the face-centered central composite method.[59] We optimize for efficiency as opposed to power as it increases waste heat use while also lowering cell cooling requirements.

To speed up the optimization, we hold constant the parameters with fixed values listed in Fig. 1. This includes the cap and BSF layer doping concentrations, which are set at readily achievable values[48–50] to maximize current collection and quench contact resistance. This choice necessitates a thin BSF layer to minimize free-carrier absorption. We employ an intrinsic InAs absorber layer to maximize absorption[31] while minimizing the Auger recombination that dominates in cells using p-InAs.[40] See Sec. 7 of the supplementary material for effects of varying Cap and BSF layer thickness and doping on performance.

We consider the radiator to be semi-infinite, but instead using a 500-μm thickness decreases total radiation transfer by less than 1%. A separate optimization showed that our chosen radiator doping of 5×10^{18} cm^{-3} maximizes above-bandgap (ABG) radiation transfer for realistic radiator thicknesses (on the order of a typical 500 μm Si substrate or less). Thinner radiators demand higher doping concentrations to maximize ABG radiation transfer, but such radiators also increase SBG radiation transfer, which hurts efficiency.

Layer thicknesses and doping not specified in Fig. 1 are included as parameters for optimization. The optimization domain and results for all designs illuminated by a 750 K radiator with $d_{R\text{-}FSF} = 0.1$ μm are

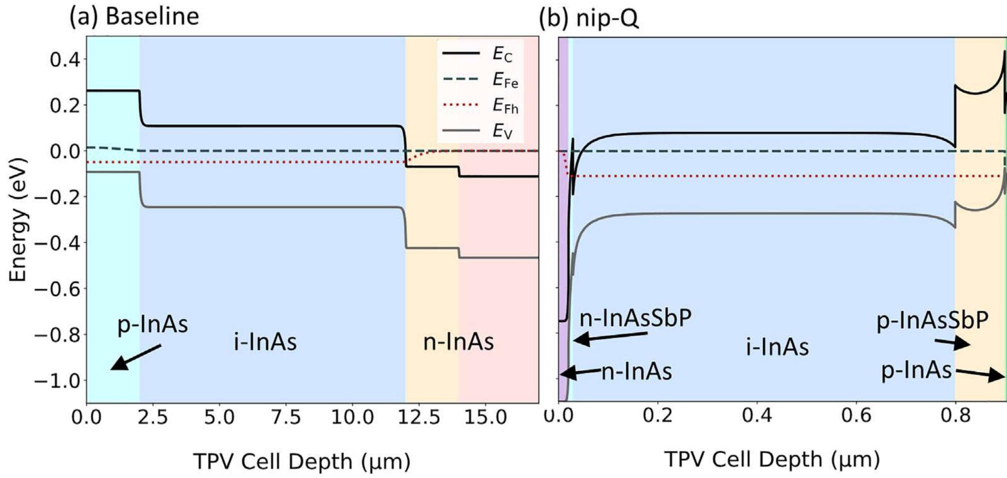

FIG. 2. Band diagram, with cutline through the top contact, at maximum power point voltage (V_{mpp}) of the (a) baseline and (b) optimized nip-Q TPV cells, illuminated by a 750 K radiator with $d_{R\text{-}FSF} = 0.1$ μm. Note the different horizontal scales.

© Author(s) 2022

TABLE I. Optimized NFTPV cell structure for a 750 K p-Si radiator and $d_{R\text{-}FSF} = 0.1\ \mu$m, with their optimization bounds and performance metrics.

	Parameter	Units	Range	Baseline[a]	pin	pin-Q	nip-Q
Input	$d_{G\text{-}G}$	μm	20–300	206	49	49	78
	FSF thickness	μm	0.005–2.0	2.0	0.0053	1.1	0.0089
	FSF $InAs_xSb_{0.31(1-x)}P_{0.69(1-x)}$		$x = 0.4$–1.0	1.0	1.0[a]	0.4	0.46
	FSF doping	cm^{-3}	6×10^{14}–10^{19}	$p = 10^{18}$	$p = 10^{19}$	$p = 2\times10^{17}$	$n = 4\times10^{15}$
	Absorber thickness	μm	0.1–3.0	10.0	0.72	0.77	0.77
	Base thickness	μm	0.005–2.0	2.0	0.062	0.055	0.10
	Base $InAs_xSb_{0.31(1-x)}P_{0.69(1-x)}$		$x = 0.4$–1.0	1.0	1.0[a]	0.76	0.4
	Base doping	cm^{-3}	6×10^{14}–10^{19}	$n = 10^{18}$	$n = 6\times10^{14}$	$n = 7\times10^{16}$	$p = 2\times10^{15}$
Output	J_{sc}	A cm^{-2}	...	1.75	2.39	2.46	2.36
	V_{oc}	V	...	0.065	0.108	0.143	0.145
	P_{mpp}	mW cm^{-2}	...	34	121	204	203
	η	%	...	0.29	4.8	8.0	9.0

[a]Fixed at a given value.

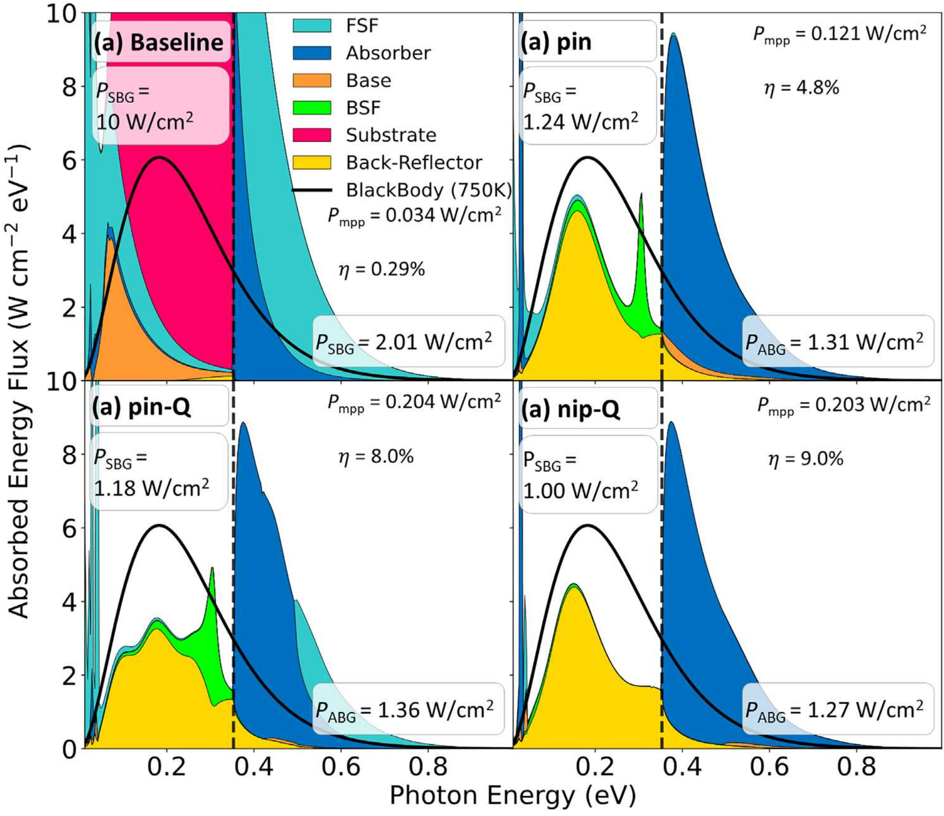

FIG. 3. Spectral absorption distribution within NFTPV cell layers for a 750 K radiator and $d_{R\text{-}FSF} = 0.1\ \mu$m, for designs: (a) baseline and optimized (b) pin, (c) pin-Q, and (d) nip-Q. Solid black line represents the blackbody radiative limit at 750 K. The vertical dashed lines represent the bandgap of InAs, which separates parasitic sub-bandgap (SBG) and useful above-bandgap (ABG) absorption, respectively. We include total SBG and ABG absorbed power, P_{SBG} and P_{ABG}, respectively.

© Author(s) 2022

given in Table I. The optimized As mole fraction (x) of $InAs_xSb_{0.31(1-x)}P_{0.69(1-x)}$, for the FSF and base layers of the pin-Q and nip-Q designs, respectively, reached the lower bound of 0.4, which we constrained to high quality compositions[60,61] outside the miscibility gap.[62] The p-type doping concentration for the FSF layer of the pin design reached the upper bound of $10^{19}\,cm^{-3}$, which we limited to readily achievable concentrations for these devices.[49–51] These bounded values minimize parasitic electron diffusion; the lower bound Q has the largest bandgap with favorable band-alignment as a p-type material (see Fig. 2) while the pin design requires high p-doping to perform the same task.

The FSF conductivity effects can only be captured with 2+ dimension drift-diffusion solvers, highlighting the importance of our electrical model. To minimize lateral series resistance, the p-type FSF layer must be thick and moderately doped (pin-Q) or thin and highly doped (pin). The n-type FSF layer of the nip-Q device further reduces top sheet resistance, since electron mobility is higher than hole mobility, allowing for a thin and moderately doped FSF layer with 60% larger $d_{G\text{-}G}$, increasing power output density.

Comparing parameters of the optimized designs to the baseline design, the optimized designs have smaller $d_{G\text{-}G}$ values and are composed of much thinner layers. Thinner cells improve device performance due to higher carrier collection efficiency and lower parasitic free carrier absorption but reduce current generation. However, the thin designs have higher J_{sc} than the baseline due to shorter penetration depth of evanescent vs propagating waves and high reflection at the gold BR layer. The base layers optimally reached lower doping concentrations to reduce SBG power transfer (P_{SBG}) originating from free-carrier absorption.

Our optical model calculates a significant enhancement of useful ABG power transfer (P_{ABG}) over the blackbody radiative limit for all devices. Figure 3 shows the layer-resolved spectral absorbed energy flux for each device. A 750 K blackbody radiative spectrum represented by the solid black line is included for comparison, along with a vertical dashed black line denoting the bandgap of InAs (0.353 eV). The optimized devices have P_{SBG} approximately 10% of that in the baseline design. P_{SBG} is not converted to useful power and instead raises the TPV cooling requirements. P_{SBG} could be further reduced with a more reflective BR.[16,63] The optimized designs [Figs. 3(b)–3(d)] have 4–6 times higher total P_{ABG} and 0.68–0.85 times lower P_{SBG} compared to the blackbody limit. Although P_{ABG} of the efficiency-optimized designs are about 70% of the baseline design, we see much

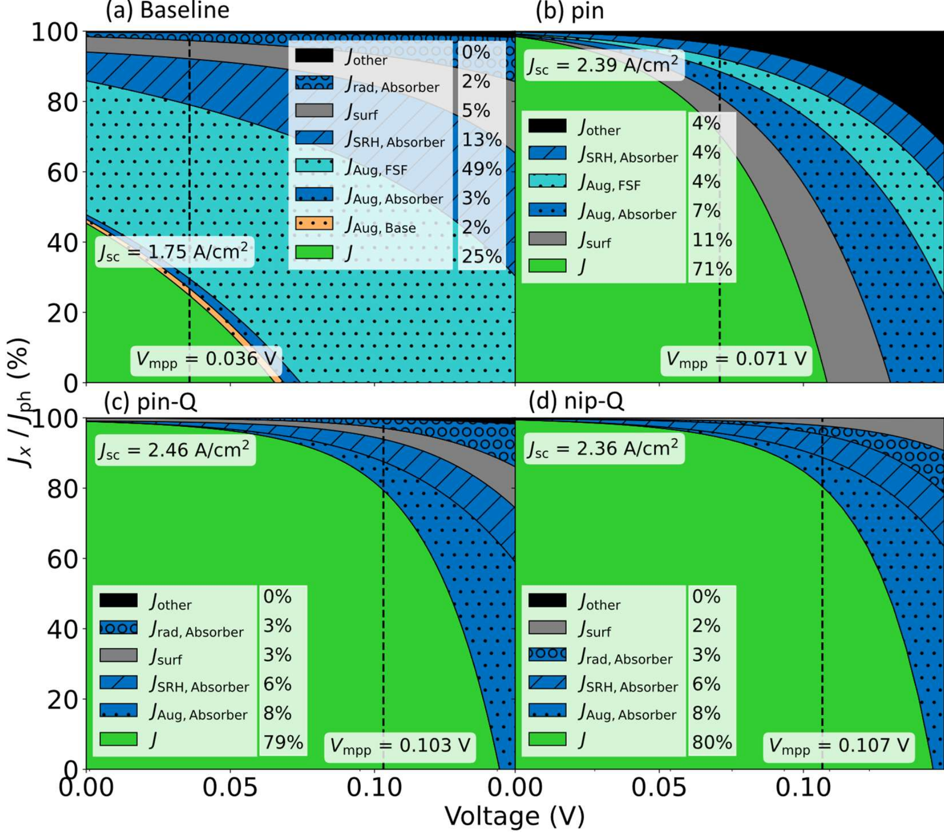

FIG. 4. Current–voltage curves of extracted (J) and region-resolved recombination currents (J_x) normalized to the total photogenerated current (J_{ph}) for a 750 K radiator and $d_{R\text{-}FSF} = 0.1\,\mu m$ for designs: (a) baseline, (b) pin, (c) pin-Q, and (d) nip-Q. The vertical dashed lines show V_{mpp} operation of the devices. Current recombination types are stacked from largest to smallest contributor at V_{mpp}, which are then stacked following the cell structure. Currents that account for less than 1.5% of J_{ph} at V_{mpp} are lumped in J_{other}. Current contributions at V_{mpp} are provided in the legend.

© Author(s) 2022

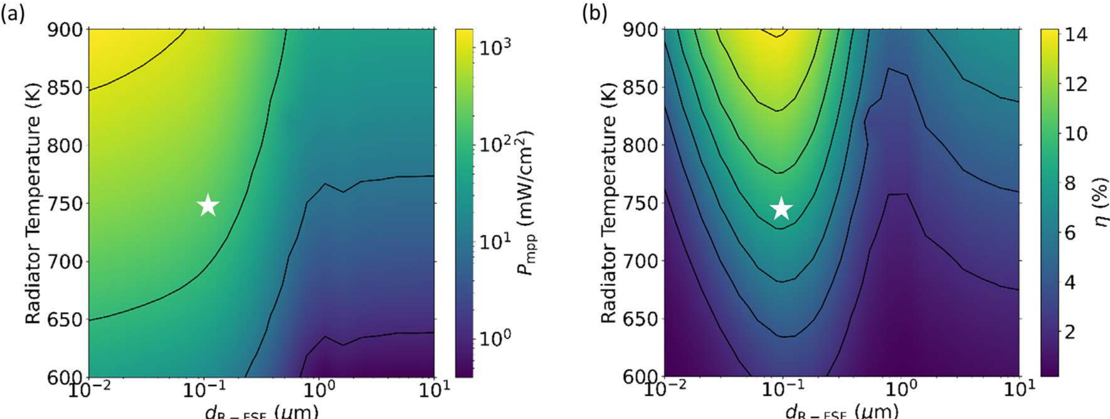

FIG. 5. (a) Power output and (b) efficiency of our optimized nip-Q device as a function of radiator temperature and radiator-TPV gap. Stars depict parameters used for device optimization.

higher efficiency and power output (Table I) due to order-of-magnitude thinner absorption layers, which improves current collection.

Up to 80% of available current is collected at V_{mpp} for the optimized designs compared to just 39% for the baseline, highlighting the importance of optimizing electronic device properties for near-field operation. Figure 4 shows the current–voltage characteristics, normalized to the total photo-generated current (J_{ph}), of the four designs. We include extracted current (J), surface recombination at the vacuum/FSF and electrode/semiconductor interfaces (J_{surf}), as well as Auger ($J_{Aug,l}$), radiative ($J_{rad,l}$), and Shockley–Read–Hall ($J_{SRH,l}$) recombination currents in layer l. All currents that contribute less than 1.5% to J_{ph} at V_{mpp} are combined into J_{other}. Auger recombination is the main electrical loss mechanism for all designs, consuming 8%–54% of J_{ph} at V_{mpp}. However, the devices could be further improved using higher quality absorber layer material, i.e., lowering SRH recombination. Comparing Figs. 4(b) and 4(c), we find that the introduction of the quaternary InAsSbP in the FSF and base layers reduces surface recombination by two-third and eliminates recombination in all but the absorber layer, contributing to a 45% larger V_{mpp}. Designs with InAsSbP, nip-Q and pin-Q, have similar normalized current–voltage characteristics [see Figs. 4(c) and 4(d)]; therefore, nip-Q's performance enhancement (Table I) is due to better P_{SBG} management and larger $d_{G\text{-}G}$.

Using our best design, the optimized nip-Q device, we explore the impact of radiator temperature and $d_{R\text{-}FSF}$ on the power output and efficiency in Fig. 5. The star represents the parameter values used during the nip-Q device optimization. We calculate a significant power output enhancement from near-field energy transfer for all radiator temperatures investigated, with the largest enhancement being 107-fold larger than the far-field ($d_{R\text{-}FSF} = 10\,\mu$m), occurring with $d_{R\text{-}FSF} = 0.01\,\mu$m and a 600 K radiator. We also calculate an improved efficiency under near-field illumination for all radiator temperatures within 600–900 K, reaching up to a 3.7-fold increase with a 600 K radiator and $d_{R\text{-}FSF} = 0.12\,\mu$m compared to a far-field device.

The maximum efficiency for a given radiator temperature varies with $d_{R\text{-}FSF}$. The optimal $d_{R\text{-}FSF}$ decreases as temperature increases, going from 0.12 to 0.09 μm for a 600–900 K radiator, respectively. This shift toward smaller $d_{R\text{-}FSF}$ occurs because there is proportionally less near-field P_{SBG} transfer to the FSF layer for higher radiator temperatures. Finally, the dip in efficiency at $d_{R\text{-}FSF} \approx 1\,\mu$m is caused by a lowered P_{ABG} relative to P_{SBG} due to propagative wave interference effects. Since the relative fraction of P_{ABG} vs P_{SBG} increases with radiator temperature, the highest efficiency and power output of 14.2% and 1.55 W/cm^2 occur at 900 K. P_{ABG} increases as $d_{R\text{-}FSF}$ decreases, but P_{SBG} absorbed in the FSF layer also increases rapidly below 0.1 μm, which reduces efficiency without impacting power output. Therefore, the maximum efficiency and power output occur at different $d_{R\text{-}FSF}$ of 0.09 and 0.01 μm (lower limit), respectively.

Simulation of our optimized nip-Q design significantly outperforms the simulated p-InAs/n-InAs design studied in Ref. 31. At 800 K and with $d_{R\text{-}FSF} = 0.1\,\mu$m, we calculate approximately 2.7- and 3.3-times higher efficiency and power density relative to that device (compared to their efficiency that assumes no absorption in the substrate). The nip-Q device performance enhancement is attributed to our BR layer, use of Q material, and n–i–p doping configuration.

In summary, three NFTPV cell designs containing InAs and/or InAsSbP were optimized and compared under near-field illumination by a 750 K p-Si radiator at $d_{R\text{-}FSF} = 0.1\,\mu$m, using a validated optoelectronic model solving full 2D drift-diffusion equations and fluctuational electrodynamics. The optimized devices have 4–6 times higher above-bandgap and 0.68–0.85 times less sub-bandgap radiation transfer than the blackbody limit. Over the 600–900 K radiator temperature range, we calculate up to 14.2% efficiency and 1.55 W/cm^2 power output for the best performing device design. According to these results, our best design could significantly outperform the best measured NFTPV device for the conversion of 600–900 K waste heat, providing important guidelines for the design of future NFTPV cells.

See the supplementary material for further details and validation of the optical and electrical model, the calculated temperature gradient of the device, and the impact on device performance of parameters that were fixed during optimization.

The authors thank University of Ottawa colleagues C. Zhang and M. Giroux for discussions on this topic. This work was supported in part by the Natural Sciences and Engineering

© Author(s) 2022

Research Council of Canada (No. NSERC CGS-D) and by the New Frontiers in Research Fund (No. NFRFE-2019-00334). They are also grateful to CMC Microsystems for providing access to the Synopsys Sentaurus software (vS-2021.06).

AUTHOR DECLARATIONS

Conflict of Interest

The authors have no conflicts to disclose.

Author Contributions

Gavin Paul Forcade: Data curation (lead); Formal analysis (lead); Funding acquisition (supporting); Investigation (lead); Methodology (lead); Software (equal); Validation (lead); Visualization (lead); Writing – original draft (lead); Writing – review & editing (lead). **Christopher E. Valdivia:** Funding acquisition (supporting); Supervision (equal); Writing – review & editing (equal). **Sean Molesky:** Methodology (supporting); Software (equal); Supervision (supporting); Writing – review & editing (supporting). **Shengyuan Lu:** Investigation (supporting); Software (supporting); Validation (supporting). **Alejandro Rodriguez:** Conceptualization (equal); Funding acquisition (supporting); Software (supporting); Writing – review & editing (supporting). **Jacob J Krich:** Methodology (supporting); Software (equal); Supervision (supporting); Writing – review & editing (equal). **Raphael St-Gelais:** Conceptualization (lead); Funding acquisition (lead); Investigation (supporting); Software (supporting); Supervision (supporting); Writing – review & editing (supporting). **Karin Hinzer:** Conceptualization (equal); Funding acquisition (supporting); Resources (equal); Supervision (lead); Writing – review & editing (supporting).

DATA AVAILABILITY

The data that support the findings of this study are available from the corresponding author upon reasonable request.

REFERENCES

[1]C. Forman, I. K. Muritala, R. Pardemann, and B. Meyer, Renewable Sustainable Energy Rev. **57**, 1568 (2016).
[2]See https://thermoelectric-generator.com/ for thermoelectric generators (2022).
[3]I. A. Okanimba Tedah, F. Maculewicz, D. E. Wolf, R. Schmechel, I. A. O. Tedah, F. Maculewicz, D. E. Wolf, and R. Schmechel, J. Phys. D: Appl. Phys. **52**, 275501 (2019).
[4]B. Zhao, K. Chen, S. Buddhiraju, G. Bhatt, M. Lipson, and S. Fan, Nano Energy **41**, 344 (2017).
[5]A. Fiorino, L. Zhu, D. Thompson, R. Mittapally, P. Reddy, and E. Meyhofer, Nat. Nanotechnol. **13**, 806 (2018).
[6]G. R. Bhatt, B. Zhao, S. Roberts, I. Datta, A. Mohanty, T. Lin, J. M. Hartmann, R. St-Gelais, S. Fan, and M. Lipson, Nat. Commun. **11**, 2545 (2020).
[7]T. Inoue, T. Koyama, D. D. Kang, K. Ikeda, T. Asano, and S. Noda, Nano Lett. **19**, 3948 (2019).
[8]R. Mittapally, B. Lee, L. Zhu, A. Reihani, J. W. Lim, D. Fan, S. R. Forrest, P. Reddy, and E. Meyhofer, Nat. Commun. **12**, 4364 (2021).
[9]C. Lucchesi, D. Cakiroglu, J. P. Perez, T. Taliercio, E. Tournié, P. O. Chapuis, and R. Vaillon, Nano Lett. **21**, 4524 (2021).
[10]W. Shen, J. Xiao, Y. Wang, S. Su, J. Guo, and J. Chen, J. Appl. Phys. **128**, 035105 (2020).
[11]M. D. Whale and E. G. Cravalho, IEEE Trans. Energy Convers. **17**, 130 (2002).
[12]J. I. Watjen, X. L. Liu, B. Zhao, and Z. M. Zhang, J. Heat Transfer **139**, 052704 (2017).
[13]M. Laroche, R. Carminati, and J. J. Greffet, J. Appl. Phys. **100**, 063704 (2006).
[14]K. Park, S. Basu, W. P. King, and Z. M. Zhang, J. Quant. Spectrosc. Radiat. Transfer **109**, 305 (2008).
[15]Q. Cai, P. Chen, S. Cao, Q. Ye, and X. Wu, Int. J. Thermophys. **41**, 161 (2020).
[16]T. Inoue, T. Suzuki, K. Ikeda, T. Asano, and S. Noda, Opt. Express **29**, 11133 (2021).
[17]R. Wang, J. Lu, and J. H. Jiang, Chin. Phys. Lett. **38**, 024201 (2021).
[18]J. Song, M. Lim, S. S. Lee, and B. J. Lee, Phys. Rev. Appl. **11**, 44040 (2019).
[19]T. Inoue, K. Watanabe, T. Asano, and S. Noda, Opt. Express **26**, A192 (2018).
[20]B. Wang, C. Lin, and K. H. Teo, J. Photonics Energy **7**, 044501 (2017).
[21]H. Yu, D. Liu, Y. Duan, and Z. Yang, J. Quant. Spectrosc. Radiat. Transfer **217**, 235 (2018).
[22]A. Karalis and J. D. Joannopoulos, Sci. Rep. **6**, 22270 (2016).
[23]G. T. Papadakis, S. Buddhiraju, Z. Zhao, B. Zhao, and S. Fan, Nano Lett. **20**, 1654 (2020).
[24]T. Liao, X. Zhang, X. Chen, and J. Chen, J. Appl. Phys. **125**, 203103 (2019).
[25]T. Liao, Z. Yang, W. Peng, X. Chen, and J. Chen, Energy Convers. Manag. **152**, 214 (2017).
[26]B. Zhao, P. Santhanam, K. Chen, S. Buddhiraju, and S. Fan, Nano Lett. **18**, 5224 (2018).
[27]M. M. Wilkins and K. Hinzer, *Handbook of Optoelectronic Device Modeling and Simulation* (CRC Press, 2017).
[28]M. Wilkins, C. E. Valdivia, and A. M. Gabr, J. Appl. Phys. **118**, 143102 (2015).
[29]C.-K. Li and Y.-R. Wu, IEEE Trans. Electron Devices **59**, 2 (2012).
[30]E. M. Tonita, C. E. Valdivia, M. Martinez-Szewczyk, M. R. Lewis, M. I. Bertoni, and K. Hinzer, Sol. Energy Mater. Sol. Cells **230**, 111293 (2021).
[31]D. Milovich, J. Villa, E. Antolin, A. Datas, A. Marti, R. Vaillon, and M. Francoeur, J. Photonics Energy **10**, 025503 (2020).
[32]A. Datas and R. Vaillon, Appl. Phys. Lett. **114**, 133501 (2019).
[33]M. Lim, J. Song, J. Kim, S. S. Lee, I. Lee, and B. J. Lee, J. Quant. Spectrosc. Radiat. Transfer **210**, 35 (2018).
[34]R. Vaillon, J.-P. Pérez, C. Lucchesi, D. Cakiroglu, P.-O. Chapuis, T. Taliercio, and E. Tournié, Opt. Express **27**, A11 (2019).
[35]J. Legendre and P. O. Chapuis, Sol. Energy Mater. Sol. Cells **238**, 111594 (2022).
[36]E. Blandre, P.-O. Chapuis, and R. Vaillon, Sci. Rep. **7**, 15860 (2017).
[37]D. Feng, E. J. Tervo, D. Vasileska, S. K. Yee, A. Rohatgi, and Z. M. Zhang, J. Appl. Phys. **129**, 213101 (2021).
[38]D. Feng, S. K. Yee, and Z. M. Zhang, Sol. Energy Mater. Sol. Cells **237**, 111562 (2022).
[39]W. A. Callahan, D. Feng, Z. M. Zhang, E. S. Toberer, A. J. Ferguson, and E. J. Tervo, Phys. Rev. Appl. **15**, 54035 (2021).
[40]Q. Lu, X. Zhou, A. Krysa, A. Marshall, P. Carrington, C. H. Tan, and A. Krier, Sol. Energy Mater. Sol. Cells **179**, 334 (2018).
[41]A. Krier, M. Yin, A. Marshall, and S. E. Krier, J. Electron. Mater. **45**, 2826 (2016).
[42]A. Krier, M. Yin, A. R. J. Marshall, M. Kesaria, S. E. Krier, S. McDougall, W. Meredith, A. D. Johnson, J. Inskip, and A. Scholes, Infrared Phys. Technol. **73**, 126 (2015).
[43]B. A. Matveev, V. I. Ratushnyi, and A. Y. Rybal'chenko, Tech. Phys. **64**, 1164 (2019).
[44]V. A. Gevorkyan, V. M. Aroutiounian, K. M. Gambaryan, I. A. Andreev, L. V. Golubev, and Y. P. Yakovlev, Tech. Phys. Lett. **34**, 69 (2008).
[45]E. V. Kunitsyna, I. A. Andreev, V. V. Sherstnev, T. V. L'Vova, M. P. Mikhailova, Yu. P. Yakovlev, M. Ahmetoglu, G. Kaynak, and O. Gurler, Opt. Mater. (Amst.) **32**, 1573–1577 (2010).
[46]V. P. Khvostikov, L. S. Lunin, V. V. Kuznetsov, V. I. Ratushny, V. Oliva, O. A. Khvostikova, and M. Z. Shvarts, Tech. Phys. Lett. **29**, 851 (2003).
[47]S. Adachi, *Handbook on Physical Properties of Semiconductors*, 1st ed. (Springer, New York, 2017).
[48]A. Baraskar, V. Jain, M. A. Wistey, U. Singisetti, Y. J. Lee, B. Thibeault, A. Gossard, and M. J. W. Rodwell, in *International Conference on Indium Phosphide and Related Materials* (IPRM, 2010),p. 481.
[49]A. Katz, S. N. G. Chu, and B. E. Weir, J. Vac. Sci. Technol. B **8**, 1125 (1990).
[50]W. Lu, B. R. Bennett, J. B. Boos, and J. A. Del Alamo, Electron. Lett. **36**, 546 (2000).

© Author(s) 2022

[51]M. T. H. Reid, A. W. Rodriguez, and S. G. Johnson, Proc. IEEE **101**, 531 (2013).
[52]S. Molesky and S. Lu, "heatSlabs" (2020). https://Github.Com/SeanMolesky/HeatSlabs
[53]A. Rogalski and Z. Orman, Infrared Phys. **25**, 551 (1985).
[54]S. Marchetti, M. Martinelli, and R. Simili, J. Phys: Condens. Matter **14**, 3653 (2002).
[55]G. A. Sukach, A. B. Bogoslovskaya, P. F. Oleksenko, Y. Y. Bilynets, and V. N. Kabacij, Infrared Phys. Technol. **41**, 299 (2000).
[56]A. Raymond, J. L. Robert, and C. Bernard, J. Phys. C **12**, 2289 (1979).
[57]M. Grigoryev, E. Ivanov, and K. Moiseev, Semiconductors **45**, 1334 (2011).
[58]R. St-Gelais, L. Zhu, S. Fan, and M. Lipson, Nat. Nanotechnol. **11**, 515 (2016).
[59]*Sentaurus TCAD User's Manual* (Synopsys, Inc., 2021).
[60]I. A. Andreev, O. Y. Serebrennikova, N. D. Il'inskaya, A. A. Pivovarova, G. G. Konovalov, E. V. Kunitsyna, V. V. Sherstnev, and Y. P. Yakovlev, Semiconductors **49**, 1671 (2015).
[61]E. Tournie, J. L. Lazzari, H. Mani, F. Pitard, C. L. Alibert, and A. F. Joullie, Proc. SPIE **1361**, 641 (1991).
[62]I. Vurgaftman, J. R. Meyer, and L. R. Ram-Mohan, J. Appl. Phys. **89**, 5815 (2001).
[63]D. Fan, T. Burger, S. McSherry, B. Lee, A. Lenert, and S. R. Forrest, Nature **586**, 237 (2020).

© Author(s) 2022

Efficiency-optimized near-field thermophotovoltaics using InAs and InAsSbP: Supplementary Material

1. Carrier Mobility

Both the optical and electrical models need accurate doping-dependent carrier mobilities for InAs and InAsSbP, therefore we employ the low-field doping-dependent mobility model at room temperature:[1]

$$\mu(N) = \mu_{\min} + \frac{\mu_{\max} - \mu_{\min}}{1 + \left(\frac{N}{N_{\text{ref}}}\right)^{\lambda_\mu}} \tag{S1}$$

where $\mu_{\min}$, $\mu_{\max}$, N_{ref}, and λ_μ are positive fitting parameters. To calculate the carrier mobilities of InAsSbP, we interpolate parameters between binaries, applying Matthiessen's Rule to interpolate $\mu_{\min}$ and $\mu_{\max}$, and linear interpolation for N_{ref} and λ_μ. We employ fitting parameter values from Refs. 1,2 to describe both carrier mobilities for InSb and InP, and the hole mobility of InAs. For the electron mobility of InAs, we fit Eq. (*S1*) to experimental data from Refs. 3–8 to calculate its fitting parameters, shown in Fig. S1. For comparison, we also include the curve calculated using parameters proposed by Sotoodeh et al.[1], showing their proposed parameters are inappropriate for doping concentrations higher than ~1×10^{17} cm^{-3}. We provide our best fit values in Table S1, and compare to values from Sotoodeh et al.[1].

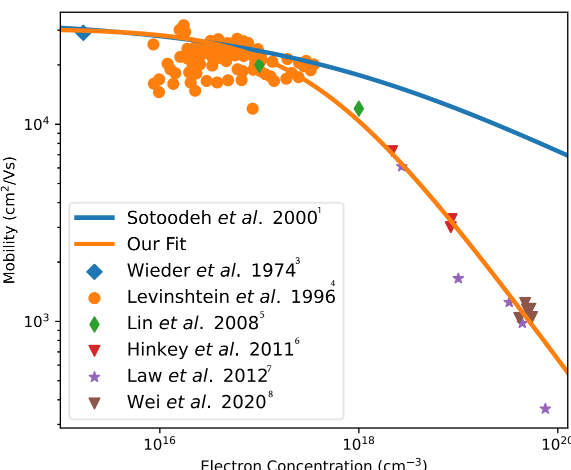

Figure S1. InAs electron mobility data as a function of electron concentration, together with the model fitting obtained by Sotoodeh et al.[1] and by this work. The experimental data are taken from Refs. 3–8.

Table S1. Parameters to describe electron mobility of InAs. We compare the parameters from our fit to parameters from Sotoodeh et al.[1]

Parameters	Units	Sotoodeh et al.[1]	Our Fit
$\boldsymbol{\mu_{\min}}$	cm^2/Vs	1000	0.3
$\boldsymbol{\mu_{\max}}$	cm^2/Vs	34000	30600
$\boldsymbol{N_{\text{ref}}}$	cm^{-3}	1.1×10^{18}	3.6×10^{17}
$\boldsymbol{\lambda_\mu}$		0.32	0.68

2. Cell temperature calculations

We assume the TPV cells are kept uniformly at 300 K. To verify this assumption, we can estimate the temperature gradient of our nip-Q design using Fourier's Law for heat conduction[9]:

$$q = -\frac{\kappa \Delta T}{L} \tag{S2}$$

where κ is the room-temperature thermal conductivity (0.3 W cm^{-1} K^{-1} for bulk InAs),[10] L is the layer thickness, and ΔT is the temperature gradient between both ends of L. Figure Figure **S2** depicts the temperature (relative to 300 K) through the cell for the optimized nip-Q design, illuminated by a 900 K radiator and a 10 nm radiator-cell gap. We find a maximum temperature difference of ΔT ~ 0.005 K which has negligible effects on our optoelectronic model. This agrees with a previous study[11] of a similar NFTPV system: a thin film $In_{0.53}Ga_{0.47}As$ cell bonded with Parylene-C on a Silicon wafer handle, and illuminated by a 1270 K Si radiator. They calculated a maximum temperature gradient of ΔT ~ 1.5 K for their system. Their temperature gradient is much higher than our value, albeit still negligible, and is due to the low thermal conductivity of the Parylene-C layer.

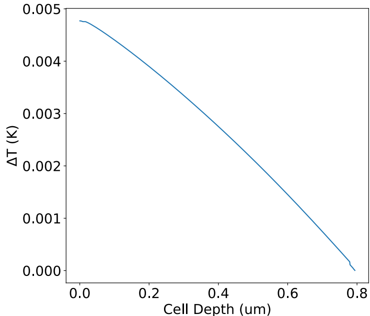

Figure S2. Depth resolved temperature, relative to 300 K, of the nip-Q cell illuminated by a 900 K radiator and a 10 nm radiator-cell gap.

3. Optical model details

The model incorporates dielectric functions of all materials for photon energies from 0.01−1 eV; heat transfer is negligible outside this range for this system. We use the temperature and doping dependent dielectric function model proposed by Fu and Zhang[12] for the Si radiator, however we replace their free-carrier concentration model with the model proposed by Basu et al.[13] We use the temperature-dependent bandgap model of Si from Ref. 14. The dielectric function described in Ref. 15 is applied to the gold back-reflector. To model the optical properties of InAs and InAsSbP, we consider interband, lattice, and free carrierd processes. To model the frequency (ω) dependent optical properties of InAs and InAsSbP, we employ the Drude-Lorentz model:[16,17]

$$\epsilon(\omega) = \epsilon_{IB}(\omega) + \epsilon_\infty \left(\sum_j \frac{S_j(\omega_{LO,j}^2 - \omega_{TO,j}^2)}{\omega_{TO,j}^2 - \omega^2 - i\omega\gamma_j} - \frac{\omega_p^2}{\omega(\omega + i\Gamma)} \right) \tag{S3}$$

where

$$\omega_\mathrm{p}^2 = \frac{N_q e^2}{\epsilon_0 \epsilon_\infty m_q^*} \quad , \quad \Gamma = \frac{e^2}{m_q^* \mu_q} \qquad q = \mathrm{e,h} \tag{S4}$$

where e is the elementary charge, ϵ_0 is the vacuum permittivity, ϵ_∞ is the high-frequency permittivity, m_e^* and m_h^* are the electron and hole effective masses, respectively, μ_e and μ_h are the electron and hole mobilities, respectively, N_e and N_h are the concentrations of free electrons and holes (assuming fully ionized dopants), respectively, S_j is the anion atom fraction, $\omega_{\mathrm{LO},j}$ and $\omega_{\mathrm{TO},j}$ are the longitudinal and transverse optical phonon frequencies, respectively, and γ_j is the damping constant due to phonons of the jth lattice oscillator (binary constituent). We calculate the interband contribution (ϵ_IB) following the method from Ref. 17 with some parameters from Ref. 18, however instead of calculating the refractive index with Kramers-Kronig relations as was done in Ref. 17, we assume $n_\mathrm{IB} = \sqrt{\epsilon_\infty}$ to improve computational speed by approximately a factor of 13 by avoiding integrals when evaluating the dielectric function. We investigated the impact of this approximation, finding that our method underestimates the total power

transfer by approximately 1.5% compared to using the Kramers-Kronig relations for the optimized nip-Q design separated by 0.1 μm from a 750 K radiator.

With donor doping of the quaternary InAsSbP of 1×10^{20} cm^{-3}, the Fermi level goes about 0.1 eV into the conduction band for all stoichiometric compositions of InAsSbP lattice matched to InAs. Nonparabolic corrections to the band structure then become important as well as increasing the apparent electron effective mass when describing optical properties.[19] We therefore model a doping-dependent electron effective mass ($m^*_{\mathrm{e,InAsSbP}}(N_\mathrm{e})$) by assuming it has the same dependence on electron concentration N_e as is observed in InAs. We find the effective mass by interpolating the effective masses of the binary compounds given in Table S2 ($m^*_{\mathrm{e,InAsSbP}}(0)$) and add the difference between the electron effective masses of InAs from Ref. 19 ($m^*_{\mathrm{e,InAs}}(N)$) and Table S2 ($m^*_{\mathrm{e,InAs}}(0)$):

$$m^*_{\mathrm{e,InAsSbP}}(N_\mathrm{e}) = m^*_{\mathrm{e,InAsSbP}}(0) + \left(m^*_{\mathrm{e,InAs}}(N_\mathrm{e}) - m^*_{\mathrm{e,InAs}}(0)\right) \tag{S5}$$

All other parameters employed in the optical model are given in Table S2. See Section 1 for further details on the carrier mobility model.

Table S2. Parameters to describe optical properties of InAs and InAsSbP, with references. $\boldsymbol{m_0}$ is the free-electron mass.

Parameters	Units	InAs	InSb	InP	Ref
$\boldsymbol{\epsilon_\infty}$		11.6	15.3	9.9	20
$\boldsymbol{m^*_\mathrm{e}}$	m_0	0.024	0.013	0.079	9
$\boldsymbol{m^*_\mathrm{h}}$	m_0	0.36	0.38	0.72	9
$\boldsymbol{\gamma_j}$	10^{11} rad/s	9.23	5.41	3.58	16
$\boldsymbol{\omega_{\mathrm{LO},j}}$	10^{13} rad/s	4.55	3.59	6.52	9
$\boldsymbol{\omega_{\mathrm{TO},j}}$	10^{13} rad/s	4.14	3.38	5.74	9

4. Optical model validation

We validated the predictions of our custom optical model by reproducing the independently calculated spectral absorption of the InGaAs/InP device structure from Mittapally et al.[11] under a 1270 K radiator. Figure S3 compares their results (dashed line) to our simulations (stack plot) for three radiator-TPV gaps, showing only minor discrepancies which are due to slight differences between dielectric functions employed. We calculate at most a 5% relative difference for both above and below bandgap power transfer compared to Ref. 11 (see Table S3). Note, for the 100 nm gap configuration, spectral data from Ref. 11 is cut-off at 30 W cm^{-2} eV^{-1} below 0.07 eV, therefore the sub bandgap power transfer within Table S3 is integrated down to 0.07 eV instead of 0 eV.

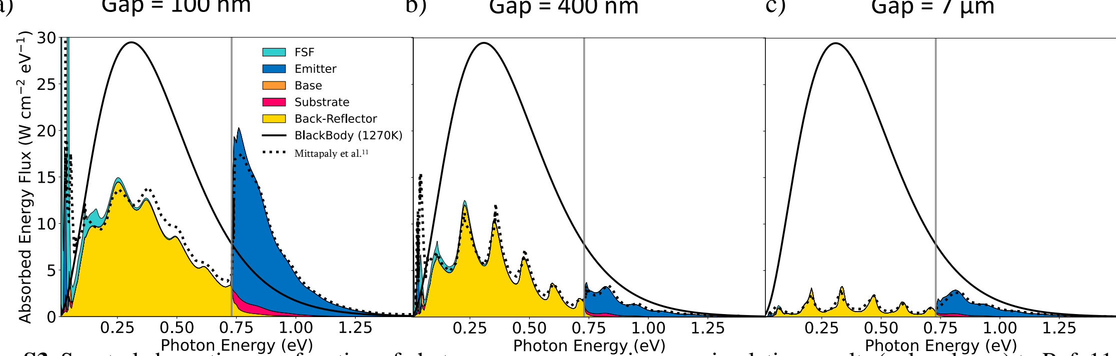

Figure S3. Spectral absorption as a function of photon energy, comparing our simulation results (colored area) to Ref. 11 (dashed line). We include an equivalent blackbody spectrum for scale (solid line). The bandgap of the absorber layer is given by the solid gray line. The three plots represent different radiator-TPV gaps: (a) 0.1 μm, (b) 0.4 μm, and (c) 7 μm.

Table S3. Comparing calculated above bandgap and sub bandgap power transfer from our simulations to results from Mittapally et al.[11]

Power Transfer (W cm^{-2})		100 nm	400 nm	7 µm
Above bandgap	This work	3.8	0.69	0.61
	Mittapally et al. [11]	4.0	0.66	0.60
Sub bandgap	This work	5.9	3.7	0.67
	Mittapally et al. [11]	6.1	3.7	0.70

5. Surface recombination model

As surface recombination velocity can be highly dependent on doping concentration,[21] we model the doping-dependent surface recombination velocity (S in cm/s) for the vacuum/FSF interface with the empirical function:

$$\log_{10}(S) = \frac{1}{\exp\left(\left(a - \log_{10}(N_q)\right)b\right) + c}, \quad q = \mathrm{D}, \mathrm{A} \tag{S6}$$

where a, b, and c are fitting parameters, N_D and N_A are the donor and acceptor doping concentrations in cm^{-3}, respectively. Figure S4 shows our fit of Eq. (S6) to measured data from Refs. 22,23 and an extracted value from Table S4 of Lu et al.[24], yielding $a = 14.5$, $b = 2.4$, and $c = 0.19$. We apply identical values for both n- and p-type doping and for all Sb- and/or P- compositions of InAsSbP.

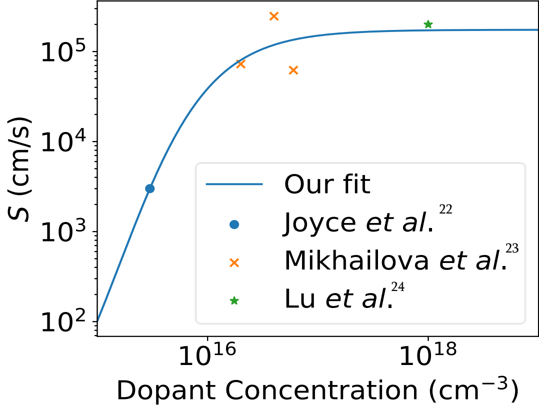

Figure S4. InAs surface recombination velocity as a function of doping concentration, together with the model fitting obtained by this work. The experimental data are taken from Refs. 22,23 as well as from our best fit to the TPV cell from Lu et al.[24]

6. Electrical model validation

To validate the electrical model, we compare measured and simulated dark current-voltage curves of devices from Refs. 24,25. Figure S5(a) shows the simulation structure for the device from Lu et al.[24], which we simulate as a 3D cylindrical device. We assumed the substrate thickness and doping to be 500 µm and 2×10^{18} cm^{-3}, respectively, and extracted the contact width (20 µm) from Figure 1 within the article. Figure S5(c) shows the simulation structure for the device from Krier et al.[25]. We assumed the substrate thickness to be 500 µm. We extracted the contact width (20 µm) and distance between contacts (75 µm) from Figure 2 within the article. The remaining parameters for both devices were taken from the text of the articles.

The fits to data from Ref. 24 and Ref. 25 are shown in Fig. Figure **S5**(b) and Fig. Figure **S5**(d), respectively. In our simulations, we added a resistor in series with the TPV cells to account for resistive losses arising from the electrode sheet and contact resistances. We allow the SRH recombination lifetime of InAs, the surface recombination velocity at the TPV cell surface, and the resistance of the resistor in series to vary to obtain a good fit. For the device from Krier et al.[25], we also included the Hurkx trap-assisted tunneling model to improve the fit at reverse bias. The model simulates field-dependent trap-assisted tunneling and requires a single extra parameter, a tunneling mass. As shown in Figure S5(d), the Hurkx model does not affect the properties of the current-voltage curve under forward bias and therefore does not affect the results in this manuscript. Results of the fits are shown in Table S4.

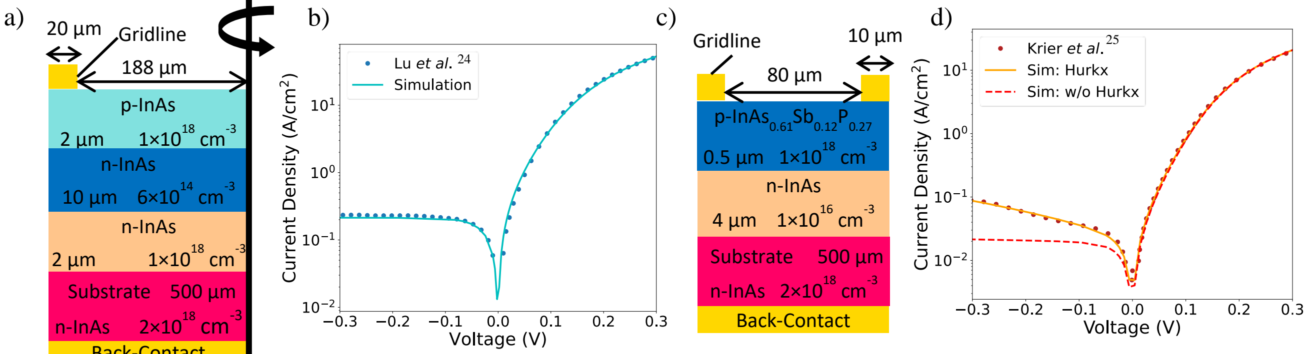

Figure S5. (a,c) Simulated device structure, and (b,d) dark current density as a function voltage plots, comparing our simulations to measurements for devices from Lu et al.[24] and Krier et al.[25], respectively. We assume TPV cell temperatures of 300 K.

Table S4. Parameter values after our fit to measured dark current-voltage data.

Parameters	Units	Lu et al.[24]	Krier et al.[25]
SRH lifetime	s	3.7×10^{-7}	2.7×10^{-7}
Series resistance	Ω	1.6	1.06
Surface recombination velocity	cm/s	2×10^{5}	2×10^{5}
Hurkx tunneling mass	m_0	-	7.5×10^{-4}

7. Cap and BSF Parameter Impact on Performance

We fixed the Cap and BSF layer thicknesses and doping during our optimization to help with computation time. To verify the robustness of our optimization results, we explore the impact of these parameters on the optimized nip-Q design, in Figure S6, for a 750 K radiator and $d_{R\text{-}FSF} = 0.1$ µm. In general, the device efficiency is maximized with highly doped Cap and BSF layers as they maximize the built-in electric field. For the cap layer (Figure S6(a)), we calculate maximized efficiency if doping concentration is above 3×10^{18} cm^{-3}, irrespective of layer thickness. Conversely, device efficiency is strongly affected by the BSF layer thickness, see Figure S6(b). We require a thickness less than 0.08 µm to stay within 1% absolute of the maximal efficiency, due to higher sub-bandgap photon absorption for thicker layers.

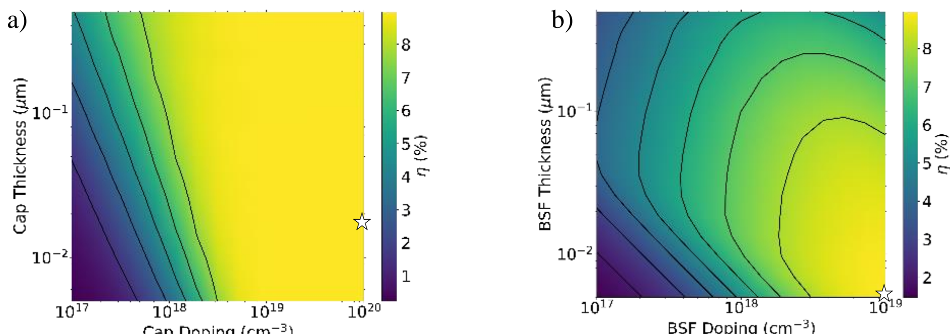

Figure S6. Device efficiency for a 750 K radiator and $d_{R\text{-}FSF}$= 0.1 µm for the optimized nip-Q device, as a function of layer thickness and doping for the (a) Cap layer and (b) BSF layer. Stars depict parameters used for device optimization of the nip-Q design.

References

[1] M. Sotoodeh, A.H. Khalid, and A.A. Rezazadeh, J. Appl. Phys. **87**, 2890 (2000).

[2] X. Peng, B. Zhang, G. Li, J. Zou, Z. Zhu, Z. Cai, S. Zhou, Y. Li, Z. Wang, and W. Jiang, Infrared Phys. Technol. **54**, 454 (2011).

[3] H.H. Wieder, Appl. Phys. Lett **25**, 206 (1974).

[4] M. Levinshtein, S. Rumyantsev, and M. Shur, *Handbook Series on Semiconductor Parameters, Vol. 1* (1996).

[5] Y. Lin, A.R. Arehart, and A.M. Carlin, Appl. Phys. Lett **93**, 62109 (2008).

[6] R.T. Hinkey, Z. Tian, and R.Q. Yang, J. Appl. Phys **110**, 43113 (2011).

[7] S. Law, D.C. Adams, A.M. Taylor, and D. Wasserman, (2012).

[8] D. Wei, S. Maddox, P. Sohr, S. Bank, S. Bank, S. Law, and S. Law, Opt. Mater. Express, Vol. 10, Issue 2, Pp. 302-311 **10**, 302 (2020).

[9] S. Adachi, *Properties of Semiconductor Alloys: Group-IV, III-V and II-VI Semiconductors* (John Wiley & Sons, LTD., 2009).

[10] M.Y. Swinkels, M.R. Van Delft, D.S. Oliveira, A. Cavalli, I. Zardo, R.W. Van Der Heijden, and A.M. Bakkers, (2015).

[11] R. Mittapally, B. Lee, L. Zhu, A. Reihani, J.W. Lim, D. Fan, S.R. Forrest, P. Reddy, and E. Meyhofer, Nat. Commun. 2021 121 **12**, 1 (2021).

[12] C.J. Fu and Z.M. Zhang, Int. J. Heat Mass Transf. **49**, 1703 (2006).

[13] S. Basu, B.J. Lee, and Z.M. Zhang, J. Heat Transfer **132**, 1 (2010).

[14] V. Alex, S. Finkbeiner, and J. Weber, J. Appl. Phys. **79**, 6943 (1996).

[15] A. Derkachova, K. Kolwas, and I. Demchenko, Plasmonics **11**, 941 (2016).

[16] S. Adachi, *Optical Properties of Crystalline and Amorphous Semiconductors: Materials and Fundamental Principles* (Kluwer Academic Publishers, 1999).

[17] D. Milovich, J. Villa, E. Antolin, A. Datas, A. Marti, R. Vaillon, and M. Francoeur, J. Photonics Energy **10**, 025503 (2020).

[18] I. Vurgaftman, J.R. Meyer, and L.R. Ram-Mohan, J. Appl. Phys. **89**, 5815 (2001).

[19] Y.B. Li, R.A. Stradling, T. Knight, J.R. Birch, R.H. Thomas, C.C. Phillips, and I.T. Ferguson, Semicond. Sci. Technol. **8**, 101 (1993).

[20] S. Adachi, *Properties of Group-IV, III-V and II-VI Semiconductors* (Wiley Blackwell, 2005).

[21] H. Ito and T. Ishibashi, Jpn. J. Appl. Phys. **33**, 88 (1994).

[22] H.J. Joyce, C.J. Docherty, Q. Gao, H.H. Tan, C. Jagadish, J. Lloyd-Hughes, L.M. Herz, and M.B. Johnston, Nanotechnology **24**, (2013).

[23] M.P. Mikhailova, D.N. Nasledov, and S. V. Slobodchikov, Phys. Status Solidi **11**, 529 (1965).

[24] Q. Lu, X. Zhou, A. Krysa, A. Marshall, P. Carrington, C.H. Tan, and A. Krier, Sol. Energy Mater. Sol. Cells **179**, 334 (2018).

[25] A. Krier, M. Yin, A.R.J.J. Marshall, and S.E. Krier, J. Electron. Mater. **45**, 2826 (2016).

4.2 Fabricated NFTPV devices

The following section describes my work on fabricating and characterizing NFTPV devices. It starts by detailing the fabrication of the devices and then ends with a manuscript submitted for publication.

4.2.1 Device design and epi-growth

We sought III-V epi-growers capable of growing our optimized epi-stack of n-InAsSbP/i-InAs/p-InAsSbP from Section 4.1, but encountered difficulties. None of the epi-growers we contacted had the necessary expertise in growing InAsSbP, meaning it would take considerable effort to grow the layers. Besides the growth issues, our fabrication expert advised that designs requiring the replacement of the substrate with a metal back-reflector would be challenging and time-consuming, and would probably not fit within my timeline.

Considering these constraints, I redesigned the NFTPV device using the model described in Section 4.1. I optimized the design assuming a highly-doped silicon radiator at 750 K and a 0.1 μm gap. The final design is shown in Fig. 4.1a, with performance metrics provided in Fig. 4.1b. To minimize parasitic sub-bandgap absorption in the substrate, the new design includes an n+-InAs sub-bandgap reflector layer (BR), which reflects most sub-bandgap photons, as shown in the spectral absorption distribution in Fig. 4.1c, compared to the design on substrate in Section 4.1. At 930 K, the new design is estimated to outperform the best NFTPV device in literature [5], with 44$\%_{\mathrm{rel}}$ higher efficiency at 2.16% and 20 times higher power output at 0.64 W/cm^2. Our device's much higher power output comes from our use of a lower bandgap absorber material of 0.36 eV instead of 0.75 eV, allowing more interband absorption from the incoming spectrum.

The NFTPV device design shown in Fig. 4.1a was grown by MBE at the University of Waterloo. An isotype design without the BR layer was also grown for use as a baseline and as practice for fabrication.

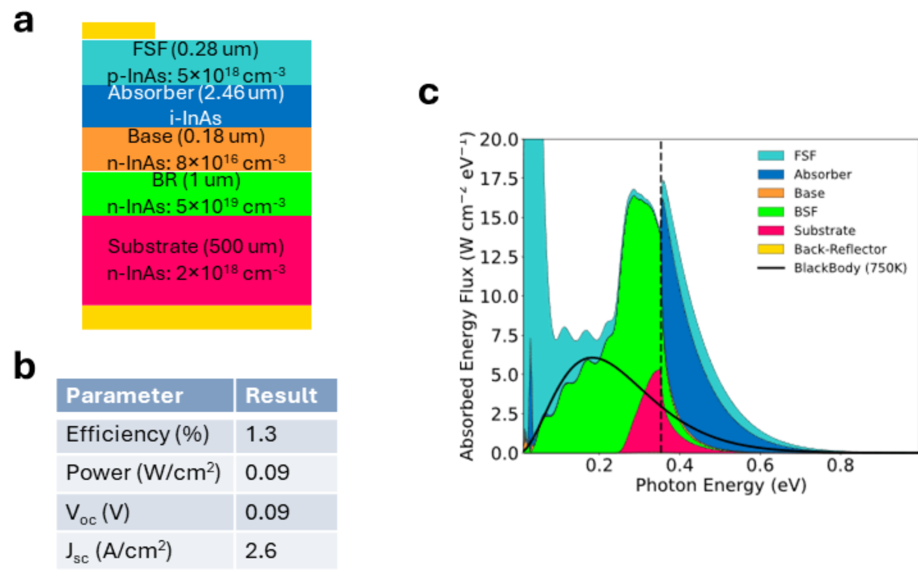

Parameter	Result
Efficiency (%)	1.3
Power (W/cm^2)	0.09
V_{oc} (V)	0.09
J_{sc} (A/cm^2)	2.6

Figure 4.1: Redesigned near-field thermophotovoltaic device to follow constraints for fabrication, designed for a highly doped Silicon radiator at 750 K and a 0.1 μm gap. **a** Schematic of the new design. **b** Simulated performance of the device. **c** Stack plot of the simulated spectral absorption within each layer.

4.2.2 Fabrication process

I fabricated NFTPV devices from the epigrown design shown in Fig. 4.1 using the University of Ottawa's Nanofab facilities, with assistance from SUNLAB's postdoc, Mathieu de Lafontaine. Mathieu created the necessary photolithography masks, trained me on all the tools, and provided continuous guidance. The fabrication process, outlined in Fig. 4.2, involves four main steps: epitaxy, back metallization, front metallization, and mesa etching.

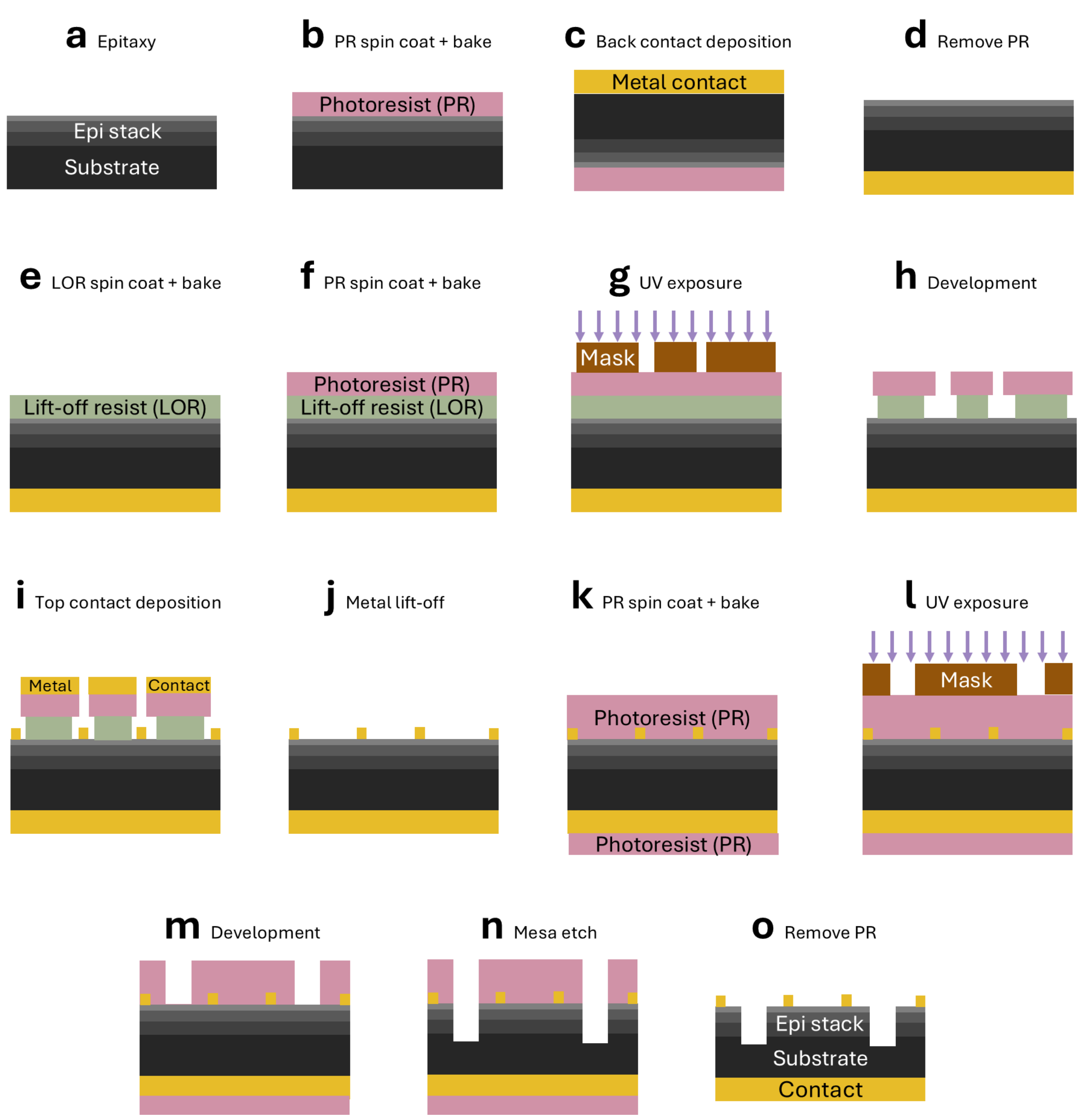

Figure 4.2: Fabrication process for the near-field thermophotovoltaic device.

For back-metallization on n-InAs, we first spin-coated SPR955 photoresist using a WS-650-23 Laurell Spin Processor at 6000 rpm and baked it on a hot plate at 90 °C for 5 min (Fig. 4.2b) to protect the epi-stack during back contact deposition. Before depositing the contacts, the samples were submerged in a deoxidizing NH_4F/HF solution for 30 s and then promptly loaded into an Angstrom Nexdep Series evaporator chamber to minimize the regrowth of the native oxide. The evaporator chamber was vacuum-pumped for about 4 h to reach a pressure below 3 μtorr. Then, Ni/Ge/Au layers with thicknesses 43/30/87 nm were deposited by electron-beam evaporation (Fig. 4.2c). After contact metallization, the photoresist was striped with Remover 1165 (Fig. 4.2d).

To deposit the front contact pattern on p-InAs, a lift-off resist and photoresist were deposited sequentially and developed to create an overhang to facilitate metal lift-off. LOR10B lift-off resist was spin-coated at 3000 rpm and baked at 170 °C for 5 min (Fig. 4.2e). Then, SPR955 photoresist was spin-coated at 6000 rpm, baked at 90 °C for 5 min (Fig. 4.2f), and cured by UV exposure with a dose of 95 mJ/cm^2 under a custom fabrication mask using a OAI Model 204IR Mask Aligner (Fig. 4.2g). The exposed photoresist and lift-off resist layers were removed using MF-24A developer for 60 s creating an undercut (Fig. 4.2h). Following lithography and development, the samples were deoxidized, and Ti/Pt/Au layers with thicknesses 25/30/50 nm were deposited by electron-beam evaporation (Fig. 4.2i). Finally, the resists were removed (Fig. 4.2j).

To etch the mesa structures, the front mesa pattern was developed by photolithography, and a protective resist was deposited on the backside. SPR955 was spun at 6000 rpm and baked at 100 °C for 90 s (Fig. 4.2k). After aligning the mask with the underlying metallic contacts, the photoresist was cured by UV exposure at a dose of 95 mJ/cm^2 (Fig. 4.2l) and then developed with MF-24A for 2 min (Fig. 4.2m). The prepared samples were submerged in a solution of citric acid:H_2O_2 at a volumetric ratio of 2:1 for 3.5 h while being mixed with a spinner set to 300 rpm (Fig. 4.2n). The citric acid solution consisted of a ratio of 200 ml of deionized water and 5 g of citric acid powder. Finally, the photoresist was stripped (Fig. 4.2o).

4.2.3 Ohmic contact deposition

Specialized metallic contacts were deposited on either side of the junction to provide low-series resistance contacts to the semiconductor. When depositing metals on semiconductors, the interface ideally behaves as an ohmic resistor with negligible resistance but can instead have diode characteristics due to the formation of a Schottky barrier. To achieve ohmic contacts, recipes from literature [81, 82] were deposited via evaporation without thermal annealing.

To verify that we achieved ohmic contacts, I measured the current-voltage properties of circular transfer length method (TLM) structures [83], a schematic of the structures is shown in Fig. 4.3a. These structures are composed of circular contact pads surrounded by another contact pad with an even gap between the two pads. The radius of each inner pad r_{pad} was 200 μm. For each ring, the IV characteristics were measured in the dark using a four-wire configuration with two probes on the inner circular pad and two probes on the outer pad. The curves followed Ohm's law, allowing us to extract the electrical resistance from linear fits between the collected current and the applied voltage. The total resistance R_{T} as a function of gap spacing d_{TLM} for the p-InAs contact is shown in Fig. 4.3b.

The total resistance is given by [83]:

$$R_{\mathrm{T}} = \frac{R_{\mathrm{sheet}}}{2\pi r_{\mathrm{pad}}}(d_{\mathrm{TLM}} + 2L_{\mathrm{T}})C_{\mathrm{TLM}} \tag{4.1}$$

and

$$C_{\mathrm{TLM}} = \frac{r_{\mathrm{pad}}}{d_{\mathrm{TLM}}} \ln\left(1 + \frac{d_{\mathrm{TLM}}}{r_{\mathrm{pad}}}\right) \tag{4.2}$$

where R_{sheet} is the sheet resistance of the semiconductor layer underneath the metal contact and L_{T} is the transfer length. From these values, we can calculate the contact resistivity as follows:

$$\rho_{\mathrm{c}} = R_{\mathrm{sheet}} L_{\mathrm{T}}^2 \tag{4.3}$$

The contact resistivity of the p-InAs contact was $(2 \pm 1)\mu\Omega\text{cm}^2$. The backside of the wafer was unpolished which made for faulty TLM measurements. However, as the back side is blanketed with metal, it has a higher tolerance for contact resistance compared to the front contacts.

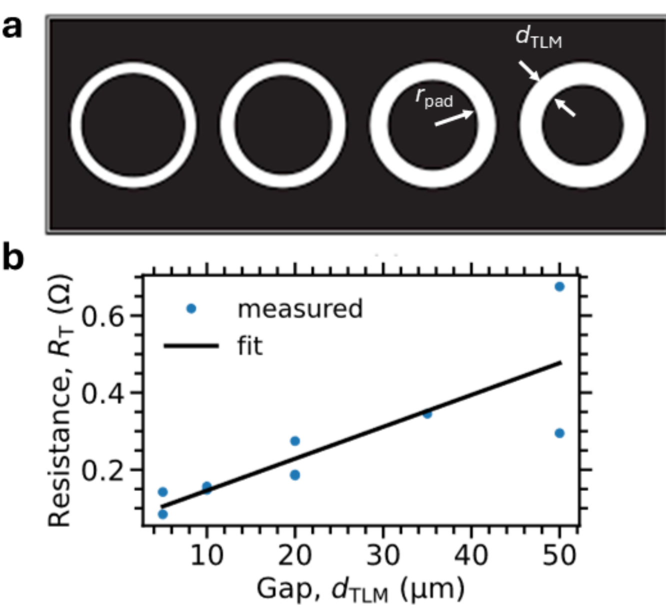

Figure 4.3: **a** Schematic diagram of circular transfer length method contact pads. **b** Sample transfer length method measurements for an ohmic contact to p-InAs compared to the fit to Eq. (4.1).

4.2.4 Mesa etching

The PV devices were formed from the wafer by wet etching mesas using a citric acid solution. Targeting a specific etch depth, I etched six practice InAs wafer samples without stirring the solution for different durations and measured the etch depth at three locations on each sample using a Bruker DektakXT profilometer. The results are shown in Fig. 4.4 as "No stirring". Aiming for slightly more than a 4 μm etch depth, I etched a larger sample for 215 min. Although the edges slightly exceeded the target depth, the center etched only 2.3 μm (see "Large sample"

in Fig. 4.4). Consequently, I conducted three new experiments, etching with the citric acid while stirring the solution with a magnetic stirrer at 300 rpm but for different durations to determine the etch rate of this new process (see "Stirring" in Fig. 4.4). With the etch rate determined while stirring, I fabricated devices on three samples named "G0953-1", "G0953-2", and "G0953-3". The etching results are shown in Fig. 4.4.

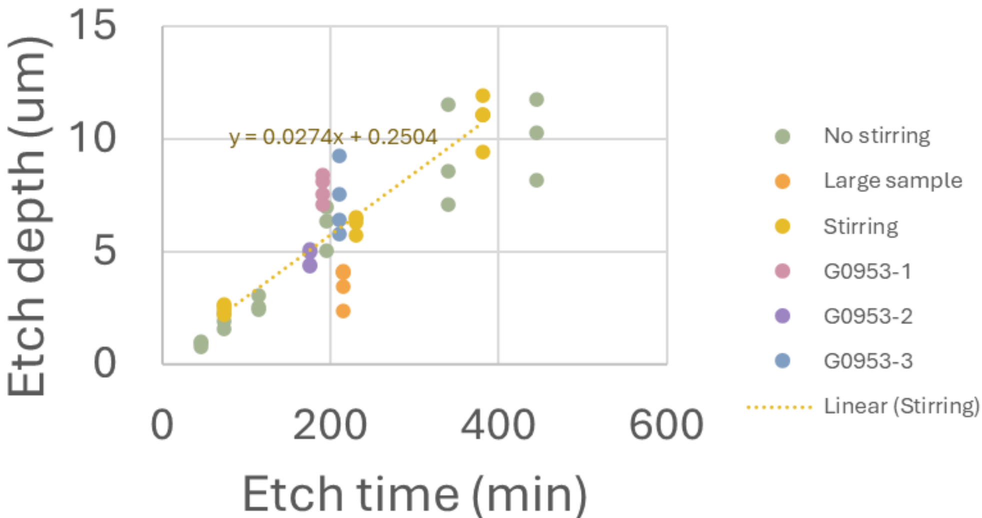

Figure 4.4: Measured etched depth as a function of etching time for InAs etched with a citric acid solution. "No stirring" and "Large sample" were both not stirred. The rest were etched with a stirred solution.

4.2.5 Manuscript

The following section is an unpublished manuscript that details my work designing, fabricating, and characterizing an InAs-based NFTPV device for waste-heat to electrical power conversion. I combine the near-field heat transfer model and the electrical model described in Sections 2.2.5 and 2.1 to design the device. This research aims to showcase a new sub-bandgap photon back reflector for use in thermophotovoltaics and NFTPV applications. In this manuscript, we aim to

maximize the spectral efficiency, which we define as the difference between the total blackbody radiated power and the absorbed sub-bandgap power, divided by the total blackbody power.

Impact

The manuscript has the following novelties:

1. Developed an InAs-based thermophotovoltaic device featuring an epitaxially grown broadband sub-bandgap reflector.
2. Calculated a $50\%_{\mathrm{rel}}$ increase in spectral efficiency for a 600 K blackbody spectrum for structures with a back reflector compared to those without it.
3. Determined that the epitaxially grown back reflector could double the spectral efficiency compared to not having the back reflector.
4. Validated a predictive electrical model, confirming that the new back reflector layer does not impact the electrical properties of the device.

Our results showcase a new epitaxially grown broadband sub-bandgap back reflector that enhances thermophotovoltaic and NFTPV device performance without adding complex fabrication steps. This innovative back reflector could also be applied to general InAs-based optoelectronic devices requiring sub-bandgap back reflectors, such as heat sensors.

Author contribution

Gavin P. Forcade: As the lead University of Ottawa-based graduate student associated with the project, I developed and validated the optoelectronic model, used it to design the devices, fabricated the devices, and characterized their optoelectronic properties. I am the lead author of the manuscript.

Dr. Mathieu de LaFontaine: As a postdoctoral researcher at the University of Ottawa, Mathieu trained me on all the fabrication tools, advised me throughout the fabrication process, designed the lithography masks, provided detailed feedback, and assisted in editing the manuscript.

Mathieu Giroux: As a uOttawa graduate student associated with the project, Mathieu expanded the optical model for free carrier absorption.

Dr. Alan Tam: As a postdoctoral researcher at the University of Waterloo, Alan epitaxially grew the devices.

Prof. Zbig Wasilewski: As a professor at the University of Waterloo, Zbig led the epitaxial growth of the devices.

Prof. Jacob J. Krich: As a professor at the University of Ottawa, Jacob helped to guide my research and provided detailed feedback during the analysis of my simulation results.

Prof. Raphael St-Gelais: As the principal investigator of the project and professor at the University of Ottawa, Raphael led the conceptualization of the project, helped to guide my research, and provided detailed feedback during the analysis of my simulation results.

Prof. Karin Hinzer: As the director of the University of Ottawa's SUNLAB research group, Karin oversaw my research, provided detailed feedback during the analysis of my simulation results, and assisted in editing the manuscript.

The submitted version of the manuscript:

> G.P. Forcade, M. de Lafontaine, M. Giroux, A. Tam, Z. Wasilewski, J.J. Krich, R. St-Gelais, and K. Hinzer, "Epi-grown broadband reflector for InA-based thermophotovoltaics", under review 2024.

Epi-grown broadband reflector for InAs-based thermophotovoltaics

Gavin P. Forcade[1,2], Mathieu de Lafontaine[1], Mathieu Giroux[3], Alan Tam[4,6], Zbig Wasilewski[4,5,6], Jacob J. Krich[1,2], Raphael St-Gelais[2,3], Karin Hinzer[1]

[1] SUNLAB, Nexus for Quantum Technologies Institute, University of Ottawa, Ottawa, K1N 6N8, Canada
[2] Department of Physics, University of Ottawa, Ottawa, K1N 6N8, Canada
[3] Department of Mechanical Engineering, University of Ottawa, Ottawa, K1N 6N8, Canada
[4] Department of Electrical and Computer Engineering, University of Waterloo, Waterloo, N2L 3G1, Canada
[5] Waterloo Institute for Nanotechnology, University of Waterloo, Waterloo, N2L 3G1, Canada
[6] Institute for Quantum Computing, University of Waterloo, Waterloo, N2L 3G1, Canada

Abstract: Reflecting sub-bandgap photons is crucial for maximizing the efficiency of thermophotovoltaic devices. However, existing metal-deposited reflectors rely on back-side metallization, which cannot be grown epitaxially, necessitating additional processing steps. In this study, we fabricate InAs-based thermophotovoltaic devices featuring a straightforward, epitaxially grown sub-bandgap reflector composed of a single layer of n-doped InAs at a doping concentration of 2.4×10^{19} cm^{-3}. This high doping produces long-wavelength metallic-like reflection, and our devices demonstrate high sub-bandgap reflectivity from 3.5-17 µm, achieving up to 93% reflectivity compared to 30-40% for designs without the reflector. Using a calibrated optical model, we predict that the sub-bandgap reflectivity of this layer enhances spectral efficiency from 38% to 79% under a 600 K normally incident blackbody spectrum. This improvement rivals that of a standard gold back reflector, which achieves a spectral efficiency of 94%. Additionally, our predictive electrical model, calibrated with fabricated devices, indicates that the reflective layer does not adversely affect the electrical properties of the thermophotovoltaic devices. This sub-bandgap reflector can be integrated into existing InAs-based thermophotovoltaic fabrication processes, eliminating complex substrate removal steps required for traditional gold reflectors.

1. Introduction

A significant amount of waste heat is released into the environment, with approximately 10% of primary energy lost at temperatures above 600 K [1]. This temperature corresponds to a limiting Carnot efficiency of at least 50% for a cold sink at room temperature, making it attractive for conversion into electrical power. Solid-state converters are most interesting for waste heat harvesting as they offer superior modularity compared to thermo-mechanical engines [2]. Among solid-state converters, thermophotovoltaics (TPV) and near-field thermophotovoltaics (NFTPV) exhibit some of the highest predicted efficiencies [2]. Their efficiencies are maximized with small absorber bandgaps to achieve sufficient power output densities, and by reflecting sub-bandgap radiation back to reheat the radiator [3]. InAs is an excellent absorber material for TPV and NFTPV technologies, particularly for 600-1100 K waste heat due to its ideal bandgap of 0.353 eV [4]. TPV and NFTPV devices with InAs absorber layers theoretically allow for efficiencies of up to 15% and 46% for 600 K and 1100 K radiator temperatures, respectively, when the devices are held at room temperature [5]. However, present room-temperature InAs-based devices [4], [6], [7], [8], [9], have only achieved efficiencies up to 0.5% for a radiator at 800 K for TPV [4] and 0.015% for a radiator at 655 K for NFTPV [8] technologies.

One of the main challenges in achieving high efficiencies for NFTPV and TPV systems is mitigating parasitic sub-bandgap photon absorption [2], [9], [10], [11], [12]. At temperatures above 600 K, photons with energy less than InAs's bandgap account for up to 92% of blackbody irradiance. Minimizing sub-bandgap photon absorption is crucial, as that absorption does not contribute to current production for the devices but

increases their internal temperature, negatively impacting performance [6], [9], or increasing cooling requirements. For instance, Selvidge et al. [9] reported a 60 K rise in internal temperature, relative to a cold sink, in an InAs-based NFTPV device illuminated by a 733 K radiator. This temperature increase, primarily due to sub-bandgap absorption, resulted in a fourfold reduction in power output.

Better spectral control can be accomplished by tuning the radiator emissivity or incorporating a selective filter between the radiator and the photovoltaic device, both can help to match the spectrum incident on the photovoltaic device to its spectral response [12]. Another spectral control approach replaces the photovoltaic device's substrate with a broadband back reflector, reflecting sub-bandgap photons to reheat the radiator. Promising back reflectors include planar metallic mirrors [11], the airbridge architecture [13], [14], and broadband Bragg reflectors [15]. However, these architectures add complexity to the fabrication process and may pose challenges for large-area NFTPV devices [9].

Epitaxially-grown back reflectors can offer simpler device processing. France et al. [16] epitaxially grew a Bragg reflector structure for a III-V solar cell achieving peak reflection of 98% but with a small bandwidth <100 nm. Instead, we consider a single layer of highly n-doped InAs as a broadband sub-bandgap reflector. This material has over 90% reflectivity for wavelengths longer than 5 µm [17], [18], [19], [20]. However, there has yet to be a study on integrating such a layer into TPV or NFTPV devices. In this study, we fabricate and characterize TPV devices and use these measurements to calibrate an optoelectronic model. We employ this model to understand the impact of the epi-grown back reflector on device performance and to develop optimal designs.

2. Experimental procedure

2.1 Device fabrication

Two InAs-based devices were grown by molecular beam epitaxy (MBE) on an n-type sulfur-doped InAs (100) substrate, with structures given in Fig. 1. The primary distinction between the structures lies in the exclusion (Design #1, Fig. 1a) and inclusion (Design #2, Fig. 1b) of a highly doped n-InAs sub-bandgap back reflector (BR) layer. The commercial company, Eurofins EAG laboratories, performed secondary ion mass spectrometry (SIMS) on the wafer with Design #2 grown to measure the doping concentrations as a function of the depth, the results are depicted in Fig. 1c and are compared to the values given in Fig. 1b. Metallic contacts were deposited by electron-beam evaporation without thermal annealing. Ni/Ge/Au layers with thicknesses of 43/30/87 nm were deposited to form back ohmic contacts [21]. Ti/Pt/Au with thicknesses 25/30/50 nm were deposited to form front ohmic contacts [22]. Square devices were defined by mesa

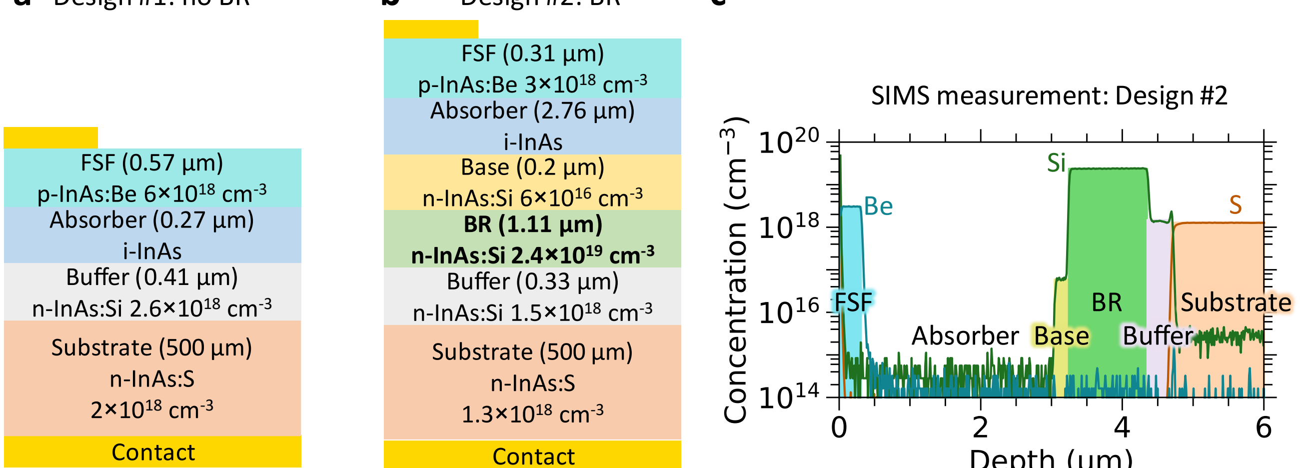

Fig. 1. Schematic diagram of the thermophotovoltaic devices (a) without a back reflector (BR) and (b) with a BR. The devices include a front surface field (FSF) layer. P-type doping was achieved with beryllium (Be), while n-type doping was achieved with silicon (Si) for epi-grown layers and sulfur (S) for the substrate. The absorber layer is nominally undoped. (c) Secondary ion mass spectrometry measuring the doping concentration as a function of the depth of the wafer with Design #2. The background colored regions indicate the structure given in (b).

etching, where masked samples were submerged into citric acid with hydrogen peroxide at a volumetric ratio of 2:1 for 3.5 h while being mixed with a spinner set to 300 rpm [23]. The citric acid solution consisted of 200 mL of deionized water with 5 g of citric acid powder, pre-stirred for at least one hour. No antireflection coating was applied.

2.2 Measurement methods

Two tools were used to measure the calibrated spectral reflectivity of both bare wafers near their centers. First, spectral reflectivity was measured with Bruker's INVENIO Fourier transform infrared (FTIR) instrument coupled with their HYPERION II microscope and their LN-MCT-D316-025 detector, spanning 0.07-0.98 eV. The data were cross-calibrated with spectral reflectivity measured with a calibrated Newport Oriel IQE 200 (QE) tool, spanning 0.78-0.98 eV. The QE tool measured reflectivity for normally incident light, whereas the FTIR tool used an apertured microscope with an approximate maximum incidence angle of 30°. Nevertheless, light incident at angles between 0° to 30° exhibit similar spectral reflectivity. The spectral reflectivity of the wafers was measured at room temperature (approximately 295 K) and is presented in Fig. 2. Further calibration details for the spectral reflectivity measurements are provided in Supporting Information. Measured and simulated reflectivity presented in this paper assume perpendicularly incident light, as the n-InAs BR layer behaves like a metal which has excellent angle-dependent reflectivity [18].

Current-voltage characteristics of the fabricated square devices were measured using a four-wire configuration with a Keithley 2420 source meter. The cells were vacuum-held on a temperature-controlled, gold-plated copper chuck, with the temperature maintained at 298 K by a thermoelectric controller.

2.3 Optoelectronic model

The optoelectronic properties of the devices were simulated within the commercial software Synopsys TCAD Sentaurus (version S-2021.06) assuming the devices were kept at 298 K. The spectral reflectivity of the epi-stacks were simulated with the transfer matrix method while the optical absorption used the model presented in ref. [11]. The electrical properties were simulated following the two-dimensional model from ref. [11] based on drift-diffusion theory. The optoelectronic properties of the materials followed that of ref. [11] unless otherwise stated. The Drude model, which is employed to simulate the impact of free carriers on the optical properties of InAs, was adjusted from that in ref. [11] to account for the overestimation of free carrier absorption [24]. Parameters differing from ref. [11] include static and high-frequency dielectric constants of 15.15 and 12.25 [25], respectively, a heavy-hole density of states effective mass of 0.6 [26], [27], and a heavy-hole conductivity effective mass of 0.46 [27].

3. Results and Discussion

3.1 Measured optical properties

Design #2, which includes a BR layer, demonstrates superior spectral control compared to Design #1, which lacks a BR layer. We measured the spectral reflectivity

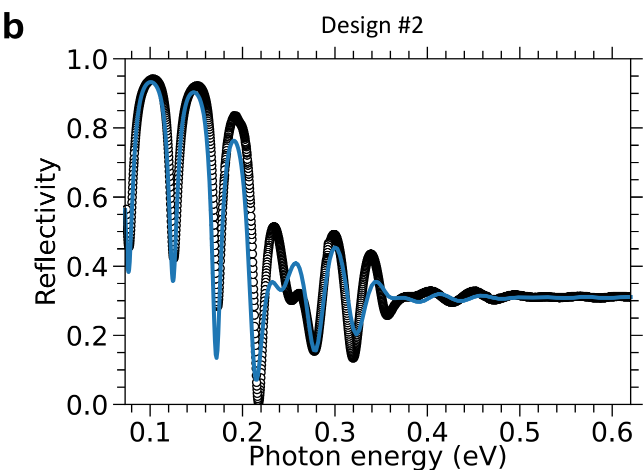

Fig. 2. Comparing measured to simulated spectral reflectivity of the wafers with epi-stacks following: (a) Design #1 without a BR and (b) Design #2 with a BR. The measured photon energy range corresponds to a wavelength range of 2-17 µm.

of the wafers with Design #1 in Fig. 2a and Design #2 in Fig. 2b. As expected, the design with a BR layer has a much higher sub-bandgap reflectivity at photon energies less than about 0.3 eV, reaching up to 93%, compared to the 30-40% reflectivity of the design without a BR layer.

Our optical model agrees with these reflectivity measurements. To validate the model, we leverage the low absorption of sub-bandgap photons, which generate interference patterns due to the doping-dependent optical properties of the layers. These patterns can be interpreted from spectral reflectivity data. For the model of Design #2, we used the layer thicknesses and doping values shown in Fig. 1b, extracted from SIMS, resulting in the solid curve in Fig. 2b. For Design #1, we extracted accurate layer thicknesses and doping concentrations by adjusting them to fit the simulated spectral reflectivity with the measurement. These values are provided in Fig. 1a, leading to the solid curve in Fig. 2a. Both simulations agree well with the measurements.

3.2 Predicted optical performance

We analyze the impact of the n-InAs BR layer's doping concentration (within an achievable range, reaching up to 10^{20} cm^{-3} [19]) and thickness on the spectral efficiency, assuming the SIMS measured device structure, and the far-field normally incident 600 K blackbody spectrum. Additionally, we compare their performance to a device with the n-InAs BR layer replaced with semi-infinitely thick gold. Here, the below bandgap spectral efficiency of the mirror (η_{spec}) is defined as:

$$\eta_{\mathrm{spec}} = \frac{P_{\mathrm{bb}}(T) - \int_{E_g}^{\infty} \mathrm{I_{bb}}(T,E)\big(1-\mathrm{R}(E)\big)\,dE}{P_{\mathrm{bb}}(T)} \quad (1)$$

where $P_{\mathrm{bb}}(T) = \int_0^{\infty} \mathrm{I_{bb}}(T,E)dE$ is the blackbody power density at temperature T, E_{g} is the absorber layer bandgap, $\mathrm{I_{bb}}$ is the blackbody spectrum, R is the spectral reflectivity over sub-bandgap photons, and E is the photon energy. The integral in Eq. 1 calculates the absorbed sub-bandgap irradiance, assuming all photons

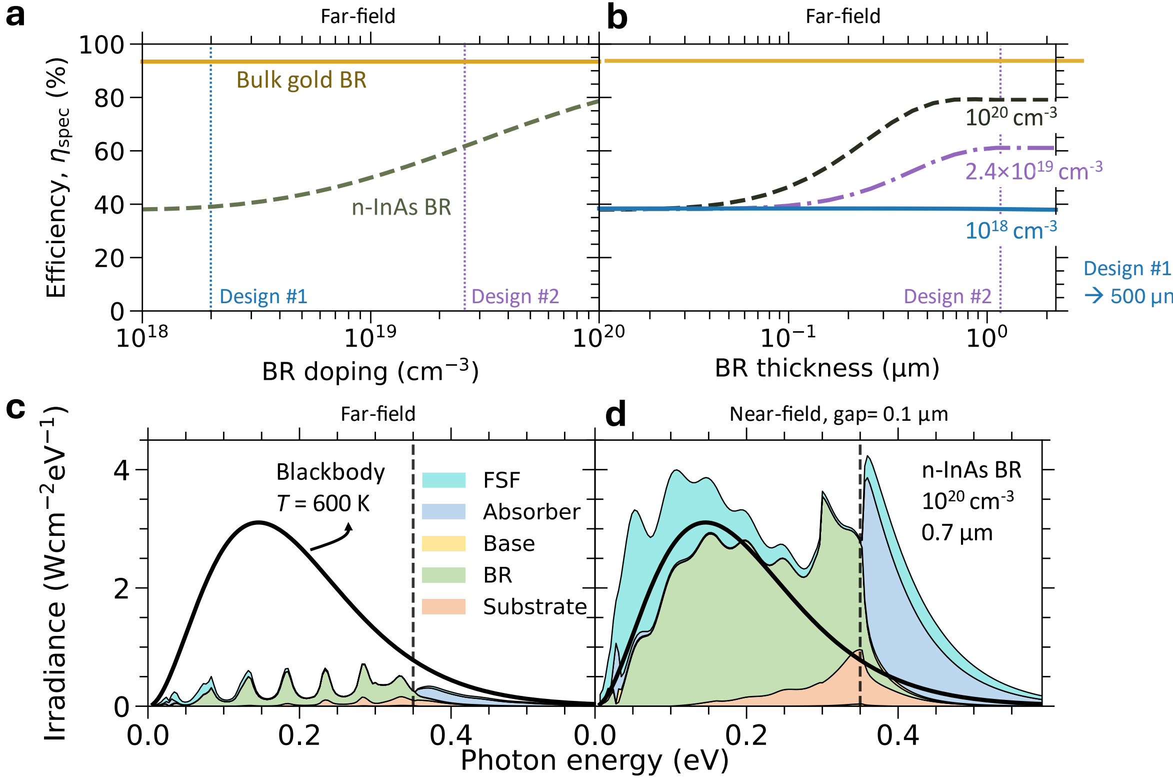

Fig. 3. Optical performance of the Design #2, which includes a back reflector (BR) layer, illuminated by a heat source at a temperature of 600 K. Spectral efficiency (Eq. 1) as a function of (a) the BR layer doping concentration and (b) the BR layer thickness, for a normally incident blackbody spectrum. A BR thickness of 1.11 µm was used in (a). Bulk gold BR represents a structure where the BR layer in Design #2 is replaced with gold. Spectral absorption distribution within the layers of the thermophotovoltaic device with a 0.7 µm thick n-InAs BR doped at 10^{20} cm^{-3}, illuminated by (c) a normally incident blackbody spectrum and (d) an undoped silicon radiator with a 0.1 µm gap between the radiator and TPV device. The black dashed vertical line indicates InAs's bandgap.

that enter the substrate are absorbed due to its high absorption coefficient from the (1-2)×10^{18} cm^{-3} doping concentration.

Higher n-InAs BR layer doping concentrations enhance spectral efficiency, as shown in Fig. 3a. A device without a BR layer (effectively a doping concentration of about 10^{18} cm^{-3}) achieves a spectral efficiency of 38%, attributed to the reflectivity from the sharp refractive index change at the air-InAs interface. Our wafer with Design #2 achieves a spectral efficiency of 63%. By maximizing the BR doping concentration to 10^{20} cm^{-3}, the spectral efficiency can more than double compared to a device without a BR layer and is only $19\%_{relative}$ lower than the spectral efficiency for a gold BR.

At high doping concentrations, the n-InAs BR can be made thinner. Fig. 3b illustrates the impact of BR layer thickness on the spectral efficiency for three doping concentrations: 10^{18} cm^{-3}, 2.4×10^{19} cm^{-3}, and 10^{20} cm^{-3}. The required layer thickness to achieve peak performance decreases as the doping concentration increases. A minimum thickness of 0.7 µm is needed to maximize spectral efficiency at the highest studied doping concentration of 10^{20} cm^{-3}, which is 37% thinner than the minimum thickness required for our fabricated device with a BR doping concentration of 2.4×10^{19} cm^{-3}.

Most sub-bandgap photon absorption occurs in the BR layer in far-field and near-field illumination scenarios. We simulated the layer resolved spectral absorption for a TPV device with the optimal n-InAs BR design ($n = 10^{20}$ cm^{-3} and thickness of 0.7 µm), illuminated by a 600 K normally incident blackbody spectrum (far-field, Fig. 3c) and a 600 K undoped silicon radiator at a 0.1 µm radiator-thermophotovoltaic gap (near-field, Fig. 3d). The vertical dashed lines in Fig. 3(c,d) indicate the bandgap of InAs; only above-bandgap absorption can contribute to current production, which is predicted to be about 11 times larger in our near-field scenario compared to far-field. The near-field above-bandgap absorbed irradiance constitutes 27% of the total absorption. In comparison, the device with a bulk gold BR shows an above-bandgap absorption of 35%, and the device without a BR layer exhibits an above-bandgap absorption of 9% (refer to the Supporting Information for those results).

3.3 Electrical properties

To verify that the electrical properties of Design #2 were not affected by the highly doped BR layer, we characterized our fabricated devices, calibrated by a predictive electrical model, and simulated the impact of the BR layer. To calibrate the model, two batches of square devices with nominal mesa widths of (700, 600, 500, 400, 300, 250, 200, and 175 µm) and corresponding nominal top contact widths of (600, 500, 400, 300, 200, 150, 100, and 75 µm) were fabricated from the wafer with Design #2. A top-view photograph

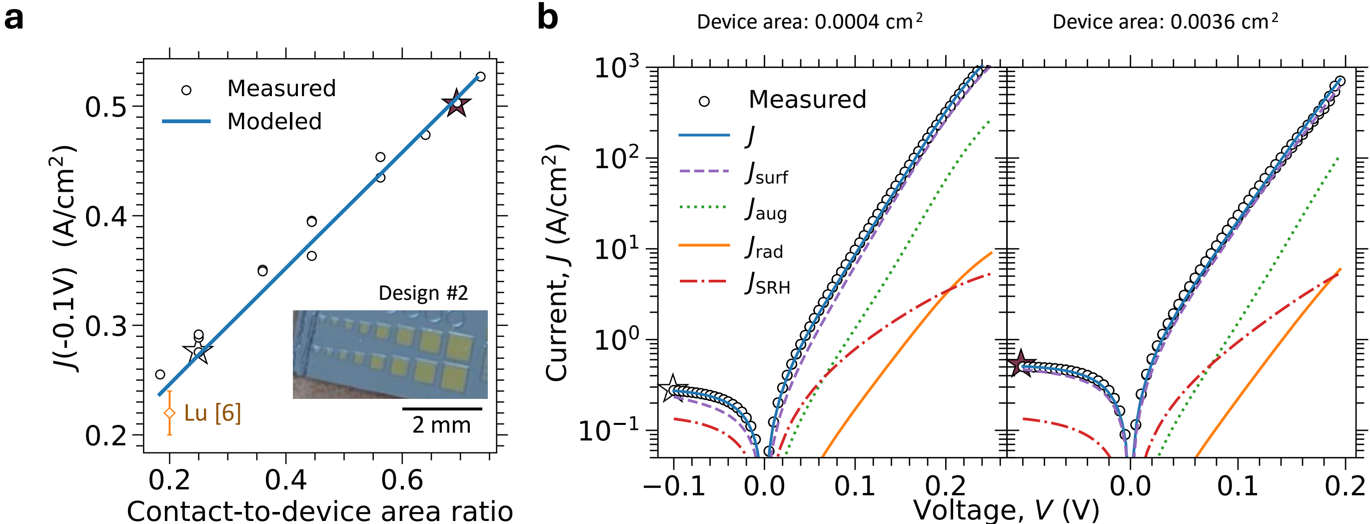

Fig. 4. Electrical characterization of the fabricated devices using the wafer with Design #2. (a) The measured current density at a reverse bias voltage of -0.1 V of square devices (see inset for example of the devices) as a function of the ratio between the metallic top contact area and the mesa area. For comparison, we have included the measured value (orange) of a similar InAs-based TPV device from ref. [6]. (b) Current density-voltage of the second smallest (left) and second largest (right) square devices, comparing measurement and simulation. The simulated currents include total current J, recombination at the metal-semiconductor interface J_{surf}, Auger recombination J_{aug}, radiative recombination J_{rad}, and Shockley-Read-Hall recombination J_{SRH}. The stars connect the data points from (a) to (b).

of a batch is shown in the inset of Fig. 4a. The dark current-voltage characteristics of these devices, presented in Fig. 4, were measured on the same day as the mesa etching. Over time (months), the devices' current in reverse bias increased, indicating sidewall deterioration. This sidewall deterioration could be mitigated by replacing the citric acid etchant with a sulfuric acid etchant [18] or by coating the sidewalls with SiO_2 [28].

The measured dark current-voltage properties of the square devices were simulated using a two-dimensional model. In the model, we used the nominal widths of the square devices and chose the width of the top contact pad to match the ratio between the contact and mesa areas of the fabricated devices. Auger coefficients of $C_p = 10^{-27}$ cm^6/s and $C_n = 1.1\times10^{-26}$ cm^6/s were used, based on values from literature [29], [30]. The front contact resistivity was varied to fit the measured curves, with a value of 1 μΩcm^2 providing a reasonable fit. This value is within the uncertainty of our measured value from the circular transmission line method (2±1 μΩ·cm^2). The absorber layer bulk SRH lifetime (τ_{srh}) was varied to fit the measured data, with $\tau_{srh} = 0.19$ μs providing the best fit.

Significant surface recombination is observed at the front metal-semiconductor interface. The current density measured at -0.1 V ($J_{-0.1V}$) is plotted against the ratio between contact and mesa areas of the square devices in Fig. 4a. The $J_{-0.1V}$ increases as the contact pad area approaches the mesa area, indicating perimeter recombination is insignificant, as it would have otherwise resulted in a negative slope [28]. Our model indicates that surface recombination dominates, as shown in Fig. 4b. The recombination mechanisms of two example dark current-voltage curves (the second smallest and second largest devices) are separated into Auger (J_{aug}), radiative (J_{rad}), SRH (J_{SRH}), and surface recombination (J_{surf}). The dominant surface recombination aligns with the results in ref. [6], which measured a small shunt resistance for a similar InAs TPV device, causing a dominant diffusion current. In both cases, this parasitic current path is due to an insufficient electron barrier from the front surface field (FSF) layer. This issue could be mitigated by replacing the homojunction FSF with a p-doped larger bandgap material that has a valence band aligned with InAs (ex: InAsSbP) [11]. However, our MBE reactor was not equipped to grow this material.

The highly doped n-InAs BR layer does not impact the device's electrical properties. Our device's $J_{-0.1V}$ nears the measured value of 0.22 A/cm^2 reported by Lu et al. [6], as shown in Fig. 4a, which had a contact-to-device area ratio of about 0.2 for a similar InAs thermophotovoltaic device without a BR layer. The similarity in $J_{-0.1V}$ suggests that the BR layer had minimal impact on the material quality of the subsequently grown absorber layer. Additionally, we simulated the dark current-voltage curves of our device with the BR layer but at a doping of 10^{18} cm^{-3} and 10^{20} cm^{-3}. In both cases, the current-voltage curves remained unaffected.

4. Conclusion

We fabricated InAs-based thermophotovoltaic devices incorporating a highly doped n-InAs sub-bandgap photon back reflector layer. Optical characterization revealed a 66%$_{relative}$ increase in spectral efficiency for a 600 K blackbody spectrum in devices with a 1.11 μm thick BR layer at a doping concentration of 2.4×10^{19} cm^{-3} compared to those without it. Our calibrated optical model suggests that increasing the BR layer's doping concentration to 10^{20} cm^{-3} reduces the required layer thickness to maximize performance to 0.7 μm—a 36% reduction—while achieving a spectral efficiency of 79% for a 600 K blackbody spectrum. The optimized BR layer is expected to have a spectral efficiency that is 19%$_{relative}$ lower than that of bulk gold. Under near-field illumination, the above-bandgap power transfer constitutes 27% of the total power transfer compared to 9% for a device without a BR layer. Our calibrated electrical model indicates that the BR layer does not affect the device's electrical properties, provided the material quality remains unaffected by the high doping levels. Preliminary results suggest that the BR layer does not compromise the quality of the subsequently grown absorber layer.

This work demonstrates the potential of an epi-grown n-InAs layer as a back reflector for thermophotovoltaics. This design can be fabricated with a shorter epitaxial growth time by ion implanting the highly doped n-InAs layer into an n-InAs wafer [17] followed by the growth of the thermophotovoltaic structure. Alternatively, the optical performance could be improved by positioning the highly n-doped layer closest to the heat source, allowing it to serve as both an FSF layer and a selective spectral filter by reflecting sub-bandgap photons before they enter the device. This

design could also enhance the device's electrical performance by minimizing recombination losses in the FSF layer, which typically has a short minority-carrier lifetime. The reduction in recombination is achieved by decreasing above-bandgap absorption within the FSF layer due to the conduction band-filling effect.

Acknowledgments

We thank Robert Hunter for providing a Python package wrapper he built to facilitate interacting with Sentaurus. This work was supported by the Natural Sciences and Engineering Research Council of Canada (NSERC), the New Frontiers in Research Fund (No. NFRFE-2019-00334), the NSERC Discovery (NSERC RGPIN-2024-04784), the NSERC STPG PowerCom (NSERC STPGP-494090-16), the Canadian Foundation for Innovation, and the Ontario Research Fund. Access to Synopsys Sentaurus software was provided by CMC Microsystems.

Declaration of generative AI and AI-assisted technologies in the writing process

During the preparation of this work the author(s) used Grammarly and MS Copilot in order to edit the text. After using this tool/service, the author(s) reviewed and edited the content as needed and take(s) full responsibility for the content of the publication.

References

[1] C. Forman, I. K. Muritala, R. Pardemann, and B. Meyer, "Estimating the global waste heat potential," *Renewable and Sustainable Energy Reviews*, vol. 57, pp. 1568–1579, May 2016, doi: 10.1016/J.RSER.2015.12.192.

[2] I. A. Okanimba Tedah *et al.*, "Thermoelectrics versus thermophotovoltaics: Two approaches to convert heat fluxes into electricity," *J Phys D Appl Phys*, vol. 52, no. 27, p. 275501, May 2019, doi: 10.1088/1361-6463/AB1833.

[3] P. F. Baldasaro *et al.*, "Thermodynamic analysis of thermophotovoltaic efficiency and power density tradeoffs," *J Appl Phys*, vol. 89, no. 6, pp. 3319–3327, Mar. 2001, doi: 10.1063/1.1344580.

[4] A. Krier, M. Yin, A. R. J. J. Marshall, and S. E. Krier, "Low Bandgap InAs-Based Thermophotovoltaic Cells for Heat-Electricity Conversion," *J Electron Mater*, vol. 45, no. 6, pp. 2826–2830, Jun. 2016, doi: 10.1007/s11664-016-4373-0.

[5] B. Zhao, K. Chen, S. Buddhiraju, G. Bhatt, M. Lipson, and S. Fan, "High-performance near-field thermophotovoltaics for waste heat recovery," *Nano Energy*, vol. 41, pp. 344–350, 2017, doi: 10.1016/j.nanoen.2017.09.054.

[6] Q. Lu *et al.*, "InAs thermophotovoltaic cells with high quantum efficiency for waste heat recovery applications below 1000 °C," *Solar Energy Materials and Solar Cells*, vol. 179, pp. 334–338, Jun. 2018, doi: 10.1016/j.solmat.2017.12.031.

[7] A. Krier *et al.*, "Low bandgap mid-infrared thermophotovoltaic arrays based on InAs," *Infrared Phys Technol*, vol. 73, pp. 126–129, Nov. 2015, doi: 10.1016/j.infrared.2015.09.011.

[8] A. Fiorino, L. Zhu, D. Thompson, R. Mittapally, P. Reddy, and E. Meyhofer, "Nanogap near-field thermophotovoltaics," *Nat Nanotechnol*, vol. 13, no. 9, pp. 806–811, Sep. 2018, doi: 10.1038/s41565-018-0172-5.

[9] J. Selvidge, R. M. France, J. Goldsmith, P. Solanki, M. A. Steiner, and E. J. Tervo, "Large Area Near-Field Thermophotovoltaics for Low Temperature Applications," Aug. 2024.

[10] R. Mittapally, A. Majumder, P. Reddy, and E. Meyhofer, "Near-Field Thermophotovoltaic Energy Conversion: Progress and Opportunities," *Phys Rev Appl*, vol. 19, no. 3, p. 037002, Mar. 2023, doi: 10.1103/PHYSREVAPPLIED.19.037002/FIGURES/9/MEDIUM.

[11] G. P. Forcade *et al.*, "Efficiency-optimized near-field thermophotovoltaics using InAs and InAsSbP," *Appl. Phys. Lett*, vol. 121, p. 193903, 2022, doi: 10.1063/5.0116806.

[12] H. Daneshvar, R. Prinja, and N. P. Kherani, "Thermophotovoltaics: Fundamentals, challenges and prospects," *Appl Energy*, vol. 159, pp. 560–575, Dec. 2015, doi: 10.1016/j.apenergy.2015.08.064.

[13] D. Fan, T. Burger, S. McSherry, B. Lee, A. Lenert, and S. R. Forrest, "Near-perfect photon utilization in an air-bridge thermophotovoltaic cell," *Nature*, vol. 586, no. 7828, pp. 237–241, Sep. 2020, doi: 10.1038/s41586-020-2717-7.

[14] D. Feng, S. K. Yee, and Z. M. Zhang, "Improved performance of a near-field thermophotovoltaic device by a back gapped reflector," *Solar Energy Materials and Solar Cells*, vol. 237, p. 111562, Apr. 2022, doi: 10.1016/J.SOLMAT.2021.111562.

[15] Z. Omair, S. Hooten, V. Menon, P. Oduor, K.-K. Choi, and A. K. Dutta, "Broadband mirrors for thermophotovoltaics," *Optics Express, Vol. 32, Issue 7, pp. 11000-11009*, vol. 32, no. 7, pp. 11000–11009, Mar. 2024, doi: 10.1364/OE.500790.

[16] R. M. France, P. Espinet-Gonzalez, N. J. Ekins-Daukes, H. Guthrey, M. A. Steiner, and J. F. Geisz, "Multijunction solar cells with graded buffer bragg reflectors," *IEEE J Photovolt*, vol. 8, no. 6, pp. 1608–1615, Nov. 2018, doi: 10.1109/JPHOTOV.2018.2869550.

[17] S. R. Bank, "STIR: sulfur doping of InAs," 2014. Accessed: Nov. 03, 2024. [Online]. Available: https://apps.dtic.mil/sti/citations/tr/AD1007860

[18] D. Wei, C. Harris, C. C. Bomberger, J. Zhang, J. Zide, and S. Law, "Single-material semiconductor hyperbolic metamaterials," *Optics Express, Vol. 24, Issue 8, pp. 8735-8745*, vol. 24, no. 8, p. 8735, Apr. 2016, doi: 10.1364/OE.24.008735.

[19] S. Law, D. C. Adams, A. M. Taylor, and D. Wasserman, "Mid-infrared designer metals," *Opt Express*, vol. 20, no. 22, p. 12155, 2012.

[20] Y. B. Li *et al.*, "Infrared reflection and transmission of undoped and Si-doped InAs grown on GaAs by molecular beam epitaxy," *Semicond Sci Technol*, vol. 8, no. 1, pp. 101–111, 1993, doi: 10.1088/0268-1242/8/1/017.

[21] Y. Zhao, M. J. Jurkovk, and W. I. Wang, "Characterization of AuGe-and AuTe-Based Ohmic Contacts on InAs n-Channel High Electron Mobility Transistors," *The Electrochemical Society Proceedings Series*, vol. 144, no. 3, p. 174, 1997.

[22] E. M. Lysczek, J. A. Robinson, and S. E. Mohney, "Ohmic contacts to p-type InAs," *Materials Science and Engineering B*, vol. 134, pp. 44–48, 2006, doi: 10.1016/j.mseb.2006.07.016.

[23] G. C. Desalvo, R. Kaspi, and C. A. Bozada, "Citric Acid Etching of GaAs,_xSbx, AI0.sGa0.sSb, and InAs for Heterostructure Device Fabrication," *Journal of electrochemical society*, vol. 141, no. 3526, 1994.

[24] M. Giroux, S. Molesky, R. St-Gelais, and J. Krich, "Radiator Tailoring for Enhanced Performance in InAs-Based Near-Field Thermophotovoltaics," *in preparation*.

[25] J. Piprek, *Semiconductor Optoelectronic Devices: Introduction to Physcis and Simulation*. Academic Press, 2003. doi: 10.1016/c2009-0-22633-x.

[26] J. Wróbel *et al.*, "InAs light-to-heavy hole effective mass ratio determined experimentally from mobility spectrum analysis," *Opto-Electronics Review*, vol. 31, no. e144567, 2023, doi: 10.24425/opelre.2023.144567.

[27] W. Nakwaski, "Effective masses of electrons and heavy holes in GaAs, InAs, A1As and their ternary compounds," *Physica B Condens Matter*, vol. 210, no. 1, pp. 1–25, Apr. 1995, doi: 10.1016/0921-4526(94)00921-H.

[28] R. Peng, S. Jiao, H. Li, and L. Zhao, "Dark current mechanisms investigation of surface passivation InAs/GaSb photodiodes at low

temperatures," *J Alloys Compd*, vol. 632, pp. 575–579, May 2015, doi: 10.1016/J.JALLCOM.2015.01.137.

[29] K. L. Vodopyanov, H. Graener, C. C. Phillips, and T. J. Tate, "Picosecond carrier dynamics and studies of Auger recombination processes in indium arsenide at room temperature," *PHYSICAL REVIEWB*, vol. 46, no. 20, 1992.

[30] S. Marchetti, M. Martinelli, and R. Simili, "The Auger recombination coefficient in InAs and GaSb derived from the infrared dynamical plasma reflectivity," *J. Phys.: Condens. Matter*, vol. 14, pp. 3653–3656, 2002.

Supporting Information: Epi-grown broadband reflector for InAs-based thermophotovoltaics

Gavin P. Forcade[1,2], Mathieu de Lafontaine[1], Mathieu Giroux[3], Alan Tam[4], Zbig Wasilewski[4], Jacob J. Krich[1,2], Raphael St-Gelais[2,3], Karin Hinzer[1]

[1] SUNLAB, Nexus for Quantum Technologies Institute, University of Ottawa, Ottawa, K1N 6N8, Canada

[2] Department of Physics, University of Ottawa, Ottawa, K1N 6N8, Canada

[3] Department of Mechanical Engineering, University of Ottawa, Ottawa, K1N 6N8, Canada

[4] Department of Electrical and Computer Engineering, University of Waterloo, Waterloo, N2L 3G1, Canada

1. Measuring the optical properties of the designs

Two tools were used to measure the calibrated spectral reflectivity. First, spectral reflectivity of the wafers with Design#1 (no BR) and Design#2 (BR) were measured with a Bruker's Fourier transform infrared (FTIR) microscope with HYPERION II and the LN-MCT-D316-025 detector. The results are shown in Fig. S1a as dashed curves (pre-shift) and span 1.27-17.0 µm. The reflectivity measured by FTIR was above 1.0, which is nonphysical and was attributed to a dirty gold-plated reference sample. To calibrate this measurement, we compared the FTIR-measured reflectivity to that measured by a calibrated Newport Oriel IQE 200 (QE) tool previously used in the following reference [1], with results shown in Fig. S1b. The FTIR measurement was higher than the QE tool measurement in the well-behaved wavelength overlap range of 1.27-1.6 µm. Assuming the QE tool measured data within that range

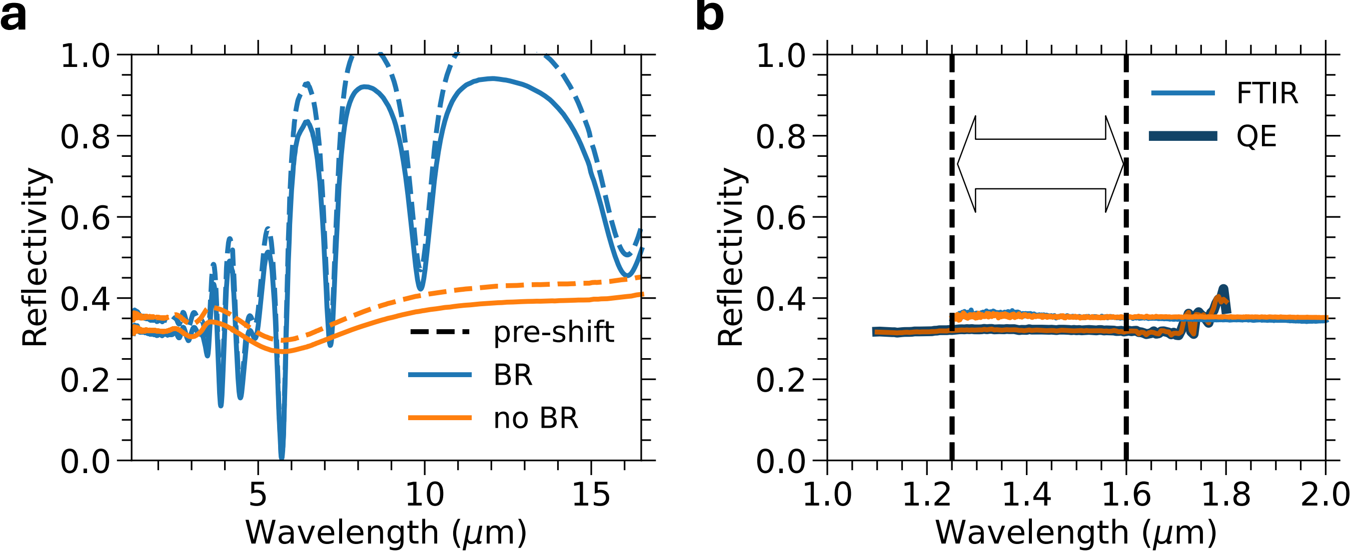

Fig. S1. Measured spectral reflectivity of wafers with and without a back reflector (BR) layer. (a) Measured spectral reflectivity from the Fourier transform infrared spectroscopy (FTIR) tool (solid) and after applying a multiplicity factor (dashed). (b) Comparing measured reflectivity from FTIR and quantum efficiency (QE) instruments. Calculated the multiplicity factor by comparing QE to FTIR results.

with higher accuracy, we calculated multiplicity factors to adjust FTIR values to align with the QE measurements for both wafers. This resulted in mean values and standard deviations of 0.899±0.008 for the wafer with Design#1 (no BR) and 0.906±0.006 for the wafer with Design#2 (BR). The correction factor, the average of the two mean multiplicity factors, was calculated to be 0.90. Applying this correction factor to the full spectral FTIR reflectivity measurement gives the solid curves in Fig. S1a. The shifted reflectivity remains below 1.0, therefore we consider it the calibrated spectral reflectivity. The modeled reflectivity results, which use parameters from literature, align well with these measurements (Fig. 2 in the article), further validating our calibration method.

2. Near-field irradiance simulations: extra structures

We simulated the spectral absorption within two alternative TPV device structures, illuminated in the near-field by a 600 K undoped silicon radiator at a 0.1 µm radiator-TPV gap. These structures are based on Design #2 (Fig. 1b in the article) with the following modifications: (Fig. S2a) the BR layer is replaced by bulk gold and (Fig. S2b) the BR layer is removed. Note that the vertical axis in Fig. S2 spans a wider range than in Fig. 3(c,d), to capture the substrate absorption.

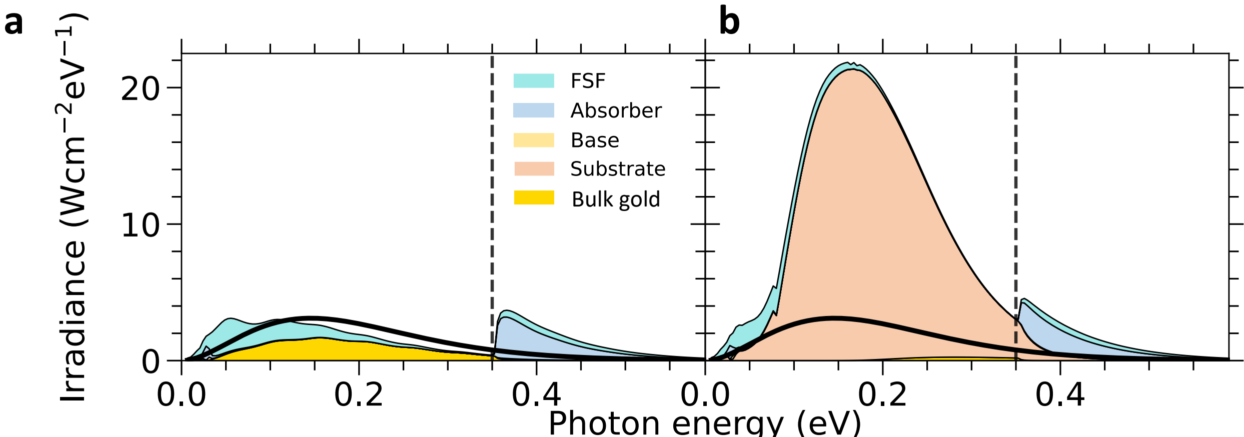

Fig. S2: Spectral absorption distribution within the layers of a TPV device based on Design #2 (Fig. 1b in the article), illuminated by a 600 K undoped silicon radiator with a 0.1 µm gap between the radiator and TPV device, for (a) bulk gold replacing the BR layer and (b) without the BR layer. The black dashed vertical lines indicate InAs's bandgap.

References

[1] G. P. Forcade *et al.*, "Microstructured antireflective encapsulant on concentrator solar cells," *Progress in Photovoltaics: Research and Applications*, vol. 30, no. 2, pp. 132–140, Feb. 2022, doi: 10.1002/PIP.3468.

Chapter 5

Photonic power converters (PPCs) for 1-1.6 μm laser wavelengths

This chapter presents my work optimizing PPC device designs, initially introduced in Section 1.3, by leveraging the physics described in Sections 2.1, 2.2.3, 2.3 and 2.4. There are two sections, the first is a published work on characterizing and comparing O-band single-junction PPCs grown on InP and GaAs substrates. The second is a work submitted for publication on characterizing and optimizing multi-junction PPCs grown on InP for wavelengths within the transparency window of optical fibers.

5.1 InP- and GaAs-based photonic power converters under O-band laser illumination: performance analysis and comparison

This article includes my research on simulating the optoelectronic properties of single-junction O-band PPCs, utilizing the distributed circuit model described in Section 2.4.2. One of the research objectives was to identify the mechanism limiting performance at high irradiances: device heating or resistive losses. Another objective was to compare two PPCs: one with

an InGaAsP absorber material lattice-matched to InP, and another with an InGaAs absorber material lattice-mismatched to a GaAs substrate, which is a more cost-effective and scalable alternative.

Impact

The manuscript has the following novelties:

1. Measured record efficiency of 52.8% for O-band PPCs.
2. Measured a commendable efficiency of 48.7% for the lower-cost lattice-mismatched device.
3. Demonstrated impact of illumination uniformity in PPCs.
4. Developed model which indicated that heating was the primary factor in limiting efficiency at high irradiances for these devices, although resistive losses were non-negligible.

The manuscript's results guided future research directions, confirming a satisfactory metallic contact design and process. The record efficiency demonstrates a pathway to high-efficiency O-band devices, while the notable efficiency of the lower-cost lattice-mismatched device warrants further investigation.

Author contribution

Dr. Meghan Beattie: As the lead University of Ottawa-based graduate student associated with the project, Meghan designed and performed the experiments, provided detailed feedback during the analysis of my simulation results, wrote the article, and prepared the figures.

Dr. Henning Helmers: As a researcher at the Fraunhofer Institute for Solar Energy Systems, Henning designed the PPCs, provided detailed feedback during the analysis of the results, and assisted in editing the manuscript.

Gavin P. Forcade: As a University of Ottawa graduate student associated with the project, I set up the distributed circuit model, analyzed its results, and assisted in editing the manuscript.

Dr. Christopher E. Valdivia: As a senior research scientist within the University of Ottawa's SUNLAB research group, Chris helped to guide the research, provided detailed feedback during the analysis of the results, and assisted in editing the manuscript.

Dr. Oliver Höhn: As a researcher at Fraunhofer Institute for Solar Energy Systems, Oliver fabricated the devices, assisted in the device design, provided detailed feedback during the analysis of the results, and assisted in editing the manuscript.

Prof. Karin Hinzer: As the director of the University of Ottawa's SUNLAB research group, Karin oversaw the research, provided detailed feedback during the analysis of the results, and assisted in editing the manuscript.

© 2022 IEEE. Reprinted, with permission, from

> M.N Beattie, H. Helmers, G.P. Forcade, C.E. Valdivia, O. Hohn, and K. Hinzer, "InP- and GaAs-Based Photonic Power Converters Under O-Band Laser Illumination: Performance Analysis and Comparison", *IEEE Journal of Photovoltaics*, 13, 1, 2023. DOI: 10.1109/JPHOTOV.2022.3218938

In reference to IEEE copyrighted material which is used with permission in this thesis, the IEEE does not endorse any of the University of Ottawa's products or services.

InP- and GaAs-Based Photonic Power Converters Under O-Band Laser Illumination: Performance Analysis and Comparison

Meghan N. Beattie, Henning Helmers, *Member, IEEE*, Gavin P. Forcade, Christopher E. Valdivia, Oliver Höhn, and Karin Hinzer, *Senior Member, IEEE*

***Abstract*—Photonic power converters (PPCs), which convert narrow-band light to electricity, are essential components in power-by-light systems. When designed for telecommunications wavelengths such as the O-band, near 1310 nm, the devices are well-suited to power-over-fiber applications. Despite the potential for very high power conversion efficiencies ($>50\%$), PPCs can be adversely affected by high-intensity nonuniform illumination conditions. In this work, we characterized two O-band PPC designs based on: high-quality InGaAsP absorber material lattice-matched to an InP substrate, and metamorphic InGaAs absorber material lattice-mismatched to a GaAs substrate, a more cost-effective and scalable alternative. We measured each device under O-band laser illumination with five beam profiles having peak-to-average ratios ranging from 2 to 11. Both devices were insensitive to the beam uniformity for input illumination with average irradiance below 2 W/cm^2 over their 5.4-mm^2 active areas, but exhibited better open-circuit voltages under larger, more uniform illumination profiles at higher incident powers. Measured efficiencies reached 52.8% and 48.7% for the lattice-matched and mismatched devices, respectively. Distributed circuit modeling results suggested that both lateral conduction losses and localized heating effects were responsible for the measured dependence on beam-size. Our work demonstrates the potential for O-band PPCs, presenting two highly efficient designs suitable for powering devices requiring $\lesssim 250$ mW, with an appropriate illumination profile.**

***Index Terms*—1310 nm, III-V, InGaAs, InGaAsP, laser power converter, metamorphic, o-band, optical power transmission, photonic power converter (PPC), power-over-fiber.**

Manuscript received 20 June 2022; revised 14 September 2022; accepted 21 October 2022. Date of publication 18 November 2022; date of current version 12 January 2023. This work was supported in part by the Government of Canada's AI for Design National Research Council Collaborative Science, Technology and Innovation Program under Grant INT-014-1, in part by the Natural Sciences and Engineering Research Council of Canada (funding reference numbers 497981 and RGPIN-2015-04782), and in part by the German Federal Ministry of Education and Research under Grant 01DM21006 A. We acknowledge financial support from the Canadian Foundation for Innovation and the Government of Ontario. *(Corresponding author: Meghan N. Beattie.)*

Meghan N. Beattie, Christopher E. Valdivia, and Karin Hinzer are with the SUNLAB, School of Electrical Engineering and Computer Science, University of Ottawa, Ottawa, ON K1N 6N5, Canada (e-mail: mbeattie@uottawa.ca; valdivia@uottawa.ca; khinzer@uottawa.ca).

Henning Helmers and Oliver Höhn are with the Fraunhofer Institute for Solar Energy Systems ISE, 79110 Freiburg, Germany (e-mail: henning.helmers@ise.fraunhofer.de; oliver.hoehn@ise.fraunhofer.de).

Gavin P. Forcade is with the SUNLAB, Department of Physics, University of Ottawa, Ottawa, ON K1N 6N5, Canada (e-mail: gforc034@uottawa.ca).

Color versions of one or more figures in this article are available at https://doi.org/10.1109/JPHOTOV.2022.3218938.

Digital Object Identifier 10.1109/JPHOTOV.2022.3218938

I. Introduction

POWER-BY-LIGHT systems, also known as photonic or optical power systems, offer an alternative to conventional power delivery over conductive wires, with several advantages for sensitive electronics applications. Unlike the flow of electric current in wires, light neither produces nor is it affected by electromagnetic interference, and it does not spark. Power-by-light systems are well-suited to power sensitive devices that require electrical isolation, or to supply power in electrically noisy or hazardous environments [1], [2], [3]. They can also be integrated with optical communications systems for simultaneous power and data transmission [4], [5], [6], [7]. The application space for photonic power is diverse and rapidly growing. Examples include transmission line [8] and wind turbine monitoring [9], biomedical implants [10], [11], powering the Internet of Things [12], radio-over-fiber [7], [13], DC–DC power conversion [14], and many others [1], [2], [15].

Photonic power systems transmit power in the form of narrow-band light, which is generated by a laser or LED. After transmission, the light is converted back to electrical power using a photonic power converter (PPC), which generates electricity through the photovoltaic effect [1], [2]. PPCs are similar to solar cells in their operation, however, they are designed to convert narrow-band light rather than the broad-band solar spectrum. The efficiency of a power-by-light system has three key components: the electrical-to-optical power conversion efficiency of the light source, the photonic power transmission efficiency, and the optical-to-electrical power conversion efficiency of the PPC. This article is concerned with the second and third efficiency components.

The optical-to-electrical power conversion efficiency of the PPC depends on the chip design and material quality, the wavelength, intensity, and illumination profile of the incident light, and the cell temperature. The most efficient PPCs to date are based on GaAs and absorb in the wavelength range of 800–850 nm [2], [16], [17], [18], [19], [20], [21], [22], yielding power conversion efficiencies up to 69% [16]. Other material systems have been explored for PPCs targeting operation at different wavelengths [2] such as 980 nm [23], 1064 nm [24], [25], [26], and 1550 nm [23], [27], [28], [29], [30]. For transmission through optical fiber, wavelengths in the telecommunications O- or C-bands (~1310 or ~1550 nm) offer reduced attenuation

This work is licensed under a Creative Commons Attribution 4.0 License. For more information, see https://creativecommons.org/licenses/by/4.0/

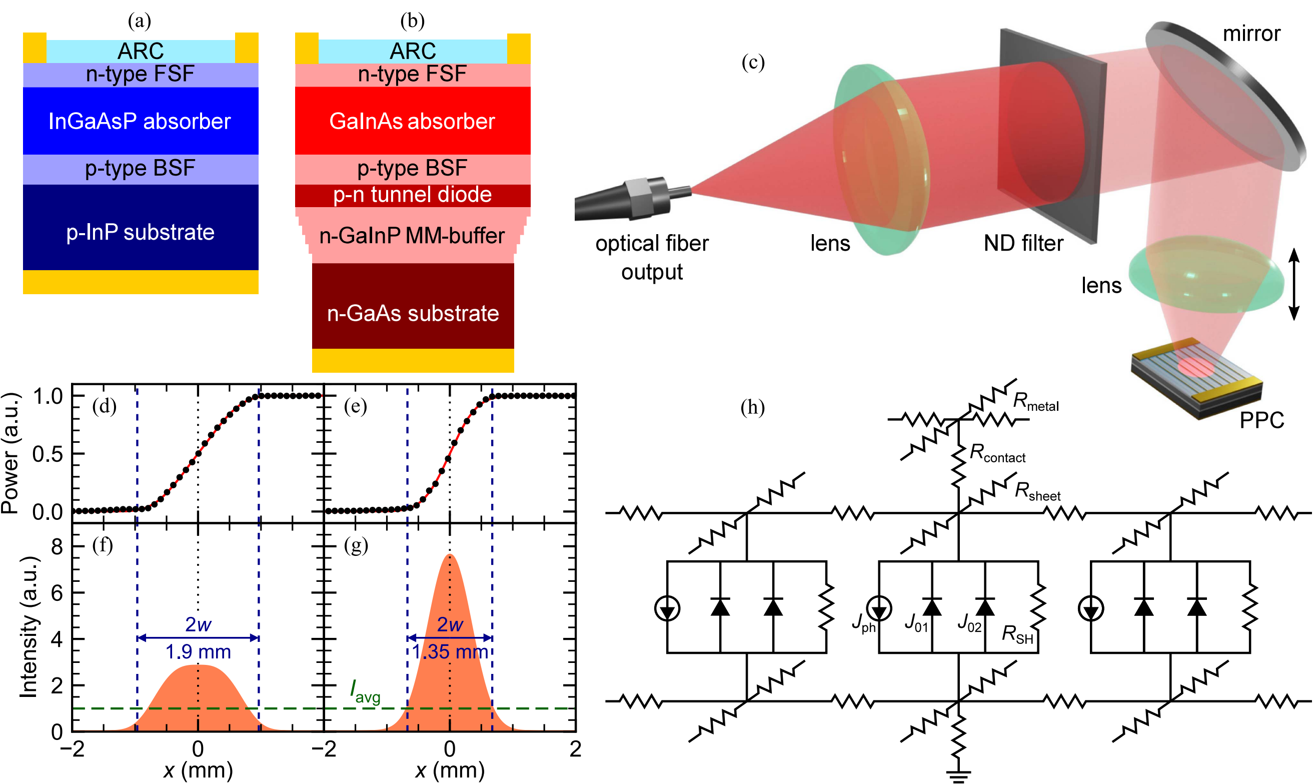

Fig. 1. PPC design schematics for (a) InGaAsP/InP and (b) MM-GaInAs/GaAs. ARC: anti-reflection coating; FSF: front surface field; BSF: back surface field. (c) Visualization of the experimental setup. (d), (e) Knife-edge profiles and (f), (g) beam intensity profiles for two different beam widths. The $1/e^2$ beam diameters $(2\,w)$ and the average irradiance $(I_{\rm avg})$ relative to the peak beam intensity for a nominal designated area of $0.054\ {\rm cm}^2$ are indicated. (h) Electrical circuit diagram for the PPC device DCM. The photocurrent $(J_{\rm ph})$, two-diode parameters $(J_{01}\ {\rm and}\ {\rm J}_{02})$, and relevant resistances are indicated.

and much better transmission efficiencies than 850 nm light for distances beyond a few hundred meters [3]. Here, we explore O-band PPCs, for which the comparatively larger photon energy leads to larger output voltages than could be produced for comparable C-band PPCs.

O-band PPCs have been less studied than their 850-nm-band counterparts. To date, only a handful of O-band PPC devices have been experimentally characterized and reported in the literature [31], [32], [33], [34], based on InP and GaAs substrates. Other studies have investigated pathways to increased power conversion efficiencies in O-band PPCs [35], [36]. For InP-based devices, high-quality lattice-matched quaternary materials such as InGaAsP or InAlGaAs can provide high absorptance in the O-band. For GaAs-based PPCs, there is no convenient lattice-matched absorber material for O-band operation and lattice-mismatched growth processes are required [32], [37]. Highly efficient GaAs-based devices represent a path toward large-scale manufacturing of O-band PPCs, as GaAs substrates are less expensive and available in larger sizes than InP. Noting that materials with smaller bandgaps yield lower efficiencies than their larger-bandgap counterparts, detailed-balance modeling of O-band devices predicts theoretical power conversion efficiencies exceeding 67% in the radiative limit [36]. This compares to the predicted efficiency of 73.7% for a comparable GaAs PPC operating at 830 nm in the radiative limit at room temperature [38].

In this article, we analyze high-performance O-band PPCs based on both InP and GaAs substrates. We examine the impact of the illumination profile on device performance and employ a distributed circuit model (DCM) to better understand the mechanisms responsible for reduced performance of the 6.4-mm^2 PPCs under nonuniform illumination with average irradiance in the range of 2–10 $\mathrm{W/cm^2}$.

II. Methods

A. Design and Fabrication of PPC Devices

The design and fabrication of PPCs for operation under 1310-nm laser illumination was carried out at Fraunhofer ISE [32]. The devices were grown by metal–organic vapor phase epitaxy (MOVPE) using an AIXTRON G4 2800TM reactor. Two designs were considered, similar to existing literature [39], [40], [41], both using an n–p homojunction architecture for the active layers sandwiched between wider bandgap front and back surface field layers, which prevent the loss of minority carriers generated in the absorber region through electrical passivation. The first design, shown in Fig. 1(a), was grown on a 4-inch p-type InP substrate making use of lattice-matched $\mathrm{In_{0.32}Ga_{0.68}As_{0.69}P_{0.31}}$ (InGaAsP/InP) with a measured bandgap of $E_{\rm g} = 0.890$ eV for the absorber material. The second design, shown in Fig. 1(b), was grown on a 4-inch n-type GaAs substrate. Lattice-mismatched $\mathrm{Ga_{0.56}In_{0.44}As}$

(MM-GaInAs/GaAs) with a measured bandgap of $E_g = 0.855$ eV was used for the absorber layers and the change in lattice constant was accommodated using an n-type GaInP-based step-graded metamorphic (MM) buffer [37], [39]. This polarity was chosen due to the superior mobility of majority carriers in n-type material. The change in doping polarity between the active n–p junction and the n-type MM buffer and substrate, which employ well-known growth techniques, required the addition of a tunnel diode (TD) between the active layers of the device and the MM buffer to swap the doping polarity.

Following epitaxy, ohmic contacts and an antireflection coating (ARC) were deposited. The front metallization consisted of two busbars on opposite sides of the cell and a comb grid design with parallel fingers. Wet-chemical mesa etching was used to separate individual PPC devices on the wafer. All devices were fabricated with a total area of $A = 6.4\ \mathrm{mm}^2$, an active area between the busbars of $2.2 \times 2.2\ \mathrm{mm}^2$, and a nominal designated area of $A_{\mathrm{nom}} = 5.4\ \mathrm{mm}^2$, which is the total area excluding the busbars.

B. Illuminated Electrical Measurements

We characterized the performance of the fabricated PPC devices on a gold-plated temperature-controlled copper chuck at 25° C. Current–voltage (I–V) characteristics were measured with a Keithley 2420 source-meter using a four-wire configuration, ramping voltage in the forward direction. Two probes collected current from the top contact, with one for each busbar, and a third probe contacted one busbar to measure voltage. Two leads connected to the chuck conducted current and measured voltage at the back of the device.

The devices were illuminated using a fiber-coupled laser with a central wavelength of 1319 nm and a full width at half maximum of 9 nm. The laser output was coupled into an optical fiber with a core diameter of 400 µm and a numerical aperture of 0.22. The fiber output was collimated and then focused onto the device using a lens positioned directly above the measurement stage as shown in Fig. 1(c), forming a circular spot with radially decreasing light intensity.

The size of the laser spot on the device was controlled by manipulating the lens-to-device distance. We measured the beam profile at the device surface using the knife-edge profiling technique [42] revealing a symmetrical super-Gaussian beam shape where the intensity in the xy-plane was given by

$$I_{\mathrm{light}}(x, y) = I_{\mathrm{peak}} e^{-2\left(|x|^\beta + |y|^\beta\right)/w^\beta} \tag{1}$$

where I_{peak} is the peak beam intensity, w is the $1/e^2$ beam radius, and β is the beam shape parameter. For a perfectly Gaussian beam, $\beta = 2$. Knife-edge measurements and corresponding super-Gaussian profiles are shown in Fig. 1(d)–(g) for two beam sizes. We characterize the uniformity of these illumination profiles by the peak-to-average ratio (PAR), defined as the peak beam intensity divided by the average irradiance (I_{avg}) across the nominal designated area

$$\mathrm{PAR} = \frac{I_{\mathrm{peak}}}{I_{\mathrm{avg}}} = \frac{I_{\mathrm{peak}}}{P_{\mathrm{in}}/A_{\mathrm{nom}}} \tag{2}$$

TABLE I
ILLUMINATION PARAMETERS FOR THE FIVE SPOT SIZES

$2w$ (mm)	β	PAR
2.3 ± 0.2	3.4 ± 0.8	2.0
1.9 ± 0.1	3.1 ± 0.5	2.8
1.7 ± 0.1	3.0 ± 0.4	4.0
1.35 ± 0.08	2.0 ± 0.3	7.6
1.17 ± 0.08	1.6 ± 0.2	11.4

TABLE II
DCM PARAMETERS FOR INGAASP/INP PPC

Parameter	Value (top, bottom)	Units
J_{01}	5.5×10^{-12}	$\mathrm{A/cm^2}$
J_{02}	1.8×10^{-7}	$\mathrm{A/cm^2}$
R_{SH}	10^9	$\Omega\ \mathrm{cm}^2$
R_{sheet}	7.7, 0.67	$\Omega/\square$
R_{contact}	1.8×10^{-6}, 1.0×10^{-4}	$\Omega\ \mathrm{cm}^2$
ρ_{Ag}	1.59×10^{-6}	Ω cm

where P_{in} is the power incident on the nominal designated area.

We measured each device under five beam sizes, listed in Table I. For the largest beam size ($2w = 2.3$ mm), the $1/e^2$ diameter was not fully contained within the active area of the device. In this case, P_{in} was adjusted to discount the portion of the beam that extended beyond the active area. The laser was allowed to stabilize before beginning measurements, which were completed in 1–2 s for each I–V curve. The laser beam was blocked between measurements for average irradiance $> 1\ \mathrm{W/cm^2}$, where heating began to impact device behavior. For comparison, I–V measurements were also performed during the 1-ms irradiance plateau of a xenon flash lamp, providing broadband and uniform illumination.

C. Distributed Circuit Modeling

To better understand the impact of nonuniform illumination, we used a DCM [43] to simulate uniform and Gaussian ($\beta = 2$) illumination profiles on the lattice-matched InGaAsP/InP PPC. The simulated device area was $6.4\ \mathrm{mm}^2$ with an active area of $2.2 \times 2.2\ \mathrm{mm}^2$ and busbars extending to the edges of the device on either side of the active region. The area was divided into discrete unit cells, each represented by an equivalent circuit described by parameters that were fit to or derived from experimental measurements. Simulation input parameters are given in Table II.

The n–p junction unit cells in the DCM were described by the two-diode model

$$J(V) = J_{\mathrm{ph}} - J_{01} \exp\left(\frac{qV}{kT}\right) - J_{02} \exp\left(\frac{qV}{2kT}\right) - \frac{V}{R_{\mathrm{SH}}} \tag{3}$$

where J is current density, J_{ph} is the photocurrent, J_{01} and J_{02} are the dark saturation current densities, k is the Boltzmann constant, $T = 298$ K is the temperature, q is the elementary charge, and R_{SH} is the shunt resistance. The values of J_{01}, J_{02}, and R_{SH} were found by fitting (3) to experimental J–V curves

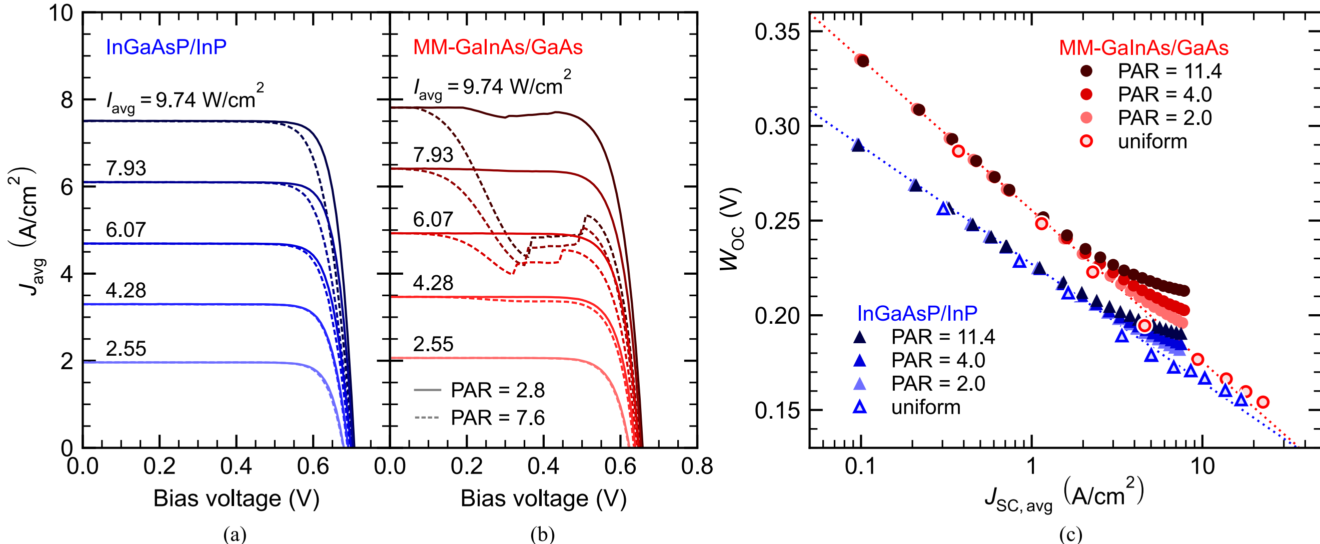

Fig. 2. (a), (b) J–V characteristics measured under O-band laser illumination at five different incident powers for (a) InGaAsP/InP and (b) MM-GaInAs/GaAs PPCs. The solid and dashed lines correspond to PARs of 2.8 and 7.6, respectively. Average irradiance values are given for each measurement. (c) W_{OC} as a function of $J_{SC,avg}$ for the InGaAsP/InP and MM-GaInAs/GaAs PPCs. Measured data is shown for three of the five O-band laser illumination profiles and for broad spectrum uniform illumination. Dotted lines are fits to (4), see Table III for fitting parameters.

for the InGaAsP/InP device, averaging over 20 measurements under average laser irradiance below 0.57 $\mathrm{W/cm^2}$, well below the threshold of $\sim 2\ \mathrm{W/cm^2}$ above which nonuniform illumination effects were observed. The large value obtained for R_{SH} signifies that shunting was insignificant for this device. The n–p junction unit cells were interconnected with resistive elements in the lateral and vertical directions to form a complete circuit model representing the device [43], [44], shown in Fig. 1(h). The sheet resistances and the top contact resistance listed in Table II were measured experimentally. The bottom contact resistance is an estimate based on other devices and had a negligible impact on the simulated I–V curve. Resistances in the metal busbars and gridlines were approximated using the resistivity of silver (ρ_{Ag}).

III. Results and Discussion

A. Current–Voltage Characteristics

Sample current–voltage (J–V) characteristics are shown in Fig. 2(a) and (b) for the InGaAsP/InP and MM-GaInAs/GaAs PPCs, respectively, where the current density J_{avg} is averaged over the total device area. We measured the devices under a range of incident laser powers between 7 and 526 mW, corresponding to average irradiance between 0.13 and 9.74 $\mathrm{W/cm^2}$. For clarity, only five incident powers and two beam diameters are shown in Fig. 2(a) and (b).

For both PPCs, the short-circuit current density (J_{SC}) scales linearly with increasing incident power, regardless of the beam diameter, with average responsivities of 0.912 and 0.957 A/W for the InGaAsP/InP and MM-GaInAs/GaAs PPCs, respectively. Smaller spot sizes are associated with reduced fill factors (FF) and open-circuit voltages (V_{OC}) compared to the larger spot sizes for both PPCs.

The larger responsivity of the lattice-mismatched device is due to its smaller bandgap and correspondingly larger optical absorption in the O-band. The smaller bandgap of the MM-GaInAs/GaAs PPC also gives rise to smaller (V_{OC}) values in general compared to the InGaAsP/InP PPC. By adjusting the alloy compositions, the bandgaps of both InGaAsP and MM-GaInAs can be tuned to optimize the trade-off between absorptance and voltage. In the case of the MM material, smaller bandgaps correspond to greater lattice mismatch between GaInAs and the GaAs substrate, increasing the difficulty in maintaining high material quality [39].

For the MM-GaInAs/GaAs PPC, its TD [see Fig. 1(b)] impacts the shape of the J–V curves and each maximum power point. TDs are characterized by a peak tunneling current density, above which tunneling is no longer possible and the TD switches from low-resistance tunneling to higher-resistance thermal diffusion (the dominant electrical transport mechanism in standard pn-junction diodes) [45]. When embedded in a photovoltaic device, the switch from tunneling to thermal diffusion significantly increases the device's total series resistance [46], [47], [48], [49], [50], [51], [52]. Fig. 2(b) shows this effect for the MM-GaInAs/GaAs PPC, where a dip in total current is observed for bias voltages > 0.1 V. Note that the J–V curves were measured in the forward direction from J_{SC} to V_{OC}, and hysteresis is often observed in the J–V curves of photovoltaic cells that contain TDs [47], [50], [51]. Measuring in the forward direction gives a more accurate assessment of the threshold beyond, which the TD begins to influence the cell performance [47]. In Fig. 2(b), we observe that the dip in the J–V curve becomes more pronounced with increasing illumination power and is more significant for smaller beam sizes, which are characterized by higher PAR values and correspondingly higher peak illumination intensities (and peak current densities) at the center of the laser spot. The TD begins to impact the J–V curves for the lattice-mismatched MM-GaInAs PPC on GaAs when the peak illumination intensity $I_{peak} \gtrsim 20\ \mathrm{W/cm^2}$.

TABLE III
ILLUMINATION PARAMETERS FOR THE FIVE SPOT SIZES

	InGaAsP/InP		MM-GaInAs/GaAs	
PAR	n	J_0 $\left(\mathrm{A/cm^2}\right)$	n	J_0 $\left(\mathrm{A/cm^2}\right)$
11.4	1.04	1.61×10^{-11}	1.34	2.81×10^{-8}
7.6	1.05	2.15×10^{-11}	1.35	3.27×10^{-8}
4.0	1.06	2.85×10^{-11}	1.36	3.53×10^{-8}
2.8	1.06	2.40×10^{-11}	1.35	3.08×10^{-8}
2.0	1.07	2.89×10^{-11}	1.35	3.16×10^{-8}
Average	1.06	2.4×10^{-11}	1.35	3.2×10^{-8}
Ideal	*1*	3.0×10^{-13}	*1*	1.1×10^{-12}

Whereas the maximum power is strongly impacted by TD and resistive effects, the open-circuit voltage is determined largely by the bandgap and material quality. One measure of quality is the bandgap-voltage offset, defined as $W_{\mathrm{OC}} = E_{\mathrm{g}}/q - V_{\mathrm{OC}}$. Lower values of W_{OC} indicate better device performance [53]. W_{OC} for both PPCs is plotted in Fig. 2(c) as a function of the short-circuit current density averaged over the total device area ($J_{\mathrm{SC,avg}}$). Data are shown for three of the five laser spot sizes. For comparison, data measured under broad spectrum uniform illumination is also shown for the exact same InGaAsP/InP device [32] and for a substantially similar MM-GaInAs/GaAs device with the same layer structure.

In general, V_{OC} increases logarithmically with increasing $J_{\mathrm{SC,avg}}$ because of the larger carrier concentrations in photovoltaic devices under higher irradiance. Correspondingly, the obtained W_{OC} decreases logarithmically with increasing $J_{\mathrm{SC,avg}}$ for $J_{\mathrm{SC,avg}} < 1\ \mathrm{A/cm^2}$. When $J_{\mathrm{SC,avg}} > 1\ \mathrm{A/cm^2}$, the measurements deviate from the logarithmic trend. Fits were performed for the laser-illuminated measurements in the region $J_{\mathrm{SC,avg}} \leq 1\ \mathrm{A/cm^2}$ using the nonideal one-diode equation

$$V_{\mathrm{OC}}\left(J_{\mathrm{SC,avg}}\right) = \frac{nkT}{q} \ln\left(\frac{J_{\mathrm{SC,avg}}}{J_0} + 1\right) \quad (4)$$

where n is the ideality factor and J_0 is the average dark saturation current density over the total area. We used the one-diode equation here to allow for direct comparison between the two PPC designs, because the experimental J–V curve of the MM-GaInAs/GaAs PPC with an embedded TD was not well-represented by the two-diode equation (equation 3) across the fitting regime. The one-diode fit with $n \neq 1$, however, was highly representative of the J–V characteristics throughout this range. For the InGaAsP/InP PPC, the one-diode and two-diode models were found to agree with each other within the fitting regime.

Fitting parameters for each device are given in Table III, including average values for each device. The fits are consistent with the measured J–V characteristics in the power quadrant for both PPCs within the fitting regime $J_{\mathrm{SC,avg}} < 1\ \mathrm{A/cm^2}$. For comparison, ideal parameters in the radiative limit are also shown, where $n_{\mathrm{ideal}} = 1$ and $J_{0,\mathrm{ideal}}$ is calculated from the measured bandgaps assuming a cell temperature of $T = 298$ K [53]

$$J_{0,\mathrm{ideal}}\left(E_{\mathrm{g}}, T\right) = \frac{2\pi(kT)^3}{h^3c^2}\left(\frac{E_{\mathrm{g}}}{kT} + 1\right)^2 \exp\left(-\frac{E_{\mathrm{g}}}{kT}\right). \quad (5)$$

The lattice-matched InGaAsP/InP PPC exhibits an average ideality factor of 1.06 and an average dark saturation current density of $2.4 \times 10^{-11}\ \mathrm{A/cm^2}$. The smaller bandgap of the MM-GaInAs/GaAs PPC is expected to produce a larger dark saturation current [see (5)], however, comparison between the corresponding experimental and ideal parameters in Table III shows that its behavior is less ideal compared to the lattice-matched device. The average ideality factor is 1.35 and the average dark saturation current density is $3.2 \times 10^{-8}\ \mathrm{A/cm^2}$. Even though a direct quantitative comparison of dark saturation current densities is complicated by the significant difference in ideality factor, this data shows more pronounced nonradiative recombination for the MM-GaInAs/GaAs PPC, as expected for a lattice-mismatched device [54].

B. Impact of Nonuniform Illumination on V_{OC}

For all laser-illuminated measurements, the W_{OC} values deviated from the logarithmic trend when $J_{\mathrm{SC,avg}} > 1\ \mathrm{A/cm^2}$. More significant deviations were observed for smaller beam diameters with larger PARs. We used a DCM to estimate the impact of lateral conduction losses on V_{OC} for the InGaAsP/InP PPC. Under nonuniform illumination, charge carriers diffuse from regions of high to low irradiance, producing lateral current flows that increase with PAR, even under external open-circuit conditions [44], [55]. This causes resistive losses that are more significant for small beam sizes and high incident powers.

The model results for Gaussian ($2w = 1.35$ mm) and uniform illumination profiles are shown in Fig. 3(a) with experimental data for comparison. The DCM shows good agreement with uniform illumination measurements, within 1% for all measured data points. For the Gaussian beam profile, the DCM predicts a deviation in V_{OC} away from the logarithmic trend at higher currents, similar to experimental measurements. However, this deviation was much more pronounced in the measured data than in the DCM. This discrepancy suggests that localized heating, which was not accounted for in the DCM, contributed in part to the deviation in measured V_{OC}. As described in Section II-B, the uniform illumination measurements were collected using a flash measurement to mitigate heating. As such, the uniform data are directly comparable to and agree well with the model, which does not account for temperature effects.

Temperature dependence in the parameter J_0 leads to an approximately linear reduction in V_{OC} with increasing temperature [56], [57], [58], [59], [60]. From Dupré et al. [57], we assume that

$$\frac{dV_{\mathrm{OC}}}{dT} = -\frac{E_{\mathrm{g}}/q - V_{\mathrm{OC}}\left(J_{\mathrm{SC}}, T\right) + \gamma kT/q}{T} \quad (6)$$

where $\gamma \approx 3$ describes the temperature sensitivity when bulk and surface recombination processes are dominant such that the ideality factor $n \approx 1$, which is satisfied for the lattice-matched PPC device (see Table III). We estimated $\frac{dV_{\mathrm{OC}}}{dT}$ by taking $T = 298$ K, $E_{\mathrm{g}} = 0.890$ eV, and using the simulated values of V_{OC} at 298 K from the DCM. For $V_{\mathrm{OC,298\,K}} = 0.7$ V, corresponding to $J_{\mathrm{SC}} \sim 4\ \mathrm{A/cm^2}$, we obtain $\frac{dV_{\mathrm{OC}}}{dT} \approx -0.9$ mV/K, which is approximately -0.13 %/K. This is in the range of what was observed experimentally for GaInP and GaAs solar cells [56].

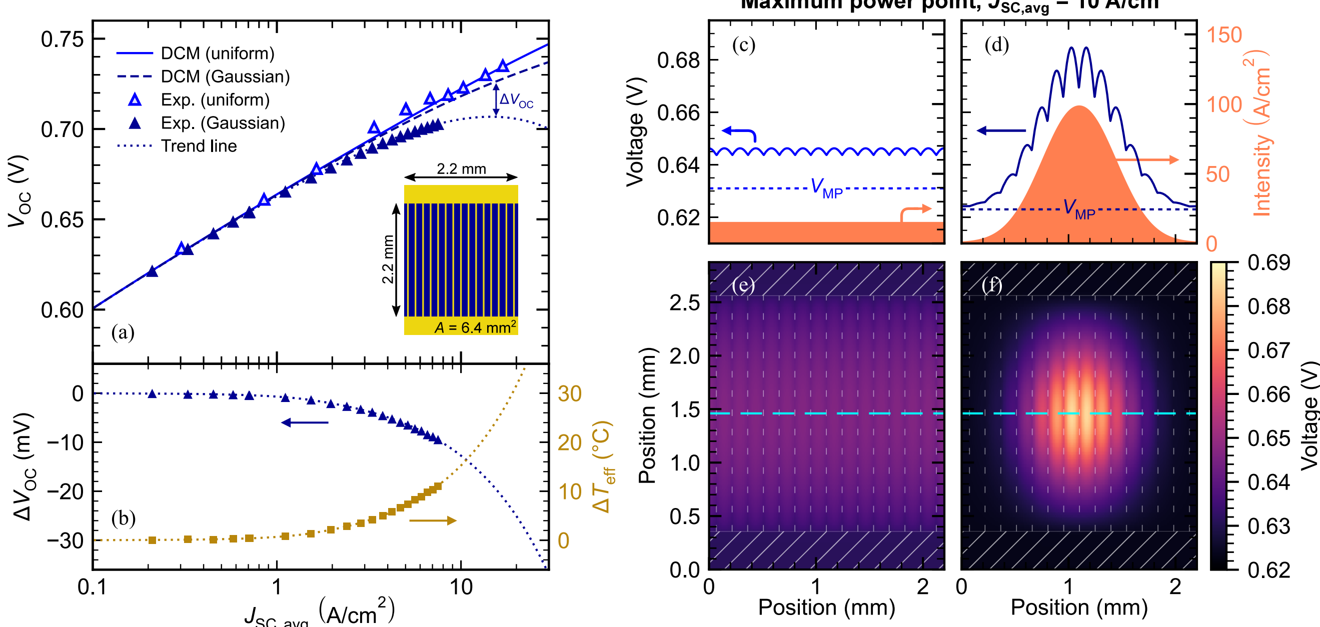

Fig. 3. (a) V_{OC} as a function of $J_{\mathrm{SC,avg}}$ from the DCM and experiment for the InGaAsP/InP PPC under uniform and Gaussian illumination. Inset: schematic of the modeled cell geometry. (b) Difference in experimental V_{OC} compared to simulation and estimated change in effective temperature $(\Delta T_{\mathrm{eff}})$ to account for ΔV_{OC}, calculated from (6). Dotted lines in (a) and (b) are extrapolated trend lines. (c), (d) Voltage vs. position at the top of the PPC cell along a line perpendicular to the gridlines and equidistant between the busbars, as calculated by the DCM at the maximum power point for (c) uniform and (d) Gaussian illumination when $J_{\mathrm{SC,avg}} = 10\mathrm{A/cm}^2$. V_{MP} is indicated by the dashed lines and the shading indicates the shape of the incident illumination profile. (e), (f) 2D map showing the modelled voltage as a function of position at the maximum power point for (e) uniform and (f) Gaussian illumination. The busbars and gridlines are shown in white, and the cross-sections for (c) and (d) are indicated by the cyan dashed lines through the center (perpendicular to gridlines).

Considering the difference in voltage between the model and experiment, ΔV_{OC}, and using $\frac{dV_{\mathrm{OC}}}{dT}$ from (6), we found an effective difference in average cell temperature $(\Delta T_{\mathrm{eff}})$ that increased with $J_{\mathrm{SC,avg}}$. The result is shown in Fig. 3(b). Given the significant nonuniformity in the illumination profile, localized heating from the laser is expected to produce a similar nonuniformity in the temperature profile across the device, with more significant heating at the center of the illumination spot. ΔT_{eff} does not account for this nonuniformity, which depends on the thermal and electrical conductivities of the cell materials and the thermal contact efficiency between the cell and the temperature-controlled chuck.

In Fig. 3(c)–(f), the simulated voltage at the maximum power point is shown for uniform (c) and Gaussian (d) illumination conditions as a function of position when $J_{\mathrm{SC,avg}} = 10\ \mathrm{A/cm}^2$. The profiles in 3(c) and (d) follow a line through the center of the modeled device, perpendicular to the gridlines. The extracted voltage at maximum power (V_{MP}) is the simulated voltage at the outer edge of the busbars. Full 2-D voltage maps across the entire device surface are shown in Fig. 3(e) and (f). Under uniform illumination, small dips in voltage are found beneath each gridline, where the cell is shaded. Across the entire device, a voltage deviation of only 15.3 mV is calculated, with the peak voltage in the center and the lowest voltage in the shaded regions beneath the busbars. A more significant voltage gradient is simulated under Gaussian illumination. The peak voltage occurs at the center of the device where the illumination intensity is largest. The lowest voltage is found at the edges of the device, which are not illuminated, and beneath the busbars. Under this highly nonuniform illumination condition, the total difference in voltage between the central peak and V_{MP} is 61.7 mV, a factor of four larger than the maximum voltage gradient under uniform illumination.

Despite the significantly larger peak voltage simulated under Gaussian illumination, the value of V_{MP} is largest under uniform illumination [see Fig. 3(c) and (d)]. This is because lateral conduction losses are more significant under nonuniform illumination, and the darker regions at the cell's periphery bring down V_{MP}. Given that the DCM does not account for localized heating, the temperature-induced voltage drop [see Fig. 3(a) and (b)] may be even more significant than lateral conduction losses in a physical device, resulting in a larger drop in V_{MP} under nonuniform illumination than predicted by the model.

Fig. 2(c) shows that deviations from the logarithmic trend in W_{OC} at higher illumination powers are more significant for the lattice-mismatched MM-GaInAs/GaAs PPC compared to the lattice-matched InGaAsP/InP PPC. This suggests that the MM-GaInAs material has lower lateral conductivity compared to the lattice-matched InGaAsP, resulting in more significant resistive losses. This observation is consistent with the sheet resistances measured in the window layers of each device, which are $7.7 - 8\ \Omega/\square$ and $39 - 49\ \Omega/\square$ for the InGaAsP/InP and the MM-GaInAs/GaAs PPCs, respectively. Improving the lateral conductivity within the metamorphic device may help to enhance its voltage under nonuniform illumination. Lower thermal conductivity within the MM-GaInAs/GaAs PPC compared to the lattice-matched device may also contribute to its increased W_{OC}, but this effect has not been quantified.

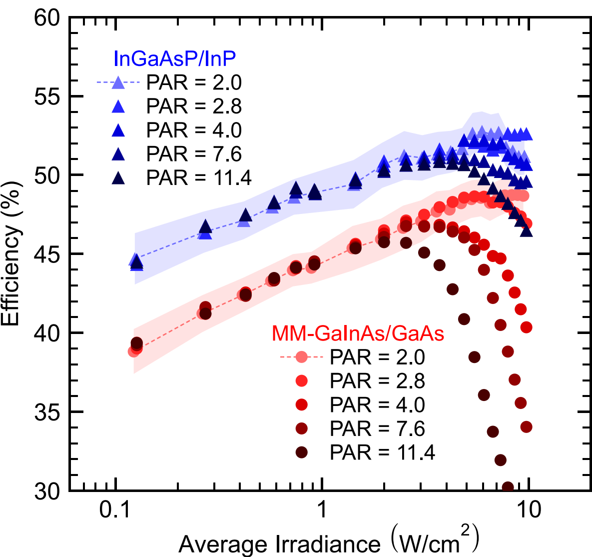

Fig. 4. Efficiency as a function of average irradiance for the InGaAsP/InP and MM-GaInAs/GaAs PPCs. Measured data is shown for the five laser spot sizes. The shaded regions indicate the uncertainty on the datasets with $\mathrm{PAR} = 2$.

C. Optical-to-Electrical Conversion Efficiency

Though analysis of the V_{OC} is critical to understanding PPC performance, it is not the only factor influencing device efficiency. The optical-to-electrical conversion efficiency is plotted in Fig. 4 as a function of average irradiance for the five laser beam diameters. The largest efficiency for the InGaAsP/InP PPC was 52.8% ± 1.3% (abs.), measured at an average irradiance of $5.94 \pm 0.14\ \mathrm{W/cm^2}$. The largest efficiency for the MM-GaInAs/GaAs PPC was 48.7% ± 1.1% (abs.) at $8.84 \pm 0.20\ \mathrm{W/cm^2}$. The primary source of error is uncertainty in the incident beam power (see Appendix). The maximum efficiency measurements for both devices were recorded for the largest beam diameter of $2w = 2.3$ mm with the correspondingly smallest nonuniformity with $\mathrm{PAR} = 2$. Further efficiency enhancements could be obtained through design optimization and the integration of a back-reflector to enhance the output voltage through photon recycling and optical resonance effects [16], [35].

In general, both PPCs were tolerant to nonuniform illumination profiles up to an average irradiance of $\sim 2\ \mathrm{W/cm^2}$. Efficiency losses observed for smaller beam diameters at higher incident powers can be explained by the reduction in V_{OC} and fill factor observed with increasing PAR. Note that, like V_{OC}, fill factor is also impacted by localized heating effects and series resistance losses. The observed trends indicate that more uniform laser illumination profiles would improve PPC performance under high illumination powers. Transitioning to multijunction device structures would also improve the tolerance to nonuniform illumination by lowering the current density through the device structure, mitigating resistive losses [43]. These measures have the potential to enhance the performance of PPCs at any operation wavelength, but are especially important for long-wavelength PPCs that operate in the O- or C-bands because of the larger number of incident photons per watt of power compared to shorter-wavelength PPCs.

IV. Conclusion

We measured two 6.4-mm² O-band PPCs under laser illumination. The lattice-matched InGaAsP/InP device exhibited a record power conversion efficiency for the O-band of 52.8% ± 1.2% (abs). A robust efficiency of 48.7% ± 1.1% (abs.) was measured for the MM-GaInAs/GaAs PPC, demonstrating the potential for GaAs as a more cost-effective, scalable alternative to InP for O-band PPCs. Even higher efficiencies could likely be achieved for both material systems through design optimization and the integration of a back-reflector.

For both PPCs, the nonuniformity of the illumination profiles had minimal impact on device performance for $I_{\mathrm{avg}} < 2\,\mathrm{W/cm^2}$ and, for $J_{\mathrm{SC,avg}} < 1\ \mathrm{A/cm^2}$, a logarithmic relation was observed between the W_{OC} and $J_{\mathrm{SC,avg}}$ in accordance with the nonideal diode equation. A deviation from this trend under nonuniform illumination occurred for $J_{\mathrm{SC,avg}} > 1\ \mathrm{A/cm^2}$, which can be explained by: 1) lateral conduction losses, as shown by the DCM, and 2) localized heating. Overall, both PPCs are suitable for powering sensors and other devices requiring $\lesssim$ 250 mW, with an appropriate illumination profile. Better performance at higher illumination powers could be achieved by engineering a more uniform illumination profile, optimizing the front metallization, or adopting multi-junction device architectures.

Appendix
Uncertainty in Measured Efficiency

The dominant source of error in the determination of PPC optical-to-electrical conversion efficiencies is uncertainty in the incident illumination power. During the experiment, the incident laser power was determined from the laser diode current, which was controlled directly. The relationship between optical power and diode current was established through a calibration experiment in which the current was stepped up in discrete intervals from the threshold current and the resultant laser power was measured using a Newport 918D-IR-OD2 photodiode detector. Neutral density (ND) filters were used to attenuate the beam power and their transparencies were measured experimentally. The measured efficiencies are shown in Fig. 5 along with the associated error bars, which account for the following sources of error.

1) $\pm 2\%$ calibration uncertainty for the photodiode detector.
2) ±0.1 mW uncertainty for power meter precision.
3) Uncertainty in the filter transparency T:
   – ND1: $T = 10.05 \pm 0.04\%$
   – ND2: $T = 1.373 \pm 0.004\%$
4) $\pm 0.02\%$ uncertainty in laser diode current to account for power fluctuations.
5) Uncertainty of $\pm(0.012\% + 1.3\ \mathrm{mV})$ in the V_{MP}.
6) Range-dependent uncertainties in I_{MP} of:
   $I_{\mathrm{MP}} < 10$ mA: $\pm(0.035\% + 5.6\ \mu\mathrm{A})$
   $10\ \mathrm{mA} \leq \mathrm{I_{MP}} < 100$ mA: $\pm(0.055\% + 56\ \mu\mathrm{A})$
   $100\ \mathrm{mA} \leq \mathrm{I_{MP}} < 1$ A: $\pm(0.066\% + 1.57\ \mathrm{mA})$

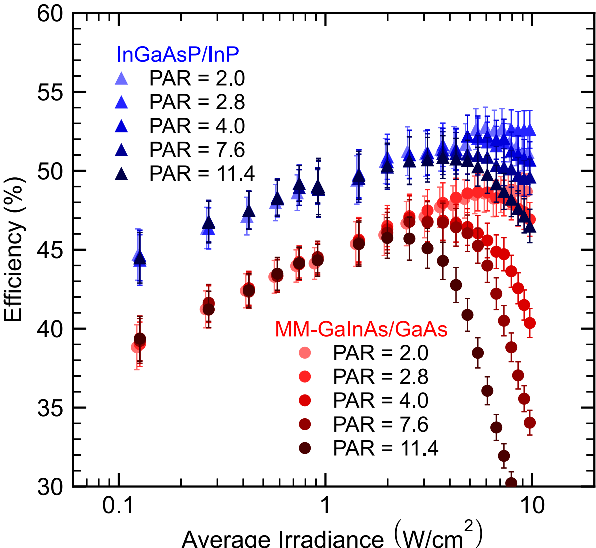

Fig. 5. Efficiency as a function of average irradiance for the InGaAsP/InP and MM-GaInAs/GaAs PPCs. Measured data are shown for the five O-band laser spot sizes. Error bars for each data point are shown.

Acknowledgment

The authors would like to thank Fraunhofer ISE colleagues D. Lackner, S. Stättner, S. Maier, A. Franke, R. Freitas, C. Kopiniok, R. Koch, E. Oliva, E. Schäffer, F. Martin, E. Fehrenbacher, A. Wekkeli, M. Schachtner, and G. Sieferand for fabrication of the PPCs and for measurement support. They would also like to thank CMC Microsystems for providing access to the Synopsys HSPICE software (P-2019.06-1).

References

[1] C. Algora et al., "Beaming power: Photovoltaic laser power converters for power-by-light," *Joule*, vol. 6, pp. 340–368, 2022.

[2] S. Fafard and D. P. Masson, "Perspective on photovoltaic optical power converters," *J. Appl. Phys.*, vol. 130, 2021, Art. no. 160901. [Online]. Available: https://aip.scitation.org/doi/10.1063/5.0070860

[3] M. Matsuura, "Recent advancement in power-over-fiber technologies," *Photonics*, vol. 8, 2021, Art. no. 335.

[4] H. Helmers, C. Armbruster, M. V. Ravenstein, D. Derix, and C. Schoner, "6-W optical power link with integrated optical data transmission," *IEEE Trans. Power Electron.*, vol. 35, no. 8, pp. 7904–7909, Aug. 2020.

[5] J. Fakidis, H. Helmers, and H. Haas, "Simultaneous wireless data and power transfer for a 1-Gb/s GaAs VCSEL and photovoltaic link," *IEEE Photon. Technol. Lett.*, vol. 32, no. 19, pp. 1277–1280, Oct. 2020.

[6] J. W. Shi et al., "GaAs/In $_{0.5}$ Ga$_{0.5}$P laser power converter with undercut mesa for simultaneous high-speed data detection and DC electrical power generation," *IEEE Electron Device Lett.*, vol. 33, no. 4, pp. 561–563, Apr. 2012.

[7] M. Matsuura et al., "Over 40-W electric power and optical data transmission using an optical fiber," *IEEE Trans. Power Electron.*, vol. 36, no. 4, pp. 4532–4539, Apr. 2021.

[8] F. V. B. de Nazaré and M. M. Werneck, "Hybrid optoelectronic sensor for current and temperature monitoring in overhead transmission lines," *IEEE Sensors J.*, vol. 12, no. 5, pp. 1193–1194, May 2012.

[9] K. Worms et al., "Reliable and lightning-safe monitoring of wind turbine rotor blades using optically powered sensors," *Wind Energy*, vol. 20, pp. 345–360, 2017.

[10] A. Ahnood et al., "Laser driven miniature diamond implant for wireless retinal prostheses," *Adv. Biosyst.*, vol. 4, 2020, Art. no. 2000055.

[11] C. Algora and R. Peña, "Recharging the battery of implantable biomedical devices by light," *Artif. Organ.*, vol. 33, pp. 855–860, 2009.

[12] J. D. Lopez-Cardona, D. S. Montero, and C. Vazquez, "Smart remote nodes fed by power over fiber in Internet of Things applications," *IEEE Sensors J.*, vol. 19, no. 17, pp. 7328–7334, Sep. 2019.

[13] T. Umezawa et al., "100-ghz radio and power over fiber transmission through multicore fiber using optical-to-radio converter," *J. Lightw. Technol.*, vol. 36, no. 2, pp. 617–623, Jan. 2018.

[14] M. M. Wilkins et al., "Ripple-free boost-mode power supply using photonic power conversion," *IEEE Trans. Power Electron.*, vol. 34, no. 2, pp. 1054–1064, Feb. 2019.

[15] J. B. Rosolem, "Power–over–fiber applications for telecommunications and for electric utilities," in *Proc. Opt. Fiber Wireless Commun.*, R. Róka, Ed. InTechOpen, 2017, pp. 255–278.

[16] H. Helmers et al., "68.9% efficient GaAs-based photonic power conversion enabled by photon recycling and optical resonance," *Physica Status Solidi - Rapid Res. Lett.*, vol. 15, 2021, Art. no. 2100113.

[17] S. Fafard et al., "High-photovoltage GaAs vertical epitaxial monolithic heterostructures with 20 thin p/n junctions and a conversion efficiency of 60%," *Appl. Phys. Lett.*, vol. 109, 2016, Art. no. 131107.

[18] S. Fafard et al., "Ultrahigh efficiencies in vertical epitaxial heterostructure architectures," *Appl. Phys. Lett.*, vol. 108, 2016, Art. no. 071101.

[19] J. Huang et al., "Characterizations of high-voltage vertically-stacked GaAs laser power converter," *J. Semicond.*, vol. 39, 2018, Art. no. 094006.

[20] C. E. Valdivia et al., "Five-volt vertically-stacked, single-cell GaAs photonic power converter," in *Proc. SPIE 9358*, Physics, Simulation, and Photonic Engineering of Photovoltaic Devices IV, vol. 9358. SPIE, 3 2015, Art. no. 93580E.

[21] J. Schubert et al., "High-voltage GaAs photovoltaic laser power converters," *IEEE Trans. Electron Devices*, vol. 56, no. 2, pp. 170–175, Feb. 2009.

[22] E. Oliva, F. Dimroth, and A. Bett, "GaAs converters for high power densities of laser illumination," *Prog. Photovolt., Res. Appl.*, vol. 16, pp. 289–295, 2008.

[23] S. Fafard et al., "Power and spectral range characteristics for optical power converters," *Energies*, vol. 14, 2021, Art. no. 4395.

[24] N. A. Kalyuzhnyy et al., "Optimization of photoelectric parameters of InGaAs metamorphic laser ($\lambda = 1064$ nm) power converters with over 50% efficiency," *Sol. Energy Mater. Sol. Cells*, vol. 217, 2020, Art. no. 110710.

[25] V. P. Khvostikov et al., "GaInAsP/InP-based laser power converters ($\lambda = 1064$ nm)," *Semiconductors*, vol. 52, pp. 1748–1753, 2018.

[26] M. A. Green, J. Zhao, A. Wang, and S. R. Wenham, "45% efficient silicon photovoltaic cell under monochromatic light," *IEEE Electron Device Lett.*, vol. 13, no. 6, pp. 317–318, Jun. 1992.

[27] A. C. Wang et al., "Characteristics of 1520 nm InGaAs multijunction laser power converters," *Appl. Phys. Lett.*, vol. 119, 2021, Art. no. 243902.

[28] H. Helmers, "Photonic power converters for telecom optical wavelength bands," in *Proc. Tech. Dig. 4th Opt. Wireless Fiber Power Transmiss. Conf. (OWPT2-05)*, 2022.

[29] V. P. Khvostikov et al., "GaSb laser-power ($\lambda = 1550$ nm) converters: Fabrication method and characteristics," *Semiconductors*, vol. 50, pp. 1338–1343, 2016.

[30] S. D. Jarvis, J. Mukherjee, M. Perren, and S. J. Sweeney, "Development and characterisation of laser power converters for optical power transfer applications," *IET Optoelectron.*, vol. 8, pp. 64–70, 2014.

[31] M. N. Beattie et al., "Two-junction III-V photonic power converter operating at monochromatic telecom wavelengths," in *Proc. IEEE 47th Photovoltaic Specialists Conf. (PVSC)*, 2020, pp. 1062–1066.

[32] H. Helmers et al., "51% efficient photonic power converters for O-band wavelengths around 1310 nm," in *Proc. IEEE 47th Photovoltaic Specialists Conf. (PVSC)*, 2020, pp. 2471–2474.

[33] H. Helmers, A. Franke, D. Lackner, O. Höhn, and F. Dimroth, "Photovoltaic laser power converter for O-band wavelengths around 1310 nm," in *Proc. Tech. Dig. 2nd Opt. Wireless Fiber Power Transmiss. Conf. (OWPT3-03)*, 2020.

[34] M. N. Beattie et al., "Non-uniform illumination impacts on O-band InGaAsP and metamorphic GaInAs photonic power converters," in *Proc. Tech. Dig. 3 rd Opt. Wireless Fiber Power Transmiss. Conf. (OWPT3-04)*. American Institute of Physics Inc., 2021.

[35] N. Nouri, C. E. Valdivia, M. N. Beattie, M. S. Zamiri, and K. Hinzer, "Thin photonic power converters designs with back reflector operating at a 1310 nm wavelength," in *Proc. 47th IEEE Photovoltaic Specialists Conf. (PVSC)*, vol. 2020-June. Institute of Electrical and Electronics Engineers Inc., 2020, pp. 2359–2362.

[36] D. Xia et al., "Opportunities for high efficiency monochromatic photovoltaic power conversion at 1310 nm," in *Proc. IEEE 46th Photovoltaic Specialists Conf. (PVSC)*, 2019, pp. 2303–2306.

[37] H. Helmers, A. Franke, J. Ohlmann, F. Dimroth, and D. Lackner, “GaAs based engineered substrates for lattice matched epitaxial growth on lattice constants between GaAs and InP,” in *Proc. Tech. Dig. 2nd Opt. Wireless Fiber Power Transmiss. Conf. (OWPT4-02)*, 2020.

[38] D. Xia and J. J. Krich, “Efficiency increase in multijunction monochromatic photovoltaic devices due to luminescent coupling,” *J. Appl. Phys.*, vol. 128, 2020, Art. no. 0 13101.

[39] R. M. France et al., “Design flexibility of ultra-high efficiency 4-junction inverted metamorphic solar cells,” *IEEE J. Photovolt.*, vol. 6, no. 2, pp. 578–583, Mar. 2016.

[40] F. Dimroth et al., “Four-junction wafer-bonded concentrator solar cells,” *IEEE J. Photovolt.*, vol. 6, no. 1, pp. 343–349, Jan. 2016.

[41] R. M. France, F. Dimroth, T. J. Grassman, and R. R. King, “Metamorphic epitaxy for multijunction solar cells,” *MRS Bull.*, vol. 41, pp. 202–209, 2016.

[42] Y. Suzaki and A. Tachibana, “Measurement of the μm sized radius of gaussian laser beam using the scanning knife-edge,” *Appl. Opt.*, vol. 14, pp. 2809–2810, 1975.

[43] C. E. Valdivia et al., “Many-junction photovoltaic device performance under non-uniform high-concentration illumination,” in *Proc. 13th Int. Conf. Concentrator Photovoltaic Syst. (CPV-13)*, vol. 1881. American Institute of Physics Inc., 2017, Art. no. 0 70005.

[44] P. Sharma, M. M. Wilkins, H. P. Schriemer, and K. Hinzer, “Concentrating optical system optimization for 3- and 4-junction solar cells: Impact of illumination profiles,” *J. Photon. Energy*, vol. 7, 2017, Art. no. 0 14501.

[45] G. Kolhatkar et al., “Current-voltage measurements within the negative differential resistance region of AlGaAs/AlGaAs tunnel junctions for high concentration photovoltaics,” *Int. J. Nanoscience*, vol. 11, 2012, Art. no. 1240014.

[46] M. Steiner et al., “A validated spice network simulation study on improving tunnel diodes by introducing lateral conduction layers,” *Prog. Photovolt., Res. Appl.*, vol. 20, pp. 274–283, 2012.

[47] W. Guter and A. W. Bett, “I-V characterization of tunnel diodes and multijunction solar cells,” *IEEE Trans. Electron Devices*, vol. 53, no. 9, pp. 2216–2222, Oct. 2006.

[48] P. Espinet, I. García, I. Rey-Stolle, C. Algora, and M. Baudrit, “Distributed simulation of real tunnel junction effects in multi-junction solar cells,” in *Proc. 6th Int. Conf. Concentrating Photovol- taic Syst. (CPV-6)*, 2010, pp. 24–27.

[49] A. Braun et al., “Localized irradiation effects on tunnel diode transitions in multi-junction concentrator solar cells,” *Sol. Energy Mater. Sol. Cells*, vol. 93, pp. 1692–1695, 2009. [Online]. Available: http://dx.doi.org/10.1016/j.solmat.2009.04.022

[50] V. M. Andreev et al., “Tunnel diode revealing peculiarities at I-V measurements in multijunction III-V solar cells,” in *Proc. IEEE 4th World Conf. Photovoltaic Energy Convers. (WCPEC)*, IEEE Computer Society, 2006, vol. 1, pp. 799–802.

[51] J. M. Gordon, E. A. Katz, W. Tassew, and D. Feuermann, “Photovoltaic hysteresis and its ramifications for concentrator solar cell design and diagnostics,” *Appl. Phys. Lett.*, vol. 86, 2005, Art. no. 0 73508.

[52] M. N. Beattie et al., “High current density tunnel diodes for multi-junction photovoltaic devices on InP substrates,” *Appl. Phys. Lett.*, vol. 118, 2021, Art. no. 0 62101.

[53] R. R. King et al., “Bandgap-voltage offset and energy production in next-generation multijunction solar cells,” in *Proc. 5th World Conf. Photovoltaic Energy Convers. 25th Eur. Photovoltaic Sol. Energy Conf.*, 2010, pp. 6–10.

[54] I. Garcia et al., “Metamorphic III-V solar cells: Recent progress and potential,” *IEEE J. Photovolt.*, vol. 6, no. 1, pp. 366–373, Jan. 2016.

[55] A. Cuevas and S. López-Romero, “The combined effect of non-uniform illumination and series resistance on the open-circuit voltage of solar cells,” *Sol. Cells*, vol. 11, pp. 163–173, 1984.

[56] H. Helmers, M. Schachtner, and A. W. Bett, “Influence of temperature and irradiance on triple-junction solar subcells,” *Sol. Energy Mater. Sol. Cells*, vol. 116, pp. 144–152, 2013. [Online]. Available: http://dx.doi.org/10.1016/j.solmat.2013.03.039

[57] O. Dupré, R. Vaillon, and M. A. Green, “Physics of the temperature coefficients of solar cells,” *Sol. Energy Mater. Sol. Cells*, vol. 140, pp. 92–100, 2015.

[58] G. Siefer and A. W. Bett, “Analysis of temperature coefficients for III-V multi-junction concentrator cells,” *Prog. Photovolt., Res. Appl.*, vol. 22, pp. 515–524, 2014.

[59] M. Z. Shvarts et al., “Temperature tweaking of the output photovoltaic parameters of laser power converters,” *IEEE Electron Device Lett.*, vol. 41, no. 9, pp. 1324–1327, Sep. 2020.

[60] K. Nishioka et al., “Annual output estimation of concentrator photovoltaic systems using high-efficiency InGaP/InGaAs/Ge triple-junction solar cells based on experimental solar cell’s characteristics and field-test meteorological data,” *Sol. Energy Mater. Sol. Cells*, vol. 90, pp. 57–67, 2006.

5.2 53.6% Efficient multi-junction laser power converters for extended telecom range operation

The following journal article presents my research on simulating and characterizing the opto-electronic properties of InGaAs and InGaAsP PPCs for about 1.5 μm wavelengths, utilizing the drift-diffusion and RCWA models described in Section 2.4.3. Using quantum efficiency and IV measurements, I validate a predictive optoelectronic model to show realistic photonic power performances over the 1.0-1.6 μm laser wavelength range.

Impact

The following novelties are presented in the journal article:

1. Measured record-breaking efficiency of 53.6% for a four-junction InGaAsP PPC illuminated by a 1.446 μm laser, predicted and designed using our model.
2. Demonstrated above 5 V operation of a ten-junction InGaAs PPC, used to calibrate the model and improve PPC designs.
3. Developed a rapid optimization method that produces PPC designs that could outperform standard absorption-matched designs. Additionally reported realizable efficiencies over the 1.0-1.6 μm laser wavelength range.
4. Validated a method to non-destructively extract layer thicknesses of multi-junction devices, which can facilitate the fabrication-measurement cycle.

The centerpiece of our work is a predictive model for designing multi-junction PPCs. This model's predictive nature, highlighted by our record-breaking proof-of-concept devices, can be combined use with machine learning to further enhance PPC designs.

Author contribution

Gavin P. Forcade: As a University of Ottawa-based graduate student associated with the project, I led the optoelectronic model development and validation. I performed all simulations. I also measured reflectivity, light IV, and dark IV characteristics of the multi-junction PPCs. I setup and calibrated the PPC measurement setup for the 1.446 μm laser. I conceptualized and performed the reverse bias method measurement to extract layer thicknesses. I was the lead author of the article.

Dr. D. Paige Wilson: As a postdoctoral researcher within the University of Ottawa's SUNLAB research group, Paige built and calibrated the PPC measurement setup for the 1.52 μm laser, helped with setting up the 1.446 μm laser, helped measure the PPC devices, provided detailed feedback during the analysis of the results, and assisted in editing the manuscript.

Dr. Meghan Beattie: As a postdoctoral researcher within the University of Ottawa's SUNLAB research group, Meghan built the PPC measurement setup, measured the quantum efficiency of single-junction InGaAs isotypes, provided detailed feedback during the analysis of the results, and assisted in editing the manuscript.

Dr. Carmine Pellegrino: As a researcher at the Fraunhofer Institute for Solar Energy Systems, Carmine grew the PPCs, measured the epitaxial layer thicknesses with cross-sectional scanning electron microscope imaging, measured quantum efficiencies of single-junction InGaAsP isotypes, provided detailed feedback during the analysis of the results, and assisted in editing the manuscript.

Dr. Henning Helmers: As a researcher at the Fraunhofer Institute for Solar Energy Systems, Henning oversaw the research, provided detailed feedback during the analysis of the results, and assisted in editing the manuscript.

Robert F.H. Hunter: As a University of Ottawa-based graduate student associated with the project, Robert wrote software tools to expedite data analysis, helped to measure the quantum efficiency of the single-junction InGaAs isotypes, helped to design the four-junction InGaAsP PPC, provided detailed feedback during the analysis of the results, and assisted in editing the manuscript.

Dr. Oliver Höhn: As a researcher at Fraunhofer Institute for Solar Energy Systems, Oliver

helped to guide the research, fabricated the devices, provided detailed feedback during the analysis of the results, and assisted in editing the manuscript.

Dr. David Lackner: As a researcher at the Fraunhofer Institute for Solar Energy Systems, David helped to guide the research, oversaw epi-growth, provided detailed feedback during the analysis of the results, and assisted in editing the manuscript.

Louis-Philippe St-Arnaud: As a University of Ottawa-based undergraduate student associated with the project, Louis-Philippe helped with light and dark current-voltage measurements of the single-junction InGaAs devices.

Dr. Thomas N.D. Tibbits: As a researcher at the Fraunhofer Institute for Solar Energy Systems, Thomas helped with epi-growth.

Dr. Christopher E. Valdivia: As a senior research scientist within the University of Ottawa's SUNLAB research group, Chris helped to guide the research and provided detailed feedback during the analysis of the results.

Dr. Yuri Grinberg: As a research scientist at the National Research Council of Canada, Yuri assisted in editing the manuscript.

Dr. Alexandre W. Walker: As a research scientist at the National Research Council of Canada, Alexandre helped to guide the research, provided detailed feedback during the analysis of the results, and assisted in editing the manuscript.

Prof. Jacob J. Krich: As a University of Ottawa based professor associated with the project, Jacob helped to guide the research, provided detailed feedback during the analysis of the results, and assisted in editing the manuscript.

Prof. Karin Hinzer: As the director of the University of Ottawa's SUNLAB research group, Karin oversaw the research, provided detailed feedback during the analysis of the results, and assisted in editing the manuscript.

The submitted version of the manuscript:

> G.P. Forcade, D.P. Wilson, M.N. Beattie, C. Pellegrino, H. Helmers, R.F.H. Hunter, O. Hohn, D. Lackner, L-P. St-Arnaud, T.N.D. Tibbits, C.E. Valdivia, Y. Grinberg,

A.W. Walker, J.J. Krich, and K. Hinzer, "53.6% efficient multi-junction laser power converter for extended telecom range operation", under revisions 2024.

53.6% Efficient Multi-Junction Laser Power Converter for Extended Telecom Range Operation

Gavin P. Forcade[1], D. Paige Wilson[2], Meghan N. Beattie[2], Carmine Pellegrino[3], Henning Helmers[3], Robert F. H. Hunter[2], Oliver Höhn[3], David Lackner[3], Louis-Philippe St-Arnaud[2], Thomas N.D. Tibbits[3], Christopher E. Valdivia[2], Yuri Grinberg[2,4], Alexandre W. Walker [1,5], Jacob J. Krich[1], Karin Hinzer[1,2]

SUMMARY

Photonic or laser power converters are crucial components in power-by-light systems. However, their deployment in 5G telecom has been hindered by low efficiencies and output voltages within the optical fiber transmission window of 1.3-1.6 µm laser wavelengths. Here, we improve and simplify the design and characterization processes for photonic power converters, achieving a significant breakthrough by exceeding the 50% efficiency barrier. We develop a calibrated predictive model that anticipates designs with up to 57% efficiency when combined with our rapid optimization method, outperforming standard absorption-matched designs. As a first demonstration, we produce a record-efficiency device: a four-junction InGaAsP photonic power converter with a conversion efficiency of 53.6% ± 1.3% and an output voltage above 2 V under 15.2 W/cm^2 of 1.446 µm laser light. These advances open new, practical pathways for integrating photonic power converters in 5G telecom and unlock the potential of combining the model with machine learning to further optimize their design.

[1] Department of Physics, University of Ottawa, Ottawa, ON, Canada
[2] SUNLAB, School of Electrical Engineering and Computer Sciences, University of Ottawa, Ottawa, ON, Canada
[3] Fraunhofer Institute for Solar Energy Systems ISE, 79110 Freiburg, Germany
[4] Digital Technologies Research Center, National Research Council of Canada, Ottawa, ON, Canada
[5] Quantum and Nanotechnologies Research Center, National Research Council of Canada, Ottawa, ON, Canada

INTRODUCTION

Power-by-light systems[1,2] benefit from end-to-end electrical and galvanic isolation and are safer and more secure than conventional electrical power transmission. For instance, power-by-light systems can be helpful for reducing risk of fires or explosions,[3] preventing malfunction near high voltages,[4,5] remote powering of rechargeable batteries[6], space exploration,[7] and powering 5G technologies.[8,9] They can be used to transmit photonic power and data simultaneously.[3,5,10–12]

Typically, power-by-light systems transmit laser light to a photonic power converter (PPC),[1,2] sometimes called a laser power converter. PPCs are photovoltaic cells that convert monochromatic light into electrical power. They are designed to produce the operating voltages needed to power electrical devices (such as 1.8 V, 3.3 V, or 5 V)[13] above the open-circuit voltage of any single-junction photovoltaic device. The most effective method of achieving such an output voltage is using the III-V semiconductor-based multi-junction architecture, consisting of an epitaxially grown stack of photovoltaic *p-n* junctions interconnected with tunnel diodes.[2,13–16] However, multi-junction cells have demonstrated greater wavelength sensitivity compared to single-junction devices due to current matching constraints,[2,17,18] which must be accounted for in system designs.

When designing PPCs, maximizing the optical-to-electrical power conversion efficiency is crucial. Tuning the laser wavelength and the bandgap of the PPC's absorber material can minimize thermalization, transparency, and current-collection losses. For long-distance power transmission through optical fibers, laser wavelengths within 1.3-1.6 µm (see Figure 1A) minimize attenuation losses.[2] Where higher laser power and efficiency are necessary but optical fiber

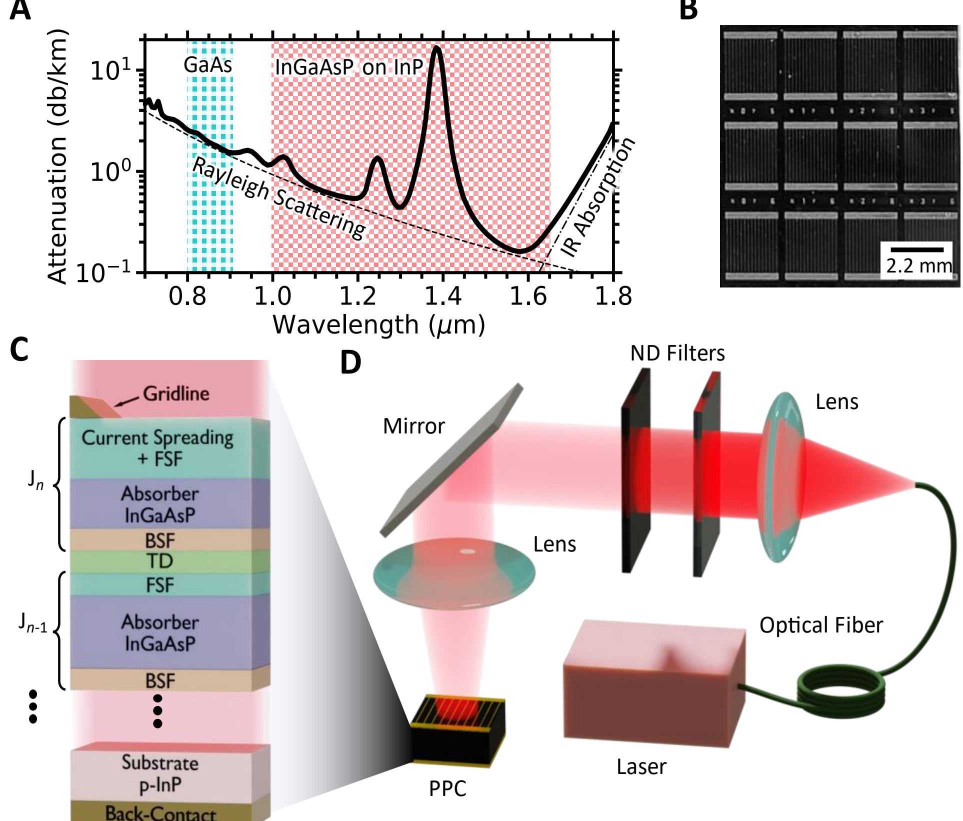

Figure 1. Photonic power converter (PPC) device structure and measurement setup

(A) Attenuation of light's electromagnetic spectrum within an optical fiber, highlighting in red mesh the range of wavelengths targeted in this study. Our target corresponds to the frequency range $(1.9\text{-}3)\times10^{14}$ Hz which is equivalent to a photon energy range of 0.736-1.215 eV.

(B) Top-view photograph of our 2.2×2.9 mm^2 PPC chips, the designated area (mesa minus busbar area) is 0.054 cm^2.

(C) Schematic cross-section of the multi-junction PPC which is comprised of subcells containing InGaAsP absorber layers cladded with larger bandgap front and back surface field (FSF and BSF) layers. The *n* subcells are connected in series with tunnel diodes (TD).

(D) Schematic diagram of the PPC measurement setup.

transmission losses are negligible, 1 µm is of interest.[19] Therefore, we employ absorber materials composed of InGaAsP (bandgap 0.736-1.215 eV) lattice-matched to InP to cover this range. So far, single-junction PPCs using this material have achieved efficiencies up to 52.8% at 1.31 µm,[20] but suffer from low output voltages of 0.6 V. However, multi-junction PPCs designed for these wavelengths have yet to achieve efficiencies above 50%.[13] We present a four-junction PPC with InGaAsP (bandgap 0.8 eV) absorber layers that surpasses the 50% efficiency barrier at 1.446 µm, realized through rigorous design optimization using a comprehensive model. Without such models, high efficiencies of multi-junction PPCs are inaccessible.

Various techniques have been used to model PPCs,[21–23] providing different pathways to optimization. Friedman et al.[24] predicted enhanced efficiencies of high-quality material photovoltaic devices beyond the absorption-matching thicknesses by optimizing devices while considering luminescent coupling[17,25,26] – radiative recombination that is reabsorbed in any junction other than the one in which it was emitted. Xia and Krich[22] presented a detailed-balance model including luminescent coupling and parametrized all nonradiative processes through an internal radiative efficiency but omitted optical interference effects arising from changes in refractive indices between layers, as well as realistic electrical transport effects. We employ a

calibrated drift-diffusion model that includes luminescent coupling, which promises more accurate predictions at the cost of being more computationally expensive[27,28] than both Friedman[24] and Xia[22] models.

To maximize the integration of power-by-light systems into 5G telecom systems, it is desirable to use the same fiber for simultaneous power and data transmission. However, this dual-use fiber configuration requires careful wavelength optimization to avoid negatively impacting data quality;[9,29] it is therefore essential to understand PPC performance versus wavelength. Thus, we use our model within the corresponding 1.0-1.6 µm laser wavelength range (see Figure 1A) and predict attainable efficiencies up to 67%. Within the optical fiber transmission window (1.3-1.6 µm), we anticipate efficiencies of up to 57%. We perform a sensitivity analysis, varying laser wavelength and absorber material bandgap to investigate the tolerance of our PPC efficiency to operational conditions and epitaxy variances.

We present the optoelectronic properties of processed single-, four-, and ten-junction PPCs. The single- and ten-junction PPCs, featuring $In_{0.53}Ga_{0.47}As$ (bandgap 0.736 eV) absorber layers, are used to calibrate our model, enhance our understanding of multi-junction PPCs during operation, demonstrate our ability to achieve an output voltage above 5 V, and validate a technique for non-destructively determining PPC absorber thicknesses. Using our calibrated model, we designed the four-junction PPCs with InGaAsP (bandgap 0.8 eV) absorber layers, showcasing the model's predictive capabilities and achieving record efficiencies.

RESULTS

Ten-junction InGaAs/InP PPC

Ten-junction PPCs were grown and fabricated at Fraunhofer ISE (see "Experimental Procedures"). A top-down view photo of these devices is shown in Figure 1B and the schematic structure in Figure 1C. The absorber layers of our fabricated ten-junction devices are $In_{0.53}Ga_{0.47}As$ and the bottom junction is J_1, as labeled in Figure 1C. Single-junction isotypes were also fabricated for model calibration purposes.

We tested the performance of our ten-junction PPCs under high-powered 1.52 µm laser illumination. These devices were designed to be absorption-matched at 1.55 µm, ensuring each junction absorbs an equal number of photons, assuming Beer-Lambert absorption with an extinction coefficient of 0.12 and a cumulative thickness to absorb 97% of the semiconductor-impinging light. The ten-junction device was processed before acquiring the nominally 1.55 µm laser, which lased at a measured 1.52 µm. The 30 nm discrepancy between the nominal and actual laser wavelength highlights the importance of considering laser wavelength variation during PPC optimization. The extinction coefficient used for designing the ten-junction device was 37% larger than the value later measured from the single-junction isotypes (see Supporting information for measured values), this difference was not due to the 30 nm wavelength shift. We show this overestimation was the dominating factor in lowering the ten-junction PPC efficiency from the optimal 53% by $15\%_{rel}$. A schematic of the experimental setup is shown in Figure 1D. Details on the setup and the power calibration procedure are presented in "Experimental Procedures".

Modeling the ten-junction PPC

We develop a 1D optoelectronic model coupling drift-diffusion theory and rigorous coupled wave analysis (RCWA),[30,31] while accounting for luminescent coupling,[26] to simulate the PPC. Our model employs uniform normally incident radiation and assumes a 3% gridline shading. This gridline configuration was optimized to minimize the competing lateral resistance and shading losses, based on the anticipated current densities under high illumination.

To accurately model the device, absorber layer thicknesses and absorption coefficients must be known precisely (<5% error). We obtain absorption coefficients using reverse internal quantum

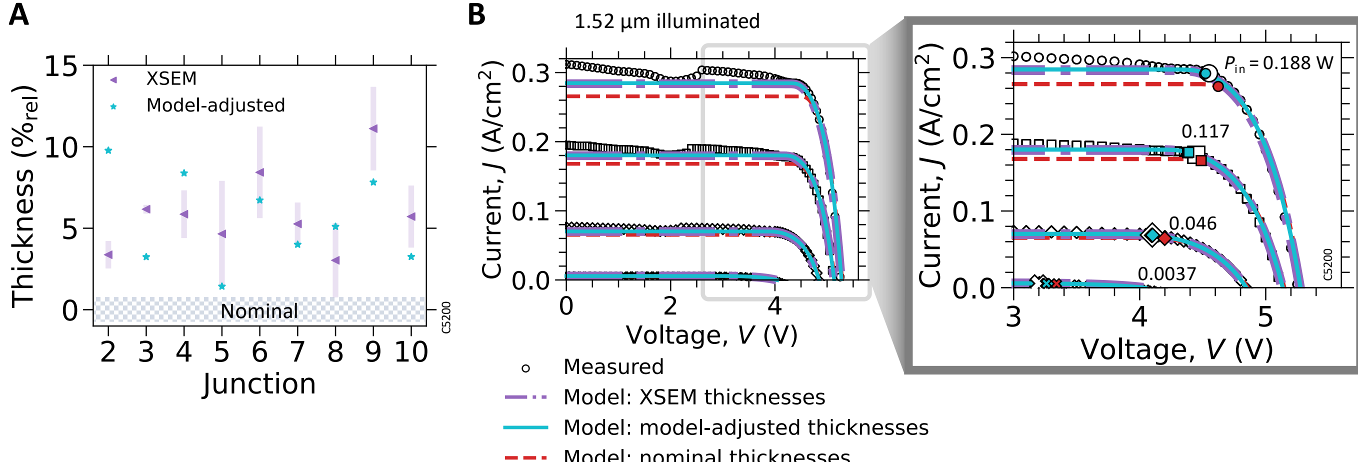

Figure 2 . Ten-junction InGaAs PPC characterization and model calibration

(A) Comparing junctions' absorber layer thicknesses relative to nominal targets with values obtained from cross-sectional scanning electron microscope images (XSEM) and the reverse bias method (model-adjusted). Note, that the XSEM measurement uncertainty generally increases with junction number as the absorber gets thinner. Also, we do not include confidence intervals for the model-adjusted thicknesses. (B) Comparing current-density-voltage (*J-V*) characteristics of a 1.52 µm laser-illuminated PPC with varying input powers. We include measurements (white symbols) and simulation results that assume XSEM thicknesses (dot/dash-purple), model-adjusted thicknesses (solid-blue), and nominal thicknesses (dashed-red). (Right) Zoom in on the *J-V* curves with maximum power-point highlighted with large color-coded symbols. The simulated *J-V* curves from XSEM and model-adjusted thicknesses are on top of each other.

efficiency measurements of single-junction isotypes (see "Experimental Procedures"). We obtain the thicknesses in two ways: a reverse bias measurement coupled with optical-only simulations (reverse bias method), a method that can be easily and non-destructively applied to other devices, and cross-sectional scanning electron microscopy after cleaving samples (XSEM method). Both procedures are detailed in "Experimental Procedures". We compare absorber layer thicknesses acquired with each method and compare them to their growth targets (nominal thicknesses) in Figure 2A. Both methods indicate that absorber layers were thicker than the target, with a mean deviation of the layer thicknesses from the target of 5% for the reverse bias method and 6% for the electron microscopy method. The mean absolute thickness difference between methods is 2.9% and could originate from performing the methods at different locations on the wafer. However, Figure 2C shows that simulated current-voltage curves for both model-adjusted and electron microscopy thicknesses are indistinguishable from each other but significantly different from those that would have been produced by a device with nominal thicknesses. These results validate our reverse bias method, a powerful tool that could also be used to simultaneously extract absorber bandgaps and thicknesses of multi-junction devices by using multiple illumination wavelengths.

To complete the drift-diffusion model, we use the model-adjusted layer thicknesses and assume that all absorber layers have the same Shockley-Read-Hall lifetime (τ_{SRH}), a parameter that reflects the material's quality, and find that τ_{SRH}=0.11 µs gives the best agreement between the measured and simulated current-voltage characteristics. The results for the ten-junction PPC under 0.06-3 W/cm^2 irradiance with 1.52 µm wavelength, are shown in Figure 2B. Our τ_{SRH} is shorter than those in Refs.[32,33] which ranged from 1.7-2.6 µs as well as the single-junction isotype cells that showed 3 µs from fitting the dark current measurements (see Supplemental Information for details); this reduced lifetime could be caused by the additional thermal load on the epi-material arising from the significantly longer growth time for the ten-junction device. Our model accurately predicts the measured maximum power point within <1%. The current-voltage curves fail to align with measurements near short-circuit (J_{sc}) due to the omission of reverse breakdown, Franz-Keldysh, and quantum-confined Stark effects.[34,35] However, these omissions do not impact the results presented in this paper, as we focus solely on voltages near maximum power, where no subcells are operating in a breakdown regime. It is worth noting that

the model overestimates the open-circuit voltage (V_{oc}) by 0.4% for a 0.188 W input power (2.94 W/cm^2), which we attribute to cell heating during measurement.

Ten-junction PPC characterization and performance

We measure our ten-junction PPC under 1.52 µm laser illumination and observe a maximum efficiency of 46.4 ± 1.1% at an irradiance of 35 W/cm^2, a voltage output at maximum power of 5.01 V, and an open-circuit voltage of 5.78 V. The measured open-circuit voltage and the efficiency as a function of irradiance are shown in Figure 3A (top) and (bottom) respectively. We also include calculated values from our validated model and the radiative limit for the device structure. We obtain good agreement between the validated model, which uses the model-adjusted thicknesses and τ_{SRH} of 0.11 µs, and the measurements for average irradiances up to 10 W/cm^2. We attribute the deviation above 10 W/cm^2 to cell heating, which our model does not account for. The measured V_{oc} was up to 0.4 V lower than the simulated voltage at an irradiance of 50 W/cm^2, corresponding to an average 0.04 V drop per junction. This voltage reduction is similar to the 0.035 V heating-induced drop of the single-junction GaAs PPC from Geisz et al.[36] when illuminated with the same intensity. The radiative limit is calculated with the detailed balance model presented in Ref. [22] assuming no reflection losses and 98% absorption. The measured efficiency approaches the radiative limit as irradiance increases, with a minimum difference of 27%$_{rel}$ at 10 W/cm^2.

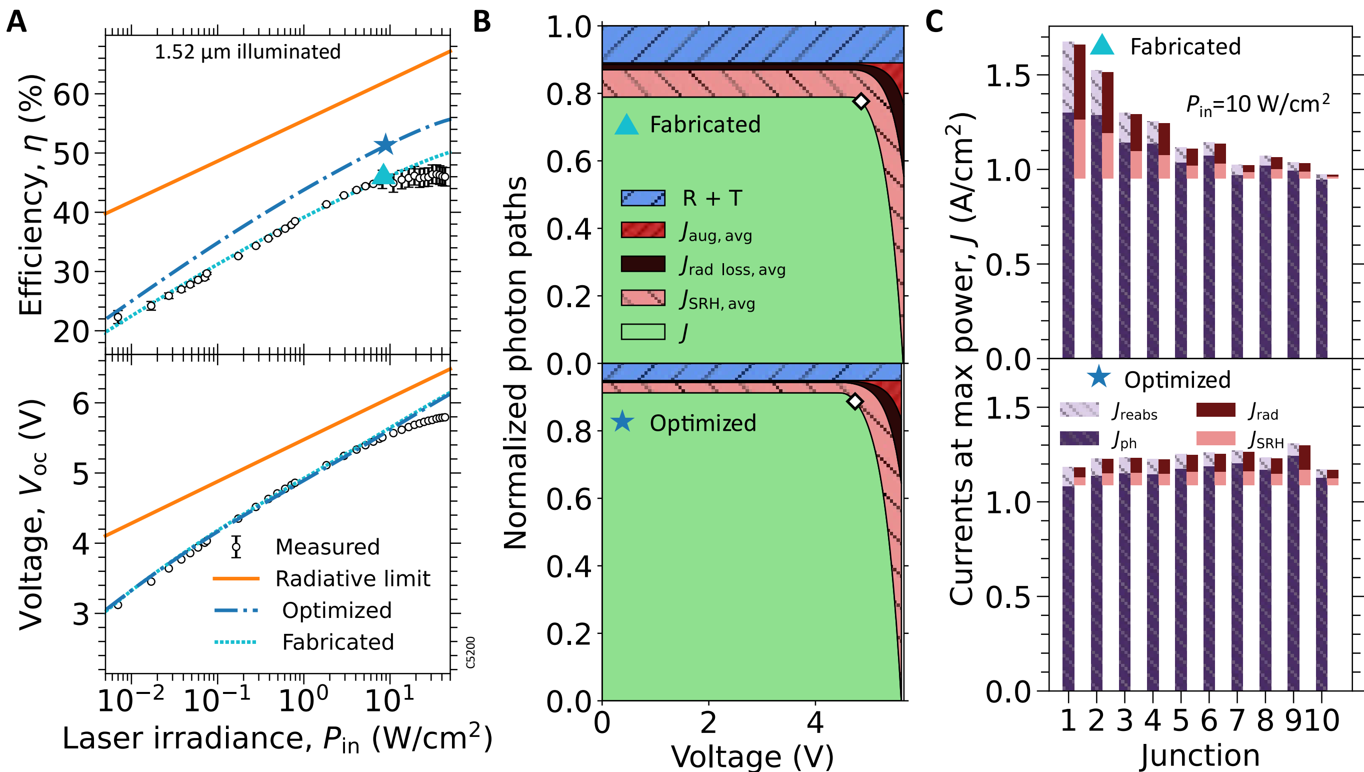

Figure 3. Ten-junction InGaAs PPC performance

(A) Efficiency (top) and open-circuit voltage (bottom) versus 1.52 µm laser irradiance, comparing calibrated measurements with simulation (short-dash). The plots also include the performances of the layer thickness optimized design (long-dash) and the radiative limit (solid).

(B) The stack plots depict the extracted current (J) and loss mechanisms averaged over all the subcells, normalized to the incident photon flux, of the fabricated (top) and optimized (bottom) PPC designs illuminated with a 1.52 µm laser at 10 W/cm^2. The white diamond highlights the maximum power point.

(C) Bar charts separating current generations and recombinations in each subcell at the maximum power point of the fabricated (top) and optimized (bottom) PPC designs illuminated with a 1.52 µm laser at 10 W/cm^2.

(B,C) The currents include reabsorbed photons (J_{reabs}), first-pass photon absorption (J_{ph}), first-pass photon loss from reflection at the top surface and transmission into the substrate (R+T), SRH recombination (J_{SRH}), Auger recombination (J_{aug}), radiative recombination (J_{rad}), and photons from radiative recombination that escape into the substrate or outside the top of the cell ($J_{rad\ loss}$). Note that the thinnest top subcell is J_{10} and currents with an avg subscript are the averaged currents over all junctions.

To improve the performance of our ten-junction PPC, we use our model to determine where it loses efficiency. We simulate the current collection and loss mechanisms normalized to the maximum achievable current from the photon flux at 10 W/cm^2 irradiance, with results shown in Figure 3B (top). The device collects at most 78% of the potential current density (J), with the remainder going to optical and recombination losses. The optical losses include a 5% transmission loss into the substrate and a 6% reflection loss from the anti-reflection coating (which was optimized for a 1.55 µm wavelength) along with gridline shading.

We can see the effects of current mismatch between the junctions by segregating the device's current generation and loss mechanisms in each junction at the maximum power point when illuminated with 10 W/cm^2, shown in Figure 3C (top). At 1.52 µm, the fabricated design absorbs 37% more light (J_{ph}) in the bottom subcell than in the top subcell. This current mismatch occurred due to designing the PPC with incorrect absorption coefficients and was not the 30 nm wavelength shift. Figure 3C shows that the bottom junctions radiate significantly (J_{rad}) and recycle much of that radiation (J_{reabs}), with less luminescent coupling to the top junctions, which need it. Although J_{sc} increased by 2.2% due to luminescent coupling, excess absorption in the bottom subcell causes radiative recombination to escape from that subcell, half of which is lost to the substrate. Redesigning the cell to have matched J_{ph} removes these problems.

Enhancing performance through layer-thickness-optimized PPC design

Despite achieving high efficiency, we sought to improve our ten-junction InGaAs PPC by determining the ideal absorber layer thicknesses, assuming the same material quality (τ_{SRH} of 0.11 µs). The layer-thickness-optimized PPC design employs luminescent coupling-optimized absorber layer thicknesses calculated using the detailed balance model,[22] see "Experimental Procedures" for details. Its performance is shown in Figure 3A. The optimized device efficiency is 19%$_{rel}$ less than the radiative limit but 15%$_{rel}$ more than the fabricated PPC design with minimal impact on V_{oc}.

The optimized device is designed to trap photons from radiative recombination. It exploits a configuration with current-limiting top (J_{10}) and bottom subcells (J_1), as shown in Figure 3C (bottom), and has its highest photogenerated current at junction 9 (J_9). This design is optimal since less than 10% of emitted photons can escape through the top due to total internal reflection and photons emitted towards the substrate are mostly reabsorbed by the accumulated thickness of the lower layers. The simulated current-voltage curve shown in Figure 3B (bottom) reveals that these changes reduce radiative recombination escape ($J_{rad\ loss,avg}$) by 81%$_{rel}$ and improve the J_{sc} gain from luminescent coupling by 50%$_{rel}$, both relative to the fabricated design. Our optimization method, based on the detailed balance model, could be improved by directly optimizing the absorber layer thicknesses using our drift-diffusion model, which includes luminescent coupling. However, this approach would incur a significantly higher computational cost.

The optimized design exhibits a higher extracted current (J) owing to increased light absorption and reduced recombination losses. The sum of the absorber layer thicknesses of the optimized design is 32% thicker than that of the fabricated design, resulting in 3% less transmission loss into the substrate. Antireflection coating optimization for 1.52 µm light eliminates a further 3% reflection loss. The optimized design has a lower recombination loss despite the same τ_{SRH} due to a more uniform distribution of current generation among the junctions. The SRH recombination ($J_{SRH,avg}$) loss near J_{sc}, shown in Figure 3B (top) is more than double for the fabricated device at 8% versus 3% for the optimized device.

In case material can be grown with higher quality, we also explore the impact of improving τ_{SRH} from 0.11 µs to 3 µs on the optimized multi-junction PPC performance. We generate a layer-thickness-optimized design following the procedure described in "Experimental Procedures"

and simulate an efficiency of 57% for a 1.52 µm wavelength irradiance of 10 W/cm^2. This efficiency is 10%$_{rel}$ above the optimized design with τ_{SRH} of 0.11 µs and only 9%$_{rel}$ below the radiative limit.

The multi-junction PPC designs investigated in this work have further opportunities for technical improvements. One pathway forward is to use transparent front contacts,[37] which could improve our device's efficiency by 3%$_{rel}$. Another strategy is to enhance heat dissipation with improved cell packaging (ex: thermal paste) and/or substrate removal. Geisz et al.[36] demonstrated that unpackaged illuminated GaAs PPCs on substrates at ~30 W/cm^2 (irradiance near our maximum measured efficiency) had an efficiency loss due to temperature of 5%$_{rel}$, which approaches the difference between our simulation and measurement of 5.6%$_{rel}$ for the fabricated device (see Figure 3A); thin films released from the growth substrates had a negligible loss. Replacing the substrate with light trapping structures can also enable a 10%$_{rel}$ efficiency gain[37,38] by improving minority carrier collection through 10 times reduced cumulative absorber thickness and reducing radiative loss out of the device. This effect is important for the thick bottom junctions and can reduce epitaxy-related costs. Finally, a pyramidal-shaped gold back-reflector and transparent top contacts could improve our PPC's efficiency to 63% for 35 W/cm^2 irradiance, assuming the above-mentioned gains. In addition, the back-reflector could benefit from luminescent coupling, making it even more robust to temperature and laser wavelength changes. However, including a back-reflector requires careful layer thickness optimization.

Layer-thickness-optimized designs outperform absorption-matched designs

We simulate the optoelectronic performance of the layer-thickness-optimized design and compare it to a similar ten-junction design with simple absorption-matched layer thicknesses calculated using rigorous coupled wave analysis. The efficiency and maximum power point voltage gains achieved by the layer-thickness-optimized design as a function of irradiance are shown in Figure 4 (dashed curve) for a 1.52 µm laser wavelength. Compared to the absorption-matched design, the layer-thickness-optimized design gains up to 0.25%$_{rel}$ in efficiency and up to 0.2% in the maximum power point voltage assuming τ_{SRH}=0.11 µs.

For luminescent coupling to significantly enhance performance, we require a much longer τ_{SRH} than our calculated radiative lifetime of 0.8 µs.[22,39] Therefore, we also investigate the performance gains from a new layer-thickness-optimized design using a τ_{SRH} of 3 µs (procedure detailed in "Experimental Procedures"), representing our average material quality for single-junction isotype cells. This PPC shows greater performance gains than the PPC designed for lower-quality material, as was suggested in Ref.[24]. Also, the layer-thickness-optimized design outperforms the absorption-matched design across the entire range of irradiance we explore

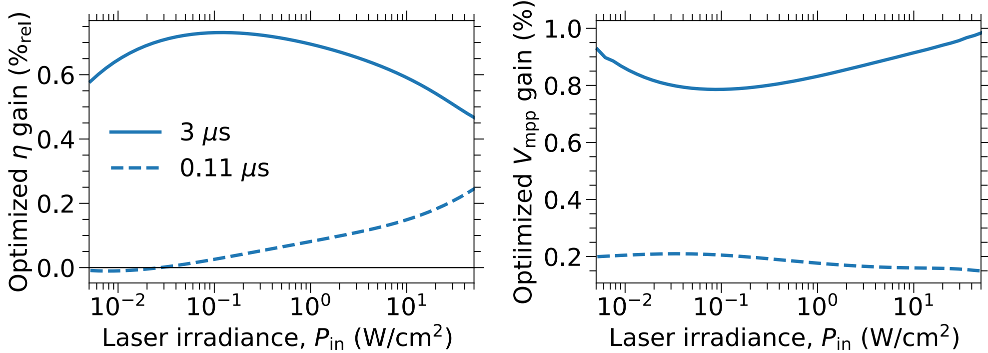

Figure 4. Layer-thickness-optimized designs outperform absorption-matched designs
Efficiency (left) and voltage (right) at maximum power point of ten-junction InGaAs PPCs with layer-thickness-optimized designs relative to absorption-matched designs as a function of 1.52 µm laser irradiance. We explore two material qualities, τ_{SRH} of 0.11 µs and 3 µs.

(solid curve in Figure 4). Efficiency gains can reach up to 0.75%$_{rel}$, while output voltage gains can be up to 1%.

PPCs designed for 1.0-1.6 µm wavelengths

We explore the flexibility and potential of a layer-thickness-optimized PPC design for the 1.0-1.6 µm wavelength range with 10 W/cm^2 irradiance. We consider multi-junction devices with the same metallic grid and layer structure as our fabricated device but instead use InGaAsP absorbers lattice matched to InP, assuming identical quaternary composition for all subcells. We report the bandgap of the material based on the simulated quantum efficiency of single-junction isotypes with 4 µm thick absorber layers, using the method from Helmers et al. [40]. We use the optimization method described in "Experimental Procedures" to select the absorber layer thicknesses, with τ_{SRH} = 0.11 µs. We determine the number of junctions required to achieve an operating voltage V_{mpp} > 5 V by simulating the current-voltage characteristics as a function of the absorber bandgap. This simulation employs input photon energy 30 meV larger than the bandgap, for 4 to 11 junctions, with each variation using a new optimized PPC design. We show the intersections with 5 V in Figure 5A.

Using the minimum number of junctions obtained from Figure 5A to ensure the operating voltage of each device is at least 5 V, we evaluate the efficiency of optimized devices as a function of laser wavelength and absorber bandgap (see Figure 5B). We observe no discontinuity arising from changes in the number of junctions, which agrees with the results from Algora et al.[2] that predicted a flat efficiency profile for PPCs with 5 or more subcells and output powers around

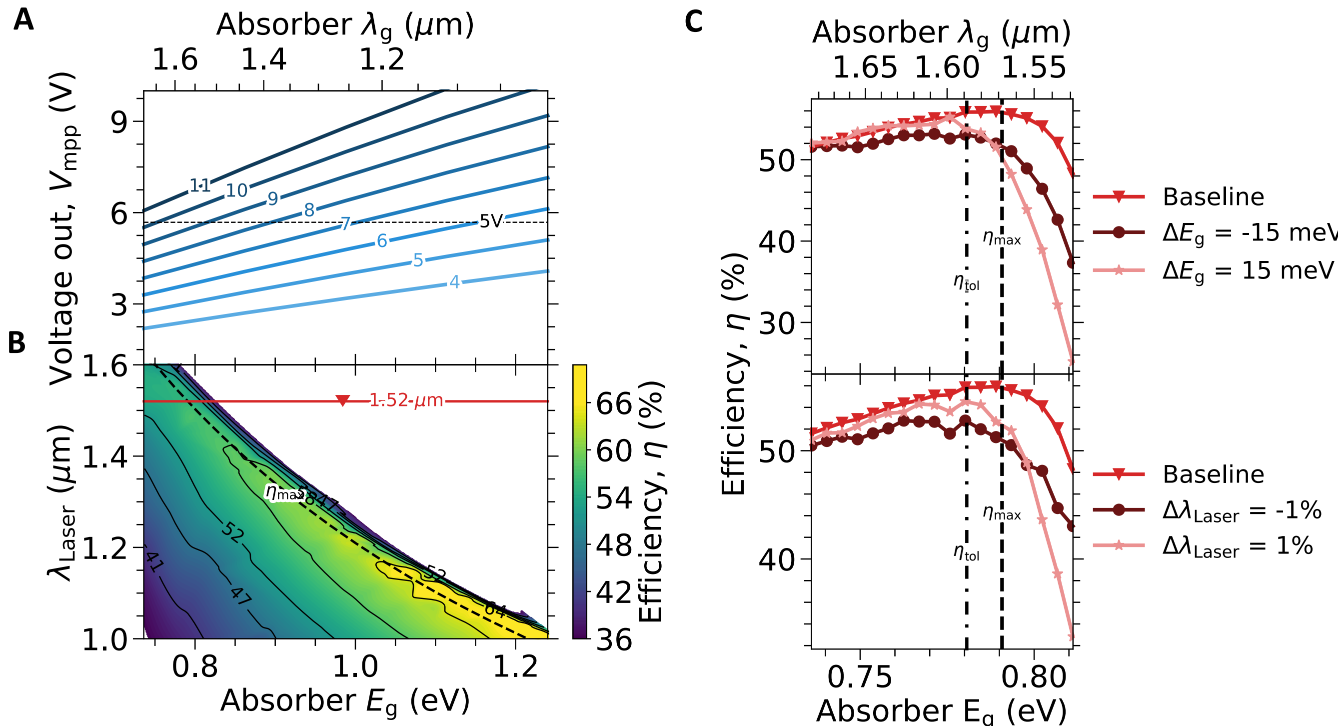

Figure 5. Multi-junction PPCs designed for 1-1.6 um laser wavelengths

(A) Maximum power point voltage of four- to eleven-junction InGaAsP PPCs as a function of absorber bandgap. We employ laser photon energies that are 0.03 eV larger than the absorber bandgap. The horizontal dashed line indicates the 5 V threshold.

(B) Efficiency as a function of layer-thickness-optimized devices' laser wavelength and absorber bandgap. The dashed line follows the maximum efficiency (η_{max}) designs attained for each laser wavelength.

(C) Sensitivity analysis of the efficiency for PPCs optimized for each absorber bandgap and 1.52 µm laser wavelength. Presenting the impact of varying, (top) the absorber bandgap (ΔE_g) and (bottom) the laser wavelength ($\Delta\lambda_{Laser}$), on the baseline system. We highlight the more tolerant device to sub-optimal scenarios (η_{tol}), designed with a photon energy offset of 35 meV from the bandgap.

In all panels, the laser irradiance is 10 W/cm^2 and τ_{SRH} = 0.11 µs.

10 W/cm^2. The black dashed curve in Figure 5B shows the maximum efficiency (η_{max}) for all laser wavelengths and occurs at photon energies 25 meV larger than the absorber bandgap over the investigated range. This offset varies from the value of 87 meV found by Höhn et al.[21] for single-junction GaAs PPCs. Their absorber was only 3 µm thick compared to our 7 µm, so closer-to-bandgap photon energies suffered from large transmission losses for the thin absorber. Following the dashed curve in Figure 5B also reveals that the efficiency increases from 53% to 67% as the absorber bandgap increases and that there is a steep drop-off as wavelength approaches the absorber bandgap.

We varied the absorber bandgap and the laser wavelength in simulations to gauge the sensitivity of optimized devices in sub-optimal scenarios. The results are depicted in Figure 5C, where the baseline shows the optimized systems, and the other curves are perturbations to the systems without re-optimization of the structure. The results shown are for optimized PPC structures at a laser wavelength of 1.52 µm. Similar behavior was simulated for optimized PPC structures at 1.06 µm and 1.31 µm laser wavelengths. We vary the bandgap by ±15 meV as it corresponds to a reasonable target range assuming no significant temperature drift during long epi-growths. We vary the wavelength by ±1% (±15 nm), which corresponds to the room-temperature wavelength range observed over the output powers for the 1.52 µm laser used in the experiments.

Our sensitivity analysis suggests a better compromise between maximum achievable efficiency and system tolerance when designing PPCs using a larger offset between the photon energy and bandgap (see Figure 5C). For example, designing with an offset of 35 meV (η_{tol}, vertical dot-dashed line in Figure 5C) lowers the baseline efficiency by 0.5%$_{rel}$ compared to the design with a 25 meV offset (η_{max}, vertical dashed line in Figure 5C) but can operate at efficiencies up to 3%$_{rel}$ higher for sub-optimal scenarios of ±1% laser shift or ±15 meV bandgap shift. In either case, positive wavelength and bandgap shifts (light red curves in Figure 5C) are preferable over negative shifts (dark red curves in Figure 5C) for the η_{tol} design, resulting in up to 3.2%$_{rel}$ higher efficiencies. These higher efficiencies appear to be due to a smaller absorption mismatch from positive shifts compared to negative shifts.

Proof of concept: characterization of high-efficiency PPC device

Four-junction PPCs targeting lattice-matched InGaAsP absorber material with a bandgap of 0.8 eV were fabricated at Fraunhofer ISE and characterized in detail to showcase the model's predictive capabilities. The PPC design was optimized using our interpolated optical coefficients assuming 1.48 µm laser illumination and includes: an optimized anti-reflection coating, absorber layer thicknesses that are absorption-matched based on Beer-Lambert absorption, and a cumulative absorber thickness that absorbs 98% of the light. We chose Beer-Lambert thicknesses over layer-thickness-optimized thicknesses to maintain consistency with the ten-junction devices. This new wavelength and bandgap combination has the potential to maximize PPC efficiency (Figure 5B) while remaining transparent in optical fibers (Figure 1A). Additionally, the design offers a large fabrication and system tolerance with a 38 meV offset between photon energy and bandgap.

We measure current-voltage characteristics of the four-junction PPC under 1.446 µm laser illumination and observe an average efficiency of 53.3% at an irradiance of 15.1 W/cm² with a standard deviation of 0.3%$_{abs}$ over 10 randomly selected devices spread across a quarter of one substrate, from center to edge (see Supplemental Information for details). The best device has a maximum efficiency of 53.6 ± 1.3% at an irradiance of 15.2 W/cm², with a voltage output at maximum power of 2.176 V. The measurement, shown in Figure 6A, is compared to simulation using our model with nominal layer thicknesses, a τ_{SRH} of 0.35 µs, and a 5.6% increase on the interpolated extinction coefficients, as measured for a single-junction isotype calibration device (see Experimental Procedures for method details) . The τ_{SRH} of 0.35 µs is over 3 times longer than in the ten-junction InGaAs-based PPC but still an order of magnitude shorter than in the single-

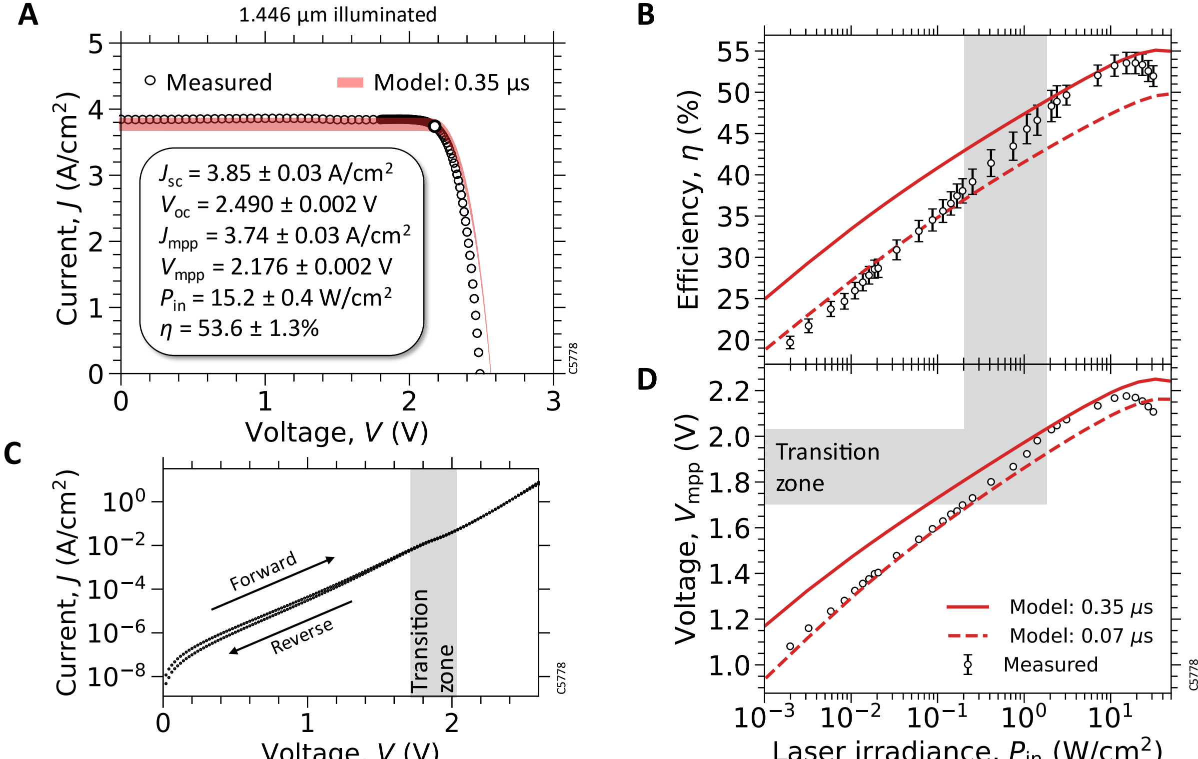

Figure 6. Four-junction InGaAsP PPC performance

(A) Current-density-voltage (*J-V*) characteristics of a 1.446 µm laser illuminated PPC operating at its highest efficiency at an irradiance of 15.2 W/cm². Comparing to simulations with τ_{SRH} of 0.35 µs, the red-shaded region spans the measured input power uncertainty.
(B) Efficiency versus 1.446 µm laser irradiance, comparing calibrated measurements to simulations with τ_{SRH} of 0.35 µs and 0.07 µs.
(C) Measured dark current-density-voltage curve of the high-efficiency PPC, including a forward (top data points) and reverse voltage sweep. The shaded area named "transition zone" highlights the voltages near the hump in the curve.
(D) Measured voltages at the maximum power point as a function of 1.446 µm laser irradiance. The voltages within the "transition zone" from (C) are highlighted here and the shaded area is extrapolated along the laser irradiance values that intersect the "transition zone".
All simulations use nominal thicknesses.

junction InGaAs isotypes, possibly due to the growths' thermal budget difference. The current-voltage data agree except at open-circuit voltage (V_{oc}), where device heating, not accounted for in the model, reduces the voltage by 0.019 V per junction. This drop aligns with the temperature-induced V_{oc} drop observed for single-junction GaAs PPCs at a similar input power.[36] The efficiency as a function of irradiance is shown in Figure 6B, where we compare measurements to simulations with τ_{SRH} of 0.35 µs. We obtain good agreement between the validated model and the irradiance measurements between 1-20 W/cm². We attribute the deviation above 20 W/cm² to cell heating and below 1 W/cm² to a change in the nonradiative recombination behavior.

The behavior at low irradiances could be explained by a very resistive path to a high recombination center[41], but is most likely due to carrier concentration-dependent bulk SRH recombination.[42,43] The behavior is evident by the appearance of a hump in the dark current-voltage curve as shown in Figure 6C, emphasized by the shaded grey area named transition zone. We correlate the transition zone to the maximum power point voltages and then relate it to the laser irradiances in Figure 6D. This zone corresponds to the region in Figure 6B where the measured efficiencies lie between simulated curves that assume a τ_{SRH} of 0.07 µs and 0.35 µs.

Our model predicts the four-junction PPC will achieve an efficiency of 55% at an irradiance of 15.2 W/cm² when illuminated by its intended laser wavelength of 1.48 µm. The slight 2.6%$_{rel}$ drop in efficiency from using a 2.4% shorter laser wavelength demonstrates the PPC's robustness to laser wavelength variation. We designed the device before acquiring the laser.

DISCUSSION

Our work paves the way for integrating PPCs into 5G telecommunication systems and beyond, yielding four significant outcomes. (1) We demonstrate that >50% PPC efficiencies are achievable in the transparent window of optical fibers through careful design optimization using a calibrated predictive model combined with precise epitaxial growth, as evidenced by our record-setting four-junction InGaAsP PPC. This device sets a new standard with an optical-to-electrical efficiency of 53.6 ± 1.3% for a 1.446 µm laser wavelength and 15.2 W/cm^2 irradiance. (2) We develop a model that accurately predicts PPC performance. This predictive model could be combined with machine learning methods[44] for PPC design optimization. (3) We introduce a PPC design optimization process leveraging a computationally efficient method to include luminescent coupling effects, resulting in predicted higher efficiencies and output voltages than a simple absorption-matched design. (4) We propose and validate a method that accurately estimates the thicknesses of absorber layers for multi-junction devices using a single non-destructive measurement.

We also report on realizable PPC efficiencies over the critical laser wavelength range of 1.0-1.6 µm. Within this range, our validated optoelectronic model predicts efficiencies of up to 67% for InGaAsP PPCs. These findings will serve as a valuable guide for future 5G system optimizations and could potentially inspire the development of more energy-efficient long-range power-by-light systems.

Our PPC designs are essential for long-distance power-by-light systems, whether they are deployed in optical fibers or within the earth's atmosphere, due to the low attenuation in the 1.0-1.6 µm wavelength range.[1,2] For example, if the electrical-to-optical laser efficiencies are the same for 0.82 µm and 1.6 µm wavelengths and PPC efficiencies are 65% [14] and 52%, respectively, the longer-wavelength system exhibits a higher efficiency for travel distances exceeding 0.43 km within optical fibers (assuming attenuation from Figure 1A). Given the input power limits of optical fibers,[8] we can reduce the quantity and diameter of fibers required for long-haul (>1 km) power-by-light applications with more efficient PPCs in the 1.0-1.6 µm range.

EXPERIMENTAL PROCEDURES

PPC fabrication

Ten-junction InGaAs PPCs and four-junction InGaAsP PPCs grown lattice-matched on a p-type InP substrate were fabricated at Fraunhofer Institute for Solar Energy Systems. Employing metal-organic vapor phase epitaxy (MOVPE) on an Aixtron G4 2800TM reactor, the epitaxial layer structures were grown on 4" InP wafers. More details regarding the epitaxy process can be found elsewhere.[45] All junctions were grown with tunnel diodes between each junction within one growth run. The subcells have either $In_{0.53}Ga_{0.47}As$ or InGaAsP absorber layers lattice matched to InP and cladded between larger bandgap front and back surface field (FSF and BSF) layers. The subcells are all the same, except for the individual absorber layer thicknesses, the bottommost BSF layer material, and the topmost FSF layer thickness. The topmost FSF layer was designed as a lateral conduction layer [46] comprising 1000 nm of $n=5\times10^{18}$ cm^{-3} InP. The absorber layer thickness decreases from the bottom subcell (J_1) to the topmost subcell (J_{10}/J_4). After completing the epitaxy, ohmic contacts and a Ta_2O_5/MgF_2 antireflection coating were deposited. Individual PPCs on the wafer were isolated using unselective wet-chemical mesa etching. The resulting total chip area was 2.2×2.9 mm^2, with a nominal mesa area of 0.064 cm^2 and a designated area discounting busbars of 0.054 cm^2. For all densities provided in this work, we divide by the nominal mesa area.

Quantum efficiency and reflectivity measurements

The PPC devices' external quantum efficiency and spectral reflectivity were measured with an Oriel IQE200. The reflectivity measurement only includes perpendicularly reflected light as an

integrating sphere was not used for the measurements. See Supplemental Information for results.

Calibrated efficiency measurements: 1.52 µm laser

The cells were vacuum-held on a temperature-controlled, gold-plated copper chuck with the temperature fixed at 25 ˚C. The current–voltage characteristics (*I*-*V*) of each photovoltaic device was measured using a Keithley 2420 in a four-wire configuration under laser illumination. One wire was divided from the amperemeter to connect to three probes, and two probes were placed on one busbar and the last on the second busbar. A voltmeter wire was connected to a probe that was placed on the busbar with a single current-collecting probe. The second amperemeter and voltmeter wires were connected to the chuck. No device preconditioning was performed. The cells were measured and stored in a laboratory room with a temperature of 21-22 ˚C and relative humidity of 30-40% at one atmospheric pressure. The maximum power point of the illuminated *I-V* measurements was determined with a cubic spline interpolation.

A QPC LASERS 6015-0007 15W laser with a nominal lasing wavelength of 1.55 µm was used but lased at 1.52 µm. The laser light path passed through a ~1 m fiber optic cable and was then collimated by a lens. The intensity was optionally attenuated with two interchangeable ND filters to reach a wide range of input powers. The collimated beam was redirected by a mirror and concentrated with a lens onto the PPC device. The working distance between the lens and the PPC was set to achieve under-illumination, i.e., a smaller light spot than the area between the busbars, and to maximize illumination uniformity while providing alignment reproducibility. Variations in illumination intensity due to alignment and laser current fluctuations were within ±1.5%.

The current to the laser driver was varied over a range of 10-18 A to modify the laser power. The measured 1.52 µm central wavelength varied with the laser's current and operating temperature; the spectrum was measured within 6 months of cell illuminated measurements. To keep lasing at 1.520±0.002 µm, the laser temperature was adjusted for given laser currents as follows: 25 ˚C for 6-10 A, 24 ˚C for 10-14 A, 23 ˚C for 14-18 A. Between measurements with the laser, the beam was blocked in front of the ND filters until the laser temperature stabilized to within 0.05 ˚C of our target. Each light I-V measurement was collected within 2 s or more, setting the Keithley's number of power line cycles (NPLC) parameter to 1.

The laser power was calibrated with a 3-step process and the calibration was based on a Newport 919P-030-18 thermopile calibrated December 8th 2021 with certificate number 3038470-001. According to the calibration spec sheet, the thermopile was 1.001 times more sensitive relative to the calibration wavelength of 1.064 µm for the 1.52 µm wavelength, thus the measured input power was adjusted accordingly. First, using the thermopile placed at the PPC's location in Figure 1C, the incident power ($P_{in,th}$) as a function of the drive current in the absence of ND attenuators was measured. Each thermopile measurement required at least 30 seconds to allow for stabilization. Next, the short-circuit current (I_{sc}) of single-junction isotypes with 60 nm and 180 nm absorber layer thicknesses at the same laser driver currents was directly measured. Data showing device heating effects were filtered out to ensure a linear relationship between I_{sc} and $P_{in,th}$ was obtained. Using these datasets that do not include ND filters, the spectral response (*SR*) was extracted by fitting to $I_{sc} = SR \times P_{in,th}$. The fits followed the data closely with minimal scatter. The *SR* values for the 60 nm and 180 nm isotypes averaged over 4 devices for each thickness were 0.04857±0.00009 A/W and 0.1259±0.0002 A/W, respectively. The isotypes' I_{sc} for all filter combinations was measured and their input powers ($P_{in,iso}$) were calculated using

$$P_{\mathrm{in,iso}} = I_{\mathrm{sc}}/SR \qquad (1)$$

Finally, the average of $P_{in,iso}$ from the 8 devices was taken to calculate the calibrated input power (P_{in}). The incident power dominated the uncertainty of our calibrated measurements. The sources of error for our efficiency measurement included:

1. ±1.9% calibration uncertainty for the thermopile.
2. Uncertainty on $P_{in,th}$: ±max(0.5 mW, 1.5%) where the first is the power meter precision and the second is from fluctuations in measurement conditions.
3. Uncertainty on V_{mpp} from the source meter: ±(0.012%+ 1.3 mV).
4. Uncertainty on I_{sc} and I_{mpp} from the source meter:
    - I < 10 mA: ±(0.035%+ 5.6 µA)
    - 10 mA ≤ I < 100 mA: ±(0.055%+ 56 µA)
    - 100 mA ≤ I < 1 A: ±(0.066%+ 1.57 mA)

Calibrated efficiency measurements: 1.446 µm laser

A BWT KE70HAEFN-7.0W laser was used with a nominal lasing wavelength of 1.47 µm. A 1.446 µm central wavelength was measured which varied with the laser's output power by ±0.001 µm. We found little change in laser wavelength as a function of laser output power, compared to the 1.52 µm laser, probably due to better heat dissipation within the laser. The calibrated input power (P_{in}) without filters was measured using the same procedure as that of the 1.52 µm laser. According to the calibration spec sheet, the thermopile was 1.002 times more sensitive relative to the calibration wavelength of 1.064 µm for the 1.446 µm wavelength, thus the measured input power was adjusted accordingly. The input powers with filters were calculated by applying a multiplicity factor to the unfiltered input powers such that the efficiencies matched between the unfiltered and filtered values where they overlapped. The uncertainties to the filtered input powers were propagated accordingly. The measurement and device storage procedure are detailed in "Calibrated efficiency measurements: 1.52 µm".

Drift-diffusion model

The Synopsys TCAD Sentaurus software version S-2021.06 US was used to simulate the PPC devices, employing a one-dimensional drift-diffusion model that treated the devices as laterally infinite layered structures. Through the S4 open-source software[30,31] based on rigorous coupled wave analysis (RCWA), the optical behavior was simulated to enable calculations of the depth-resolved generation rate of electron-hole pairs. Monochromatic illumination was assumed from the lasers. Complex refractive indices (*n* and *k*) from literature[47,48] or measurement (see Supplemental Information for *n* and *k* data for InP) for the FSF, BSF, and TD layers were used. For the quaternary alloy InGaAsP, the morphing algorithm from Schygulla et al.[49] was used to interpolate the *n* and *k* data from three experimental supporting points $In_{0.53}Ga_{0.47}As$ to $In_{0.69}Ga_{0.31}As_{0.67}P_{0.33}$ to InP. Spectroscopic ellipsometry based on J.A. Woolam WVASE32 software was used to measure *n*-data for InGaAs (see Supplemental Information for *n*&*k* data for InGaAs). The $In_{0.69}Ga_{0.31}As_{0.67}P_{0.33}$ *n*-data was calculated by interpolating with an initial morph from InGaAs to InP. The *k* of InGaAs and $In_{0.69}Ga_{0.31}As_{0.67}P_{0.33}$ were calculated from external quantum efficiency (*EQE*) and reflectance (*R*) measurements of single-junction isotypes with the respective absorber materials, assuming Beer-Lambert absorption,

$$k = \frac{-\lambda \ln(EQE/(1-R))}{4\pi x} \tag{2}$$

where λ is the wavelength of light and x is the absorber layer thickness. For the highly doped n-type absorber layer in the homojunction, carrier-density dependent *k* was calculated following the model from Anderson et al. [50] due to the strong dependence in InGaAs.[51] Also, it was assumed that all transmitted light into the substrate was lost due to free-carrier absorption.[52]

To model electrical transport, Poisson's equation coupled with carrier drift and diffusion equations were solved, assuming Fermi statistics, to determine the *J*-*V* curves as well as depth-resolved recombination rate profiles accounting for radiative, Auger, and Shockley-Read-Hall

recombination.[53] Data from the plots generated by Bardyszewski and Yevich[54] were used to relate the Auger coefficient to the InGaAsP composition. The model and parameters provided by Sotoodeh et al.[55] was used to simulate the charge carrier mobilities, assuming equivalent minority and majority carrier mobilities. For the rest of the InGaAsP electrical parameters, the interpolation schemes and values from Vurgaftmann et al.[56] were used. Due to the PPCs' high-quality material, a detailed model of luminescent coupling from Wilkins et al.[26] was used to account for radiative reabsorption in all parts of the device. To correctly model the heterointerfaces, thermionic emission and charge carrier tunneling was used.[27] The tunnel diode was modeled using the structure given in Soresi et al.[53].

Absorber layer thicknesses: reverse-bias method

To non-destructively extract absorber layer thicknesses, the reverse of the method described by Wang et al.[57] was performed. This method uses fast and simple optical simulations; however, it requires junctions with high shunt resistance, accurate knowledge of the optical properties of the absorber layer, minimal luminescent coupling, and a current-voltage measurement under large reverse-bias under a known illumination spectrum causing current mismatching. Having extracted the absorption coefficient of the absorber material from quantum efficiency measurements of optically thin single-junction isotypes (see Drift-diffusion model subsection in "Experimental Procedures"), we aim to determine the relative absorption of each junction in the ten-junction PPC. The PPC is illuminated with a 1.31 µm laser and the current as a function of voltage is measured from open-circuit to a negative bias of -45 V, as shown in Figure 7A. The 1.31 µm laser induces a large current mismatch between all 10 junctions, and the photogenerated current is assumed to monotonically decrease from the top (J_{10}) to the bottom (J_1) junction. As the bias voltage is varied, a phenomenon is observed where the bottom cell (J_1) limits the current until the reverse bias is large enough to put it into reverse breakdown, at which point the current increases up to the new limiting current of the second-from-the-bottom subcell (J_2).[34,57,58] This process repeats for each subcell until the entire device enters breakdown, producing the 10 steps seen in Figure 7A. The sample is illuminated with an irradiance near 0.1 W/cm^2 to minimize the effect of luminescent coupling on the current of each junction.[57] The absence of luminescent coupling is verified in our measurement, see Supplemental Information for results. In the absence of luminescent coupling, large subcell dark current, and absorption losses, the *I-V* curve's steps correspond to each subcell's photogenerated currents.

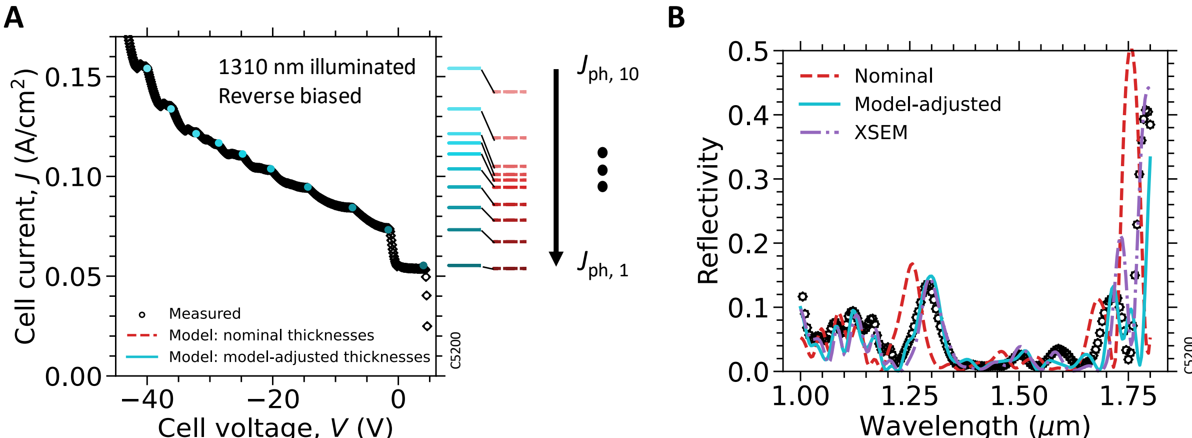

Figure 7. Reverse-bias method for the ten-junction device

Comparing measurement (circles) to simulations that assumes growth-targeted thicknesses (dashed-red) and best-fit thicknesses (solid-blue).
A) Measured current-voltage of the fabricated ten-junction PPC, in far reverse bias, when illuminated with a 1310 nm laser. The horizontal lines are the simulated photogenerated currents of each junction, starting with the top (J_{10}) to the bottom (J_1).
(B) Spectral reflectivity of the PPC, also comparing to simulations assuming cross-sectional scanning electron microscope (XSEM) measured thicknesses.

Based on nominal thicknesses, the measured and simulated subcell photocurrents deviate by up to 10%, as shown to the right of Figure 7A. Therefore, a fit is performed, allowing all subcell thicknesses to vary, keeping the thickness ratios between layers within a constant. The photogenerated currents of each junction are fit to the measured steps and the simulated spectral reflectivity is fit to measurement with the results given in Figure 7. To fit the data, the root-mean-square-relative difference between measured and simulated results are calculated for both the photocurrent and the spectral reflectivity. Python's SciPy minimization package with the Nelder-Mead method is used to minimize the sum of those two root-mean-square values. The bottom junction absorbs more than 99% of light reaching it, since a much shorter wavelength is used than what the device was designed for, thus changing its thickness had no impact on the fit. The model-adjusted thicknesses exceeded the targets, with a deviation of up to 10%. We attribute this thickness deviation to a temperature drift during epi-growth. Figure 7B shows that simulated reflectivity assuming the model-adjusted layer thicknesses agrees more closely with the reflectivity measurement than the nominal thicknesses, reducing the root-mean-square-relative-difference from 2.9 to 0.6.

Absorber layer thicknesses: XSEM method

To validate the values determined with the reverse bias method, the thicknesses of individual absorber layers were determined via cross-sectional scanning electron microscope (XSEM) measurements using a Hitachi model SU-70 scanning electron microscope equipped with a back-scattered electron (BSE) detector. Devices were cleaved from the processed wafer and arranged in vise holders, allowing imaging perpendicular to the cleaving plane, and ensuring proper mechanical stability and charge dissipation. The acceleration voltage was kept constant at 10 keV and the working distance as well as the sample stage configurations were optimized to boost the BSE signal contrast and reduce misalignment errors. An exemplary cross-sectional picture of the ten-junction device is shown in Figure 8. To accurately determine absorber layer thicknesses, cross-sectional images of individual junctions were acquired with a magnification up to 110000X, achieving a resolution of 1.1 nm/pixel. The absorber layer boundaries were determined as the

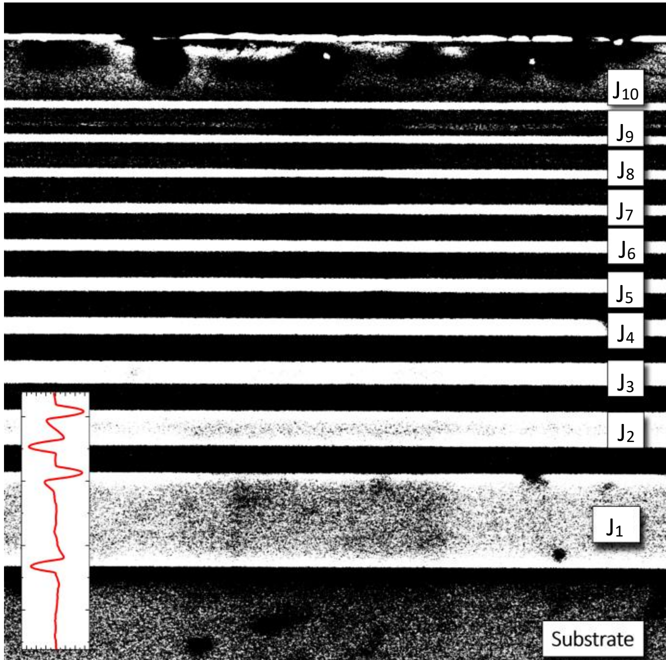

Figure 8. High-contrast cross-sectional SEM image of the ten-junction PPC

The bright areas are the $In_{0.53}Ga_{0.47}As$ absorber layers whereas the dark areas are the barrier/interlayers of each junction. The junction number is indicated in the picture. The red curve in the inset superimposed to the image is the derivative of the pixel intensity as a function of the vertical position, in this case limited to J_1 and J_2.

peak of the spatial derivative of the signal intensity. The layer thickness is then computed as the distance between layer boundary peaks. The thickness values obtained from measurements were averaged over four different regions of one sample to enhance the statistical robustness of the method. The standard deviation for the absorber thickness values ranged between 2-6 nm for the subcells J_1 to J_6, and 2-3 nm for the subcells J_7 to J_{10}.

Layer-thickness-optimized design method

To establish feasible targets for crystal growers, the total thickness of all absorber layers and the absorber layer thickness of the thickest subcell were constrained to below 7 µm and 4 µm, respectively. A two-step procedure was performed by first optimizing layer thicknesses and then determining device performance. First, a layer-thickness optimization was performed using the detailed balance model from Xia and Krich,[22] which includes luminescent coupling but does not include changes in the index of refraction between layers, which can impact luminescent coupling through internal reflections between subcells. Assumptions for the detailed-balance-model input parameters included; an internal radiative efficiency of 0.73 or 0.92 for a τ_{SRH} of 0.11 µs and 3 µs, respectively (see Supplementary Information for details on the choice of internal radiative efficiency), no reflection loss, 98% absorption, and 10 W/cm^2 irradiance at a 1.52 µm wavelength. Then, these optimized absorber thicknesses, calculated from the detailed balance model, were used in our validated drift-diffusion model. For the second step, the antireflection layer thicknesses were optimized and current-voltage properties were simulated with the drift-diffusion model. Note that the efficiencies of the optimized design (τ_{SRH} of 0.11 µs) calculated by our validated drift-diffusion model are up to 8%$_{rel}$ less than the values calculated with the detailed balance model. Unlike our drift-diffusion model, the detailed balance model assumes infinite carrier mobilities and no changes in the index of refraction between layers.

ACKNOWLEDGMENTS

We thank Daisy Xia for providing her detailed balance model software. We also thank Simon Fafard and Denis Masson for their advice and loan of a laser. Funding was provided by Government of Canada's AI for Design National Research Council Collaborative Science, Technology and Innovation Program under Grant INT-014-1, the German Federal Ministry of Education and Research under Grant 01DM21006A, the Natural Sciences and Engineering Research Council of Canada (NSERC), the Canadian Foundation for Innovation, and the Government of Ontario.

REFERENCES

1. Matsuura, M. (2021). Recent advancement in power-over-fiber technologies. Photonics *8*, 335. https://doi.org/10.3390/PHOTONICS8080335.
2. Algora, C., García, I., Delgado, M., Peña, R., Vázquez, C., Hinojosa, M., and Rey-Stolle, I. (2022). Beaming power: Photovoltaic laser power converters for power-by-light. Joule *6*, 340–368. https://doi.org/10.1016/j.joule.2021.11.014.
3. Spillman, W.B., Crowne, D.H., and Woodward, D.W. (1992). Optically powered and interrogated rotary position sensor for aircraft engine control applications. Opt Lasers Eng *16*, 105–118.
4. Batista De Nazaré, F.V., and Werneck, M.M. (2012). Hybrid optoelectronic sensor for current and temperature monitoring in overhead transmission lines. IEEE Sens J *12*, 1193–1194. https://doi.org/10.1109/JSEN.2011.2163709.
5. Worms, K., Klamouris, C., Wegh, F., Meder, L., Volkmer, D., Philipps, S.P., Reichmuth, S.K., Helmers, H., Kunadt, A., Vourvoulakis, J., et al. (2017). Reliable and lightning-safe monitoring of wind turbine rotor blades using optically powered sensors. Wind Energy *20*, 345–360. https://doi.org/10.1002/we.2009.
6. Goto, K., Nakagawa, T., Nakamura, O., and Kawata, S. (2001). An implantable power supply with an optically rechargeable lithium battery. IEEE Trans Biomed Eng *48*, 830–833.
7. Grandidier, J., Akins, A., Crisp, D., Lee, J., Schwartz, J., Bugga, R., Hall, J.L., Limaye, S., and Brandon, E.J. (2023). Feasibility of power beaming through the Venus

atmosphere. Acta Astronaut *211*, 376–381. https://doi.org/10.1016/j.actaastro.2023.06.042.

8. Vázquez, C., Dayron López-Cardona, J., Lallana, P.C., Montero, D.S., Abdulhussein Al-Zubaidi, M., Pérez-Prieto, S., and Garcilópez, I.P. (2019). Multicore fiber scenarios supporting power over fiber in radio over fiber systems. MCF Scenarios Supporting Power Over Fiber in Radio Over Fiber Systems *7*, 158409–158418. https://doi.org/10.1109/ACCESS.2019.2950599.
9. Al-Zubaidi, F.M.A., López Cardona, J.D., Montero, D.S., and Vázquez, C. (2021). Optically powered radio-over-fiber systems in support of 5G cellular networks and IoT. Journal of Lightwave Technology *39*, 4262–4269. https://doi.org/10.1109/JLT.2021.3074193.
10. Helmers, H., Armbruster, C., Von Ravenstein, M., Derix, D., and Schöner, C. (2020). 6-W optical power link with integrated optical data Transmission. IEEE Trans Power Electron *35*, 7904–7909. https://doi.org/10.1109/TPEL.2020.2967475.
11. Fakidis, J., Helmers, H., and Haas, H. (2020). Simultaneous wireless data and power transfer for a 1-Gb/s GaAs VCSEL and photovoltaic link. IEEE Photonics Technology Letters *32*, 1277–1280. https://doi.org/10.1109/LPT.2020.3018960.
12. Emelyanov, V.M., Pokrovskiy, P. V, Kalyuzhnyy, N.A., Nakhimovich, M. V, and Shvarts, M.Z. (2019). Capacitive characteristics of high-speed photovoltaic converters at combined lighting. Semiconductors *53*, 1959–1963. https://doi.org/10.1134/S1063782619140069.
13. Fafard, S., and Masson, D.P. (2022). High-efficiency and high-power multijunction InGaAs/InP photovoltaic laser power converters for 1470 nm. Photonics *9*. https://doi.org/10.3390/PHOTONICS9070438.
14. Fafard, S., and Masson, D.P. (2021). Perspective on photovoltaic optical power converters. J Appl Phys *130*, 160901. https://doi.org/10.1063/5.0070860.
15. Helmers, H., Wagner, L., Garza, C.E., Reichmuth, S.K., Oliva, E., Philipps, S.P., Lackner, D., and Bett, A.W. (2015). Photovoltaic cells with increased voltage output for optical power supply of sensor electronics. In SENSOR 2015 (AMA Conferences 2015), pp. 519–524. https://doi.org/10.5162/SENSOR2015/D1.4.
16. Schubert, J., Oliva, E., Dimroth, F., Guter, W., Loeckenhoff, R., and Bett, A.W. (2009). High-voltage GaAs photovoltaic laser power converters. IEEE Trans Electron Devices *56*, 170–175. https://doi.org/10.1109/TED.2008.2010603.
17. Lopez, E., Höhn, O., Schauerte, M., Lackner, D., Schachtner, M., Reichmuth, S.K., and Helmers, H. (2021). Experimental coupling process efficiency and benefits of back surface reflectors in photovoltaic multi-junction photonic power converters. Progress in Photovoltaics: Research and Applications *29*, 461–470. https://doi.org/10.1002/PIP.3391.
18. Reichmuth, S.K., Helmers, H., Philipps, S.P., Schachtner, M., Siefer, G., and Bett, A.W. (2017). On the temperature dependence of dual-junction laser power converters. Progress in Photovoltaics: Research and Applications *25*, 67–75. https://doi.org/10.1002/PIP.2814.
19. Crump, P., Erbert, G., Wenzel, H., Frevert, C., Schultz, C.M., Hasler, K.H., Staske, R., Sumpf, B., Maaßdorf, A., Bugge, F., et al. (2013). Efficient high-power laser diodes. IEEE Journal on Selected Topics in Quantum Electronics *19*. https://doi.org/10.1109/JSTQE.2013.2239961.
20. Beattie, M.N., Helmers, H., Forcade, G.P., Valdivia, C.E., Hohn, O., and Hinzer, K. (2023). InP- and GaAs-based photonic power converters under O-band laser illumination: Performance analysis and comparison. IEEE J Photovolt *13*, 113–121. https://doi.org/10.1109/JPHOTOV.2022.3218938.
21. Höhn, O., Walker, A.W., Bett, A.W., and Helmers, H. (2016). Optimal laser wavelength for efficient laser power converter operation over temperature. Appl Phys Lett *108*, 241104. https://doi.org/10.1063/1.4954014/914187.
22. Xia, D., and Krich, J.J. (2020). Efficiency increase in multijunction monochromatic photovoltaic devices due to luminescent coupling. J Appl Phys *128*, 13101. https://doi.org/10.1063/5.0009870/157547.
23. Emelyanov, V.M., Sorokina, S. V., Khvostikov, V.P., and Shvarts, M.Z. (2016). Simulation of the characteristics of InGaAs/InP-based photovoltaic laser-power converters. Semiconductors *50*, 132–137. https://doi.org/10.1134/S1063782616010097.

24. Friedman, D.J., Geisz, J.F., and Steiner, M.A. (2014). Effect of luminescent coupling on the optimal design of multijunction solar cells. IEEE J Photovolt *4*, 986–990. https://doi.org/10.1109/JPHOTOV.2014.2308722.
25. Steiner, M.A., Geisz, J.F., Moriarty, T.E., France, R.M., McMahon, W.E., Olson, J.M., Kurtz, S.R., and Friedman, D.J. (2013). Measuring IV curves and subcell photocurrents in the presence of luminescent coupling. IEEE J Photovolt *3*, 879–887. https://doi.org/10.1109/JPHOTOV.2012.2228298.
26. Wilkins, M., Valdivia, C.E., Gabr, A.M., Masson, D., Fafard, S., and Hinzer, K. (2015). Luminescent coupling in planar opto-electronic devices. J Appl Phys *118*, 143102. https://doi.org/10.1063/1.4932660.
27. Wilkins, M.M., and Hinzer, K. (2017). Multi-junction solar cells, Chapter 40. In Handbook of Optoelectronic Device Modeling and Simulation (Taylor & Francis).
28. Walker, A.W., Höhn, O., Micha, D.N., Wagner, L., Helmers, H., Bett, A.W., and Dimroth, F. (2015). Impact of photon recycling and luminescence coupling on III–V single and dual junction photovoltaic devices. J Photonics Energy *5*, 053087. https://doi.org/10.1117/1.JPE.5.053087.
29. Hui, R., and O'Sullivan, M. (2023). Fiber-Optic Measurement Techniques 2nd ed. (Academic Press) https://doi.org/10.1016/B978-0-323-90957-0.00002-3.
30. Pearce, P., and Liu, V. (2023). S4 - RCWA. https://github.com/phoebe-p/S4.
31. Liu, V., and Fan, S. (2012). S4 : A free electromagnetic solver for layered periodic structures. Comput Phys Commun *183*, 2233–2244. https://doi.org/10.1016/J.CPC.2012.04.026.
32. Gfroerer, T.H., Cornell, E.A., and Wanlass, M.W. (1998). Efficient directional spontaneous emission from an InGaAs/InP heterostructure with an integral parabolic reflector. J Appl Phys *84*, 5360–5362. https://doi.org/10.1063/1.368790.
33. Walker, A.W., and Denhoff, M.W. (2017). Heavy and light hole minority carrier transport properties in low-doped n-InGaAs lattice matched to InP. Appl. Phys. Lett *111*, 162107. https://doi.org/10.1063/1.5002677.
34. Wang, A.-C., Yin, J.-J., Yu, S.-Z., Sun, Y.-R., and Dong, J.-R. (2023). Origins of the short circuit current of a current mismatched multijunction photovoltaic cell considering subcell reverse breakdown. Opt Express *31*, 14482–14494. https://doi.org/10.1364/OE.488576.
35. Fafard, S., and Masson, D. (2023). Onset of quantum-confined Stark effects in multijunction photovoltaic laser power converters designed with thin subcells. Photonics *10*, 1243. https://doi.org/10.3390/PHOTONICS10111243.
36. Geisz, J.F., Friedman, D.J., Steiner, M.A., France, R.M., and Song, T. (2023). Operando temperature measurements of photovoltaic laser power converter devices under continuous high-intensity illumination. IEEE J Photovolt *13*, 808–813. https://doi.org/10.1109/JPHOTOV.2023.3304360.
37. Nouri, N., Valdivia, C.E., Beattie, M.N., Krich, J.J., and Hinzer, K. (2022). Light management in ultra-thin photonic power converters for 1310 nm laser illumination. Opt Express *30*, 23417. https://doi.org/10.1364/OE.459680.
38. Helmers, H., Lopez, E., Höhn, O., Lackner, D., Schön, J., Schauerte, M., Schachtner, M., Dimroth, F., and Bett, A.W. (2021). 68.9% Efficient GaAs-based photonic power conversion enabled by photon recycling and optical resonance. Physica Status Solidi - Rapid Research Letters *15*, 2100113. https://doi.org/10.1002/PSSR.202100113.
39. Van Roosbroeck, W., and Shockley, W. (1954). Photon-radiative recombination of electrons and holes in germanium. Physical Review *94*, 1558–1560. https://doi.org/10.1103/PhysRev.94.1558.
40. Helmers, H., Karcher, C., and Bett, A.W. (2013). Bandgap determination based on electrical quantum efficiency. Appl Phys Lett *103*, 32108. https://doi.org/10.1063/1.4816079.
41. McIntosh, K.R. (2001). Lumps, humps and bumps : three detrimental effects in the current-voltage curve of silicon solar cells. https://doi.org/10.26190/UNSWORKS/4284.
42. Ahrenkiel, R.K., Keyes, ; B M, and Dunlavy, ; D J (1991). Intensity-dependent minority-carrier lifetime in III-V semiconductors due to saturation of recombination centers. J. Appl. Phys *70*, 225–231. https://doi.org/10.1063/1.350315.

43. Walker, A.W., Heckelmann, S., Karcher, C., Höhn, O., Went, C., Niemeyer, M., Bett, A.W., and Lackner, D. (2016). Nonradiative lifetime extraction using power-dependent relative photoluminescence of III-V semiconductor double-heterostructures. J. Appl. Phys *119*, 155702. https://doi.org/10.1063/1.4945772.
44. Melati, D., Grinberg, Y., Kamandar Dezfouli, M., Janz, S., Cheben, P., Schmid, J.H., Sánchez-Postigo, A., and Xu, D.-X. (2019). Mapping the global design space of nanophotonic components using machine learning pattern recognition. Nat Commun *10*. https://doi.org/10.1038/s41467-019-12698-1.
45. Schygulla, P., Klitzke, M., Höhn, O., Predan, F., Lackner, D., Schön, J., Tibbits, T., Helmers, H., and Dimroth, F. (2022). Increasing transferability between design and epitaxial growth of multi-junction solar cells. In 17th International Conference on Concentrator Photovoltaic Systems, p. 020009. https://doi.org/10.1063/5.0099724.
46. Oliva, E., Dimroth, F., and Bett, A.W. (2008). GaAs converters for high power densities of laser illumination. Progress in Photovoltaics: Research and Applications *16*, 289–295. https://doi.org/10.1002/PIP.811.
47. Adachi, S. (1989). Optical dispersion relations for GaP, GaAs, GaSb, InP, InAs, InSb, AlxGa1−xAs, and In1−xGaxAsyP1−y. J Appl Phys *66*, 6030–6040. https://doi.org/10.1063/1.343580.
48. Dinges, H.W., Burkhard, H., Losch, R., Nickel, H., and Schlapp, W. (1992). Refractive indices of InAlAs and InGaAs/InP from 250 to 1900 nm determined by spectroscopic ellipsometry. Appl Surf Sci *54*, 477–481.
49. Schygulla, P., Fuß-Kailuweit, P., Höhn, O., and Dimroth, F. (2020). Determination of the complex refractive index of compound semiconductor alloys for optical device modelling. J Phys D Appl Phys *53*, 495104. https://doi.org/10.1088/1361-6463/abb270.
50. Anderson, W.W. (1980). Absorption constant of Pb1-xSnxTe and Hg1-xCdxTe alloys. Infrared Phys *20*, 363–372. https://doi.org/10.1016/0020-0891(80)90053-6.
51. Hahn, D., Jaschinski, O., Wehmann, H.-H., Schlachetzki, A., and Von Ortenberg, M. (1995). Electron-Concentration Dependence of Absorption and Refraction in n-lno.53Gao.47As Near the Band-Edge. J Electron Mater *24*.
52. Beattie, M. (2021). Semiconductor materials and devices for high efficiency broadband and monochromatic photovoltaic energy conversion. https://doi.org/10.20381/ruor-26695.
53. Soresi, S., Hamon, G., Larrue, A., Alvarez, J., Pires, M.P., and Decobert, J. (2018). InP:S/AlInAs:C Tunnel Junction Grown by MOVPE for Photovoltaic Applications. Physica Status Solidi (A) Applications and Materials Science *215*, 1–4. https://doi.org/10.1002/pssa.201700427.
54. Bardyszewski, W., and Yevick, D. (1985). Compositional dependence of the Auger coefficient for InGaAsP lattice matched to InP. J Appl Phys *58*, 2713. https://doi.org/10.1063/1.335909.
55. Sotoodeh, M., Khalid, A.H., and Rezazadeh, A.A. (2000). Empirical low-field mobility model for III-V compounds applicable in device simulation codes. J Appl Phys *87*, 2890–2900. https://doi.org/10.1063/1.372274.
56. Vurgaftman, I., Meyer, J.R., and Ram-Mohan, L.R. (2001). Band parameters for III-V compound semiconductors and their alloys. J Appl Phys *89*, 5815–5875. https://doi.org/10.1063/1.1368156.
57. Wang, A.C., Sun, Y.R., Yu, S.Z., Yin, J.J., Zhang, W., Wang, J.S., Fu, Q.X., and Dong, J.R. (2021). A method to analyze current mismatch in a multijunction laser power converter based on I-V measurements. Appl Phys Lett *118*, 233902. https://doi.org/10.1063/5.0048466/39779.
58. Schauerte, M., Höhn, O., and Helmers, H. (2022). Subcell spectral response determination for multi-junction photonic power converters based on negative bias I-V measurements. In 4th Optical Wireless and Fiber Power Transmission Conference.

Supplemental Information: 53.6% Efficient Multi-Junction Laser Power Converters for Extended Telecom Range Operation

Gavin P. Forcade[1], D. Paige Wilson[2], Meghan N. Beattie[2], Carmine Pellegrino[3], Henning Helmers[3], Robert F. H. Hunter[2],Oliver Höhn[3], David Lackner[3], Louis-Philippe St-Arnaud[2], Thomas N.D. Tibbits[3], Christopher E. Valdivia[2], Yuri Grinberg[2,4], Alexandre W. Walker [1,4], Jacob J. Krich[1], Karin Hinzer[1,2]

[1] Department of Physics, University of Ottawa, Ottawa, ON, Canada

[2] SUNLAB, School of Electrical Engineering and Computer Sciences, University of Ottawa, Ottawa, ON, Canada

[3] Fraunhofer Institute for Solar Energy Systems ISE, 79110 Freiburg, Germany

[4] Digital Technologies Research Center, National Research Council of Canada, Ottawa, ON, Canada

[5] Quantum and Nanotechnologies Research Center, National Research Council of Canada, Ottawa, ON, Canada

Complex refractive index of InP and InGaAs

We measure the complex refractive index (*n* and *k*) of InP and InGaAs by spectroscopic ellipsometry based on J.A. Woolam WVASE32 software. The results for InP are displayed in Fig. S1. The fitting results for the refractive index (*n*) of InGaAs are presented in Fig. S2a. For the extinction coefficient (*k*) of InGaAs, as depicted in Fig. S2b, we have opted to use results from single-junction external quantum efficiency measurements. For details, refer to the "Methods" section in our paper.

We also compare our complex refractive indexes with those found in literature references [1–11]. To improve the interpolation between InGaAs and InP using the morphing algorithm[12], we modified our measured InP absorption coefficient at the band-edge and called it "Corrected" in Fig. S1b. This modification was achieved by fitting an exponential decay at 1.337-1.342 eV and extrapolating to lower photon energies. For modeling the optical properties of InP, we employ "Our work" for the refractive index and "Corrected" for the absorption coefficient datasets. For smaller bandgap materials such as InGaAs, they have an n-type doping dependent extinction coefficient due to conduction band filling effects. Hahn et al.[8] measured the n-doping dependent extinction coefficient for doping concentrations: 3×10^{15} cm^{-3}, 5×10^{17} cm^{-3}, 2×10^{18} cm^{-3}. To generalize to any doping concentration we use Anderson's model[13], and compare its results to Hahn's measurements in Fig. S2b.

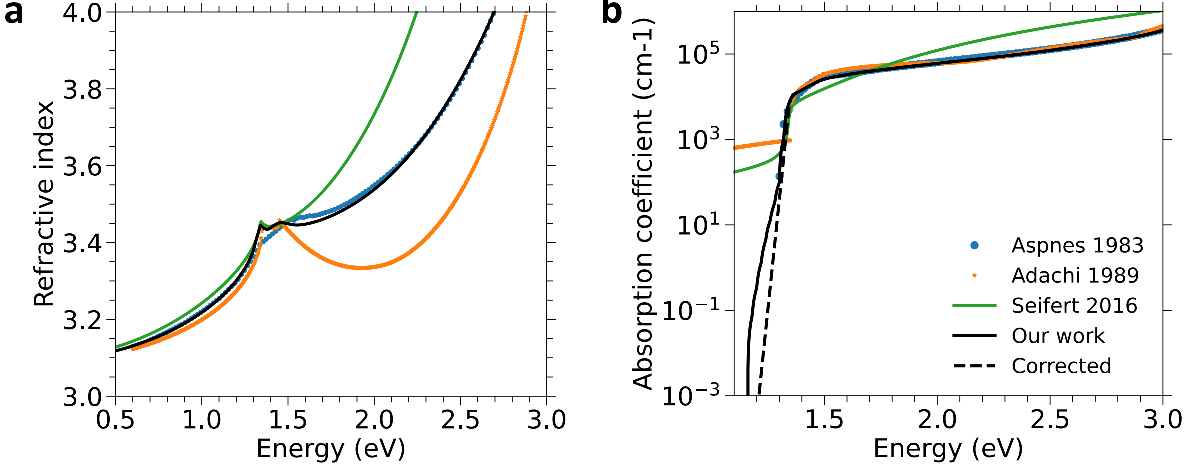

Fig. S1. Complex refractive index of InP. a Real part of the refractive index of InP. **b** Absorption coefficient of InP. We compare our measured values (Our work and Corrected) to the literature: Aspnes[1], Adachi[2], and Seifert[3].

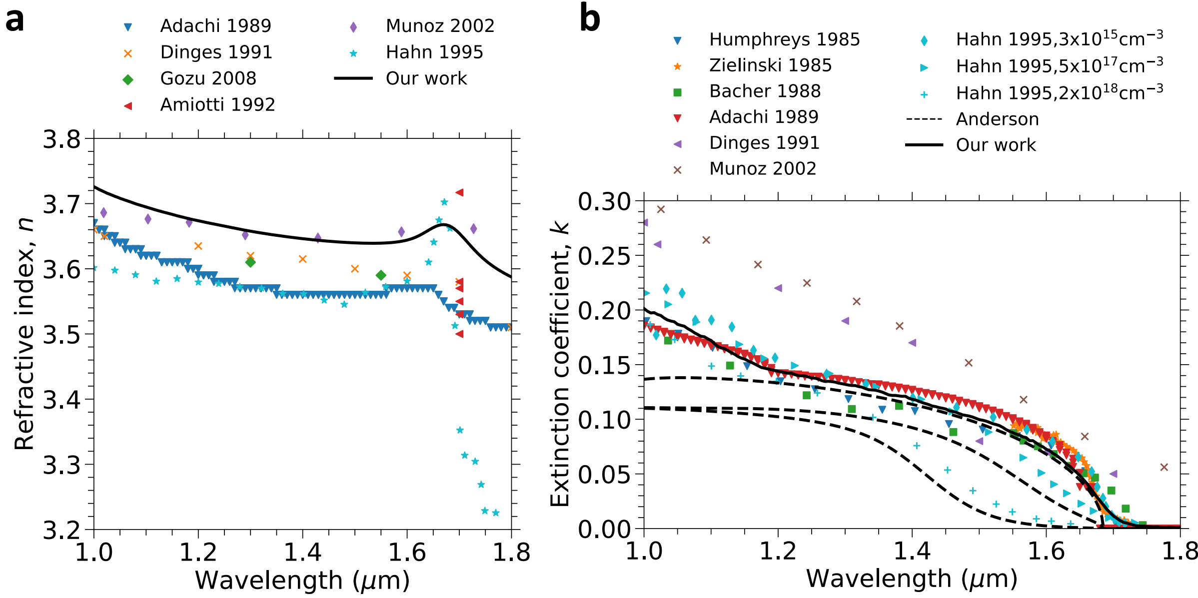

Fig. S2. Complex refractive index of InGaAs. a Real part of the refractive index of InGaAs. **b** Extinction coefficient of InGaAs. We compare our measured values (Our work) to the literature: Adachi[2], Dinges[4], Gozu[5], Amiotti[6], Munoz[7], Hahn[8], Humphreys[9], Zielinski[10], Bacher[11], Anderson[13].

Single-junction measurements and model validation

We fabricated seven single-junction photovoltaic isotypes with varying $In_{0.53}Ga_{0.47}As$ absorber layer thicknesses lattice-matched to InP at Fraunhofer Institute for Solar Energy Systems. We use a four-wire configuration to measure the current density–voltage (*J-V*) characteristics of each photovoltaic device in the dark and under 1.52 µm laser illumination, sweeping the voltage in both directions and taking the average. Of all the seven samples, we measure hysteresis only on the 180 nm thick absorber device. To measure each device's reflectivity and external quantum efficiency (*EQE*), we use an Oriel IQE200. We select the devices with the lowest dark current at -0.02 V from each sample and use them to calibrate our drift-diffusion model.

We apply the same model for the single-junction devices as for the ten-junction devices (see "Methods" for model details). However, for the single-junction devices, we also include trap-assisted and band-to-band tunneling to better fit the dark *J-V* curves in reverse bias[14]. [14]

To validate and acquire parameters for our model, we calculate the root-mean-square-relative difference between measured and simulated results for both the dark *J-V* and spectral reflectivity. We use Python's SciPy SLSQP optimizer to minimize the sum of those two root-mean-square values with the fits shown in Fig. S3a,b. We vary layer thicknesses, absorber layer SRH lifetime, absorber layer Huang-Rhys factor for the trap-assisted tunneling, series resistance, and the peak position and standard deviation of the Gaussian p-doping profile. In addition, we include an EQE and reflectivity multiplicity factor to account for shading from the gridlines. The optimizer reached layer thicknesses within 10% of the targeted growth values. The SRH recombination lifetime was fit to 3±2 µs, which agrees with the measured values of 1.7--2.6 µs from references [15,16]. The Huang-Rhys factor of 8±3 is comparable to a previously published value of 6.8 [14]. The fitted EQE and reflectivity multiplicity factor is 0.96±0.01.

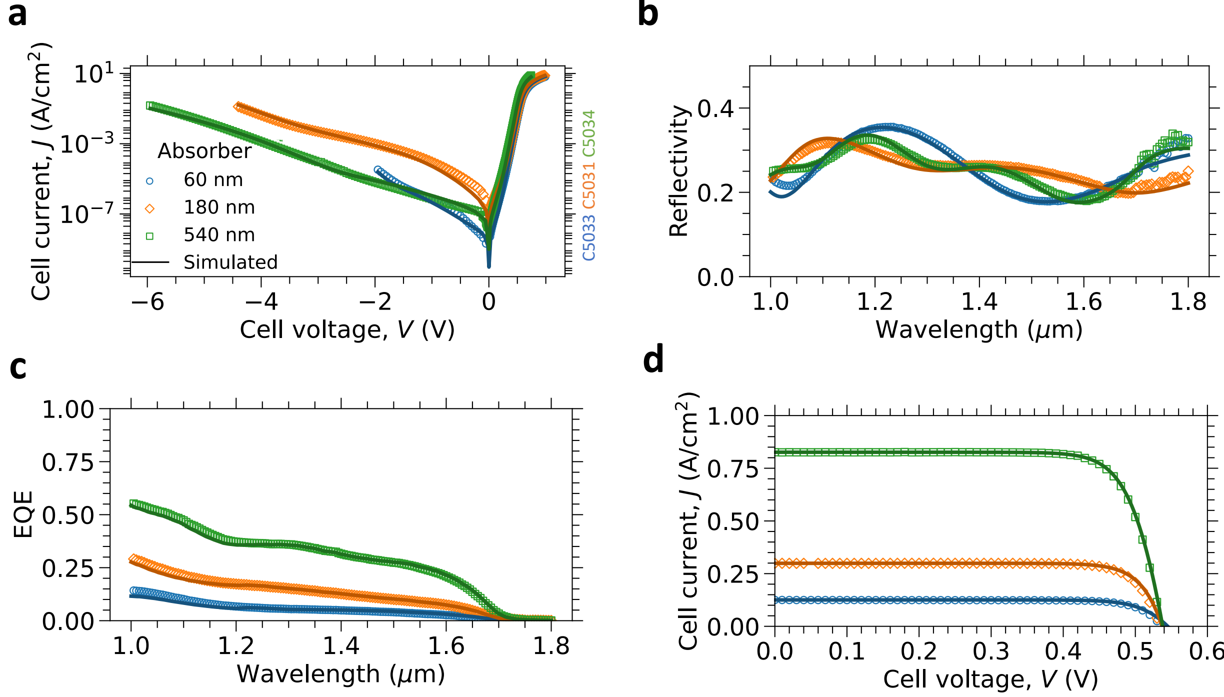

Fig. S3. Single-junction photonic power converter isotypes characterized. Measured (empty markers) and simulated (lines) **a** dark *J-V*, **b** reflectivity, **c** external quantum efficiency, and **d** light *J*-V curves. Simulated optoelectronic model curves are fit to our measured data. The legend provides the device's absorber layer thickness. The light *J-V* curves are measured under 2.66 W/cm² incident 1.52 um laser powers.

Our model describes the single-junction devices well, as seen in Fig. S3a,b, which compares simulated fits to measurements for three samples with different absorber thicknesses; other samples show similar results. At small biases, current generation/recombination is dictated by SRH and trap-assisted tunneling, which are tuned with the SRH lifetime and the Huang-Rhys factor. We attribute the small discrepancy near 0 V for the 180 nm device in Fig. 1a to hysteresis effects, which could arise from traps around the perimeter of the device. At large forward bias, radiative recombination dominates, highlighting the quality of the epi-growth. Finally, series resistance throttles current above 0.5 A/cm^2. Reflectivity curve fitting (Fig. S3b) is dominated by the FSF and absorber layer thicknesses. We attribute the discrepancy for wavelengths larger than 1.7 μm to measurement noise due to the lower sensitivity of the Ge detector.

We further validate our model by comparing simulated to measured *EQE* and light *J-V* in Fig. S3c,d. The root-mean-square difference between measured and simulated EQE is within 1%, which supports our method of extracting the extinction coefficient for InGaAs (see "Methods" in the main article). For the light *J-V* properties, we match the short-circuit current density to the measured value by varying the input power. The resulting simulated input powers are within 4% of the measured values.

No luminescence coupling during reverse bias measurement

Luminescent coupling can increase the current of current-limiting junctions in multi-junction devices. We check for LC during our reverse bias method measurement as the method relies on a deliberately produced current mismatch between the junctions to create steps in reverse bias. Extracting layer thicknesses from those steps requires assuming they are the photogenerated currents of junctions without luminescent coupling contribution. However, the internal radiative efficiency increases with input power[17], therefore luminescent coupling should as well. Luminescent coupling increases the ratio of subcell current to input power, defined as the subcell's *spectral response*, for the current-limiting subcells. Thus, we demonstrate the absence of luminescent coupling by measuring the I-V curve in reverse bias for several 1310 nm laser illumination powers (equal to and larger than our reverse-bias-method power of 1.7 mW). We then calculate the spectral response of each junction assuming the current at the plateaus is the short-

circuit current of the junctions, with the results shown in Fig. S4. As the spectral responses of all the junctions are flat within our measurement uncertainty, we conclude that luminescent coupling is insignificant for these measurements.

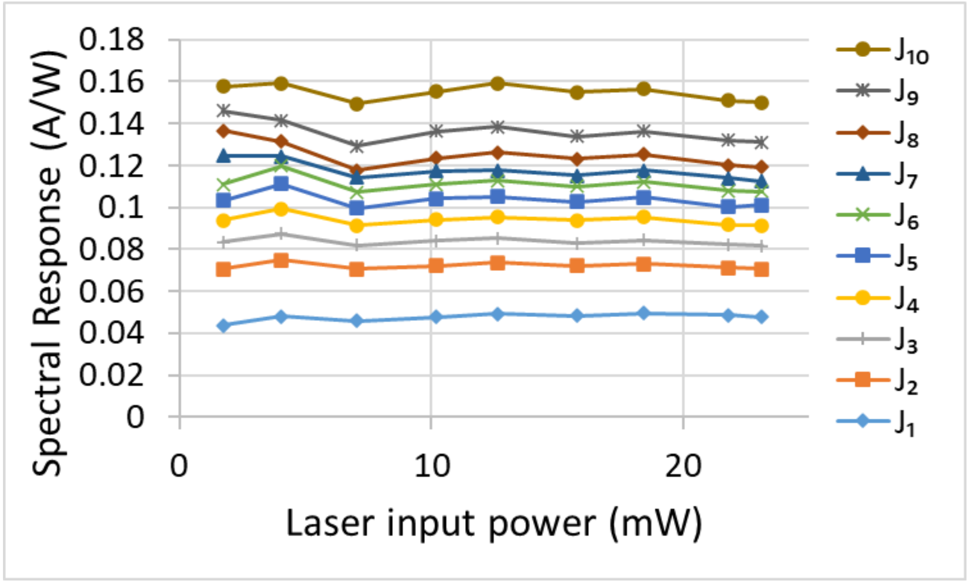

Fig. S4. Luminescent coupling investigation. Spectral response of each junction in the ten-junction InGaAs photonic power converter as a function of 1310 nm laser input power. J_{10} is the top junction.

Detailed balance model: choosing the internal radiative efficiency

To predict luminescent-coupling-optimized layer thicknesses, we employ the detailed balance model from Xia and Krich[18]. We assume an irradiance of 10 W/cm^2, an absorption of 98%, and InGaAs's complex refractive index and bandgap with the same values that we use in our drift-diffusion model. We also implement the absorber thickness constraint detailed in "Methods". The detailed balance model runs quickly, permitting optimization for layer thicknesses. We then implement those thicknesses into our calibrated drift-diffusion model, which includes the carrier mobilities and varying refractive index between materials, to assess the PPC's performance.

The detailed balance model requires an internal radiative efficiency(IRE) value. The detailed balance model contains the physics of luminescent coupling but does not have the correct physics for transport and optical propagation. We therefore use it to create a one-parameter family of device thicknesses, all of which take advantage of luminescent coupling. We artificially vary the IRE of the absorber material in the detailed balance model and find the optimized layer thicknesses for each IRE. While the detailed balance efficiency increases monotonically with IRE, we use these optimized thicknesses in the drift-diffusion model to calculate the efficiency of the PPC device; the results are provided in Fig. S5. The black symbols indicate internal radiative efficiency values of 0.73 and 0.91 produce layer thicknesses that maximize drift-diffusion efficiencies for τ_{SRH} values of 0.11 µs and 3 µs, respectively.

Note that the IRE can also be calculated at the maximum power point from the drift-diffusion model by considering the fraction of radiative losses; that calculation gives 0.5 and 0.92 for the two structures. For τ_{SRH} of 3 µs, the IRE from the drift-diffusion model is within 1% of the IRE in the detailed balance calculations that produce layer thicknesses with maximum drift-diffusion efficiency. This agreement makes sense and is what we expect if the key physics of the two models agree. However, when τ_{SRH} is 0.11 µs, the drift-diffusion IRE at maximum power is 0.5 while the detailed balance IRE of 0.73 produces layer thicknesses with the highest power. Neither of these IRE's is strongly radiative, and Fig. S5 shows that the change of efficiency with the detailed balance IRE is quite small. Since the device does not have strong luminescent coupling, we cannot expect perfect agreement in the IRE's from these methods.

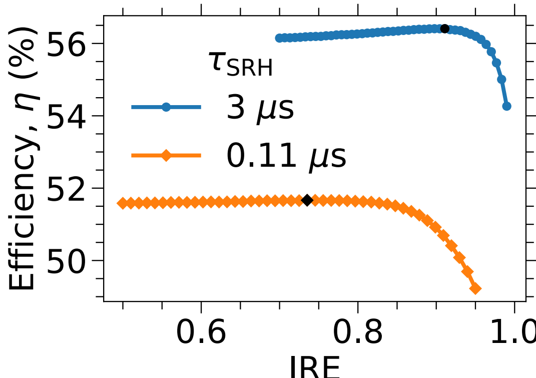

Fig. S5. Impact of internal radiative efficiency on design performance. The efficiency of luminescent coupling-optimized devices calculated by the drift-diffusion model with absorber layer thicknesses provided by the detailed balance model as a function of the input internal radiative efficiency (IRE) values. The black symbols indicate the maximum value.

Number of junctions versus bandgap

For a single-junction device, the open-circuit voltage (V_{oc}) can be related to its absorber material's bandgap (E_g) by[19,20]

$$V_{oc,1} = \frac{E_g}{q} - W_{oc,1} \tag{S1}$$

where $W_{oc,1}$ is the bandgap-voltage offset at open-circuit voltage and is a parameter indicating the quality of the material. However, to maximize PPC efficiency, the devices must operate at the maximum power point with a voltage $V_{mpp,1}=aV_{oc,1}$. Assuming a similar relation as Eq. S1 for $V_{mpp,1}$, we can rearrange to relate the bandgap-voltage offset at maximum power point ($W_{mpp,1}$) to E_g, a, and $W_{oc,1}$ as follows:

$$W_{mpp,1} = \frac{E_g}{q}(1-a) + aW_{oc,1} \tag{S2}$$

For a multi-junction device with N similar subcells, we can sum up the contributions from each subcell to get the total device output voltage at open-circuit:

$$V_{oc,N} = \sum_i^N V_{oc,i} = \left(\frac{E_g}{q} - W_{oc,1}\right)N \tag{S3}$$

For dissimilar junctions, which is generally the case, Eq. S3 averages the open-circuit voltage and then multiplies that voltage by the number of junctions. Combining Eq. S3 (but with "mpp" instead of "oc") with Eq. S2, we get:

$$V_{mpp,N} = \left(\frac{E_g}{q} - \left(\frac{E_g}{q}(1-a) + aW_{oc,1}\right)\right)N = \left(\frac{E_g}{q} - W_{oc,1}\right)aN \tag{S4}$$

To extract a and $W_{oc,1}$, we iterate a two-step fitting procedure targeting $V_{mpp,N}$=5 V and fitting to simulation results from our drift-diffusion model, assuming a Shockley-Read-Hall lifetime of 0.11 μs, a 10 W/cm^2 irradiance from a laser with photon energy 30 meV larger than the absorber bandgap. First, we fit Eq. S3 to our calculated drift-diffusion model data assuming an initial value of a=0.9 ($V_{oc,N}$=5.6 V) and extract a value for $W_{oc,1}$. Second, we fit Eq. S4 to drift-diffusion data for $V_{mpp,N}$=5 V using the fitted value of $W_{oc,1}$ and the initial value of a. We iterated over these two steps to minimize the root-mean-square difference between the drift-diffusion data assuming $V_{mpp,N}$=5 V and Eq. S4 data. The fitting results for the V_{oc} and V_{mpp} data are shown in Fig. S6 a and b, respectively. The final fitted values are a=0.88 and $W_{oc,1}$=0.185V. The slight offset at high absorber bandgaps in Fig. S6a could come from a $W_{oc,1}$ with bandgap dependence. The bandgap dependence could arise from differences in current production (since we assumed a constant irradiance but photon energy that is 30 meV larger than the bandgap), non-radiative recombination, and/or absorber layer thicknesses.

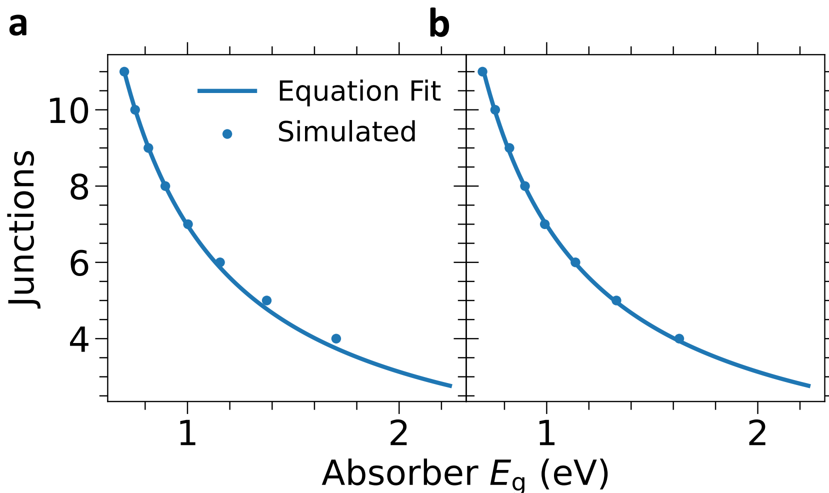

Fig. S6. Number of junctions required to reach 5 V at maximum power for a given absorber bandgap. We compare the fitted Eq. S3 (**a**) and Eq. S4 (**b**) to the values calculated from drift-diffusion simulation results.

Additional four-Junction InGaAsP PPC characteristics

The four-junction InGaAsP photonic power converters exhibit excellent stability. We measured the current at a voltage of 2.176 V for approximately 120 seconds under illumination from a 1.446 um laser with an input power of 15.1 W/cm^2, as shown in Fig. S7a. These voltage and irradiance values correspond to the maximum efficiency values of the best device. To achieve faster temporal resolution, the number of power line cycles (NPLC) of the Keithley instrument was reduced to 0.01 for this measurement. After about one second, the beam blocker was removed, resulting in an initial current of approximately 3.75 A/cm^2, which decreased to 3.73 A/cm^2 after around 0.4 seconds due to device heating. This initial current boost should not affect our measured efficiency values, as the current-voltage measurements take at least 2 seconds and start at 0 V (with the maximum power point close to open-circuit voltage). We also measured the spectral reflectivity, with results shown in Fig. S7b.

The four-junction InGaAsP photonic power converters demonstrate excellent performance across multiple devices. We measured the current-voltage characteristics of 10 devices randomly selected across a quartile of single substrate (including a device ¼" from the 4" wafer's edge) at an input power of 15.1 W/cm^2 using the 1.446 µm laser, with results shown in Fig. S7c. The essential parameters from the current-voltage curves are presented in Fig. S7d as box and whisker plots, including efficiency, short-circuit current density, open-circuit voltage, and fill factor. Note that the irradiance for measurements shown in Fig. S7 was 0.1 W/cm^2 less than the highest efficiency irradiance in Figure 6 of the paper as the system was realigned for Fig. S7 results.

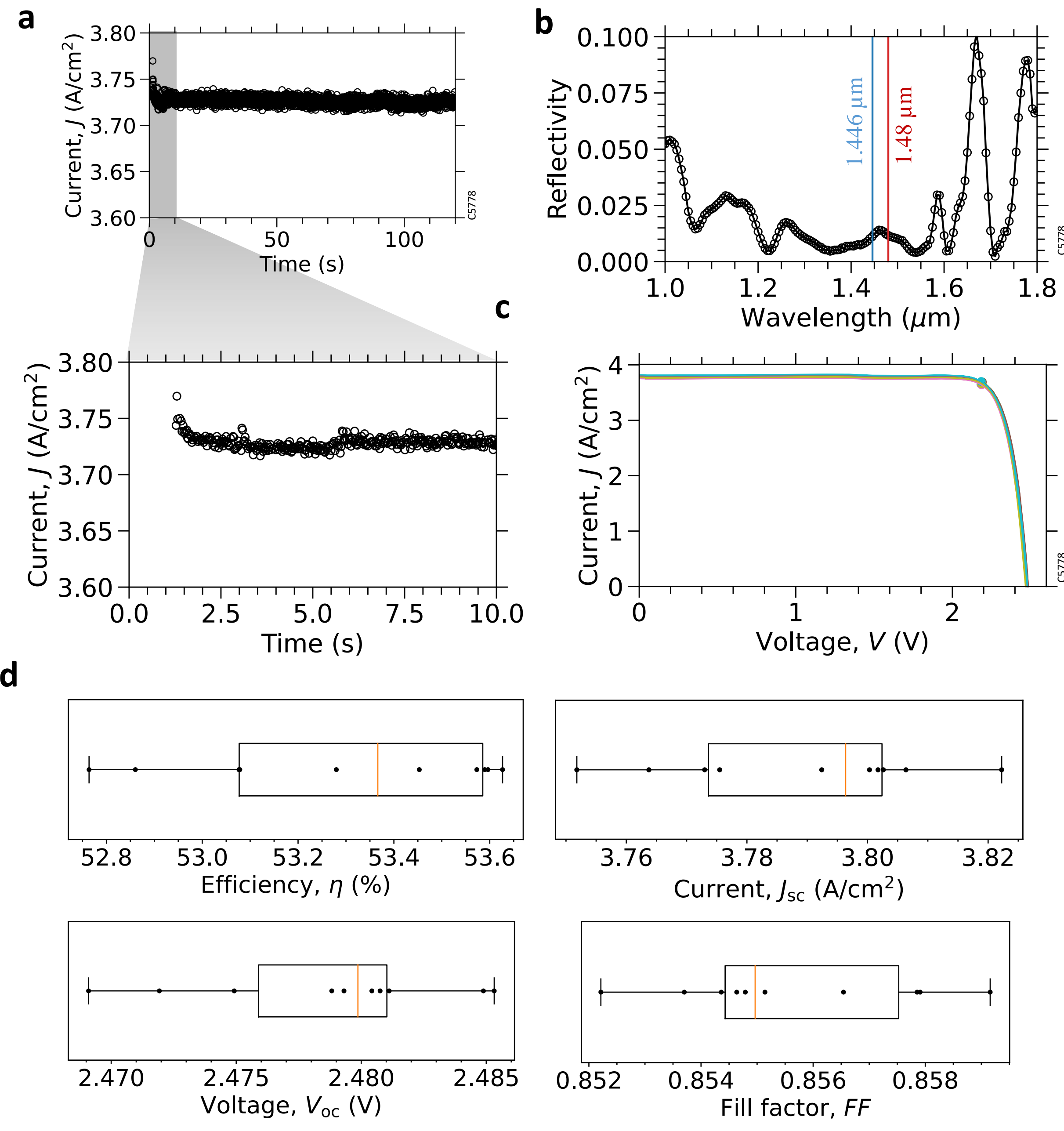

Fig. S7. Four-junction InGaAsP device characterization. (a) Measured current at an applied forward bias voltage of 2.176 V as a function of time illuminated at 15.1 W/cm² with the 1.446 µm laser. The plot below zooms in on the time axis to show the initial current boost. The beam blocker for this measurement was taken out at about 1 s. (b) Measured spectral reflectivity. (c) Current-voltage curves of 10 devices, from a single substrate, when illuminated at an input power of 15.1 W/cm² with the 1.446 µm laser. The circle symbols mark the maximum power points. (d) Box and whisker plots of the efficiency, short-circuit current density, open-circuit voltage, and fill factor extracted from the curves in (c). The box represents the 25th and 75th percentiles, and the whiskers are the minimum and maximum values. The black points are the data points from the 10 devices.

References

1. Aspnes, D.E., and Studna, A.A. (1983). Dielectric functions and optical parameters of Si, Ge, GaP, GaAs, GaSb, InP, InAs, and InSb from 1.5 to 6.0 eV. Phys Rev B *27*.
2. Adachi, S. (1989). Optical dispersion relations for GaP, GaAs, GaSb, InP, InAs, InSb, AlxGa1−xAs, and In1−xGaxAsyP1−y. J Appl Phys *66*, 6030–6040. https://doi.org/10.1063/1.343580.
3. Seifert, S., and Runge, P. (2016). Revised refractive index and absorption of InGaAsP lattice-matched to InP in transparent and absorption IR-region. Opt Mater Express *6*, 251691. https://doi.org/10.1364/OME.6.000629.
4. Dinges, H.W., Burkhard, H., Losch, R., Nickel, H., and Schlapp, W. (1992). Refractive indices of InAlAs and InGaAs/InP from 250 to 1900 nm determined by spectroscopic ellipsometry. Appl Surf Sci *54*, 477–481.
5. Gozu, S., Mozume, T., and Ishikawa, H. (2008). Refractive index of Si-doped-InGaAs. J Appl Phys *104*. https://doi.org/10.1063/1.2987473.
6. Amiotti, M., and Landgren, G. (1992). Ellipsometric determination of thickness and refractive index at 1.3, 1.55, and 1.7 μm for In(1−x)GaxAsyP(1−y) films on InP. J Appl Phys *73*, 2965. https://doi.org/10.1063/1.353028.
7. Muñoz, M.M., Holden, T.M., and Pollak, F.H. (2002). Optical constants of Experiment and modeling ARTICLES YOU MAY BE INTERESTED IN. J Appl Phys *92*, 5878. https://doi.org/10.1063/1.1515374.
8. Hahn, D., Jaschinski, O., Wehmann, H.-H., Schlachetzki, A., and Von Ortenberg, M. (1995). Electron-Concentration Dependence of Absorption and Refraction in n-lno.53Gao.47As Near the Band-Edge. J Electron Mater *24*.
9. Humphreys, D.A. (1985). Measurement of absorption coefficients of Ga0.47In0.53As over the wavelength range 1.0-1.7 um. Electron Lett *21*. https://doi.org/10.1049/el.
10. Zielinski, E., Schweizer, H., Streubel, K., Eisele, H., and Weimann, G. (1998). Excitonic transitions and exciton damping processes in InGaAs/InP. J Appl Phys *59*, 2196. https://doi.org/10.1063/1.336358.
11. Bacher, F.R., Blakemore, J.S., Ebner, J.T., and Arthur, J.R. (1988). Optical-absorption coefficient of In1-xGaxAs/InP. Phys Rev B *37*, 2551–2557. https://doi.org/10.1103/PhysRevB.37.2551.
12. Schygulla, P., Fuß-Kailuweit, P., Höhn, O., and Dimroth, F. (2020). Determination of the complex refractive index of compound semiconductor alloys for optical device modelling. J Phys D Appl Phys *53*, 495104. https://doi.org/10.1088/1361-6463/abb270.
13. Anderson, W.W. (1980). Absorption constant of Pb1-xSnxTe and Hg1-xCdxTe alloys. Infrared Phys *20*, 363–372. https://doi.org/10.1016/0020-0891(80)90053-6.
14. Schenk, A., and Sant, S. (2020). Tunneling between density-of-state tails: Theory and effect on Esaki diodes. J Appl Phys *128*. https://doi.org/10.1063/5.0008709.
15. Gfroerer, T.H., Cornell, E.A., and Wanlass, M.W. (1998). Efficient directional spontaneous emission from an InGaAs/InP heterostructure with an integral parabolic reflector. J Appl Phys *84*, 5360–5362. https://doi.org/10.1063/1.368790.
16. Walker, A.W., and Denhoff, M.W. (2017). Heavy and light hole minority carrier transport properties in low-doped n-InGaAs lattice matched to InP. Appl. Phys. Lett *111*, 162107. https://doi.org/10.1063/1.5002677.
17. Wang, A.C., Sun, Y.R., Yu, S.Z., Yin, J.J., Zhang, W., Wang, J.S., Fu, Q.X., and Dong, J.R. (2021). A method to analyze current mismatch in a multijunction laser power converter based on I-V measurements. Appl Phys Lett *118*, 233902. https://doi.org/10.1063/5.0048466/39779.
18. Xia, D., and Krich, J.J. (2020). Efficiency increase in multijunction monochromatic photovoltaic devices due to luminescent coupling. J Appl Phys *128*, 13101. https://doi.org/10.1063/5.0009870/157547.
19. King, R.R., Bhusari, D., Boca, A., Larrabee, D., Liu, X.-Q., Hong, W., Fetzer, C.M., Law, D.C., and Karam, N.H. (2011). Band gap-voltage offset and energy production in next-generation multijunction solar cells. Progress in Photovoltaics: Research and applications *19*, 797–812. https://doi.org/10.1002/pip.1044.
20. Beattie, M.N., Helmers, H., Forcade, G.P., Valdivia, C.E., Hohn, O., and Hinzer, K. (2023). InP- and GaAs-based photonic power converters under O-band laser illumination: Performance analysis and comparison. IEEE J Photovolt *13*, 113–121. https://doi.org/10.1109/JPHOTOV.2022.3218938.

Chapter 6

Substrate reuse

This chapter presents my work on developing an epitaxial growth process to planarize GaAs(100) faceted surfaces, aimed at reducing III-V photovoltaic costs through substrate reuse (see Section 1.4 for details). The work leverages physics described in Sections 2.1.1 and 2.1.2. There is a single section consisting of a submitted manuscript. This work was done during my visit to the National Renewable Energy Laboratory in Golden Colorado, USA.

6.1 Planarizing spalled GaAs(100) surfaces by MOVPE growth

The following manuscript details my experimental work on planarizing a controlled crystal fractured (spalled) GaAs(100) surface using MOVPE growth. The spalled surface of GaAs(100), a commonly used substrate in III-V PVs, consists of periodic faceted ridges that need to be planarized to facilitate the subsequent growth of high-quality PV devices. This research employs knowledge detailed in Section 2.1.2. Previous MOVPE growth processes for planarizing these surfaces have resulted in significant material waste. Therefore, this research aims to enhance material utilization during planarization to reduce fabrication cost.

Impact

The following novelties are presented in the manuscript:

1. Discovered that the orientation and degree of the initial wafer offcut angle are crucial for surface planarization.
2. Developed a process to planarize the spalled surface of GaAs(100), utilizing up to 95% of the nominally deposited material. The process requires just 8 minutes of growth, significantly less than the 7.5 hours needed for high-efficiency III-V photovoltaics [12].
3. Developed a surface morphology evolution model to identify the mechanisms behind planarization.
4. Established guidelines for planarizing semiconductor surfaces via epitaxy.

The insights gained from this research could significantly advance the development of low-cost high-efficiency photovoltaic technologies.

Author contribution

Gavin P. Forcade: As the lead University of Ottawa-based graduate student associated with the project, I developed the III-V growth recipes, prepared the spalled samples for growth, and performed the measurements and simulations. I was the lead author of the manuscript.

Dr. William E. McMahon: As a senior research scientist within the National Renewable Energy Laboratory, William guided my research, provided detailed feedback during the analysis of my results, and assisted in editing the manuscript.

Nicholas Yoo: As a graduate student at Colorado School of Mines, Nicholas performed the spalls and assisted in editing the manuscript.

Anica N. Neumann: As a graduate student at Colorado School of Mines, Anica provided feedback and trained me in wet chemical etching.

Michelle Young: As a technician who manages a III-V reactor within the National Renewable Energy Laboratory, Michelle grew the III-V materials and provided post-growth feedback.

John Goldsmith: As a technician who manages a III-V reactor within the National Renewable Energy Laboratory, John grew the III-V materials and provided post-growth feedback.

Sarah Collins: As a fabrication technician within the National Renewable Energy Laboratory, Sarah helped to guide the research.

Prof. Karin Hinzer: As the director of the University of Ottawa's SUNLAB research group, Karin assisted in editing the manuscript.

Prof. Corinne Packard: As a professor at the Colorado School of Mines, Corinne helped to guide my research, provided detailed feedback during the analysis of my results, and assisted in editing the manuscript.

Dr. Myles Steiner: As a senior research scientist within the National Renewable Energy Laboratory, Myles helped to guide my research, provided detailed feedback during the analysis of my results, and assisted in editing the manuscript.

Reprinted with permission from:

G.P. Forcade, W.E. McMahon, N. Yoo, A.N. Neumann, M. Young, J. Goldsmith, S. Collins, K. Hinzer, C.E. Packard, and M.A. Steiner, "Planarizing spalled GaAs(100) surfaces by MOVPE Growth", *Crystal Growth & Design*, 23, 24, 2024. DOI: 10.1021/acs.cgd.4c01152

Copyright 2024 American Chemical Society.

pubs.acs.org/crystal Article

Planarizing Spalled GaAs(100) Surfaces by MOVPE Growth

Gavin P. Forcade, William E. McMahon, Nicholas Yoo, Anica N. Neumann, Michelle Young, John Goldsmith, Sarah Collins, Karin Hinzer, Corinne E. Packard, and Myles A. Steiner*

Cite This: https://doi.org/10.1021/acs.cgd.4c01152

Read Online

ACCESS | Metrics & More | Article Recommendations | Supporting Information

Downloaded via Gavin Forcade on November 23, 2024 at 16:19:08 (UTC).
See https://pubs.acs.org/sharingguidelines for options on how to legitimately share published articles.

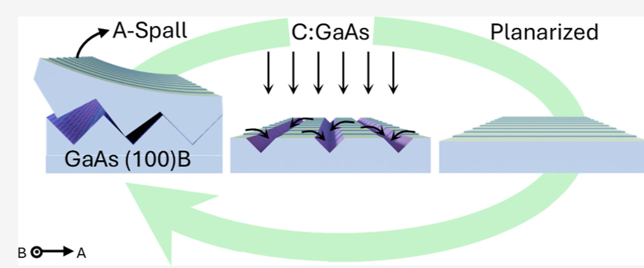

ABSTRACT: III−V photovoltaic devices have demonstrated exceptional performance across various applications, with controlled crystal fracturing, known as controlled spalling, emerging as a promising method to reduce costs by enabling substrate reuse. Spalling GaAs(100) substrates, a commonly used substrate in III−V photovoltaics, results in faceted ridges that must be planarized to grow high-quality photovoltaic devices. Here we demonstrate that a GaAs(100) wafer offcut toward $[0\bar{1}1]$ and spalled toward [011] can be efficiently planarized by growing C:GaAs by metal−organic vapor phase epitaxy (MOVPE) on the surface, with up to 95% of the nominally deposited material used to fill the valleys between ridges. We find that reducing the offcut to 2° enhances the planarizing capability of C:GaAs. A surface morphology model indicates that the density of surface dangling bonds significantly influences the growth evolution of undoped GaAs surfaces. In contrast, the model suggests that the effectiveness of C:GaAs as a smoothing layer stems from modifying the atomic surface structure and, consequently, the associated sticking coefficients of the facets, which can alter the evolution of surface morphology. Our findings provide guidelines for the epitaxial planarization of semiconductor surfaces and improve the understanding of MOVPE growth on nonplanar surfaces.

1. INTRODUCTION

III−V photovoltaics have the highest optical-to-electrical conversion efficiency of any material class, making them an attractive option for applications such as solar photovoltaics,[1,2] waste-heat recovery,[3] thermal energy grid storage,[4,5] and power-by-light.[6] III−V photovoltaics dominate space deployments[7] but require cost reductions to penetrate terrestrial markets.[8] Substrate reuse has an enormous potential to reduce III−V photovoltaic costs because substrates account for about a quarter of the cost of high-efficiency solar cells.[8] High-quality substrates are required for device growth[1] but are not generally part of the final device structure, making substrate reuse a cost-saving possibility.

Controlled spalling has the greatest potential for photovoltaic substrate reuse (see Figure 1a−d for the reuse process) among the methods proposed so far,[9] because of its high-speed throughput, low capital expenses, minimal chemical hazards, and negligible impact on photovoltaic performance.[10] Controlled spalling consists of mechanically fracturing off the epilayers from the substrate with the help of a stressor layer to control the fracture depth (Figure 1a).[9] Ideally, the spalled surfaces of GaAs(100), a common substrate for photovoltaic devices, would be smooth to facilitate the growth of the next photovoltaic devices.[1] Instead, the spalled surfaces consist of a periodic array of ridges with facets oriented on or near natural cleavage directions.[9] These ridges form around the depth directed by the applied stress field as these crystal facets have lower surface energy than the (100) facet. To grow high-quality photovoltaics, the surface needs to be planarized to avoid problems such as parasitic shunts as demonstrated in several refs[1,11 and12] This could be done *ex situ* with chemical-mechanical polishing but that proves costly,[9] or by wet chemical etching but there has yet to be a solution that fully planarizes the surface.[11,13] Also, both tend to exacerbate substrate thinning. An alternative approach we investigate here is in situ surface smoothing by growing specialized III−V epilayers before cell-layer growth. This method can replenish spalled substrate material but should be done with minimal material and growth times to minimize costs.[8]

There have been promising results for in situ smoothing of GaAs surfaces.[1,14−16] Braun et al.[15] planarized 6 μm tall faceted ridges from a GaAs(100) wafer, exfoliated by controlled spalling, by depositing undoped GaAs via hydride vapor phase epitaxy. Although hydride vapor phase epitaxy promises cost reductions for solar photovoltaic growth, most commercial III−V photovoltaics are grown by metal−organic vapor phase epitaxy (MOVPE). Thus, we require a MOVPE planarization solution to achieve substrate reuse in the short term. Schulte et al.[1] grew 2 μm of Zn:GaInP by MOVPE to partially planarize

Received: August 16, 2024
Revised: November 6, 2024
Accepted: November 7, 2024

© XXXX American Chemical Society

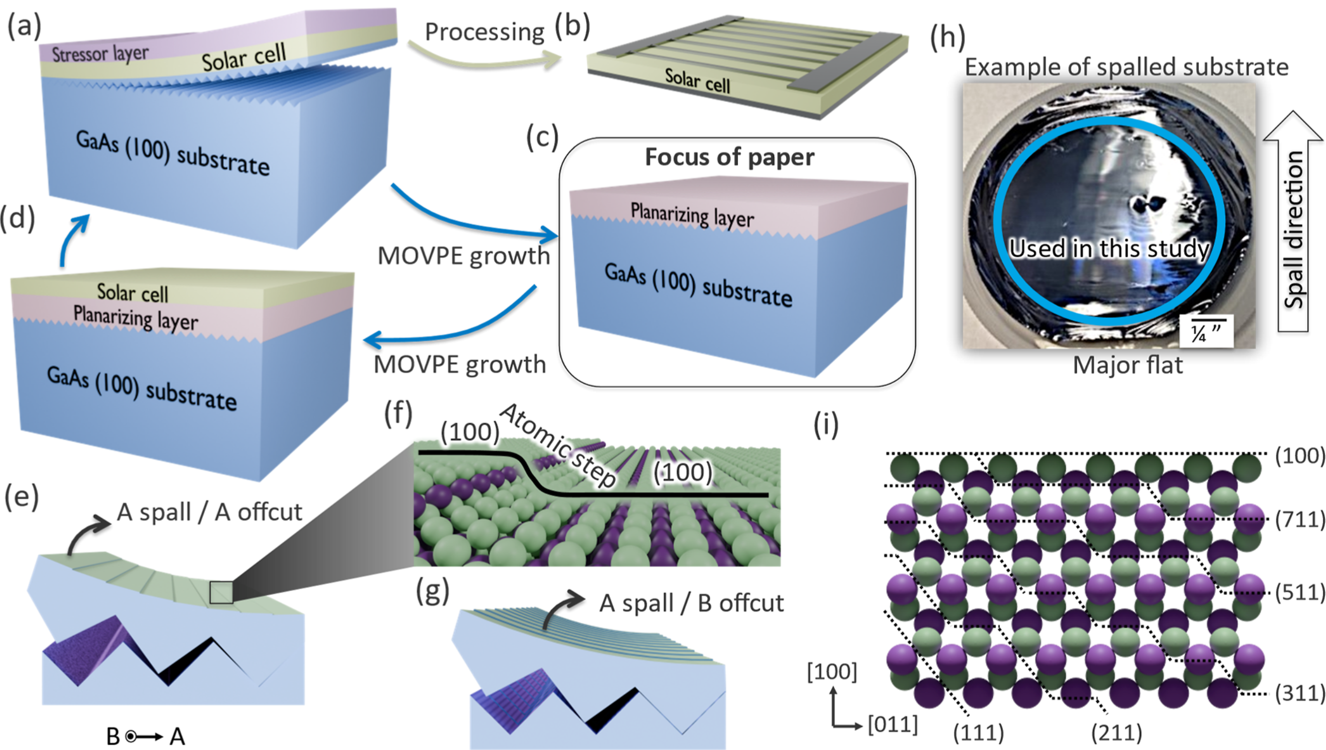

Figure 1. GaAs(100) substrate reuse process via controlled spalling. (a) Schematic diagram of the controlled spalling technique with the crack propagating near the GaAs (100) substrate surface causing a faceted surface. (b) The solar cell can be processed into devices. The spalled substrate can be reused by first (c) planarizing the surface, then (d) growing another high-quality solar cell and (a) respalling. (e) Schematic diagram of an A spall on an A offcut wafer. The lines on the light green surface represent (111) A atomic steps between two (100) terraces, as depicted in (f), with the purple spheres representing Ga atoms. The spalled purple surface is a facet comprising dense atomic steps. (g) Schematic diagram of an A spall on a B offcut wafer with atomic steps perpendicular to the ones in (e). These atomic steps can be represented by (f) but with the purple atoms being As. (h) Top view photograph of a spalled 2″ GaAs(100) wafer, spalled starting at the major flat. (i) Illustration of the atomic arrangements between the (100) and (111) surfaces. For A-type facets, purple and green spheres in (i) represent Ga and As atoms, respectively, and vice versa for B-type facets.

an acoustically spalled GaAs substrate with initial ridge heights of less than 1 μm. However, growing ternary materials on a patterned surface can spatially vary the composition, causing lattice mismatching[17−19] (see Supporting Information for an example). Kim et al.[14] explored some growth conditions for planarizing 1.5 μm deep valleys, generated by patterned etching, with C:GaAs grown by MOVPE. McMahon et al.[16] planarized 5+ μm tall faceted ridges from a GaAs(100) wafer, exfoliated by controlled spalling, using C:GaAs and Si:GaAs grown by MOVPE and demonstrated that the choice of growth material, surface dopant, along with the offcut and spall directions, have a large impact on surface planarization. Building upon this preliminary work, we find the wafer offcut angle is also crucial for surface planarization.

In this paper, we optimize the planarization process of 5+ μm tall ridges using C:GaAs by MOVPE improving material use such that the amount of growth to achieve planarization is within 5% of the theoretical minimum, given the growth rate and initial surface geometry. We study the growth evolution for varying carbon gas flow rates and GaAs(100) wafer offcuts and describe the main smoothing mechanisms involved.

2. EXPERIMENTAL SECTION

Standard single-junction GaAs solar cells were grown on epi-ready 2″ (100)GaAs wafers with 6°A, 6°B, 4°B, and 2°B offcuts. These substrates were spalled toward [011] forming A-faceted ridges, defined here as an A spall, and then growth conditions were varied to determine their impact on planarizing the spalled surface. The A spalls formed ridges that ran parallel to the (111)A "Ga-terminated" atomic steps from an A offcut as depicted in Figure 1e,f). For the spalling conditions used in this study, these spalls formed approximately 5 μm tall {h11}A faceted ridges. When a B offcut wafer was A spalled, the "As terminated" (111)B atomic steps from the offcut ran perpendicular to the (111)A facets forming the sides of the ridges, as shown in Figure 1g.

All spalled wafers were processed using the controlled spalling technique with a stressor layer made of Ni alloyed with P and a roller to peel off the top surface,[9] as illustrated in Figure 1a. The stressor layer was deposited by electrodeposition in a bath composed of 0.6 M nickel(II) chloride hexahydrate and 5 mM phosphoric acid. The deposition was done at a fixed current density of 15.6 mA/cm^2 for 18 to 30 min to tune the spall depth. After electrodeposition, the wafer was laminated with tape, and an external force was applied to the wafer surface using a linearly actuated motor to initiate and propagate the spalling fracture. Other relevant procedures followed that of ref 9. A top-view photograph of a GaAs(100) offcut wafer, exfoliated by controlled spalling is shown in Figure 1h. The interior part of the spalled wafer, demarcated by the thick blue line, was used to investigate planarizing growth, ensuring a consistent baseline for each experiment. Most samples were loaded directly into the reactor without preparation, except for one sample etched with H_2SO_4:H_2O:H_2O_2 at a bottle strength volumetric ratio of 8:1:1 for 13.5 min at 30 °C which followed the procedure of ref 13 to reduce the ridge height.

2.1. Growth Details. III−V epi-layers were grown in a custom-built atmospheric-pressure MOVPE reactor, using trimethylgallium, triethylgallium, trimethylaluminum, trimethylindium, AsH_3, PH_3,

https://doi.org/10.1021/acs.cgd.4c01152
Cryst. Growth Des. XXXX, XXX, XXX−XXX

CCl_4, Si_2H_6, H_2Se, and diethylzinc as sources. The CCl_4 was mixed with purified hydrogen in a dilution line. Although CBr_4 could have allowed for faster planarization,[20] CCl_4 was used as it was already installed on our reactor. Each planarization growth included spalled and as-received wafer samples with identical offcuts and were cleaved to be no less than 1 cm × 1 cm. The planarizing growth consisted of an initial 0.1 μm undoped GaAs layer with a subsequent 10-layer superlattice composed of 1 μm C:GaAs planarizing layers and 0.2 μm $C:Al_{0.43}Ga_{0.57}As$ marker layers. All stated layer thicknesses correspond to the nominal values expected for undoped GaAs grown on a planar GaAs(100) offcut wafer. Cross-sectional scanning electron microscopy images were acquired to characterize the growth evolution with a Hitachi S-4800 operating at 3 kV and a 7 μA beam current. The cross sections were prepared by cleaving along {110} planes, perpendicular to the spalled ridges.

The CCl_4 gas flow rate was varied from 0.0 to 0.1 sccm. At the highest rate of 0.1 sccm, C:GaAs can be doped at 10^{19} cm^{-3} (p-type) in this MOVPE reactor under typical growth conditions. This doping level is commonly used in tunnel junctions and has not been observed to adversely affect the morphology of subsequent layers. Four recipes were investigated: the recipe from McMahon et al.[16] (M), the best planarizing recipe from Kim et al.[20] (K), and two variations (K_{slow} & K_{fast}) around recipe K. Growth parameters for the recipes are provided in Table 1. They include nominal growth rates for the corresponding material grown undoped on a planar GaAs(100) offcut substrate. The AlGaAs layers were grown at a V/III ratio of 80 with CCl_4 flow rates and growth temperatures identical to the GaAs layers.

Table 1. Growth Conditions for Planarizing Epi-Layers[a]

recipe	T (°C)	GaAs growth rate (μm/h)	GaAs V/III	AlGaAs growth rate (μm/h)
M	650	6	17	4
K_{slow}	680	3.5	17	4
K	680	6	60	4
K_{fast}	680	7	60	12

[a] T is the growth temperature. Recipe M comes from McMahon et al.[16] Recipe K is the best planarizing recipe extracted from the results given by Kim et al.[20]

3. RESULTS AND DISCUSSION

3.1. Impact of CCl_4 Flow Rate on Planarization.

Increasing the CCl_4 gas flow improved the planarization capability of C:GaAs material. Cross-sectional scanning electron microscope images of four A spall/A offcut samples with CCl_4 flow rates varying from 0.0 to 0.1 sccm are shown in Figure 2. Including CCl_4 gas improved the valley filling rate of the ~5 μm ridges, reducing the nominal growth needed to fill the valley trench from 9 μm (no gas flow) to 4 μm (0.1 sccm). The mechanisms that influenced these growths will be discussed in Section 3.4.

In Figure 2, we identify the observable crystal facets formed after the valley trenches were filled. Facet emergence depends on the surface morphology, with the fastest-growing facets forming at concave areas and the slowest-growing at convex areas during growth.[21] The (100) crystal plane had the slowest growth rate among the available facets and was further inhibited by CCl_4 or its byproducts. At large CCl_4 flow rates, the highest growth rate facets shifted toward shallower facet angles, from (311)A to (711)A (see Figure 1i for a cross-sectional illustration of these atomic surfaces). However, the final surface remained nonplanar with remnant facets (Figure 2b), which are unfavorable for subsequent solar cell growth.[1] These facets can form when one side of a valley trench is taller than the other; once the trench fills, the extra height of the taller side remains as a remnant facet. Subsequent examples will show that these remnant facets can be avoided with an A spall on a B offcut wafer configuration.

The epi-layer stack at the ridge tips in Figure 2b,c) was not part of our planarization recipe, and their origins are summarized in the figure caption. These epi-stacks should not affect our planarization growth as the initial 0.1 μm undoped GaAs layer provides a constant starting point before growing our planarizing layers.

3.2. Material Flow Analysis during C:GaAs Epitaxy.

Despite the challenges posed by remnant facets imaged in Figure 2 and illustrated in Figure 3a, these growths enabled us to evaluate material flow during epitaxy before filling the valley trenches. A consistent material transfer from (100) plateaus to valley regions was observed and is depicted in Figure 3b. This transfer was evident during at least a portion of each growth cycle, with all instances exhibiting positive valley growth gains relative to conformal growth. We calculated this gain by comparing the measured cross-sectional valley growth area to the nominal cross-sectional growth area, considering the valley width of a planarizing layer as the average between the cladding marker layer corner edges, as shown in Figure 3c. We calculated the valley growth gain for each planarizing layer up to the layer that filled the valley trench and plotted the results in Figure 3d. Comparing the four red curves (recipe M) shows that the valley growth gain increases with CCl_4 flow rate.

We find that growth conditions impact the valley growth gain. By comparing the green (recipe K_{slow}) and blue (recipe K) triangles in Figure 3d, we demonstrate 71%$_{rel}$ higher

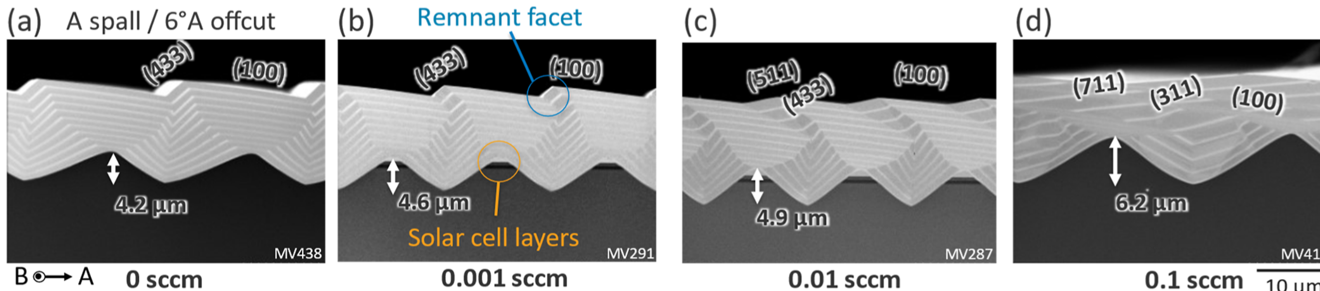

Figure 2. C:GaAs grown on A spall/6°A offcut samples. Cross-sectional scanning electron microscope images of spalled substrates with C:GaAs planarizing epi-growth at CCl_4 gas flow rates of (a) 0.0, (b) 0.001, (c) 0.01, and (d) 0.1 sccm. These growths utilize the recipe M. The horizontal epilayers at the ridge peaks in (b,c) are solar cell layers pierced by the spalling process. Note: The spall that gave the samples for (b,c) was a preliminary depth-calibration controlled spall, subsequent spalls did not pierce epilayers as shown in (a,d).

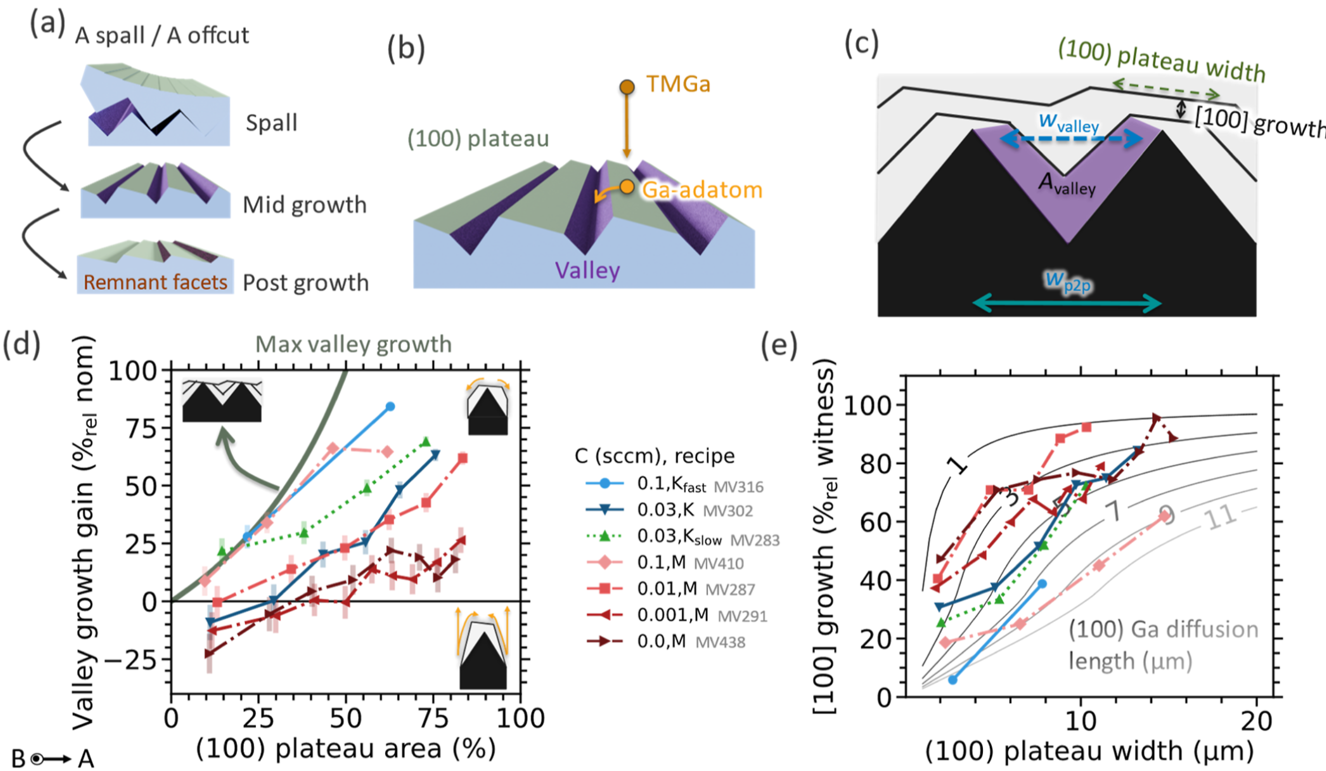

Figure 3. Ga-adatom diffusion on (100) surfaces. (a) Schematic diagram showing the growth evolution of the A spall/A offcut samples with the slowest growing crystal facet not perpendicular to the surface normal, causing remnant facets. (b) Schematic illustration of the growth process with diffusion across the (100) plateaus, starting with TMGa precursors that deposit Ga-adatoms on the (100) surface which then diffuses to the valleys. (c) Schematic diagram of C:GaAs grown on A spall/A offcut samples used to define the axis in (d,e). (d) The gain in valley growth relative to the nominal growth on a flat surface $\{(1 - A_{valley}/[w_{valley} \times \text{Nominal growth}]) \times 100\}$ as a function of the (100) plateau horizontal width relative to the periodic structure width $\{(1 - w_{valley}/w_{p2p}) \times 100\}$. The thick green curve represents the maximum valley growth gain. (e) Plotting measured [100] growth on the (100) plateaus relative to the growth on 6°A offcut witness samples as a function of the (100) plateau width. Comparing to simulated curves with the "Adatom diffusion model" detailed in Supporting Information. The error bars in (d) indicate a 50 nm uncertainty in the position of the layer interfaces. Assuming the same uncertainty, error bars for (e) are approximately ±10% absolute but are not shown, to improve the plot's clarity.

average valley growth gain for slower growth rates. We also investigated the optimal growth conditions for C:GaAs as suggested by ref 14 (recipe K), which involves a 30 °C higher growth temperature and a V/III ratio that is 3.5 times higher than our standard recipe M. Additional research is required to conclusively determine the impact of these modified growth conditions on planarizing spalled GaAs(100) surfaces.

When employing the highest CCl_4 flow rate of 0.1 sccm, we achieved the maximum valley filling gain, marked by the thick green curve in Figure 3d, for smaller (100) plateau areas. Here, the entirety of the nominally grown material contributed to filling valleys. However, for larger (100) plateaus, we observed a departure from the maximum valley filling, indicating a finite diffusion length of Ga-adatoms across these plateaus.

The diffusion length of Ga-adatoms on (100) surfaces was found to increase with the CCl_4 flow rate. This diffusion length was quantified by comparing measured and calculated [100] growth as a function of the (100) plateau width. The data are plotted in color in Figure 3e, along with modeled black/gray background curves calculated assuming diffusion lengths from 1 to 11 μm. The measured data come from taking the ratio between the [100] growth on (100) plateaus against flat 6°A offcut witness samples. The calculated values assume a simple Ga-adatom diffusion model based on geometrical considerations (see "Adatom diffusion model" section in Supporting Information for model details). The Ga-adatom diffusion length on (100) surfaces increased with carbon flow, ranging from 3 to 8 μm for 0.0 to 0.1 sccm CCl_4 flow rates, respectively. These values are about 100 times larger than the Ga-adatom diffusion lengths on crystal facets perpendicular to (111)B during MOVPE growth of undoped GaAs nanowires for growth temperatures less than 470 °C.[22] However, they are of the same order of magnitude as Ga-adatom diffusion lengths on (100) crystal facets during molecular beam epitaxy of undoped GaAs,[23,24] ranging over 0.4−8.0 μm depending on the growth conditions and movement direction. Our values may be underestimated as the model does not consider the Ehrlich-Schwoebel barrier,[25] which acts as an obstacle to adatoms descending an atomic step (hinders adatom movement to the right in Figure 1f).

3.3. Impact of B Offcut on Planarization. Unlike A spall/A offcut samples, the A spall/B offcut configuration suppresses remnant facet formation, thereby facilitating surface planarization. This outcome is visible in the scanning electron microscope images shown in Figure 4a−d. The growth experiments with C:GaAs, conducted at the highest CCl_4 flow rate of 0.1 sccm, demonstrate that smaller B offcuts improve planarization performance. We highlight the effectiveness of the best planarizing growth with the top-view photographs in Figure 4e, where we compare an as-spalled sample to a planarized sample (same sample as Figure 4d) and its corresponding witness sample. In the A spall/B offcut

https://doi.org/10.1021/acs.cgd.4c01152
Cryst. Growth Des. XXXX, XXX, XXX−XXX

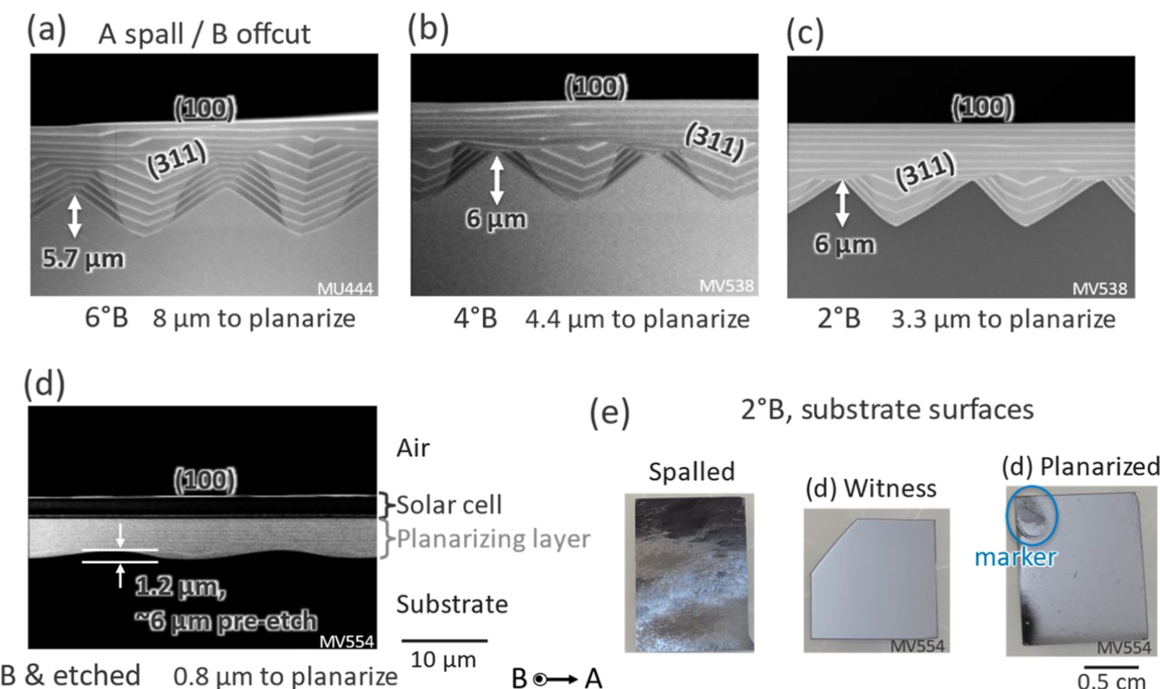

Figure 4. C:GaAs grown on A spall/B offcut substrates. Cross-sectional scanning electron microscope images of spalled substrates with C:GaAs planarizing epi-growth for GaAs substrates offcut from (100) toward (a) 6°B, (b) 4°B, and (c,d) 2°B. (d) Using an etching step before planarizing growth, with halved planarizing layer nominal thicknesses. The dark layers above the planarizing layers in (d) comprise a single-junction GaAs solar cell. (e) Top-view photographs of 2°B wafers in their A spalled state, alongside the planarized sample shown in (d) and its corresponding witness sample. All growths use recipe M and are at a CCl_4 flow rate of 0.1 sccm.

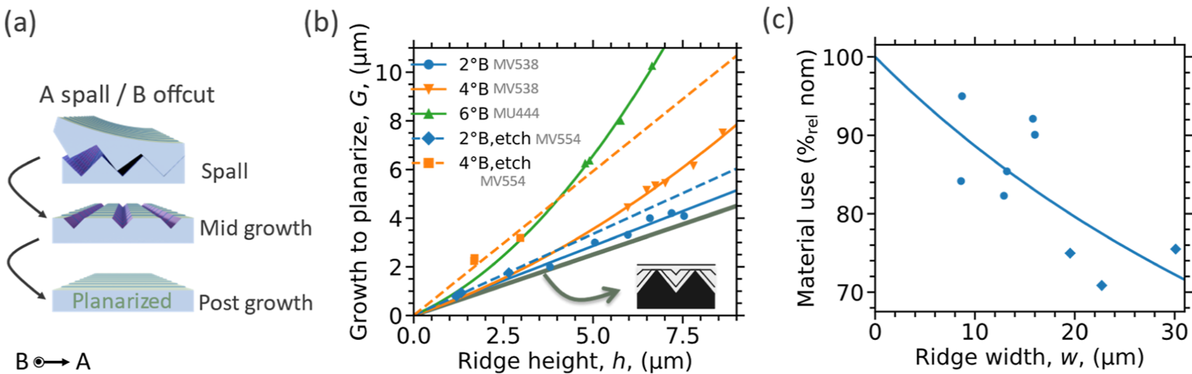

Figure 5. Quantifying C:GaAs planarizing capability on A spall/B offcut samples. (a) Schematic diagram of the growth evolution for A spall/B offcut samples where the slowest growing crystal plane is perpendicular to the surface normal. The lines on the planar surface represent atomic steps. (b) Nominal growth required to planarize the spalled surface for a given ridge height. We acquired data over multiple locations on the samples to get a range of ridge heights. The thick green curve represents the best-case scenario where all nominal material is used to planarize the surface. The other curves are quadratic fits to the data to guide the eye. (c) The material used to planarize, defined as the ratio between the minimum and nominal growth to planarize the surface for a given initial surface geometry $\{(0.5/[G/h]) \times 100\}$, as a function of the ridge width for 2°B etched and unetched samples. The solid curve in (c) is to guide the eye. The data in (b,c) were collected at the same locations. All the growths use recipe M with a 0.1 sccm CCl_4 flow rate.

configuration, the two-dimensional surface plateaus that developed at the ridge tops maintained the wafer's original B offcut orientation, as depicted in Figure 5a. These plateau surfaces were composed of (100) terraces interspersed with (111)B atomic steps.

Smaller B offcuts reduce parasitic deposition on the plateaus. Reducing the density of (111)B atomic steps decreases the nominal growth of C:GaAs needed to fill the valley trenches, defined as nominal growth to planarize. The (100)2°B surface, with nominally threefold fewer (111)B steps than the (100)6°B surface, required at least two times less nominal growth to fill the valleys for a given ridge height, as illustrated in Figure 5b. This observation suggests that the (111)B steps have a higher sticking coefficient than the (100) terraces for our growth conditions. Notice that the required growth to planarize samples with 2°B offcuts stays within 30% of the minimum growth to planarize (thick green line).

Incorporating an etching step to partially planarize the spalled surface before the growth phase can reduce the amount of material required to achieve a planar surface by decreasing the initial ridge height. Lowering the initial ridge height reduces the theoretical limit of material needed to fill in the

https://doi.org/10.1021/acs.cgd.4c01152
Cryst. Growth Des. XXXX, XXX, XXX−XXX

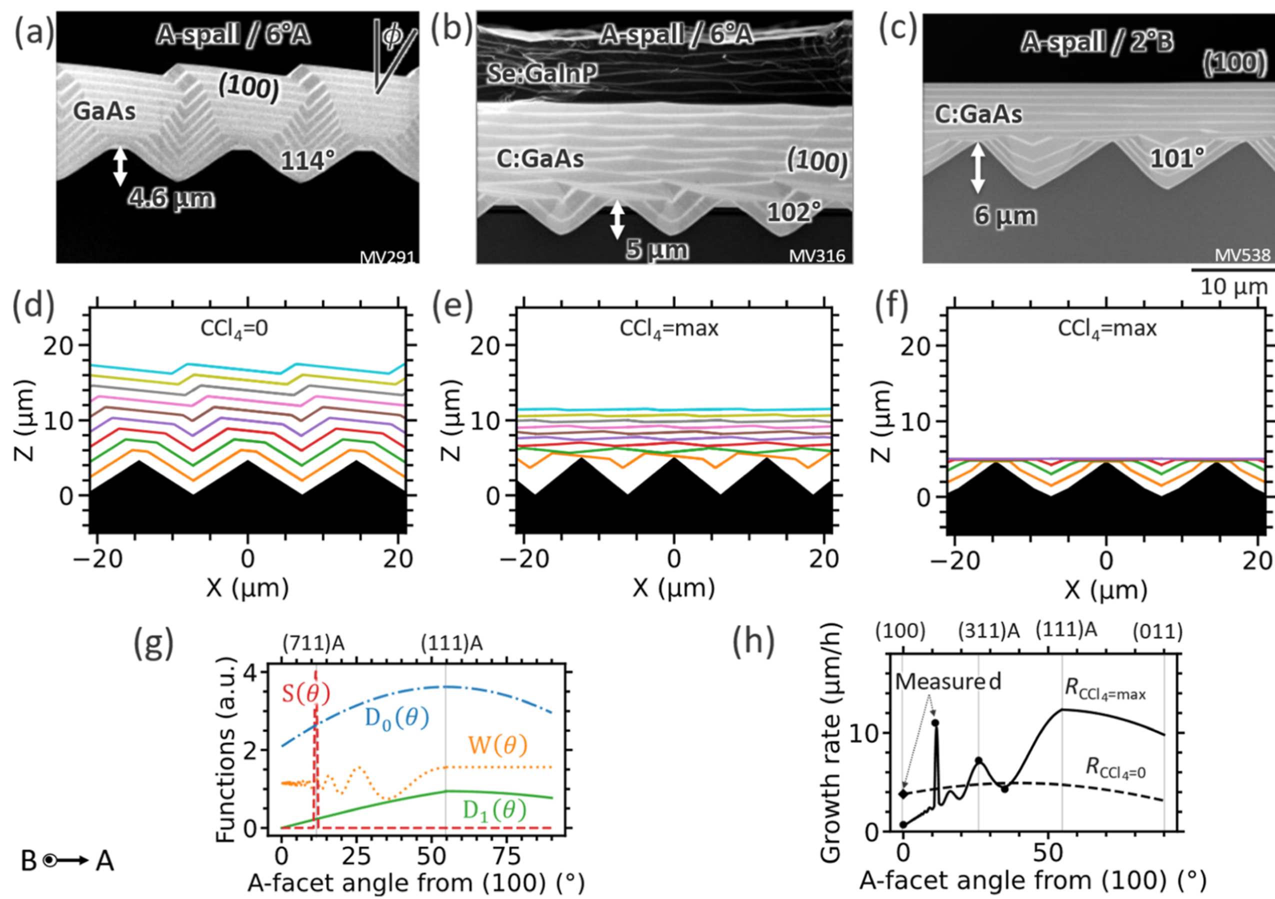

Figure 6. Modeling growth morphology. (a−c) Cross-sectional scanning electron microscope images of planarizing GaAs growth on A spalled wafers with (a) 6°A offcut and no CCl_4 (recipe M), (b) 6°A offcut and 0.1 sccm CCl_4 flow rate (recipe K), and (c) 2°B offcut and 0.1 sccm CCl_4 flow rate (recipe M). (d−f) Modeled growth morphology of the surface for the respective images above their positions. We assumed diffusion lengths (L) of 3 μm for (d) and 8 μm for (e,f), and growth rates (R) according to eq 2 with $i = 0$, $C_0 = 0.55$, and $C_1 = C_2 = 0$ for (d) and $i = 1$, $C_0 = 0.95$, $C_1 = 7$, and $C_2 = 0.7$ for (e,f). (g) Functional forms of terms in eq 2. (h) Facet growth rate as a function its angle toward [011] relative the (100) facet along the (111)A path, used for the model input parameter (R) for (d) $R_{CCl4=0}$ and for (e,f) $R_{CCl4=max}$. Measured growth rates are also included in (h). The darker 6-layer stack grown above the lighter 10-layer stack of C:GaAs in (b) is Se:GaInP with GaAs marker layers.

valleys, which can be calculated geometrically. For example, Figure 4c,d depict identical growth conditions and sample offcuts, but the sample in Figure 4d which included a planarizing etching step required four times less C:GaAs to achieve a planar surface. In addition to requiring less growth material, adding the etching step reduced the planarization growth time from approximately 33 to 8 min.

The initial ridge width influences the quantity of growth required to achieve a planar surface. The material use, defined as the ratio between the minimum and nominal growth needed to planarize a surface with a given initial geometry, as a function of initial ridge width (w) is shown in Figure 5c for the 2°B experiments. Up to 95% of the nominal material was used to fill the valleys (highest data point in Figure 5c), with the remainder either desorbed or deposited on the plateaus. The curve in Figure 5c serves as a visual guide and follows the functional form, $0.5/(0.5 + 0.0064w)$. This equation is based on the physical principle that the minimum growth to planarize an initial triangular surface geometry, is 0.5 (slope of the thick green curve in Figure 5b). The actual required growth (denominator) can be represented by the sum of the ideal case (0.5) and a perturbation ($0.0064w$) resulting from the finite diffusion length of Ga adatoms. Using values from this curve, a spalled sample with a ridge width of 30 μm would require 36% more nominal growth to achieve a planar surface compared to a sample with a 10 μm ridge width, assuming identical ridge heights.

3.4. Modeling Surface Morphology Evolution. To begin to understand the physical mechanisms that cause our observed growth modes, we simulated the surface morphology evolution during growth with the model from ref 21 that considers the facet growth rate (R) and the diffusion length (L), and compared those results to cross-sectional scanning electron microscope images in Figure 6. We used different sets of parameters, R and L, for each simulated surface morphology evolution, ensuring they remained constant within each simulation. The model assumes the time (t) dependent vertical (z) growth is given by[21]

$$\frac{\partial z}{\partial t} = \sqrt{1+p^2}\,R(\phi) - \frac{\sqrt{1+p^2}\,L^2}{2}\left(\frac{\partial^2 R(\phi)}{\partial s^2} - R(0)\frac{d^3x}{ds^3}\right)ds = \sqrt{1+p^2}\,dx,\ p = \frac{\partial z}{\partial x} \quad (1)$$

where x is perpendicular to the wafer's surface normal and ϕ is the angle deviated from the wafer's surface normal (as defined in Figure 6a). Although an atomic model combining fluid dynamics with kinetic Monte Carlo simulations can be more robust,[25,26] we chose the analytical model from ref 21 due to its simplicity, since it only has two free parameters, L and $R(\phi)$. Though it cannot be used to accurately extract physical parameters, the model reproduces surface morphology evolution allowing us to postulate dominating growth mechanisms on the faceted surfaces. The modeled results in Figure 6d−f show equally time-spaced snapshots of the surface morphology with the colored curves. Note that the model disregards growth extending into the third dimension (into the page). A detailed description of the model is given in the Supporting Information; here we summarize the main physical inputs.

Following the approach from ref 27, we assume the facet growth rate (R) at an angle θ from (100) is given by

$$R(\theta) \propto C_0 D_i(\theta)[1 + C_1 S(\theta) + C_2 W(\theta)] + (1 - C_0)\cos(\phi) \quad (2)$$

where C_j with j = 0,1,2 are weighting factors and $D_i(\theta)$ with i = 0,1 represents the unreconstructed dangling bond density of As saturated A-facets. However, $D_1(\theta)$ further assumes zero (100) terrace dangling bonds. Additionally, $S(\theta)$ represents a [711]A growth rate spike, while $W(\theta)$ represents a sinusoidal growth rate as a function of θ with maxima at (n11)A facets for n-odd. All these functions of θ (excluding $D_0(\theta)$) can serve as proxies for atomic surface reconstructions,[28,29] impacting facet sticking coefficients. Finally, $\cos(\phi)$ is a proxy for gas- or adatom-phase diffusion anisotropy; gas-phase boundary layers may enhance gas flux at the plateau tops versus the sidewalls, and/or adatoms could preferentially diffuse up the sidewalls.[16] The terms' relation with θ are shown in Figure 6g and detailed in the Supporting Information. We determined the average facet growth rates from Figure 6a−c following the method described in ref[15], with the results presented in Figure 6h. For the undoped growth, the (100) growth rate was averaged across all ten layers shown in Figure 6a. For C:GaAs growth, the (711)A facet growth rate was measured from Figure 6b, employing the layers after the valleys were filled. The (100), (211)A, and (311)A facet growth rates were measured from Figure 6c, using the layers before the valleys were filled.

We find growth for undoped GaAs with recipe M is determined by the surface's unreconstructed dangling bond density and anisotropic Ga diffusion. Qualitatively comparing Figure 6a−d, the model matches well with the features observed in the scanning electron microscope cross-section images. Both form (100) plateaus starting at the initial ridge tips and have similar remnant facets. To get this good match, we use the growth rate function shown in Figure 6h (dashed line) which assumes the following fitting parameters for eq 2: i = 0, C_0 = 0.55, C_1 = C_2 = 0. Based on the values of these fitting parameters, the dangling bond density impacts growth rate by 55% with the remaining attributed to anisotropic diffusion, while surface reconstructions have a negligible impact on growth. We also replicate the measured conformal growth of undoped GaAs on a B-faceted surface from a B spall/A offcut substrate with the model, with results in the Supporting Information, and arrive at a similar conclusion. The rising slope versus growth time on the side of the ridge in Figure 6a, which is not simulated in Figure 6d, may be attributed to a net adatom flow from the plateaus to the valleys, as indicated in Figure 3d, combined with a short adatom diffusion length on the ridge's side. This limited diffusion length could result from large facet sticking coefficients and/or Ehrlich−Schwoebel barriers.

We observed that introducing a high flow of CCl_4 during GaAs growth on A-faceted surfaces altered the physical processes dominating growth. The measured growth morphologies are reproduced with the model, as shown in Figure 6b,c,e,f, using the growth rate function shown in Figure 6h (solid line) which assumes the following fitting parameters for eq 2: i = 1, C_0 = 0.95, C_1 = 7, C_2 = 0.7 for Figure 6e,f, respectively. These values suggest that CCl_4 or its byproducts may be inducing surface reconstructions which significantly impacts growth. McMahon et al.[16] proposed that C plays a dominant role, noting that Si_2H_6, another group IV element, exhibited similar planarizing capabilities to C. They attributed this dominant role to the formation of similar surface reconstructions on GaAs(100) facets by both Si and C. However, Kim et al.[20] demonstrated poorer planarizing performance with CCl_4 compared to CBr_4 at the same gaseous mole fractions, which could be due to differing surface interactions from Cl compared to Br or a higher C deposition rate with CBr_4. Further research is required to determine the impact of CCl_4 byproducts on surface reconstructions.

The surface morphology evolution model works well to simulate growth on structured surfaces with sizes less than the Ga-adatom diffusion length as growth follows the relative probabilities of sticking to the facets. However, when only one facet is available, the growth rate instead follows the probability of adatom desorption. Consequently, after planarizing the A spall/2°B offcut sample (Figure 6c,f), the model underestimates growth on the (100)2°B facet due to the change in growth mechanism.

4. CONCLUSIONS

Reusing GaAs(100) substrates via controlled spalling presents a promising approach to reduce III−V photovoltaic costs; however, the spalling process can create faceted ridges that must be planarized to enable the growth of high-quality photovoltaics.

We grew C:GaAs by MOVPE to planarize A-faceted GaAs(100) substrates, achieving up to 95% material utilization relative to nominal deposition for surface planarization by optimizing the wafer offcut. We demonstrated that B offcut wafers produce planar surfaces and that reducing the B offcut enhances planarization performance. Introducing a wet etching step to partially planarize the spalled substrate reduced the planarizing growth time to approximately 8 min. This time is negligible compared to the 7.5 h required for the epitaxial growth of high-efficiency solar cells.[30] Additionally, we developed a method to extract adatom diffusion lengths during

MOVPE, finding values ranging from 3 to 8 μm for (100) surfaces, depending on the CCl_4 gas flow.

Our modeling efforts provided insights into the growth mechanisms, indicating that optimal planarization is achieved when the sticking coefficient is zero for the crystal facet parallel to the bulk wafer surface while neighboring facets have nonzero coefficients. First-principles calculations, as demonstrated by Batyrev et al.,[31] could further explain preferential facet growths and the impacts of surface dopants on atomic surface reconstructions. Coupling these calculations with surface morphology evolution models could enhance their predictive capabilities, allowing for a comprehensive investigation of growth conditions that significantly impact planarization.[16]

The knowledge gained from this study could guide the planarization efforts of other substrate surfaces via epitaxial growth, potentially expanding beyond GaAs(100) substrates. It could also motivate further study of the atomic structure of crystal surfaces during MOVPE growth, given the strong impact on the growth behavior for nonplanar surfaces.

■ ASSOCIATED CONTENT

Supporting Information

The Supporting Information is available free of charge at https://pubs.acs.org/doi/10.1021/acs.cgd.4c01152.

> Cross-sectional scanning electron microscope images of various growth configurations for planarization not shown in the main article, a detailed description of the adatom diffusion model and the surface morphology evolution model, an expanded derivation of the dangling bond density model to include facets between (111) and (011), and modeling results of the surface morphology evolution of undoped GaAs grown on a B spall/A offcut faceted surface (PDF)

■ AUTHOR INFORMATION

Corresponding Author

Myles A. Steiner − *National Renewable Energy Laboratory, Golden, Colorado 80401, United States;* Email: myles.steiner@nrel.gov

Authors

Gavin P. Forcade − *Department of Physics, University of Ottawa, Ottawa K1N 6N5, Canada;* orcid.org/0000-0001-9527-5661

William E. McMahon − *National Renewable Energy Laboratory, Golden, Colorado 80401, United States;* orcid.org/0000-0001-5036-2032

Nicholas Yoo − *Colorado School of Mines, Golden, Colorado 80401, United States*

Anica N. Neumann − *National Renewable Energy Laboratory, Golden, Colorado 80401, United States; Colorado School of Mines, Golden, Colorado 80401, United States*

Michelle Young − *National Renewable Energy Laboratory, Golden, Colorado 80401, United States*

John Goldsmith − *National Renewable Energy Laboratory, Golden, Colorado 80401, United States*

Sarah Collins − *National Renewable Energy Laboratory, Golden, Colorado 80401, United States*

Karin Hinzer − *Department of Physics, University of Ottawa, Ottawa K1N 6N5, Canada; SUNLAB, School of Electrical Engineering and Computer Sciences, University of Ottawa, Ottawa K1N 6N5, Canada*

Corinne E. Packard − *National Renewable Energy Laboratory, Golden, Colorado 80401, United States; Colorado School of Mines, Golden, Colorado 80401, United States;* orcid.org/0000-0002-5815-8586

Complete contact information is available at: https://pubs.acs.org/10.1021/acs.cgd.4c01152

Notes

The authors declare no competing financial interest.

■ ACKNOWLEDGMENTS

This work was supported by the U.S. Department of Energy under contract no. DE-AC36-08GO28308 with Alliance for Sustainable Energy, LLC, the Manager and Operator of the National Renewable Energy Laboratory. Funding provided by U.S. Department of Energy, Energy Efficiency and Renewable Energy Solar Energy Technologies Office under agreement number 38261. Gavin Forcade was supported by the Natural Sciences and Engineering Research Council of Canada. The U.S. Government retains and the publisher, by accepting the article for publication, acknowledges that the U.S. Government retains a nonexclusive, paid up, irrevocable, worldwide license to publish or reproduce the published form of this work, or allow others to do so, for U.S. Government purposes.

■ REFERENCES

(1) Schulte, K. L.; Johnston, S. W.; Braun, A. K.; Boyer, J. T.; Neumann, A. N.; McMahon, W. E.; Young, M.; Coll, P. G.; Bertoni, M. I.; Warren, E. L.; Steiner, M. A. GaAs Solar Cells Grown on Acoustically Spalled GaAs Substrates with 27% Efficiency. *Joule* **2023**, *7* (7), 1529−1542.

(2) Green, M. A.; Dunlop, E. D.; Siefer, G.; Yoshita, M.; Kopidakis, N.; Bothe, K.; Hao, X. Solar Cell Efficiency Tables (Version 61). *Prog. Photovoltaics* **2023**, *31*, 3−16.

(3) Forcade, G. P.; Valdivia, C. E.; Molesky, S.; Lu, S.; Rodriguez, A. W.; Krich, J. J.; St-Gelais, R.; Hinzer, K. Efficiency-Optimized near-Field Thermophotovoltaics Using InAs and InAsSbP. *Appl. Phys. Lett.* **2022**, *121*, 193903.

(4) Amy, C.; Seyf, H. R.; Steiner, M. A.; Friedman, D. J.; Henry, A. Thermal Energy Grid Storage Using Multi-Junction Photovoltaics. *Energy Environ. Sci.* **2019**, *12* (1), 334−343.

(5) Tervo, E. J.; France, R. M.; Friedman, D. J.; Arulanandam, M. K.; King, R. R.; Narayan, T. C.; Luciano, C.; Nizamian, D. P.; Johnson, B. A.; Young, A. R.; et al. Efficient and Scalable GaInAs Thermophotovoltaic Devices. *Joule* **2022**, *6*, 2566−2584.

(6) Beattie, M. N.; Helmers, H.; Forcade, G. P.; Valdivia, C. E.; Hohn, O.; Hinzer, K. InP- and GaAs-Based Photonic Power Converters under O-Band Laser Illumination: Performance Analysis and Comparison. *IEEE J. Photovolt.* **2023**, *13* (1), 113−121.

(7) Li, J.; Aierken, A.; Liu, Y.; Zhuang, Y.; Yang, X.; Mo, J. H.; Fan, R. K.; Chen, Q. Y.; Zhang, S. Y.; Huang, Y. M.; Zhang, Q. A Brief Review of High Efficiency III-V Solar Cells for Space Application. *Front. Phys.* **2021**, *8*, 631925.

(8) Horowitz, K. A. W.; Remo, T.; Smith, B.; Ptak, A. A Techno-Economic Analysis and Cost Reduction Roadmap for III-V Solar Cells; Golden, 2018. https://www.nrel.gov/docs/fy19osti/72103.pdf. (accessed 2023−11−22).

(9) Chen, J.; Packard, C. E. Controlled Spalling-Based Mechanical Substrate Exfoliation for III-V Solar Cells: A Review. *Sol. Energy Mater. Sol. Cells* **2021**, *225*, 111018.

(10) Sweet, C. A.; Schulte, K. L.; Simon, J. D.; Steiner, M. A.; Jain, N.; Young, D. L.; Ptak, A. J.; Packard, C. E. Controlled Exfoliation of (100) GaAs-Based Devices by Spalling Fracture. *Appl. Phys. Lett.* **2016**, *108*, 11906.

(11) Mangum, J. S.; Braun, A. K.; Perna, A.; Geisz, J. F.; Ptak, A. J.; Packard, C. E.; France, R. M. Improving Performance of III-V Solar Cells Grown on Spalled Germanium with Ex Situ Substrate Planarization. In *Conference Record of the IEEE Photovoltaic Specialists Conference*; IEEE, 2023, pp 1−4..

(12) Boyer, J. T.; Braun, A. K.; Schulte, K. L.; Simon, J.; Johnston, S. W.; Guthrey, H. L.; Steiner, M. A.; Packard, C. E.; Ptak, A. J. Analysis of Crystalline Defects Caused by Growth on Partially Planarized Spalled (100) GaAs Substrates. *Crystals* **2023**, *13* (4), 681.

(13) Neumann, A. N.; Coll, P. G.; Bertoni, M. I.; Steiner, M. A.; Warren, E. L. Wet-Etching of Acoustically Spalled GaAs for Substrate Reuse. *IEEE J. Photovolt.* **2024**, *14* (2), 281−287.

(14) Kim, Y.; Park, Y. K.; Kim, M.-S.; Kang, J.-M.; Kim, S.-I.; Hwang, S.-M.; Min, S.-K. Facet evolution of CCl4-doped multilayers during metalorganic chemical vapor deposition on patterned GaAs substrates. *J. Cryst. Growth* **1995**, *156*, 169−176.

(15) Braun, A. K.; Boyer, J. T.; Schulte, K. L.; McMahon, W. E.; Simon, J.; Perna, A. N.; Packard, C. E.; Ptak, A. J. 24% Single-Junction GaAs Solar Cell Grown Directly on Growth-Planarized Facets Using Hydride Vapor Phase Epitaxy. *Adv. Energy Mater.* **2024**, *14* (3), 2302035.

(16) McMahon, W. E.; Braun, A. K.; Perna, A. N.; Coll, P. G.; Schulte, K. L.; Boyer, J. T.; Neumann, A. N.; Geisz, J. F.; Warren, E. L.; Ptak, A. J.; Merkle, A. P.; Bertoni, M. I.; Packard, C. E.; Steiner, M. A. In Situ Smoothing of Facets on Spalled GaAs(100) Substrates during OMVPE Growth of III-V Epilayers, Solar Cells, and Other Devices: The Impact of Surface Impurities/Dopants. *Cryst. Growth Des.* **2024**, *24* (8), 3218−3227.

(17) Biasiol, G.; Gustafsson, A.; Leifer, K.; Kapon, E. Mechanisms of Self-Ordering in Nonplanar Epitaxy of Semiconductor Nanostructures. *Phys. Rev. B* **2002**, *65* (20), 205306.

(18) Hofmann, L.; Knauer, A.; Rechenberg, I.; Zeimer, U.; Weyers, M. Comparison of Binary and Ternary Growth over Trenches Using MOVPE. *J. Cryst. Growth* **2000**, *213* (3−4), 229−234.

(19) Hofmann, L.; Knauer, A.; Rechenberg, I.; Weyers, M. MOVPE Growth of (AlGa)As and (InGa)P on GaAs-Based Trenches. In *26th International Symposium on Compound Semiconductors*, 1999; pp 75−79.

(20) Kim, S. I.; Kim, M. S.; Kim, Y.; Hwang, S. M.; Min, B. D.; Son, C. S.; Kim, E. K.; Min, S. K. Lateral Growth Rate Control of GaAs on Patterned Substrates by CCl4 and CBr4 during MOCVD. *J. Cryst. Growth* **1997**, *170* (1−4), 665−668.

(21) Ohtsuka, M.; Miyazawa, S. Model for Molecular-Beam-Epitaxy Growth over Nonplanar Surfaces. *J. Appl. Phys.* **1988**, *64* (7), 3522−3527.

(22) Soci, C.; Bao, X. Y.; Aplin, D. P. R.; Wang, D. A Systematic Study on the Growth of GaAs Nanowires by Metal-Organic Chemical Vapor Deposition. *Nano Lett.* **2008**, *8* (12), 4275−4282.

(23) Liu, Y.; Shimomura, S.; Sano, N.; Gamo, K.; Adachi, A.; Hiyamizu, S. Improved GaAs/AlAs multilayer structures grown by MBE on patterned GaAs (100) substrates with ridges along the (001) direction. *Semicond. Sci. Technol.* **1993**, *8*, 2197−2200.

(24) López, M.; Nomura, Y. Surface Diffusion Length of Ga Adatoms in Molecular-Beam Epitaxy on GaAs(100)−(110) Facet Structures. *J. Cryst. Growth* **1995**, *150*, 68−72.

(25) Mao, H.; Jing, W.; Wang, J.; Yu, J.; Wang, L.; Dai, N. Nucleation and Growth Mechanism of GaAs Epitaxial Growth. *Thin Solid Films* **2007**, *515* (7−8), 3624−3628.

(26) Rondanini, M.; Cavallotti, C.; Moscatelli, D.; Masi, M.; Carrà, S. A Combined Fluid Dynamic and 3D Kinetic Monte Carlo Investigation of the Selective Deposition of GaAs and InP. *J. Cryst. Growth* **2004**, *272* (1−4), 52−58.

(27) Jin Kim, H.; K Park, Y.; Kyu Kim, S. I. K.; Whan Kim, T.; Kim, T. W. Facet Evolution of Al 0.5 Ga 0.5 As/GaAs Multilayers Grown on Mesa-Patterned GaAs Substrate. *Jpn. J. Appl. Phys.* **1999**, *38* (9R), 4969−4972.

(28) Xue, Q. K.; Hashizume, T.; Sakurai, T. Scanning Tunneling Microscopy of III-V Compound Semiconductor (001) Surfaces. *Prog. Surf. Sci.* **1997**, *56* (1−2), 1−131.

(29) Li, L.; Qi, H.; Gan, S.; Han, B.-K.; Hicks, R. F. Site-Specific Chemistry of Carbon Tetrachloride Decomposition on GaAs(001). *Appl. Phys. A: Mater. Sci. Process.* **1998**, *66*, 501−505.

(30) Geisz, J. F.; France, R. M.; Schulte, K. L.; Steiner, M. A.; Norman, A. G.; Guthrey, H. L.; Young, M. R.; Song, T.; Moriarty, T. Six-Junction III−V Solar Cells with 47.1% Conversion Efficiency under 143 Suns Concentration. *Nat. Energy* **2020**, *5*, 326−335.

(31) Batyrev, I. G.; McMahon, W. E.; Zhang, S. B.; Olson, J. M.; Wei, S.-H. Step Structures on III-V Phosphide (001) Surfaces: How Do Steps and Sb Affect CuPt Ordering of GaInP? *Phys. Rev. Lett.* **2005**, *94*, 096101.

Supporting Information: Planarizing Spalled GaAs(100) Surfaces by MOVPE Growth

Gavin P. Forcade[1], William E. McMahon[2], Nicholas Yoo[3], Anica N. Neumann[2,3], Michelle Young[2], John Goldsmith[2], Karin Hinzer[1,4], Corinne E. Packard[2,3], Myles A. Steiner[2]

[1] Department of Physics, University of Ottawa, Ottawa, Ontario, Canada

[2] National Renewable Energy Laboratory, Golden, CO, USA

[3] Colorado School of Mines, Golden, CO, USA

[4] SUNLAB, School of Electrical Engineering and Computer Sciences, University of Ottawa, Ottawa, Ontario, Canada

Other planarization attempts

There are many different possible dopant/material combinations, and the methods used in this study can provide a framework for evaluating their effectiveness for substrate smoothing. Here we provide some additional examples not included in the main manuscript. We also attempted to planarize controlled spalled GaAs(100) substrates with a B spall and 6°A offcut. We failed to planarize that configuration with C:GaAs as shown in Figure S1, but were partially successful with Sb:GaInP as depicted in Figure S2 with similar results to Ref. [1] where they used Zn:GaInP. Our success with Sb:GaInP as the planarizing layer required pre-etching the sample to reduce the ridge heights to less than 1um, else composition variation ensued [2]. This composition variation caused lattice mismatching thereby impacting growth quality above, as highlighted in the valleys of Figure S2a.

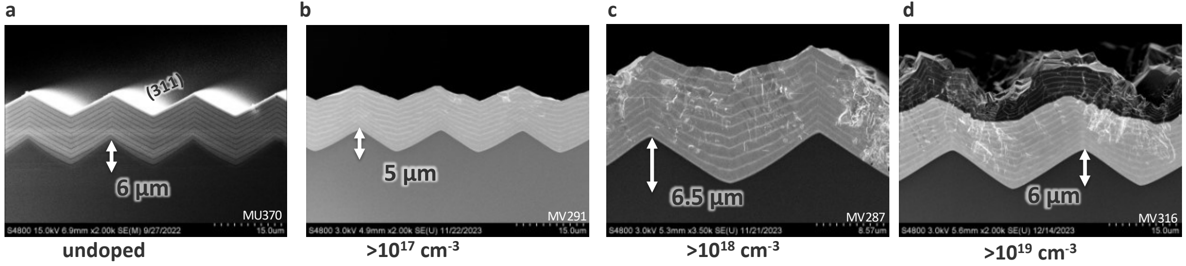

Figure S1. C:GaAs grown on B spall/6°A offcut samples. Cross-sectional scanning electron microscope images of spalled substrates with C:GaAs planarizing epi-growth at CCl_4 gas flow rates of **a** 0.0 sccm, **b** 0.001 sccm, **c** 0.01 sccm,

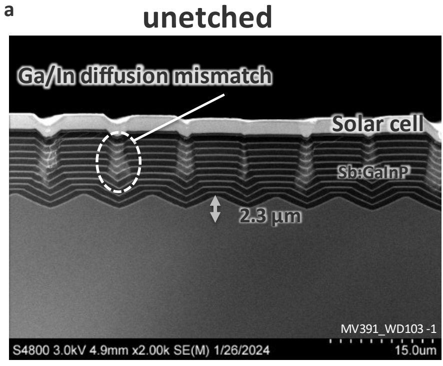

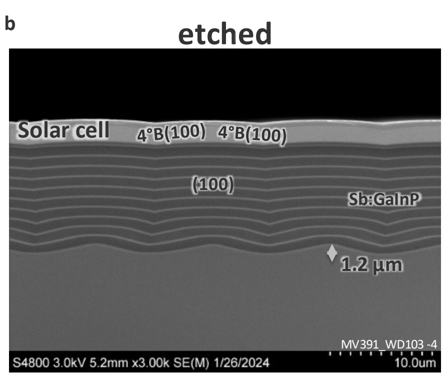

Figure S2. Sb:GaInP grown on B spall/6°A offcut samples. Cross-sectional scanning electron microscope images of spalled substrates with Sb:GaInP planarizing epi-growth lattice matched to GaAs with an **a** unetched and **b** etched sample. The Sb:GaInP thickness between GaAs marker layers is 1 µm. The lighter layers above the Sb:GaInP layer stack is a single junction solar cell.

Adatom diffusion model

Adatom diffusion model results are given in Figure 3e. We use this model to extract the diffusion length of Ga adatoms on the (100) facet during growth of C:GaAs on an A-spalled (100) 6°A substrate by MOVPE. To get an approximate value for the diffusion length, we model the [100] growth on plateaus that form by calculating the probability of Ga-adatoms reaching the edge of the plateau for a specified diffusion length. We make several assumptions in our model:

1. The initial propagation direction of adatoms is equally probable in all directions.
2. The precursor gas flow is uniform across the surface: the gas flow is coming down vertically through the chamber, thus to first order it is uniform across the microscopic landscape.
3. All directions have equal diffusion lengths: although this may not be accurate as was shown for molecular beam epitaxy of GaAs [3], it is a good first order approximation.
4. Since the valley facets have higher sticking coefficients than the (100) facet, we neglect the small amount of adatoms that migrate from the valleys to the plateaus.
5. There are no interactions between adatoms: at a growth rate of 6 μm/h and assuming the GaAs atomic density of 4.42×10^{22} cm^{-3} there is a minimum flux of 36 nm^{-2} s^{-1} Ga atoms depositing on the surface. Thus, Ga-adatoms require diffusion speeds to be at least on the order of 1000 m/s to make adatom interactions negligible. To put this velocity in perspective, the average velocity of an ideal gas made of Ga atoms is 580 m/s where we used the relation $\frac{1}{2}mv^2 = \frac{3}{2}k_BT$, m is the mass of the Ga atoms, v is the average velocity, k_B is the Boltzmann constant, and T is our growth temperature.

Let's assume a Ga-adatom lands on the (100) plateau at a distance z from the left-hand side edge as depicted in Figure S3. The probability that it stays on the (100) plateau assuming a diffusion length L and that it travels to the left-hand side can be calculated from the ratio of the non-escape angle (θ) and the quarter-circle angle of $\pi/2$. Also, when z is larger than L the atom cannot escape, thus we can formulate the following piecewise probability of the Ga-adatom staying on the (100) plateau when traveling to the left:

$$f(z) = \begin{cases} \dfrac{\sin^{-1}\left(\frac{z}{L}\right)}{\pi/2}, & \dfrac{z}{L} \leq 1 \\ 1, & \dfrac{z}{L} > 1 \end{cases} \tag{S1}$$

If the Ga-adatom travels to the right, the probability of staying on the (100) plateau is given by $f(w_{(100)}-z)$ where $w_{(100)}$ is the width of the plateau. To calculate the probability of an adatom that lands anywhere on the (100) plateau and stays ($G_{(100),\%}$) is given by taking the average of the probabilities of non-escape when traveling towards either side of the plateau and integrating over the width of the plateau as follows:

$$G_{(100),\%} = \frac{1}{w_{(100)}} \int_0^{w_{(100)}} \frac{\left(f(z) + f\left(w_{(100)} - z\right)\right)}{2} dz \tag{S2}$$

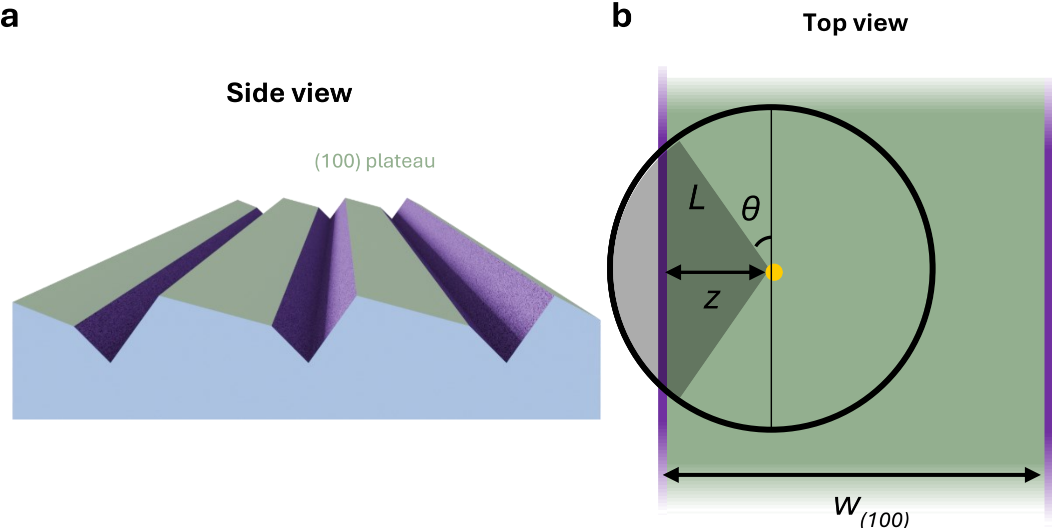

Figure S1. Ga-adatom surface diffusion. **a** Side view schematic of the surface morphology midway through the planarization with C:GaAs growth on the A spalled GaAs(100) 6°A offcut sample. **b** Top view of the (100) plateau that forms during this growth illustrating the movement of the Ga-adatom (yellow point) landing at a distance *z* from the left-hand side ledge. The shaded area subtends the escape cone of the adatom assuming a diffusion length *L*.

Surface morphology evolution model

Surface morphology evolution model results are shown in Figure 6. The model is used to postulate the highest impact mechanism affecting growth. The surface morphology evolution during epitaxy on micro/nanostructured surfaces is most accurately simulated by considering both gas phase and adatom diffusion using chemical potential gradients. Biasol et al. [2] reproduced measurements with a model considering adatom phase diffusion coupled with the chemical potential. These chemical potential gradient models are complex, requiring many input parameters. Instead, we model the surface morphology as a function of growth-time using the model from ref. [5] which only has two input parameters (R and L) and is given by:

$$\frac{\partial z}{\partial t} = \sqrt{1+p^2}R(\phi) - \frac{\sqrt{1+p^2}L^2}{2}\left(\frac{\partial^2 R(\phi)}{\partial s^2} - R(0)\frac{d^3x}{ds^3}\right) \tag{S3}$$

$$ds = \sqrt{1+p^2}dx, \qquad p = \frac{\partial z}{\partial x}$$

Where $R(\phi)$ is the growth rate in the normal direction of the local surface, θ is the angle of the local surface relative to the (100) facet, and L is the diffusion length. The model assumes the facet with the highest growth rate will emerge in concave areas and the slowest growth rate facet will emerge in convex areas. However, these facets can change with L_v. Within this modeling framework, we started by assuming the growth rate of the facets ($R(\phi)$) are proportional to the unreconstructed dangling bond density as was done in ref. [6]. We then improved the qualitative fit to measurement by adding additional functions to $R(\phi)$. Although this treatment neglects fundamental properties of an actual surface (like surface reconstruction), it does allow the surface energy as a function of facet angle to be varied, and this fundamentally underlies the changes in growth mode which are being modeled. We relate the dangling bond density between (100) to (011) facets (see "Dangling bond density model" section in the Supplementary Information for those results). To apply the model, we discretize the structured surface with equidistant spacing along the

horizontal (x) axis. We then increment small-time intervals (∂t) to calculate the vertical growth (∂z) of these points.

Dangling bond density model

As we associate the facet growth rates to the dangling bond density in Figure 6, in this section we equate the dangling bond density of unreconstructed zinc-blend/diamond crystal facets between (100) and (011) facets. The dangling bond density of unreconstructed facets between (100) to (111) was first calculated by Finnie et al. [7]. Their results on the dangling bond density (Bt/V) as a function of angle off the (100) facet (θ) up to (111) was:

$$\frac{Bt}{V} \propto 2\alpha\cos(\theta) + 2\sqrt{2}\left(\beta - \frac{\alpha}{2}\right)\sin(\theta) \tag{S4}$$

Where α is the number of bonds available on the smallest unit of (100) terrace, β is the number of bonds available on the smallest unit of (111) step.

Using their formalism, we expand the bond density equation to go from (111) to (011) facets. The surfaces between these facets can be related to a linear combination of (111) steps and (011) terraces. The (111) step is represented by the vector $b/\sqrt{3}(-2,1,1)$ where b is the bond length ($b = \sqrt{3}a/4$) and a is the crystal's lattice constant. The (011) terrace is represented by the vector $4b/\sqrt{3}(-1,0,0)$. Combining both vectors assuming there are *m* (011) terraces and p (111) steps, we get:

$$\bar{u} = \frac{bp}{\sqrt{3}}\left(\left[-\frac{4m}{p} - 2\right], 1, 1\right) \tag{S5}$$

Knowing that $\bar{u}$ should be perpendicular to the vector (*h,k,k*) representing facets between (111) and (011) with *k*>*h* and both being integers , we take the dot product and set it to zero:

$$\bar{u} \cdot (h,k,k) = \left(-\frac{4m}{p} - 2\right)h + 2k = 0 \tag{S6}$$

Assuming the minimum number of steps and terraces and *h,k* are written with no common factor, there are two cases depending on whether *h-k* is even or odd:

$$\begin{aligned} p = h, m = \frac{1}{2}(k-h) \quad &\text{for } h-k \text{ even} \\ p = 2h, m = (k-h) \quad &\text{for } h-k \text{ odd} \end{aligned} \tag{S7}$$

If γ represents the number of bonds available on the (011) terrace, then the dangling bond count is:

$$B = p\left(\frac{\gamma m}{p} + \beta\right) \tag{S8}$$

We also need the following relations provided in ref. [7] to get a nice final solution that relates *h,k* to the angle (θ) relative to the (100) surface:

$$t = \frac{a}{\mu_{h-k}\sqrt{h^2+2k^2}}, \quad \cos(\theta) = \frac{\frac{h}{k}}{\sqrt{\left(\frac{h}{k}\right)^2 + 2}}, \quad \sin(\theta) = \frac{\sqrt{2}}{\sqrt{\left(\frac{h}{k}\right)^2 + 2}} \tag{S9}$$

Where t is the thickness of the (*h,k,k*) facet, $\mu_{h-k} = 1$ for *h-k* even and $\mu_{h-k} = 2$ for *h-k* odd. Combining Equation (S8) with Equations (S9), we get the dangling bond density on surfaces from (111) to (011) as a function of the angle relative to the (100) facet:

$$\frac{Bt}{V} \propto \left(\beta - \frac{\gamma}{2}\right)\cos(\theta) + \frac{\gamma}{2\sqrt{2}}\sin(\theta) \tag{S10}$$

Where $V = a^3/4$ is the three-dimensional unit cell volume. For GaAs surfaces in an atmosphere with a high V/III ratio such as during our growth runs, As atoms terminate the surfaces. In this environment, A-surfaces have $\alpha = 2$, $\beta = 3$, and $\gamma = 4$ and B-surfaces have $\alpha = 2$, $\beta = 1$, and $\gamma = 4$.

Growth rate relations for C:GaAs

This section is to provide the mathematical representation of the facet growth rate as a function of facet angle relative to (100) given in Figure 6h. We use the following equation to empirically relate the facet growth rate of A facets relative to the (100) facets for GaAs growth with high CCl_4 gas flow:

$$R(\theta) \propto a_1\, D_1(\theta)\big(1 + a_2\, W(\theta) + a_3 S(\theta)\big) + a_4 \cos(\phi) \tag{S11}$$

Where a_i are weighting factors, and $D_1(\theta)$ is the unreconstructed dangling bond density of A facets assuming a high V/III ratio (Eqs. S4 and S10) but with $\alpha = 0$ instead of $\alpha = 2$. An $\alpha = 0$ could result from atomic surface reconstruction due to CCl_4 or its by-products, which passivate the (100) terraces, thereby minimizing its Ga adatom sticking coefficient.

The functional form of $W(\theta)$ is given by:

$$W(\theta) = \frac{\sin(-2|h - h_{int}| + 0.5)}{2n}$$

with

$$n = \begin{cases} 1 & \text{for } h < 2.5 \\ \dfrac{h-1}{2} & \text{for } h > 2.5 \end{cases}, \qquad h_{int} = round(h), \qquad h = \frac{remainder\left(\frac{j}{2}\right)}{2}, \qquad j = \frac{\sqrt{2}}{\tan(\theta)}, \tag{S12}$$

where *h,k* are integers such that they make (*hkk*)A facets. This empirical function is a proxy example for surface energy varying with facet angle relative to (100) and could be caused by atomic surface reconstructions. Equation (S12) reaches maxima for h odd and minima for h even with sinusoidal interpolations between extrema. In addition, the $W(\theta)$ has a decreasing impact as we near the (100) surface due to the division by *n*. The variable *n* represents the number of atoms forming the (100) terrace for the surface (*hkk*)A*,* we pinned it to 1.0 for *h*<2.5 to dismiss the asymptotic behavior near *h*=1.

The function $S(\theta)$ in Eq. S11 is a proxy function to represent a single growth rate spike at the (711)A facet and is given by:

$$S(\theta) = \begin{cases} W(\theta) * n & \text{for } 6.5 < h < 7.5 \\ 0 & \text{otherwise} \end{cases} \tag{S13}$$

The growth rate spike at (711)A can be due to a surface reconstruction induced by CCl_4 or its by-products which increases its Ga adatom sticking coefficient.

Modeling surface morphology evolution for B spall / A offcut

To further demonstrate the significant role of surface dangling bonds in undoped GaAs growth by MOVPE under our growth conditions, we qualitatively compared results for growth on a B-spalled 6°A offcut sample in Figure S2. The surface morphology evolution is accurately simulated with facet growth rates (*R*) either proportional to the unreconstructed dangling bond density ($D_0(\theta)$) or a cosine function (the functions are equivalent from (100) to (111)B facets), as shown in Figure S4b. However, not all facet growth rate functions are effective; a linear relation (Figure S4d) does not reproduce the measured morphology

evolution, as depicted in Figure S4c. These results highlight the importance of accurately modeling the growth rate near (100) for our configuration.

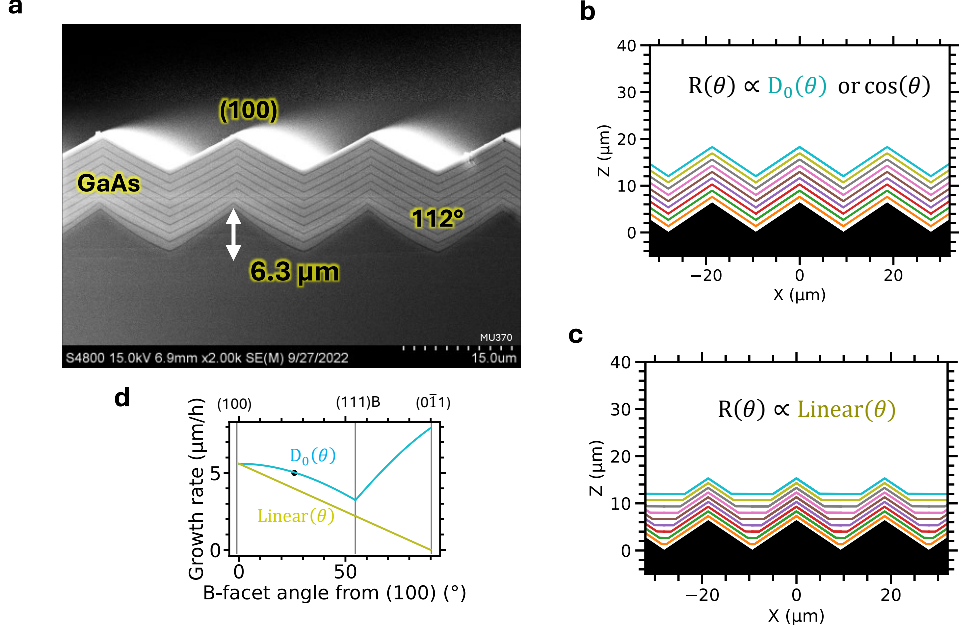

Figure S2. Surface morphology evolution of undoped GaAs on B spall / 6°A offcut substrate. **a** Cross-sectional scanning electron microscope image of the sample and the initial structural parameters used as input for the model. Modeled growth morphology assuming **b** the bond density model or a cosine function and **c** a linear function to relate the growth rate to the B-facet angle from the (100) facet. **d** Plot of the growth rate functions used in **b,c**. The black point is the measured growth rate from **a**.

Chapter 7

Summary & outlook

This thesis focuses on leveraging innovative structured surfaces, device design, and new epitaxial growth processes to promote the adoption of III-V PV devices. III-V PVs offer the highest optical-to-electrical power conversion efficiency of any material class due to their high crystalline quality and bandgap flexibility. However, the high costs of III-V materials hinder their widespread adoption. To address this challenge, this thesis integrated structured surfaces in CPV systems to enhance their optical performance, customized PV device designs for NFTPV and PPC applications to improve their performance, and developed epitaxial growth processes to enable substrate reuse.

Chapter 3 investigated a novel encapsulant for CPV systems, featuring a microstructured surface created by silica microbeads partially submerged in an encapsulating PDMS layer. This new encapsulant increased the collected current of CPV submodules by 2.6% and reduced cell-to-cell variability compared to a standard reference encapsulant. When optimized, it was predicted to improve current collection by up to 3.4%. Devices designed using this model were also shown to extend the operational performance of CPV systems over a wider temperature range. These results prompted further study, leading Leoga *et al.* [84] to conduct outdoor testing of fabricated modules. They found that the new encapsulant improved CPV module efficiency by up to $19\%_{\mathrm{rel}}$ compared to the reference encapsulant. A long-term stability study is now necessary before commercializing the technology.

Chapter 4 explored InAs-based III-V PVs designs for waste heat recovery using NFTPV

technology. The papers presented in this work provide key design guidelines for achieving efficiencies up to 15%. Despite using a gold back-reflector, significant parasitic absorption was still observed. This absorption could be further reduced with an air-bridge back-reflector [85]. Additionally, SRH recombination was found to be non-negligible, suggesting that optimizing epitaxy growth conditions could enhance NFTPV device performance, though Auger recombination remains a limiting factor. Epi-grown back reflector NFTPV devices were fabricated and characterized, showing promising optical and dark current-voltage characteristics. However, they still require testing under near-field illumination from a hot radiator.

Chapter 5 studied the performance and design of PPC devices for the optical fiber transparent window (1.0-1.6 μm wavelengths). These devices were fabricated at Fraunhofer ISE's state-of-the-art clean room facilities. A predictive drift-diffusion model was calibrated to design the epi-stack of multi-junction PPC devices, achieving a record peak efficiency of 53.6% with a 1.446 μm laser wavelength, as predicted. It was found that device designs with a current-limited bottom subcell in multi-junction PPCs ensures light-trapping of emitted photons from radiative recombination, enhancing device performance. Given the computational expense of this model, resource-conserving machine learning techniques (such as dimensionality reduction [86]) could be employed to design future devices. Using a DCM model, it was determined that device heating, rather than series resistance, was the main performance limiter at high irradiances. This finding confirmed that the front-metallic and current-spreading layer designs made by Fraunhofer ISE do not require further optimization.

Chapter 6 employed epitaxial growth by MOVPE to planarize faceted GaAs(100) substrates. The faceted surface was formed by fracturing the top epi-stack from the substrate, a process known as spalling. This approach aims to reduce the cost of III-V PV by enabling substrate reuse. Our study found that highly doped C:GaAs grown on a 2°B offcut GaAs(100) wafer showed the best planarization capability, utilizing 95% of the nominally deposited material to fill the valleys within 33 minutes. The carbon gas flow and offcut angle significantly impacted the planarizing performance. However, whether the planarized surface can produce PV devices as effectively as standard epi-ready substrates has yet to be determined. Future work will also focus on the potential for multiple reuse cycles of the substrate through repeated spalling and planarization. This substrate reuse method could lower the costs of III-V materials, making them more viable for a range of applications beyond photovoltaics, including optoelectronics,

high-speed electronics, and even certain types of sensors.

Overall, this thesis has demonstrated practical pathways for improving III-V device efficiencies while considering design cost-constraints, with applications in CPV, NFTPV, PPC, and III-V PV technologies. Further modelling and design efforts are required to continue to push technology performance towards their theoretical limits. For CPV systems, the optimized structured surface presented in this thesis eliminated reflection at the air/PDMS interface, additional optical losses in the system could be mitigated using similar methodologies. The theoretical efficiencies for InAs-based NFTPV devices operating at 900 K can reach up to 40%, which is more than double the predicted performance of the design presented in this thesis. Present designs are limited by parasitic sub-bandgap absorption. The efficiency of the PPC devices investigated in this thesis are $\sim$27$\%_{\mathrm{rel}}$ below their radiative limit, demonstrating the need for continued development of these technologies. Finally, the planarization process through epitaxial growth presented in this thesis is nearing maximum-possible material utilization, but could benefit from increased growth rates to reduce reactor time.

References

[1] M. A. Green, E. D. Dunlop, M. Yoshita, N. Kopidakis, K. Bothe, G. Siefer, D. Hinken, M. Rauer, J. Hohl-Ebinger, and X. Hao, "Solar cell efficiency tables (Version 64)," *Progress in Photovoltaics: Research and Applications*, vol. 32, pp. 425–441, 7 2024.

[2] J. Grandidier, A. Akins, D. Crisp, J. Lee, J. Schwartz, R. Bugga, J. L. Hall, S. Limaye, and E. J. Brandon, "Feasibility of power beaming through the Venus atmosphere," *Acta Astronautica*, vol. 211, pp. 376–381, 2023.

[3] Z. Aqachmar, T. Bouhal, and K. Lahrech, "Energetic, economic, and environmental (3 E) performances of high concentrated photovoltaic large scale installations: Focus on spatial analysis of Morocco," *International Journal of Hydrogen Energy*, vol. 45, pp. 10840–10861, 4 2020.

[4] S. Fafard and D. P. Masson, "Perspective on photovoltaic optical power converters," *Journal of Applied Physics*, vol. 130, p. 160901, 2021.

[5] R. Mittapally, B. Lee, L. Zhu, A. Reihani, J. W. Lim, D. Fan, S. R. Forrest, P. Reddy, and E. Meyhofer, "Near-field thermophotovoltaics for efficient heat to electricity conversion at high power density," *Nature Communications 2021 12:1*, vol. 12, pp. 1–8, 7 2021.

[6] T. Inoue, T. Koyama, D. D. Kang, K. Ikeda, T. Asano, and S. Noda, "One-Chip Near-Field Thermophotovoltaic Device Integrating a Thin-Film Thermal Emitter and Photovoltaic Cell," *Nano Letters*, vol. 19, pp. 3948–3952, 6 2019.

[7] A. Fiorino, L. Zhu, D. Thompson, R. Mittapally, P. Reddy, and E. Meyhofer, "Nanogap near-field thermophotovoltaics," *Nature Nanotechnology*, vol. 13, pp. 806–811, 9 2018.

[8] C. Amy, H. R. Seyf, M. A. Steiner, D. J. Friedman, and A. Henry, "Thermal energy grid storage using multi-junction photovoltaics," *Energy and Environmental Science*, vol. 12, pp. 334–343, 1 2019.

[9] J. Nelson, *The physics of Solar Cells*. Imperial College Press, 2003.

[10] NREL, "Champion Photovoltaic Module Efficiency Chart," 5 2024.

[11] A. Ritou, P. Voarino, and O. Raccurt, "Does micro-scaling of CPV modules improve efficiency? A cell-to-module performance analysis," *Solar Energy*, vol. 173, pp. 789–803, 2018.

[12] John F. Geisz, Ryan M. France, Kevin L. Schulte, Myles A. Steiner, Andrew G. Norman, Harvey L. Guthrey, Matthew R. Young, Tao Song, and Thomas Moriarty, "Six-junction III–V solar cells with 47.1% conversion efficiency under 143Suns concentration," *Nature Energy*, vol. 5, pp. 326–335, 2020.

[13] V. D. Rumyantsev, N. Y. Davidyuk, E. A. Ionova, P. V. Pokrovskiy, N. A. Sadchikov, and V. M. Andreev, "Thermal Regimes of Fresnel Lenses and Cells in "All-Glass" HCPV Modules," in *AIP Conference Proceedings*, pp. 89–92, 2010.

[14] G. P. Forcade, A. Ritou, P. St-Pierre, O. Dellea, M. Volatier, A. Jaouad, C. E. Valdivia, K. Hinzer, and M. Darnon, "Microstructured antireflective encapsulant on concentrator solar cells," *Progress in Photovoltaics: Research and Applications*, vol. 30, pp. 132–140, 2 2022.

[15] M. Bedjaoui, B. Despax, M. Caumont, and C. Bonafos, "Si nanocrystal-containing SiOx (x ¡ 2) produced by thermal annealing of PECVD realized thin films," *Materials Science and Engineering B: Solid-State Materials for Advanced Technology*, vol. 124-125, pp. 508–512, 12 2005.

[16] J. O. Carneiro, F. Machado, L. Rebouta, M. I. Vasilevskiy, S. Lanceros-Méndez, V. Teixeira, M. F. Costa, and A. P. Samantilleke, "Compositional, Optical and Electrical Characteristics of SiOx Thin Films Deposited by Reactive Pulsed DC Magnetron Sputtering," *Coatings*, vol. 9, p. 468, 7 2019.

[17] G. Zhang, Y. Cao, Y. Zhang, X. Song, J. Lu, and S. Li, "Preparation and characteristic analysis of ultra-low dielectric constant nano-porous silicon oxide films," in *Lecture Notes in Electrical Engineering*, vol. 600, pp. 730–736, Springer, 2020.

[18] C. Forman, I. K. Muritala, R. Pardemann, and B. Meyer, "Estimating the global waste heat potential," *Renewable and Sustainable Energy Reviews*, vol. 57, pp. 1568–1579, 5 2016.

[19] G. P. Forcade, C. E. Valdivia, S. Molesky, S. Lu, A. W. Rodriguez, J. J. Krich, R. St-Gelais, and K. Hinzer, "Efficiency-optimized near-field thermophotovoltaics using InAs and InAsSbP," *Appl. Phys. Lett*, vol. 121, p. 193903, 2022.

[20] H. Ritchie, P. Rosado, and M. Roser, "Energy Production and Consumption," *Our World in Data*, 2020.

[21] I. A. Okanimba Tedah, F. Maculewicz, D. E. Wolf, R. Schmechel, I. A. O. Tedah, F. Maculewicz, D. E. Wolf, and R. Schmechel, "Thermoelectrics versus thermophotovoltaics: Two approaches to convert heat fluxes into electricity," *Journal of Physics D: Applied Physics*, vol. 52, p. 275501, 5 2019.

[22] G. R. Bhatt, B. Zhao, S. Roberts, I. Datta, A. Mohanty, T. Lin, J. M. Hartmann, R. St-Gelais, S. Fan, and M. Lipson, "Integrated near-field thermo-photovoltaics for heat recycling," *Nature Communications*, vol. 11, no. 2545, 2020.

[23] C. Lucchesi, D. Cakiroglu, J. P. Perez, T. Taliercio, E. Tournié, P. O. Chapuis, and R. Vaillon, "Near-Field Thermophotovoltaic Conversion with High Electrical Power Density and Cell Efficiency above 14%," *Nano Letters*, vol. 21, pp. 4524–4529, 6 2021.

[24] W. B. Spillman, D. H. Crowne, and D. W. Woodward, "Optically powered and interrogated rotary position sensor for aircraft engine control applications," *Optics and Lasers in Engineering*, vol. 16, pp. 105–118, 1992.

[25] F. V. Batista De Nazaré and M. M. Werneck, "Hybrid optoelectronic sensor for current and temperature monitoring in overhead transmission lines," *IEEE Sensors Journal*, vol. 12, no. 5, pp. 1193–1194, 2012.

[26] K. Worms, C. Klamouris, F. Wegh, L. Meder, D. Volkmer, S. P. Philipps, S. K. Reichmuth, H. Helmers, A. Kunadt, J. Vourvoulakis, A. W. Bett, C. Koos, W. Freude, J. Leuthold, and W. Stork, "Reliable and lightning-safe monitoring of wind turbine rotor blades using optically powered sensors," *Wind Energy*, vol. 20, pp. 345–360, 2017.

[27] K. Goto, T. Nakagawa, O. Nakamura, and S. Kawata, "An implantable power supply with an optically rechargeable lithium battery," *IEEE Transactions On Biomedical Engineering*, vol. 48, no. 7, pp. 830–833, 2001.

[28] C. Vázquez, J. Dayron López-Cardona, P. C. Lallana, D. S. Montero, M. Abdulhussein Al-Zubaidi, S. Pérez-Prieto, and I. P. Garcilópez, "Multicore fiber scenarios supporting power over fiber in radio over fiber systems," *MCF Scenarios Supporting Power Over Fiber in Radio Over Fiber Systems*, vol. 7, pp. 158409–158418, 2019.

[29] H. Helmers, C. Armbruster, M. Von Ravenstein, D. Derix, and C. Schöner, "6-W optical power link with integrated optical data Transmission," *IEEE Transactions on Power Electronics*, vol. 35, no. 8, pp. 7904–7909, 2020.

[30] S. Fafard and D. P. Masson, "High-efficiency and high-power multijunction InGaAs/InP photovoltaic laser power converters for 1470 nm," *Photonics*, vol. 9, 6 2022.

[31] C. Algora, I. García, M. Delgado, R. Peña, C. Vázquez, M. Hinojosa, and I. Rey-Stolle, "Beaming power: Photovoltaic laser power converters for power-by-light," *Joule*, vol. 6, pp. 340–368, 2022.

[32] E. F. Schubert, *Light-emitting diodes, second edition*. Cambridge University Press, 2 ed., 2006.

[33] K. A. W. Horowitz, T. Remo, B. Smith, and A. Ptak, "A Techno-Economic Analysis and Cost Reduction Roadmap for III-V Solar Cells," tech. rep., National renewable energy laboratory, Golden, 2018.

[34] K. L. Schulte, S. W. Johnston, A. K. Braun, J. T. Boyer, A. N. Neumann, W. E. McMahon, M. Young, P. G. Coll, M. I. Bertoni, E. L. Warren, and M. A. Steiner, "GaAs solar cells grown on acoustically spalled GaAs substrates with 27% efficiency," *Joule*, vol. 7, pp. 1529–1542, 7 2023.

[35] J. Chen and C. E. Packard, "Controlled spalling-based mechanical substrate exfoliation for III-V solar cells: A review," *Solar Energy Materials and Solar Cells*, vol. 225, 6 2021.

[36] A. N. Neumann, P. G. Coll, M. I. Bertoni, M. A. Steiner, and E. L. Warren, "Wet-Etching of Acoustically Spalled GaAs for Substrate Reuse," *IEEE Journal of Photovoltaics*, vol. 14, pp. 281–287, 3 2024.

[37] M. Beattie, *Semiconductor materials and devices for high efficiency broadband and monochromatic photovoltaic energy conversion*. PhD thesis, University of Ottawa, Ottawa, 2021.

[38] Y. A. Du, S. Sakong, and P. Kratzer, "As vacancies, Ga antisites, and Au impurities in zinc blende and wurtzite GaAs nanowire segments from first principles," *PHYSICAL REVIEW B*, vol. 87, p. 75308, 2013.

[39] P. Y. Yu and M. Cardona, *Fundamentals of Semiconductors: Physics and Materials Properties, 4th Edition*. Springer, 4 ed., 2010.

[40] R. Pelzel, "A Comparison of MOVPE and MBE Growth Technologies for III-V Epitaxial Structures," in *CS Mantech Conference*, (New Orleans), 2013.

[41] Y. Liu, S. Shimomura, N. Sano, K. Garno, A. Adachi, and S. Hiyamizu, "Improved GaAs/AIAs multilayer structures grown by MBE on patterned GaAs (100) substrates with ridges along the [011] direction," *Semicond. Sci. Technoi*, vol. 8, pp. 2197–2200, 1993.

[42] M. López and Y. Nomura, "Surface diffusion length of Ga adatoms in molecular-beam epitaxy on GaAs(100)–(110) facet structures," *Journal of Crystal Growth*, vol. 150, pp. 68–72, 5 1995.

[43] Q. K. Xue, T. Hashizume, and T. Sakurai, "Scanning tunneling microscopy of III-V compound semiconductor (001) surfaces," *Progress in Surface Science*, vol. 56, pp. 1–131, 9 1997.

[44] A. Ohtake, "Surface reconstructions on GaAs(001)," *Surface Science Reports*, vol. 63, pp. 295–327, 7 2008.

[45] W. E. McMahon, A. K. Braun, A. N. Perna, P. G. Coll, K. L. Schulte, J. T. Boyer, A. N. Neumann, J. F. Geisz, E. L. Warren, A. J. Ptak, A. P. Merkle, M. I. Bertoni, C. E. Packard, and M. A. Steiner, "In Situ Smoothing of Facets on Spalled GaAs(100) Substrates during OMVPE Growth of III-V Epilayers, Solar Cells, and Other Devices: The Impact of Surface Impurities/Dopants," *Crystal Growth and Design*, vol. 24, pp. 3218–3227, 4 2024.

[46] I. Vurgaftman, J. R. Meyer, and L. R. Ram-Mohan, "Band parameters for III-V compound semiconductors and their alloys," *Journal of Applied Physics*, vol. 89, pp. 5815–5875, 6 2001.

[47] M. Sotoodeh, A. H. Khalid, and A. A. Rezazadeh, "Empirical low-field mobility model for III-V compounds applicable in device simulation codes," *Journal of Applied Physics*, vol. 87, pp. 2890–2900, 3 2000.

[48] H. H. Wieder, "Transport coefficients of InAs epilayers," *Appl. Phys. Lett*, vol. 25, p. 206, 1974.

[49] M. Levinshtein, S. Rumyantsev, and M. Shur, *Handbook Series on Semiconductor Parameters, vol. 1*. World Scientific, 1996.

[50] Y. Lin, A. R. Arehart, and A. M. Carlin, "Separation of bulk and surface electron transport in metamorphic InAs layers using quantitative mobility spectrum analysis," *Appl. Phys. Lett*, vol. 93, p. 62109, 2008.

[51] R. T. Hinkey, Z. Tian, and R. Q. Yang, "Reflectance spectrum of plasmon waveguide interband cascade lasers and observation of the Berreman effect," *Journal of Applied Physics*, vol. 110, p. 43113, 2011.

[52] S. Law, D. C. Adams, A. M. Taylor, and D. Wasserman, "Mid-infrared designer metals," *Optics Express*, vol. 20, no. 22, p. 12155, 2012.

[53] D. Wei, S. Maddox, P. Sohr, S. Bank, S. Bank, S. Law, and S. Law, "Enlarged growth window for plasmonic silicon-doped InAs using a bismuth surfactant," *Optical Materials Express, Vol. 10, Issue 2, pp. 302-311*, vol. 10, pp. 302–311, 2 2020.

[54] T. I. Voronina, T. S. Lagunova, S. S. Kizhayev, S. S. Molchanov, B. V. Pushnyĭ, and Y. P. Yakovlev, "MOCVD growth and Mg-doping of InAs layers," *Semiconductors 2004 38:5*, vol. 38, pp. 537–542, 5 2004.

[55] A. Venter, P. Shamba, L. Botha, and J. R. Botha, "Growth and electrical characterization of Zn-doped InAs and InAsSb," *This Solid Films*, vol. 517, pp. 4468–4473, 2009.

[56] L. Botha, P. Shamba, and J. R. Botha, "Electrical characterization of InAs thin films," *Physica Status Solidi (C) Current Topics in Solid State Physics*, vol. 5, no. 2, pp. 620–622, 2008.

[57] J. Wróbel, G. A. Umana-Membreno, J. Boguski, S. Złotnik, A. Kowalewski, P. Moszczyński, J. Antoszewski, L. Faraone, and J. Wróbel, "InAs light-to-heavy hole effective mass ratio determined experimentally from mobility spectrum analysis," *Opto-Electronics Review*, vol. 31, no. e144567, 2023.

[58] M. M. Wilkins and K. Hinzer, "Multi-junction solar cells, Chapter 40," in *Handbook of Optoelectronic Device Modeling and Simulation*, vol. 2, ch. 40, Taylor & Francis, 2017.

[59] A. Krier, *Mid-infrared Semiconductor Optoelectronics*. Springer Series in Optical Sciences, 2006.

[60] H. K. Raut, V. A. Ganesh, A. S. Nair, and S. Ramakrishna, "Anti-reflective coatings: A critical, in-depth review," 10 2011.

[61] P. Schygulla, P. Fuß-Kailuweit, O. Höhn, and F. Dimroth, "Determination of the complex refractive index of compound semiconductor alloys for optical device modelling," *Journal of Physics D: Applied Physics*, vol. 53, p. 495104, 2020.

[62] D. Hahn, O. Jaschinski, H.-H. Wehmann, A. Schlachetzki, and M. Von Ortenberg, "Electron-concentration dependence of absorption and refraction in n-In0.53Ga0.47As near the band-edge," *Journal of Electronic Materials*, vol. 24, no. 10, pp. 1357–1361, 1995.

[63] W. W. Anderson, "Absorption constant of Pb1-xSnxTe and Hg1-xCdxTe alloys," *Infrared Physics*, vol. 20, no. 6, pp. 363–372, 1980.

[64] S. Adachi, *Optical properties of crystalline and amorphous semiconductors: Materials and Fundamental Principles*. Kluwer Academic Publishers, 1999.

[65] S. J. Byrnes, "Multilayer optical calculations," tech. rep., arXiv, 3 2016.

[66] J. J. Hench, Z. E. Strakoš, and S. Strakoš, "The RCWA method - A case study with open questions and perspectives of algebraic computations," *Electronic Transactions on Numerical Analysis*, vol. 31, pp. 331–357, 2008.

[67] K. Han and C. H. Chang, "Numerical Modeling of Sub-Wavelength Anti-Reflective Structures for Solar Module Applications," *Nanomaterials 2014, Vol. 4, Pages 87-128*, vol. 4, pp. 87–128, 1 2014.

[68] R. St-Gelais, L. Zhu, S. Fan, and M. Lipson, "Near-field radiative heat transfer between parallel structures in the deep subwavelength regime," *Nature Nanotechnology*, vol. 11, pp. 515–520, 2016.

[69] M. T. H. Reid, A. W. Rodriguez, and S. G. Johnson, "Fluctuation-Induced Phenomena in Nanoscale Systems: Harnessing the Power of Noise," *Proceedings of the IEEE*, vol. 101, no. 2, pp. 531–545, 2013.

[70] M. Francoeur, M. Pinar Mengüç, and R. Vaillon, "Solution of near-field thermal radiation in one-dimensional layered media using dyadic Green's functions and the scattering matrix method," *Journal of Quantitative Spectroscopy and Radiative Transfer*, vol. 110, pp. 2002–2018, 12 2009.

[71] M. V. Kurik, "Urbach rule," *physica status solidi (a)*, vol. 8, no. 1, pp. 9–45, 1971.

[72] Ansys, "https://www.ansys.com/products/optics/ansys-zemax-opticstudio."

[73] J. P. Hugonin and P. Lalanne, "RETICOLO software for grating analysis," tech. rep., Institut d'Optique/CNRS, 1 2021.

[74] V. Liu and S. Fan, "S4 : A free electromagnetic solver for layered periodic structures," *Computer Physics Communications*, vol. 183, pp. 2233–2244, 10 2012.

[75] S. Molesky and S. Lu, "heatSlabs," 2020.

[76] M. N. Beattie, H. Helmers, G. P. Forcade, C. E. Valdivia, O. Hohn, and K. Hinzer, "InP- and GaAs-based photonic power converters under O-band laser illumination: Performance analysis and comparison," *IEEE Journal of Photovoltaics*, vol. 13, pp. 113–121, 1 2023.

[77] *Sentaurus TCAD User's Manual*. Synopsys Inc, 2021.

[78] R. E. Bank, D. J. Rose, and W. Fichtner, "Numerical Methods for Semiconductor Device Simulation," *IEEE Transactions on Electron Devices*, vol. 30, no. 9, pp. 1031–1041, 1983.

[79] J. H. Albers, P. Roitman, C. L. Wilson, R. E. Bank, A. H. Sherman, S. C. Eisenstat, M. C. Gursky, M. A. Schultz, A. H. Sher nan, D. P. Kennedy, D. R. Myers, and J. R. Ehrstein, "Measurement of high.field drift velocity of electrons in inversion layers on silicon," *IEEE Transactions on Electron Devices*, vol. 21, no. 9, pp. 359–377, 1983.

[80] A. W. Walker, *Bandgap engineering of multi-junction solar cells using nanostructures for enhanced performance under concentrated illumination*. PhD thesis, University of Ottawa, Ottawa, 2013.

[81] E. M. Lysczek, J. A. Robinson, and S. E. Mohney, "Ohmic contacts to p-type InAs," *Materials Science and Engineering B*, vol. 134, pp. 44–48, 2006.

[82] Y. Zhao, M. J. Jurkovk, and W. I. Wang, "Characterization of AuGe-and AuTe-Based Ohmic Contacts on InAs n-Channel High Electron Mobility Transistors," *The Electrochemical Society Proceedings Series*, vol. 144, no. 3, p. 174, 1997.

[83] J. H. Klootwijk and C. E. Timmering, "Merits and Limitations of Circular TLM structures for contact resistance determination for novel 111-V HBTs," in *IEEE Int. Conference on Microelectronic Test Structures*, vol. 17, pp. 247–252, 2004.

[84] A. J. Leoga, A. Ritou, M. Blanchard, L. Dirand, Y. Prunier, P. St-Pierre, D. Chuet, P.-O. Provost, M. Volatier, V. Aimez, G. Hamon, A. Jaouad, C. Dubuc, and M. Darnon, "Outdoor Characterization of Solar Cells With Microstructured Antireflective Coating in a Concentrator Photovoltaic Monomodule," *IEEE Journal of Photovoltaics*, vol. 13, no. 5, 2023.

[85] D. Fan, T. Burger, S. McSherry, B. Lee, A. Lenert, and S. R. Forrest, "Near-perfect photon utilization in an air-bridge thermophotovoltaic cell," *Nature*, vol. 586, pp. 237–241, 9 2020.

[86] D. Melati, Y. Grinberg, M. Kamandar Dezfouli, S. Janz, P. Cheben, J. H. Schmid, A. Sánchez-Postigo, and D.-X. Xu, "Mapping the global design space of nanophotonic components using machine learning pattern recognition," *Nature Communications*, vol. 10, no. 4775, 2019.